Structure and properties of $(Ba,Sr)(Co,Fe,Mo)O_3$ perovskite oxides

Thesis submitted in accordance with the requirements of the University of Liverpool for the degree of Doctor in Philosophy

by

Maria A. Tsiamtsouri

September 2012

Abstract

The work presented in this thesis focuses on the effect on structure and properties of the cubic perovskite system, $Ba_{0.5}Sr_{0.5}Co_{0.8}Fe_{0.2}O_{3-\delta}$ (BSCF), when Mo^{6+} partially substitutes the B-site elements (Co, Fe). BSCF is a candidate cathode material for intermediate temperature (500-750^{o}C) solid oxide fuel cells (IT-SOFCs), showing promising electrochemical activity for the oxygen reduction reaction (ORR). Doping of the parent material BSCF with Mo^{6+} targeted the retention of the cathodic performance whilst improving the reported structural thermal instability and incompatibility issues with commonly used electrolytes.

A range of $Ba_{0.5}Sr_{0.5}Co_{0.8-x}Fe_{0.2-y}Mo_{x+y}O_{3-\delta}$ (BSCFM) compositions were synthesised, with variation to the Mo content and the Co/Fe ratio. Characterization was carried out by a combination of diffraction and microscopy techniques. It was found that the introduction of Mo^{6+} into the BSCF perovskite system favored the formation of perovskite structures with double the lattice parameters of the parent BSCF compound; these are referred as double perovskite (DP) phases to distinguish them from the single perovskite (SP) counterparts. The doubling of the unit cell was attributed to B-site ordering between Mo^{6+} and Co^{2+} due to the considerable difference in cation size and charge. The SP and DP phases coexisted in all the BSCFM compositions studied, with increasing DP volume as the Mo^{6+} content was increased.

The structural and electrochemical characterisation was focused on the composition $Ba_{0.5}Sr_{0.5}Co_{0.5}Fe_{0.125}Mo_{0.375}O_{3-\delta}$, (abbreviated as BSCFMo0.375-(Co/Fe=4) which demonstrated favourable stability and compatibility properties with state the of the art electrolyte SDC ($Sm_{0.2}Ce_{0.8}O_{2-\delta}$), which was used in this study. It also displayed the best electrochemical performance among the BSCFM compositions studied by AC impedance measurements in air; an area specific resistance (ASR) of 0.13 $\Omega.cm^2$ was obtained at 650^{o}C. As observed from AC impedance measurements under variable oxygen partial pressure (pO_2) environments for this composition, the activity of the ORR was found to be limited primarily by oxygen chemical exchange. The full structural analysis of the biphasic BSCFMo0.375-(Co/Fe=4) was a great challenge and was performed by combined refinement using Neutron and X-ray data and double-checked by a range of methods including microscopy techniques, Mössbauer spectroscopy, iodometric titrations and thermogravimetric analysis. The optimal performance of BSCFMo0.375-(Co/Fe=4) among the BSCFM compositions studied was attributed to the synergistic effect of the major DP (70% by weight) phase, which was found to be an oxygen-stoichiometric Co^{2+},Mo^{6+}-rich, Fe^{3+}-poor compound, with the minor SP (30% by weight) Co^{3+},Fe^{3+}-rich, Mo^{6+}-poor component with significant oxygen vacancy concentration.

Acknowledgements

I would like to express my deep appreciation to all those who - directly or indirectly -contributed to the work presented in this thesis. First and foremost I would like to thank my primary supervisor Prof. Matt Rosseinsky for giving me the opportunity to work in his group and cooperate with excellent scientists, his continued guidance and his inspiring scientific attitude. I would also like to thank especially my secondary supervisor Dr. John Claridge for his invaluable advice and always being there for questions.

I am very grateful to Dr. Christopher Thomas for helping me at my first synthetic attempts. Special thanks go to the visitor researcher Dr. Yohann Bréard whom I consider as my mentor; his experience in scientific thinking and structural characterisation were crucial for the work presented in this thesis. It would be a serious omission if I didn't thank my teacher 'Steven', Zengqiang Deng, who taught me the secrets of cathodes and electrochemical measurements in less than a week but his training served as a light-house during my whole PhD time.

Special thanks also go to the 'BSCFM team'; Dr. Antoine Demont, for the dark field TEM images and fruitful structural discussions, as well as Dr. Ruth Sayers who helped me to develop my understanding in materials properties and for being an example to follow in organisation and presentation skills. I would like to express huge and sincere thanks to Dr. Phil Chater for his patient teaching of TOPAS software, which I finally used for the structural refinenents in my thesis, and valuable suggestions for the preparation of this manuscript. I greatly appreciate the hard microscopy work by Dr. Zhongling Xu and Dr. Simon Romani, which was detrimental for the BSCFM work**,** as well as Dr. Mike Thomas for the Mossbauer results and his kind teaching**.** I would also like to thank Dr. Carlos Martí Gastaldo for his persistence and methodic approach to successfully obtain sorption measurements of the BSCFM symmetrical cells, which I know that was not easy, and James Gallagher for valuable discussions about porosity studies. I am also very grateful to Dr. Christopher Ireland and Dr. Xinming Wang for the SEM images; without these, the work presented in this thesis would not be complete. I would also like to thank the beamiline scientists in I11, namely Prof. C. Tang, Dr. S. Thomson and Dr. J. Parker, for ensuring that the experiments were running smoothly, as well as Dr. Aziz Daoud-Aladine and Dr. Kevin Knight in HRPD for all the instrument support and emails full of valuable suggestions. Words are not enough to thank the 'invisible hero' Dr. Hongjun Niu for all the technical support.

This page is unfortunately not enough to thank all previous and present members in the MJR group for useful discussions and contributing to a pleasant working environment. I would like to thank in particular Darren Hodgeman, Dr. Mike Pitcher and Dr. Hripsime Gasparyan who spent time to read this manuscript and gave me valuable feedback. Finally, I wish to thank my family and friends, in Liverpool and back home, for their good company and support during my PhD time.

Table of Contentss

1. CHAPTER 1- INTRODUCTION

Introduction

1.1. Environmental context- Energy demands

Traditional power generation based on oil, coal and natural gas causes serious air and water pollution globally, mainly due to the carbon dioxide accumulation and its threatening consequences of global warming, climate change and rising sea levels[1, 2]. Engineers and environmentalists have long dreamed of efficient, reliable and inexpensive sources of energy, with a minimal environment impact, to meet with the growing population demands and diminishing reserves of fossil fuels[1, 3]. Solar panels and wind farms are familiar images of alternative energy technologies; however their applications are limited due to a lack of portability and reliability, as for example on a cloudy or windless day[4].

The focus of this thesis is fuel cell technologies and specifically solid oxide fuel cells (SOFCs). The fuel flexibility of fuel cells means that they can be introduced in the hydrogen based economy; hydrogen can produce electricity relatively efficiently and can be regenerated through the electrolysis of water[1, 5]. Moving away from hydrocarbons as fuels and CO_2 emissions is a step towards environmentally friendlier energy generation[3, 5].

Fuel cells have been know since 1838-1839, when the German scientist Christian Friedrich Schönbein first demonstrated that energy can be produced by combining hydrogen with oxygen while conducting electrolysis experiments[6] and Sir William Grove built the first fuel cell, which he termed a "gas voltaic battery", observing electric current generation when

combining hydrogen with oxygen in the presence of platinum[7]. The term 'fuel cell' is credited to Ludwig Mond and Carl Langer who in 1889 were using air and coal gas in their cells showing the early potential of fuel cells using fossil fuels[8]. A landmark in fuel cell technology is the development and successfully testing of the 'solid electrolyte fuel cell' by scientists in Westinghouse Electric Coorporation (now Siemens Westinghouse) in 1962[9]. Since then there has been an intense research in suitable materials that would lead to the development and large scale commercial implementation of fuel cells.

The operation concepts of fuel cells are discussed in *Section 1.2*, focusing on solid oxide fuel technology. This is followed by a brief introduction of the main structural types (*Section 1.3*) of SOFCs components and a review of both conventional and state of the art materials (*Section 1.4*). The motivation of the work undertaken in this thesis is explained in *Section 1.5*.

1.2. SOFCs

1.2.1. Principle of operation

Fuel cells [3, 10-13], in general, are electrochemical energy conversion devices which convert the chemical energy of a fuel directly to electricity, similar to batteries. However, fuel cells differ to the lifetime-limited batteries as energy is produced via the oxidation of a continuously provided fuel, like internal combustion engines do. The main advantage of fuel cells compared to conventional methods of power generation is their higher conversion efficiency. The theoretical efficiency of fuel cells, reported to be 45-60%-that is higher in comparison to heat engines, which are limited by the Carnot's law. During the operation of the fuel cells, the usual losses involved in the conversion of the chemical energy of the fuel to heat, to mechanical energy and then to electricity are avoided.

A fuel cell single cell consists of two electrodes (the anode and the cathode) separated by the electrolyte. Each of these main components serves a different function through a continuously operated cycle, which combines a fuel and an oxidant to produce electricity. Hundreds of these cells are then connected in series, by an interconnect, to form a "fuel cell stack", so that the electricity that each cell generates can be combined.

The fuel, supplied to the anode, undergoes an oxidation reaction and produces electrons. The generated electrons are used at the cathode to reduce the oxidant to oxidative species, which then migrate through the electrolyte, to the anode to complete the circuit. The electron flow from the anode to the cathode produces direct-current electricity, providing a source of useable electrical energy to an external circuit (*Figure 1.1*).

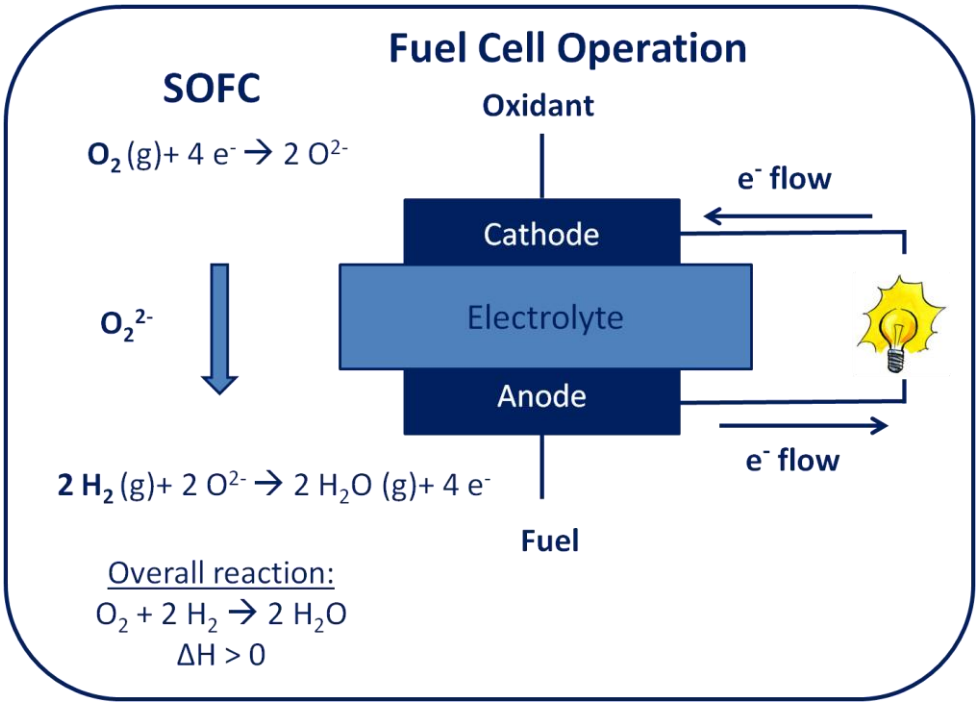

Figure 1.1: Schematic diagram of fuel cell, showing the different components and the path that the electrons follow in order to provide electrical energy to an external circuit. The principle operation of a solid oxide fuel cell (SOFC) is shown on the left, emphasizing that mobile oxygen ions are transported from the cathode, through the electrolyte, to the anode and the overall exothermic reaction results in electrical energy, water steam and heat.

In theory, any gases capable of being electrochemically oxidised and reduced can be used as fuel and oxidant accordingly in the fuel cell system[13]. Hydrogen is currently the most common fuel, since it has high electrochemical reactivity and can be derived from common fuels. Oxygen is the most common oxidant, since it is readily and economically available from air. This reaction combines hydrogen and oxygen to form electricity, water vapor and heat. The by-products water and heat can be further utilized by the fuel cell system, improving further the efficiency of the fuel cells and make them one of the most environmentally friendly power generation devices.

Waste heat can be utilised for space heating and cooling and the water vapor can be captured and used as the feedstock for additional hydrogen[14].

The key component of fuel cells is the electrolyte, which main role is to conduct ions between the two electrodes, may be solid or liquid. The ion conduction is a thermally activated process and its magnitude depends significantly on the type of the materials used. There are various types of fuel cell technologies, operating over a range of temperatures from ambient to over 1000 ^{o}C and using a diverse range of materials[15, 16]. The different fuel cell types are usually distinguished by the electrolyte and named after the mobile ionic species transported through the electrolyte to and from the electrodes. The main fuel cell technologies[10, 17] can be classified as 'low temperature', such as polymer electrolyte membranes/ fuel cells (PEM/PEFC, mobile ions: hydronium ions ($(H_2O)_nH^+$), T: 70-110^{o}C), alkaline fuel cells (mobile ions: hydroxide ions (OH), T: 100-250^{o}C) and phosphoric acid fuel cells (PAFC, mobile ions: protons (H^+), T: 150-250^{o}C), and 'high temperature'. Molten carbonate fuel cells (MCMC, mobile ions: carbonate ions (CO_3^{2-}), T: 500-700^{o}C) and solid oxide fuel fuels (SOFC, mobile ions: oxide ions (O^{2-}), T: 500-1000^{o}C) operate at elevated temperatures. The fuel cell type of interest in this thesis is the solid oxide fuel cell (SOFC), an all solid-state device, with an oxide-ion conducting solid electrolyte and mixed electronic-ionic conductors (MIEC) electrodes. SOFCs are preferred to the fuel systems containing corrosive liquids as electrolytes that limits the lifetime of their components and raises environmental issues for their disposal.

The electrode reactions for the case of a SOFC, when H_2 is the fuel and O_2 is the oxidant, are given below. Oxygen reduction occurs at the cathode producing oxygen ion species which then migrate through the electrolyte to the anode where the fuel is oxidised.

Cathode reaction: $O_2\ (g) + 4\ e^- \rightarrow 2\ O^{2-}$ *Equation 1.1*

Anode reaction: $2\ H_2\ (g) + 2\ O^{2-} \rightarrow 2\ H_2O\ (g) + 4\ e^-$ *Equation 1.2*

Overall reaction: $O_2 + 2\ H_2 \rightarrow 2\ H_2O$ *Equation 1.3*

The chemical energy of the fuel, H_2, is thus converted to electrical energy through an exothermic reaction producing water as waste.

The ceramics used in SOFCs do not become electrically and ionically active until they reach very high temperatures and as a consequence, temperatures ranging from 500 to 1000 °C are needed, due to the relatively high charge and size of oxygen species. High operation temperature also enables the internal reforming of fuels, i.e. the conversion of hydrocarbons to CO or CO_2 and H_2, which results in fuel flexibility. SOFC technology is thus not limited to high purity hydrogen, an additional advantage compared to competing fuel cell technologies, reducing operating costs and tackles the issue of hydrogen storage[3, 13].

There are two operating temperature regimes for SOFCs; high (HT-SOFCS: 750°C to 1000°C) and intermediate (IT-SOFCs: 500°C to 750°C)[10]. High operation temperature (>750^{o}C) is advantageous for the oxygen kinetics and the waste heat produced at this temperature also facilitates the integration of SOFC and a gas turbine into a power generation system which further increases the efficiency. However, materials choice in terms of stability and compatibility is limited at high temperatures and there is a tendency to move to the intermediate temperature range. IT-SOFCs are especially suitable for small scale applications, such as micro combined heat and power devices (micro-CHP) in stationary applications and auxiliary power units (APUs) in mobile applications (automotive; refrigeration units)[18].

1.2.2. Insight into the cathode processes

At the cathode, the oxygen reduction reaction (ORR) takes place, as expressed, as expressed in *Equation 1.1*. However, the actual reaction is quite complex and comprises of a number of elemental steps, mainly diffusion of oxygen molecules to the cathode, adsorption to the surface and/or the bulk of the cathode (*Equation 1.4*), dissociation of molecular to atomic species (*Equation 1.5*), oxygen exchange redox reaction between the adsorbed oxygen and the cathode material producing oxygen ions (*Equation 1.6*); the latter equation describes both the charge transfer from the cathode to oxygen species before or after the dissociation and the incorporation of oxide ions into vacancies in the crystal lattice of the cathode. The produced oxygen ions are then transported to and across the cathode-electrolyte interface and finally they are incorporated into the crystal structure of the electrolyte [19].

$$O_2(g) \rightleftharpoons O_2(ads) \qquad \textit{Equation 1.4}$$

$$O_2(ads) \rightleftharpoons 2\ O(ads) \qquad \textit{Equation 1.5}$$

$$O(ads) + Vo^{\bullet\bullet} + 2\ e^- \rightleftharpoons O_O^{2-} \qquad \textit{Equation 1.6}$$

where O_2(ads) and O(ads) indicate the adsorbed oxygen molecule and oxygen atom respectively, and $V_o^{\bullet\bullet}$ refers to oxygen vacancies, with an effective charge of +2q, in the cathode material.

Two main oxygen reduction paths can be distinguished: the 'surface path' and the 'bulk path', depending on the intrinsic ionic conductivity properties of the cathode materials. For materials which are poor ionic conductors, the surface path (*Figure 1.2A*) is strongly favored.

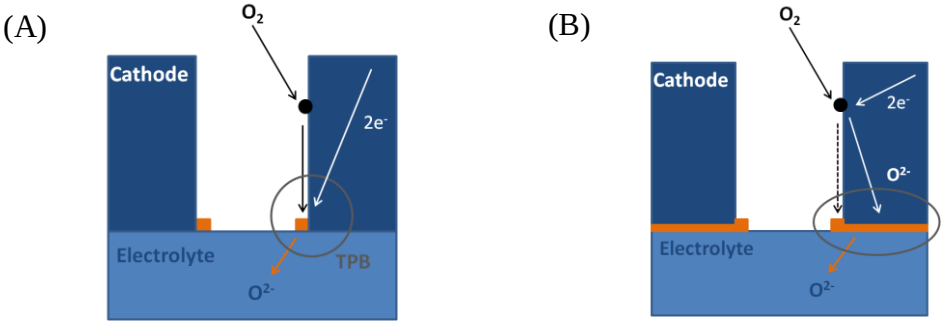

Figure 1.2: Schematic representation of the oxygen reduction reaction (ORR) at the cathode via (A) the surface path, for materials which are purely electronic conductors and (B) via the bulk path, for mixed electronic-ionic conductors (MIEC) [20].

According to this, the oxygen adsorption, dissociation, charge transfer and incorporation all take place at the surface of the cathode material and subsequently the produced oxygen ions migrate to the electrolyte. The reactive sites for the reduction of oxygen are located at the three-phase boundary (TPB) where gas, cathode and electrolyte meet, which represents only a small fraction of the whole electrode/electrolyte arrangement. On the contrary, for materials exhibiting a certain ionic conductivity besides the electronic conductivity, as in the case of mixed electronic-ionic conductors (MIEC), the oxygen incorporation can proceed mainly through the bulk path (*Figure 1.2B*). According to this, the oxygen adsorption, dissociation and charge transfer occur mainly in the bulk of the cathode and the incorporated oxygen ions migrate through the bulk cathode material to the whole cathode-electrolyte contact area and finally to the electrolyte [21, 22].

1.2.3. SOFC component requirements

The requirements for SOFC components[13, 20] are discussed below and summarised in *Table 1.1*. In general, the reactivity between the components must be as low as possible and the thermal expansion coefficients (TEC) must be as close matching, so as to minimize thermal stresses which could lead to cracking and mechanical failure. Moreover, all the SOFC components must possess enough chemical, structural and morphologic stability at the conditions required for SOFC operation and fabrication.

Table 1.1: Summary of requirements for SOFC components[13, 20]

Component	**Conductivity**		**Stability**	**Porosity**
	Ionic	Electronic		
Electrolyte	High	Negligible	In fuel and oxidant environments	Fully dense
Cathode	Desirable	High	In oxidant environments	Porous
Anode	Desirable	High	In fuel environments	Porous

An additional requirement for the anode and cathode materials is the stability in the fuel and oxidant atmospheres respectively. Similarly, the SOFC electrolyte, which separates the two electrode components, should be stable in both oxidising and reducing conditions. The anode and

the cathode materials should also possess sufficient porosity to allow gas transport to the reaction sites and have high catalytic activity for the electrochemical reduction of the oxidant and the oxidation of the fuel respectively. On the contrary, the electrolyte materials should be fully dense in order to prevent short circuiting of reacting gases through it.

The electrical requirements of the SOFC components vary according to their function in the cell. The main function of the SOFC electrolyte is to conduct oxide ions between the cathode and the anode, thus it needs to exhibit high ionic conductivity conduction (> 0.05.S $cm^{-1)}$) at a low enough temperature (<1,000^{o}C)[23] to be technically useful. It also requires negligible electronic conductivity to prevent voltage losses due to the electronic current flowing through the electrolyte.

On the contrary, the electrodes (anode and cathode) should have sufficient electronic conductivity to support the electron flow to the reactive sites. Moreover, good ionic conductivity for the electrodes is desirable, providing an oxygen path for the oxygen ions produced at the cathode and transferred, through the electrolyte, to the anode. If the electrode materials display considerable ionic conductivity, as well as high electronic conductivity, then they are called mixed electronic-ionic conductors (MIEC). The transport of electrons and oxygen ions to and from the reactive sites in the anode and the cathode is related to their activity for reduction of oxygen and oxidation of the fuel respectively. The most common way to measure the combined electronic, ionic conductive properties and the electrochemical activity is from the area specific resistance (ASR); a target value of 0.15 $\Omega.cm^2$ [24] has been set for each component at temperatures below 600^{o}C. The largest contribution to the total resistance at decreased operating temperatures is the cathode polarization resistance, associated particularly with the kinetics of oxygen reduction[3, 13].

1.2.4. Mass and charge transport in SOFC components

The operation of a SOFC is based fundamentally on the transport of charged particles in the ceramic components. The SOFC electrolytes should display high ionic conductivity, whilst the electrode materials should primarily conduct the transport of electrons with ionic conductivity also desirable. The movement of atoms and charged species in the components of a SOFC are governed by mass and charge transport.

1.2.4.1. Mass transport-Diffusion

The movement of atoms and ionic species in the components of a SOFC occurs via diffusion from an area of high concentration to an area of low concentration. The diffusion is described by Fick's first and second laws, with specific geometric and concentration boundary conditions dependent on the experimental arrangement[25]. Fick's first law (in one-dimension) states that the particle flux J, defined as the number of particles per unit area per unit time at a steady- state, is proportional to the concentration gradient (*Equation 1.7*). Fick's second law describes the accumulation or depletion of concentration C when steady-state conditions are not met (*Equation 1.8*)

$$J = -D\left(\frac{dC}{dx}\right) \qquad \textit{Equation 1.7}$$

$$\frac{\partial C}{\partial t} = -\frac{\partial J}{\partial x} = D\left(\frac{\partial^2 C}{\partial x^2}\right) \qquad \textit{Equation 1.8}$$

where *D* is the diffusion coefficient

The diffusion coefficient (D) is independent of the concentration for dilute solutions, due to the low probability of defects interacting with each other.

In most technologically interesting oxide materials for SOFC applications, the diffusion of oxygen ionic species is significantly faster than cation diffusion[26].

1.2.4.2. Charge transport

The charge transport is expressed by the electrical conductivity (σ), which is a measure of a materials ability to transport charged particles under the application of an applied electric field[25]. The electrical conductivity is defined as the charge flux (Ji) per unit electric field (E) for a particle i with charge ($Z_i \cdot e$).

$$\sigma_i = \frac{Ji\ (Z_i\ e)}{E} = \frac{C_i \nu_i\ (Z_i\ e)}{E} = C_i \mu_i\ (Z_i\ e) \qquad \textit{Equation 1.9}$$

where ν_i refers to the particle velocity, C_i is the particle concentration and μ_i denotes the particle electrical mobility per unit field of charge.

The total electrical conductivity is the sum of the individual conductivities of each charged particle. In ceramic oxide materials, electrical conductivity can be either electronic, ionic or mixed ionic-electronic and the total conductivity can be written as the sum of electrons (electronic conductivity, σ(el)) and oxygen ions (ionic conductivity, σ (ion)) contribution (*Equation 1.10*), assuming that they are transported independently of each other which in most cases is a good approximation[13, 25].

$$\sigma\ (tot) = \Sigma\sigma i = \sigma\ (el) + \sigma\ (ion) \qquad \textit{Equation 1.10}$$

As discussed previously, for the electrolyte component, the electronic contribution should be negligible and hence the ionic conductivity dominates. Conversely for the electrodes, the electronic conductivity is usually the main conductivity process. This is due to the faster electrical mobility of the smaller and less charged electrons, which is generally 10^4 to 10^8 times higher than that of the bulkier and higher charged oxygen –ion species even at elevated temperatures[13]. In this case, if ionic conduction is to dominate, a relatively high concentration of ionic carriers is required.

1.2.5. Ionic and electronic conductivity in SOFC components

1.2.5.1. Origin

The electrical conductivity properties of a material depend on the materials lattice defects. Lattice or crystal[13, 27] defects are lattice imperfections from the periodicity in a perfect crystal and they are favored up to a certain concentration, due to the reduction of free energy in the lattice. The lattice defects can be classified by the shape and size of the defect. Defects occurring at isolated atomic positions, are named as point defects, and can be due to the presence of a foreign (or interstitial) atom at particular site atoms or to a vacancy where normally one would expect an atom. Point defects in two dimensions are called dislocations (or line defects) while point defects in the whole layer in a crystal structure are called plane defects. In a crystal lattice, some of the vacancies and/or interstitials vibrate at their points and move to other vacancies and/or interstitials respectively by thermal fluctuation, chemical diffusion or an applied electric field. The vacant lattice points left can be then occupied by other lattice points.

Transition metals play an important role for the *electronic mobility/conductivity*, due to their ability to sustain multiple oxidation states and hence act like charge-carriers. This can be described by *Equation 1.11*, according to the the Kröger–Vink notation, where the reduction of transition metals (M) is accompanied by the formation of electron holes ($h^{\bullet}$) in the material[3]. Reducible transition metals such as Mn, Co, Fe, Ni are usually preferred in materials used as cathodes in solid oxide fuel cells (SOFCs)[28, 29]. As a consequence, the generation of oxygen vacancies (*Equation 1.12*) in the crystal lattice is directly linked to the transition metals environment and their oxidation state.

$$M^{\bullet}_{M} \rightleftharpoons M^{x}_{M} + h^{\bullet} \qquad \textit{Equation 1.11}$$

where $M^{\bullet}_{M}$ refers to $M^{(x+1)}$ localized on $M^{(x)}$ site, M^{x}_{M} *stands for* $M^{(x)}$ and $h^{\bullet}$ for electron holes with an effective charge of +q.

$$O^{x}_{O} + 2\,h^{\bullet} \rightleftharpoons \tfrac{1}{2}\,O_2 + Vo^{\bullet\bullet} \qquad \textit{Equation 1.12}$$

where O^{x}_{O} is the lattice oxygen and $Vo^{\bullet\bullet}$ refers to the oxygen vacancies with an effective charge of +2q.

The intrinsic electronic and ionic conductivities of a material can be enhanced by suitable heterovalent substitutions, where ions are substituted by other ions of different charge, due to charge compensation. When a cation in the crystal structure is substituted by a lower valance cation, anion vacancies and/ or cation interstitials can be produced due to ionic and/or electronic compensation respectively. Similarly, when a cation in the crystal structure is substituted by a higher valance cation, anion interstitials and/ or cation vacancies are formed to compensate the overall increase in overall charge[13, 25, 27].

1.2.5.2. Mechanisms of electronic conductivity

The transport of electrons in the SOFC components is controlled by the concentration of electrons and their mobility as expressed in *Equation 1.9*. According to the band theory, the atomic orbitals have combined to form bands, consisting of comparable energy levels, with a filled valence band, and an empty higher energy conduction band. These are separated by an energy gap (band gap, *E*g), which is defined as the difference in energy between the highest occupied state of the valance band and lowest unoccupied state of the conduction band. The electrical conductivity is described by the number of electrons situated in the conductance band. Hence, the electrons mobility is related to the electron's energy to overcome the energy gap *Eg* and exit to the conduction band (*Figure 1.3)*[27, 30, 31].

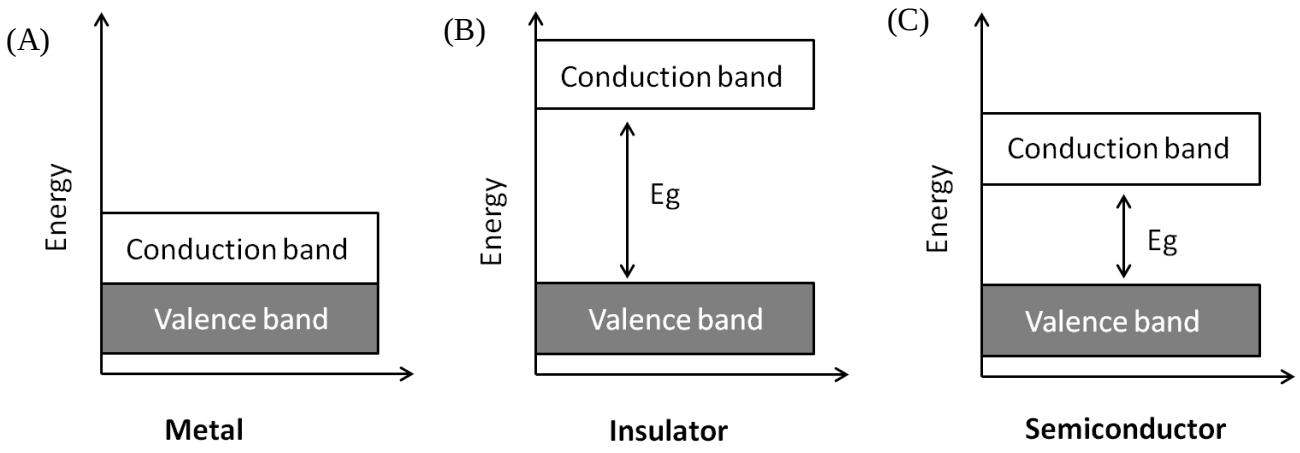

Figure 1.3: Band structure of (A) metals, (B) insulators and (C) semiconductors, where gray and white areas represent the valence band and conductance band respectively; Eg is the energy band gap between them.

Compounds displaying metallic behavior have a large number of electrons, which are completely delocalized and free to move throughout the structure. In the band theory, this is depicted as an overlap of the valence band and the conduction band so that at least a fraction of the valence electrons can move through the material (*Figure 1.3A*). With increasing the temperature, the electronic mobility in metals gradually decreases due to collisions between the electrons. On the contrary, for materials showing insulating behavior, all the valence electrons are either tightly bound to individual atoms or localized in bonds between atoms. In this case, there is a large forbidden Ed gap between the energies of the valence electrons and the energy at which the electrons can move freely through the material (*Figure 1.3B*). Semiconductivity can be described as an intermediate situation between metallic and insulting behavior, by which a certain number of valence electrons can reach the conduction band (*Figure 1.3C*). Although no conduction occurs at 0 K, at higher temperatures a finite number of electrons can reach the conduction band and provide some electronic conductivity[27, 32, 33]. Typical values for electronic conductivity for each type [27] are given in *Table 1.2*.

Table 1.2: Typical values of electronic conductivity[27]

	Electronic conductivity ($S.cm^{-1}$)
Metals	10^{-1}-10^{5}
Semiconductors	10^{-5}-10^{2}
Insulators	$<10^{-12}$

According to the band theory for semiconductors, electrons promoted into the conduction band are regarded as negative charge carriers (e^-), whereas the unoccupied states in the valence band are considered as positive holes ($h^\bullet$). The number of electrons in the conduction band is dependent on the magnitude of the band gap Eg and the temperature. The electronic conductivity of semiconductors can be enhanced by decreasing the band gap Eg and hence making the conduction band much more thermally accessible at temperatures above absolute zero. This can be done by introducing heterovalent ions (dopants) leading to semiconducting behavior that proceeds via p-type (p for positive) or n-type (n for negative) mechanism[27, 32, 33].

In the case of p-type semiconductivity (holes, $h^{\bullet}$, as carriers), the valence of the dopant is greater than the valence of the atoms in the host semiconductor material. The p-type dopant is considered as an electron acceptor promoting the formation of holes in the valence band of the host material. According to the band theory, the energy level of the p-type dopant is situated above the top of the valence band, accepts electrons from the valence and hence decreases the band gap Eg (*Figure 1.4A*). On the contrary, in n-type semiconductivity (electrons as carriers), the dopant atoms are in lower valence than the host atoms and hence are capable of providing extra conduction electrons to the semiconductor material. The energy level of the n-type dopant is situated below the bottom of the conductance band (*Figure 1.4B*), hence decreases the band gap Eg and the electrons from the valence band require less energy to excite from their valence band[27, 30, 32].

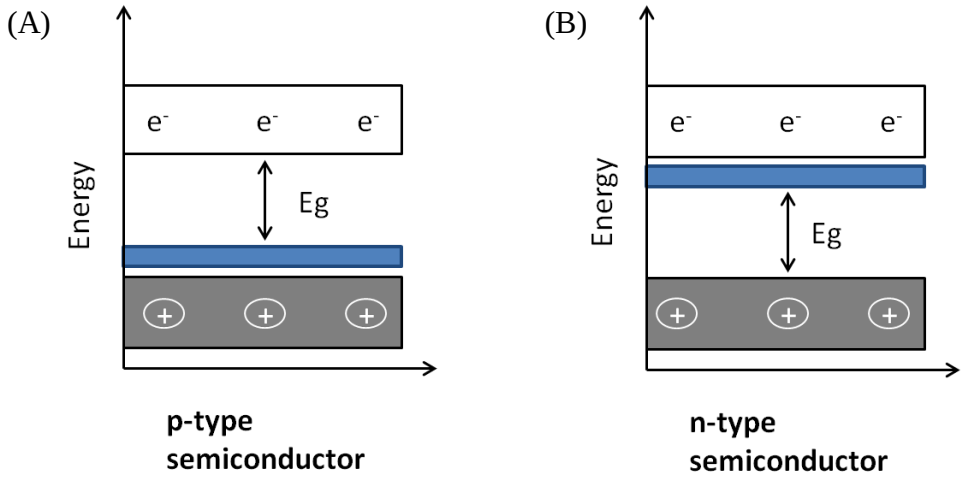

Figure 1.4: Band structure of (A) p-type and (B) n-type semiconductor, where gray, white and blue areas represent the valence, the conductance and dopant bands respectively; Eg is the energy gap for an electron (e^-) to enter the conductance band by leaving unoccupied states in the valence band, which are considered as positive holes.

1.2.5.3. Mechanisms of ionic conductivity

The movement of oxygen ionic species in the components of a SOFC can be described by both charge transfer (Section 1.2.5.1) and diffusion from an area of high concentration to an area of low concentration. For the latter, the transportation of oxygen ionic species in the components of a SOFC can mainly proceed either via vacancy or interstitial migration or a combination of both[34], depending on the concentration of oxygen vacancies or oxygen interstitial atoms in the crystal of the material. Vacancy migration (*Figure 1.5A*) occurs via a hopping mechanism, whereby an atom 'jumps' from its normal position on the lattice to a neighboring equivalent but vacant site and hence atoms move through the crystal by making a series of exchanges with vacancies. Interstitial mechanism (*Figure 1.5B*) is when an atom located on an interstitial site 'jumps' to a vacant adjacent equivalent site and migrates through the lattice by continuing this process. Interstitial diffusion is normally faster than vacancy diffusion because the probability of an empty adjacent interstitial site is greater than for a vacancy adjacent to a host atom. It is also possible that the interstitial mechanism occurs in two steps involving the displacement of an atom from an occupied lattice site by an interstitial atom, which then moves to another interstitial site; this is called indirect interstitial or interstitialcy mechanism[34] (*Figure 1.5C*).

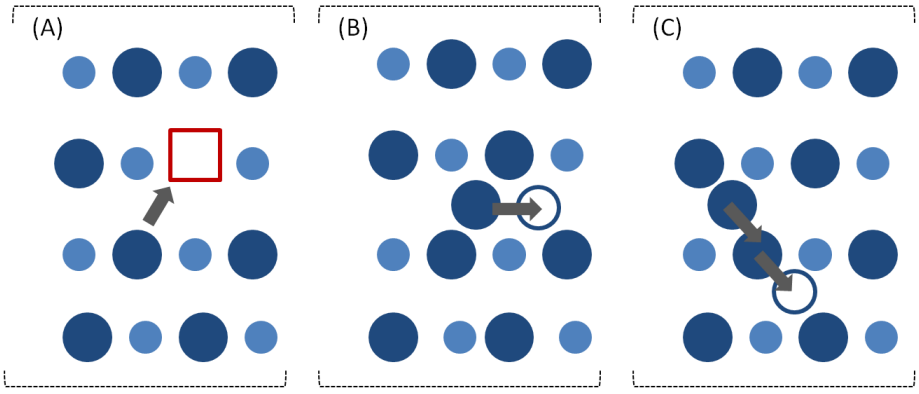

Figure 1.5: Schematic representation of oxygen atomic motion via (A) vacancy, (B) interstitial and (C) interstitialcy mechanisms [35].

The oxygen transport is generally measured by oxygen permeation and oxygen tracer diffusion methods. In SOFC oxide materials, the vacancy mechanism is predominant in a number of oxygen deficient fluorites, commonly used as electrolytes, and perovskite-related systems mainly employed as cathode materials[26, 36].

1.3. Description of structures

1.3.1. Perovskite

Perovskite structured materials, having the general formula ABO_3, are very popular as SOFC cathodes and are also used for electrolyte materials. The ideal perovskite-type structure has cubic symmetry with space group $Pm\bar{3}m$ and it can be described as a cube made by corner sharing BO_6 octahedra, consisting of 6-fold coordinated B cations (*Figure 1.6*). The BO_6 octahedra are linked by the vertices, forming a BO_3 layer which has cavities occupied by the A-cations, which are sharing of 12 atoms of oxygen. The A-site is the most commonly occupied by larger cations, such as alkaline and alkaline earth ions or rare earths, whilst the B-site is likely occupied by a smaller transition metal[27, 37].

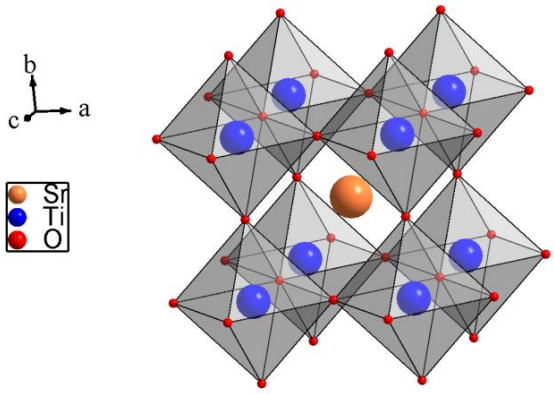

Figure 1.6: Structure of the typical perovskite $SrTiO_3$. The Sr^{2+} ions are marked in orange, the Ti^{4+} ions in blue and the O^{2-} are marked in red.

In the ideal cubic unit cell structure, where the atoms are connecting to each other, the B-O (r_B + r_O) distance is a/2 (where a is the cubic unit cell), while the A cation is situated in the middle of the cubic diagonal and the A-O (r_A + r_O) distances are $a\sqrt{2}/2$. Hence, in the ideal cubic structure, the bond lengths are related by the formula:

$$(R_A + R_O) = \sqrt{2}\,(R_B + R_O) \qquad \textit{Equation 1.13}$$

where R_A, R_B and R_O are the ionic radii of A, B and O ions respectively.

However, the flexible perovskite structure can distort itself, whilst still keeping the cubic structure; the degree of the deviation from the cubic structure is given by the tolerance factor, t

(*Equation 1.14*). Although for an ideal perovskite, t is unity, it is still possible to obtain a stable perovskite for 0.75< t < 1[38].

$$t = \frac{R_A + R_O}{\sqrt{2}\,(R_B + R_O)} \qquad \textit{Equation 1.14}$$

Hence, the cubic perovskite structure can be deformed and many substitutions in the cation-sites and a non-stoichiometry by creation of oxygen vacancies in the cation and anion-sites are allowed. This is particularly important for SOFC materials, since the strategy of heterovalent doping is commonly employed in order to enhance the electronic and ionic conductivity, as discussed in detail in *Section 1.2.5*. When the dopant-cation differs sufficiently in size and charge compared to the host-cation, and the concentration of the dopant is suffient, then A or B-site ordering is likely to occur resulting to superstructure structures adopting larger perovskite unit cells[39, 40].

1.3.2. Fluorite

Fluorite structured oxides, having the general formula AO_2 are commonly employed as electrolyte materials in SOFCs. The structure of the prototype CaF_2 is shown in *Figure 1.7*, consisted of calcium ions (Ca^{2+}) in a cubic closest-packed structure with fluorine ions (F^-) in a tetrahedral environment[27]. Appropriate heterovalent substitutions of the A cation in the AO_2 fluorite oxides results in oxygen deficiency, required for fast oxide ion conductivity in SOFCs electrolytes[3].

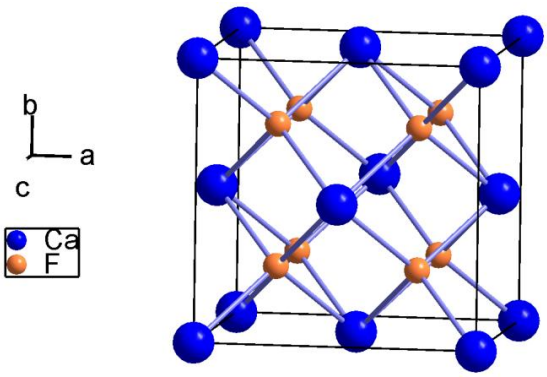

Figure 1.7: Structure of the typical fluorite CaF_2, where the Ca^{2+} atoms are represented in blue and the F^- atoms in orange.

1.4. Materials review

The SOFC operation is dictated by appropriate material selection, with each of the components needing to fulfil the requirements discussed in detail in *Section 1.2.3*. Herein, an overview of the most up to date materials for use in SOFC devices is given. A more detailed discussion for conventional and novel cathode materials is made, since it is the focus of this thesis.

1.4.1. Electrolyte materials

Three electrolyte systems namely yttrium-stabilized zirconia (YSZ: Y_2O_3-ZrO_2), gadolinium- or samarium-doped ceria (GDC010: $Ce_{0.9}Gd_{0.1}O_2$, SDC010: $Ce_{0.9}Sm_{0.1}O_2$) and strontium, magnesium-doped lanthanum gallate (LSGM: $La_{1-x}Sr_xGa_{1-y}Mg_yO_{3-\delta}$) are the most widely investigated electrolyte materials for SOFCs, due to their high ionic and low electronic conductivity[3, 20, 41, 42]. The ionic conductivity exceeds the target of 10^{-2} $S.cm^{-1}$ [41, 43]at temperatures above 700^{o}C for YSZ, which is considered as the most suitable material for HT-SOFCs, and above 550^{o}C for LSGM and the Ce-based electrolytes[20], which are the conventional electrolytes for IT-SOFCs. It is worth noticing that the thermal expansion behavior of the electrolyte component dictates the choice of anode and cathode materials. The thermal expansion coefficients (TEC) of YSZ and LSGM are similar, with reported values of 10.8 $x10^{-6}$ K^{-1} and 11.1 $x10^{-6}$ K^{-1} respectively, whilst the TEC of the ceria-based electrolytes is slightly higher with reported values of 13.5 $x10^{-6}$ K^{-1} and 12.7 $x10^{-6}$ K^{-1} for GDC and SDC[20].

1.4.1.1. Yttrium-stabilised zirconia (YSZ)

Yttrium-stabilized zirconia (YSZ: Y_2O_3-ZrO_2) is an oxygen-deficient compound that adopts the cubic fluorite structure with the addition of appropriate amount of Y_2O_3, typically 8-10 mol%, to the host ZrO_2. Zirconia (ZrO_2), in its pure form, exists in three well-defined polymorphs depending on the temperature; it adopts its monoclinic form from room temperature up to 1170^{o}C, where it transforms to tetragonal for higher temperatures and the cubic polymorph is favored for temperatures above 2370^{o}C up to the melting point of 2680^{o}C. The cubic polymorph of zirconia has improved mechanical and thermal properties such as high strength, toughness, and thermal-shock resistance and is thus preferred to the other polymorphs. In order to stabilise the cubic fluorite structure at lower temperature, appropriate divalent or trivalent substitutions (such as Y_2O_3, CaO, MgO, Sc_2O_3) are reported. The addition of a dopant with lower valency

(e.g. Y^{3+}, Ca^{2+}, Mg^{2+}, Sc^{3+}) than zirconium ion (Zr^{4+}), induces the generation of oxygen vacancies for charge compensation and the oxygen atoms can be transported through these by hopping (vacancy diffusion mechanism) giving rise to ionic conductivity. The concentration of the dopant determines the number of oxygen vacancies and the conductivity of the doped ZrO_2, with the same dopant concentration, depends on the size of the dopant cation. The highest ionic conductivity is achieved for 10mol%Sc_2O_3-ZrO_2 and it is believed to be due to the close match in size of Sc^{3+} (0.81 Å) and Zr^{4+} (0.79 Å); a conductivity of $25x10^{-2}$ $S.cm^{-1}$ is reported at 1000^oC which is more than double compared to the 8mol% Y_2O_3-ZrO_2(where Y^{3+} has an ionic radius of 92 Å). However, YSZ is most popular as SOFC electrolyte mainly due to cost and availability reasons[13].

The ionic conductivity of the Y_2O_3-ZrO_2 shows a maximum of $13x10^{-2}$ $S.cm^{-1}$ at 1000^oC for 8-10% mol Y_2O_3; this dopant level is close to the minimum quantity to fully stabilize the cubic fluorite phase from room temperature to the melting point [13, 42, 44]. Moreover, YSZ is chemically stable in the SOFC oxidising and reducing atmosphere in the oxygen partial pressure range of 1 to 10^{-17} atm[45]. The main drawback of YSZ is its reactivity with conventional perovskite oxide electrodes containing lanthanum and/or strontium especially at the high temperatures required for good conductivity in YSZ, forming $La_2Zr_2O_7$ and/or Sr_2ZrO_4 resistive layers[46, 47] which leads to long term degradation in cell performance.

An alternative to YSZ is scandia-stabilised zirconia (ScSZ: Sc_2O_3- ZrO_2), which shows a maximum of $30x10^{-2}$ $S.cm^{-1}$ for 8-12%mol Sc_2O_3 at 1000^oC[48]. However, the high conductive cubic polymorph of ScSZ exists only at temperatures above 600^oC, with the rhombohedral polymorph favored at lower temperatures; however, it has been reported that the cubic ScSZ can be stabilised at room temperature by adding small amount of dopants such as Y_2O_3[49].

1.4.1.2. Gadolinium or Samarium-doped Ceria (GDC, SDC)

The ceria (CeO_2) based electrolytes $Ce_{1-x}(Gd,Sm)_xO_{2-\delta}$ are also oxygen-deficient cubic fluorites. Typically dopant levels are 10 mol% (GDC10, SDC10) and 20 mol% (GDC20, SDC20). The substitution of the host CeO_2 with Gd^{3+} or Sm^{3+} creates significant oxygen vacancy concentration and the conductivity of GDC010 and SDC010 is reported to be as high as $3.6x10^{-2}$ $S.cm^{-1}$ and

3.5-4.0 x10^{-2} S.cm^{-1} respectively at 700^{o}C, which is comparable to YSZ at 1000^{o}C[50, 51]. Moreover, they have good compatibility with the high performance electrode materials, in particular with cobalt-containing perovskite cathodes. The main drawback for ceria-based electrolytes is their tendency to undergo reduction of Ce^{4+} to Ce^{3+}at low oxygen partial pressures of about 10^{-19} atm[43], with subsequent formation of electronic carriers and hence introduction of undesirable electronic conductivity. The use of the CeO_2-based electrolytes is thereby confined to low temperature applications, i.e. below 600^{o}C, at which the significance of electronic conductivity is suppressed to an acceptable level [3, 20, 42, 43].

1.4.1.3. Magnesium-doped Lanthanum Gallate (LSGM)

The magnesium-doped lanthanum gallate (LSGM: $La_{1-x}Sr_xGa_{1-y}Mg_yO_{3-\delta}$) is an oxygen deficient perovskite material showing negligible electronic conductivity in the oxygen partial pressure region from 1 to 10^{-20} atm[52]. The addition of strontium and magnesium as dopants to $LaGaO_{3-\delta}$ introduces vacancies into the structure leading to increased ionic conductivity of 0.17 and 0.08 S.cm^{-1} for $La_{0.8}Sr_{0.2}Ga_{0.83}Mg_{0.17}O_{0.2815}$ at 800 and 700 ^{o}C respectively and LSGM is considered for use in IT-SOFCs[52-54]. LSGM is more compatible than YSZ with lanthanum-containing perovskite cathodes, but there are reactivity issues with the Ni-LSGM anodes, forming $LaNiO_3$ and La_2NiO_4, resulting in decreased performance[55]. Moreover, the chemical stability of LSGM under reducing conditions at high temperatures remains a question[56].

1.4.2. Anode materials review

The most common anode materials at present are composite materials, consisting of a metallic component mixed with the electrolyte composition, and they are usually referred as cermets[13, 20, 42]. The metallic phase acts as electronic conductor and catalyst for oxidation of the fuel. The metal used is nickel, as it is an excellent catalyst for both hydrogen oxidation and steam reforming[20] and is preferred compared to other good metal catalysts (e.g. cobalt, platinum, palladium) mainly due to its low cost[13]. The electrolyte component acts as support maintaining the required porous structure of the metal, by inhibiting the agglomeration of metal particles over long time periods at high temperatures which would lead to decrease of the catalytic reactive area and degradation of the cell performance. Moreover, the electrolyte support provides the good match in thermal expansion behaviour of the anode material with the electrolytes,

improving the long-term operation under thermal cycling. For YSZ-based cells, the anode material is Ni-YSZ. Similarly, for IT-SOFCs cells where GDC or LSGM is the electrolyte, the anode materials usually are of Ni-GDC and Ni-LSGM type respectively[42].

The most highly investigated anode material is Ni-YSZ for HT-SOFCs [3, 13, 20, 42, 57]. It displays a total conductivity of about 500 S. cm^{-1} at 1000^{o}C, for 30% vol Ni and 30% porosity[13]. The YSZ component is considered inactive and also might play an important role in improving the ionic conductivity of the cermet [13, 20]. Both Ni and YSZ are known to be chemically stable at the fuel reducing environment, with no phase transformation between room temperature and operation temperature.

As a drawback, the Ni-based cermets have limited fuel flexibility, leading to degradation of performance if other fuel than pure hydrogen is used as the fuel. Nickel is sensitive to sulfur containing fuels in ppm concentrations and the risk of coking (carbon deposition) arises if carbon rich fuel streams are used, such as natural gas[58, 59]. One of the approaches to avoid coking and enhance sulfur tolerance is to replace Ni with another metal and Cu-CeO_2 in a porous ZrO_2-based skeleton was developed. Cu is a good electronic conductor and inactive for cracking of hydrocarbons, as well as for fuel oxidation. The catalytic activity of the system is provided by the CeO_2 component and the porous ZrO_2 skeleton was incorporated in order to assist the dimensional instability of the CeO_2 in reducing atmosphere and avoid the sintering at high temperatures. In order to enhance further the activity and stability of Cu based anodes, the alloying with Cu with a second metal such as Ni or Co that have higher catalytic activities has been investigated and a number of other bi- and tri-metallic alloy systems in combination with CeO_2 have also been also proposed[3, 13, 20, 42].

Alternative anode materials that are undergoing investigation are based on the perovskite (e.g. $La_{1-x}Sr_xCr_{1-y}TM_yO_3$), rutile ($AO_2$ and A_nO_{2n-1}, e.g. $Nb_2Ti_2O_7$), pyrochlore ($A_2B_2O_7$, e.g. Gd_2TiMoO_7) and spinnel (AB_2O_4, e.g. Mg_2TiO_4) structures[60, 61], which exhibit both electronic and ionic conductivity in the anode reducing atmosphere and are catalytically more active than ceria for the oxidation of hydrocarbons. The most promising materials are considered to be the perovskites, due to their higher total electrical conductivity[62]. The most widely studied

perovskites are the titanates and chromites because of their stability in reducing conditions[60, 61]. $SrTiO_3$ is a good electronic conductor in reducing conditions and appropriate heterovalent substitutions in the Sr or Ti side have been reported in order to enhance the ionic conductivity part. The total conductivity approaches 86 $S.cm^{-1}$ for $Sr_{0.86}Y_{0.08}TiO_3$ [63], which can be further increased by doping with niobium on the titanium site[61]. The $(La,Sr)TiO_{3-\delta}$ system is of particular interest due to resistance to sulphur[64], which as aforementioned is one of the limitations of Ni-YSZ cermet anodes. In the chromite perovskites family doped, the Ni-doped $(La,Sr)CrO_{3-\delta}$ exhibits the lowest resistance associated with higher ionic conductivity compared to the other dopants such as Mn, Fe, Co, Ni, Cu, but has poor stability in low oxygen partial pressures[60]. Composites with YSZ or ceria electrolytes is a popular approach, for which the titanate or chromite rather than a metal provides the required electronic conductivity[60, 61]. However, the main limitation of the alternative materials compared to the conventional Ni-based anodes is their low catalytic activity and low electronic conductivity, but they are advantageous in terms of low carbon deposition and sulfur tolerance[20, 65].

1.4.3. Cathode materials review

Oxides are usually employed as cathode materials for SOFCs. Several types of oxides are considered to support the fast oxygen exchange reaction between the gaseous oxygen and the lattice oxygen, as well as the ionic conductivity in the bulk of the cathode needed for the transportation of the cathode-generated oxygen ions through the electrolyte to the anode (where the oxidation of fuel takes place).

Perovskite structured materials are popular as SOFC cathodes owing the preference mainly to the structural flexible perovskite network which can tolerate deformation itself in a way that many oxygen vacancies in the cation and anion sites are allowed. For the conventional perovskite materials used as cathodes in solid oxide fuel cells (SOFCs), the A-site cation is a mixture of rare and alkaline earths, usually La and Sr or Ba, while the B-site cation is a reducible transition metal such as Mn, Co, Fe or a mixture thereof [42, 66, 67]. The Sr-doped $LaMnO_3$ (LSM) (*Sections 1.4.3.1.1*) is currently the material of choice for high temperature SOFC cathodes (HT-

SOFCs). The Co-containing perovskite compounds, such as the A-site Sr-doped $LaCoO_3$ (LSC, *Section 1.4.3.1.2*), the A-site-Sr and B-site-Fe co-doped $LaCoO_3$ (LSCF, *Section 1.4.3.1.2)* and the A-site-Ba and B-site-Fe co-doped $SrCoO_3$ (BSCF, *Section 1.4.3.1.3*), show promising electrochemical performance for intermediate temperature SOFC cathodes (IT-SOFCs). A brief overview of the properties of the perovskite cathode materials is given below; there are a lot of detailed books[3, 13, 42] and reviews[10, 20, 41, 57, 66-69] in the literature providing a more in-depth analysis.

To overcome the limitations of high Co-containing perovskites, the family of tetrahedrally coordinated cobalt compounds ('Td-Co') has been recently suggested for applications as cathode materials and is briefly discussed in *Section 1.4.3.2*. Moreover, alternative materials that can support the high electronic and ionic conductivity as well as electrochemical activity belong to perovskite related structures, such as perovskite intergrowths with rock-salt layers (Ruddlesden-Popper, *Section 1.4.3.3*) and A-site ordered double perovskites (*Section 1.4.3.4*). Compounds adopting the pyrochlore structure have also shown interesting cathode performance and a short summary of their properties is given in *Section 1.4.3.5*. More detailed analysis of alternative structures for cathode materials can be found in recent reviews. [20, 42, 67, 68].

1.4.3.1. Perovskite type cathode materials

1.4.3.1.1. LSM

The Sr-doped $LaMnO_3$ (LSM), a p-type perovskite semiconductor, is one of the most intensively investigated and commercially usable materials for HT-SOFCs. The selection of this material compared to others such as $LaCoO_3$- and $LaFeO_3$- based perovskites with superior electronic conductivity, is based on consideration of compatibility with the YSZ electrolyte used in HT-SOFCs, in terms of both reactivity and thermal expansion behavior[3, 70]. Pure $LaMnO_3$ is neither a good electrical conductor nor a good catalyst for oxygen reduction. Doping on the La site by Sr increases the overall electronic conductivity of the material by enhancing the electron-hole concentration due to oxidation of the manganese ion[71]. The electronic conductivity of LSM increases approximately linearly with increasing Sr concentration, as the Mn^{4+} fraction increases, up to a maximum around 50 mol%[13]; with conductivity of 320 $S.cm^{-1}$ at 800^oC for the $La_{0.6}Sr_{0.4}MnO_{3-\delta}$ composition[42, 72]. However, Sr doping levels greater than 30% mol result in the

significant formation of insulating zirconate phases due to reaction of LSM with YSZ at the high temperatures needed for operation[42, 67]. For this reason the most common cathode composition for use with YSZ electrolyte cells is considered to be $La_{0.8}Sr_{0.2}MnO_{3-\delta}$[3]. In LSM, the reduction of oxygen is restricted to the triple phase boundary (TPB), at the interface of the electrolyte-cathode where O_2 gas can be reduced and transferred, due to the absence of oxygen vacancies. This is due to the very low ionic conductivity in the range of 10^{-7} $S.cm^{-1}$ at 900 ^oC [17, 72]and it is considered to be the main reason that the performance of LSM is not sufficient at lower temperatures and hence not a good candidate for IT-SOFCs. The incorporation of an ionic conductive component is reported to enlarge the electrochemical reaction zone; composites with the ionically conductive electrolytes YSZ and GDC have been reported to enhance the performance of LSM[68].

1.4.3.1.2. LSC and LSCF cathodes

The Sr-doped $LaCoO_3$ (LSC) based perovskites family is a mixed electronic-ionic conductor (MIEC) as it displays both high p-type semiconductive electronic and fast ionic conductivity, due to the ability of cobalt to alter its oxidation state and subsequent formation of oxygen vacancies[73, 74]. Hence, the reactive area is extended to the bulk of the cathode and not limited to the TPB and makes it applicable for IT-SOFCs. The total electrical conductivity is reported to be very high, in the order of 1500 $S.cm^{-1}$ in air at 600°C[75]. Moreover, cobalt positioned at the right of the first transition series, results in strong covalency with oxygen and it is considered as a good electrocatalyst for the oxidative dissociation of the dioxygen O_2 molecule to oxygen ions (O^{2-})[29, 68]. However, a large amount of Co and oxygen vacancies result in high thermal expansion coefficients (TEC), typically ca. $20x10^{-6}$ K^{-1} for the LSC system[44, 76], due to the relative weak Co-O bond, resulting in significant mismatch with the common electrolytes in IT-SOFCs, such as GDC, SDC and LSGM [20, 77] *(Section1.4.1)*. This can be critical for long term operation as thermal cycling results in cracking and delamination of the cathode[42]. Introducing Fe in the place of Co in LSC lowers the TEC but results in lower MIEC properties [76, 78, 79]. The most commonly used composition is $La_{0.6}Sr_{0.4}Co_{0.2}Fe_{0.8}O_{3-\delta}$, which has a thermal expansion coefficient of $15.3x10^{-6}$ K^{-1}, giving a good match with that of ceria-based electrolytes[80]. The total electrical conductivity is reported to be 350-400 $S.cm^{-1}$ at 750°C [80, 81], with the electronic conductivity of 10^2 $S.cm^{-1}$ and ionic conductivity of 10^{-3} $S.cm^{-1}$ at 750°C [82, 83]. The development of LSCF composite cathodes with GDC has been reported to further enhance the ionic conductivity and reduce the TEC values closer to that of CGO[84, 85]. The main limitation for long-term operation of the LSCF cathodes is the degradation with time, which is due to strontium diffusion out of the cathode leading to reduced performance[86, 87].

1.4.3.1.3. BSCF

The Co-rich cubic BSCF ($Ba_{0.5}Sr_{0.5}Co_{0.8}Fe_{0.2}O_{3-\delta}$) perovskite is a recently developed IT-SOFCs cathode material, in the $BaCoO_{3-\delta}$- $SrCoO_{3-\delta}$ system, exhibiting very low electrode polarization resistance (of less than 0.1 Ω cm^2 at 600°C and high power densities of about 1 W cm^{-2} at 600°C [88]. It originates[69] from $SrCo_{0.8}Fe_{0.2}O_{3-\delta}$, which was developed for use in oxygen separation membranes and exhibiting the highest oxygen permeation flux, a property that is closely related to the oxygen ionic and electronic conductivities, in the $Ln_{1-x}A_xCo_{1-y}B_yO_{3-\delta}$ (Ln= La, Pr, Nd,

Sm, Gd; A= Sr, Ca, Ba; B =Mn, Cr, Fe, Co, Ni, Cu) system. Substitution with Ba was introduced in order to suppress the limited mechanical and phase stability encountered in the cubic $SrCo_{0.8}Fe_{0.2}O_{3-\delta}$ while sustaining the high oxygen permeation flux.

The main limitations of BSCF are the incompatibility with the commonly used electrolyte materials due to reactivity and its high thermal expansion coefficient of 19.0(5)–20.8(6) $\times 10^{-6}$ K^{-1} between 600-900^{o}C[89]. The thermal mismatching with electrolytes (common IT-SOFCs electrolytes having TEC= 10-13x10^{-6} K^{-1}) is a common feature of cobalt containing cathodes exhibiting TEC often larger than 14x$10^{-6}K^{-1}$) [90]. Moreover, BSCF undergoes decomposition into a mixture of hexagonal barium-rich, iron-free cobalt perovskite phase and a cubic strontium-rich, iron-cobalt perovskite phase at temperatures below 900^{o}C for long time periods in air[91, 92]. It is believed that the cubic perovskite tends to decompose to two of its end-members, $BaCoO_{3-\delta}$, which is known to be a hexagonal perovskite, and $SrFeO_{3-\delta}$, which adopts a cubic polymorph of the perovskite structure[93]. According to the literature, the driving force for the decomposition of the cubic BSCF, is the cobalt preference to low-spin configuration in the Co^{3+} (d6) oxidation state, upon heating at temperatures below 900^{o}C, which prefers to form smaller bonds in the hexagonal structure (chains of face-sharing BO_6 octahedra, having B-O distances of 1.84 Å) instead of longer bonds in the cubic structure (corner-sharing octahedra with B-O distances of 1.95Å)[94]. The competing hexagonal phases are favored at high (>+3) cobalt oxidation states in BSCF (cobalt oxidation state: 3-4) resulting in reducing of the concentration of oxygen vacancies as well as the number of charge carriers leading to poorer electrochemical performance compared to the highly efficient BSCF cubic polymorph[69]. It is worth noticing though that lower Co containing $Ba_{0.5}Sr_{0.5}Co_{0.2}Fe_{0.8}O_{3-\delta}$ shows improved stability compared to $Ba_{0.5}Sr_{0.5}Co_{0.8}Fe_{0.2}O_{3-\delta}$, but lower electrochemical performance[95].

1.4.3.2. Tetrahedrally coordinated Co compounds ('Td-Co')

The recently investigated family of the tetrahedrally coordinated cobalt ('Td-Co') compounds with general formula $RBa(Co,M)_4O_7$ (R=Y, Ca, In and M=Zn, Fe, Al) show improved properties compared to the Co-containing cathode materials, such as LSC, LSCF (*Section 1.4.3.1.2*) and BSCF (*Section 1.4.3.1.3*). The perovskite Co-rich cathodes suffer from high TEC and instability of their high conductive cubic phase due to the presence of octahedrally coordinated Co^{3+} that

undergoes a high to low-spin transition[68]. The Td-Co compounds are reported to exhibit as low TEC values as $6x10^{-6}$ to 13x 10-6 K^{-1} at 80-900 ^oC[96], providing good thermal expansion compatibility with the standard SOFC electrolyte materials and good thermal stability. It should be noted that reactivity issues with YSZ and LSGM are reported, but not with GDC. In terms of electrochemical performance, the most characterised material of this type so far seems to be $YBaCo_3ZnO_7$[96-99], with obtained ASR of 0.40 $\Omega.cm^2$ at 600 ^oC, which is further lowered to 0.22 $\Omega.cm^2$ for 50:50wt% composites with GDC[96].

1.4.3.3. Ruddlesden-Popper type materials

The Ruddlesden-Popper materials with the general formula $A_{n+1}B_nO_{3n+1}$ consist of n consecutive perovskite layers $(ABO_3)n$ alternating with rock salt layers (AO), with AO along the crystallographic c direction. The Ruddlesden-Popper oxides with n=1, $A_2BO_{4+\delta}$ (A: La, Pr, Nd, Ba, Sr and B: Co, Fe, Ni, Cu), are one of the most promising family of alternative cathode materials. This is due to the combination of the high electronic conductivity, due to the mixed valence of the B-site metal, and the oxygen ionic conductivity, due to the oxygen excess offering the possibility of rapid oxygen transport via an interstitial mechanism[100].

Lanthanum nickelate, $La_2NiO_{4+\delta}$ (LNO) is the most widely studied composition of these types of materials. The oxygen diffusivity of LNO is higher than that of LSCF and 1 order of magnitude lower than the very good perovskite oxide mixed conductor LSC [20, 101]. The total conductivity is reported to be approximately 30 $S.cm^{-1}$ at 700^oC[57]. The electrochemical performance is considered to be limited by surface exchange of the gaseous oxygen with the lattice oxygen with the lowest obtained ASR values of 2-3 $\Omega.cm^{-2}$ at 700^oC [57, 102] on $Ce_{0.7}Sm_{0.3}O_{2-\delta}$ electrolyte. The range of thermal expansion coefficients observed for the La_2NiO_4 compounds (11-13 $x10^{-6}K^{-1}$) matches reasonably well with the values for the electrolytes YSZ, CGO and LGSM[20, 67]. However, the main limitation of $LaNiO_{4+\delta}$ and derivatives is the chemical phase instability in the range of temperatures and oxygen partial pressures necessary for SOFCs application[103, 104].

1.4.3.4. A-site ordered double perovskites

The A-site ordered double perovskites in orthorhombic symmetry, with general formula $AA'Co_2O_{5+\delta}$ (A = rare earth (RE), Y and A' = Ba, Sr), consisting of A' layers alternating with A layers[105], are another family of compounds that has attracted attention as cathode materials, exhibiting mixed electronic and ionic conductivity. The rapid oxygen transport kinetics has been attributed to the oxygen vacancies due to the combination of RE trivalent cations and Ba,Sr divalent cations on the A-site[20, 42]. The most studied composition of this type of materials for SOFCs cathodes applications is $GdBaCo_2O_{5+\delta}$[20, 42], showing good chemical compatibility up to 1100°C and electrochemical performance with GDC and LSGM electrolytes, with obtained ASR values of 0.25 $\Omega.cm^2$ at 625°C [106], 0.53 $\Omega.cm^2$ at 645 °C [107]and about 1 $\Omega.cm^2$ at 600°C[108] respectively. Moreover, $GdBaCo_2O_{5+\delta}$ was found to exhibit very good stability in atmospheres of CO_2 (500 ppm to 100%) at temperatures up to 700°C[20].

The $SmBa_{0.5}Sr_{0.5}Co_2O_{5+\delta}$ (ASR= 0.092 $\Omega.cm^2$ at 700°C) analogues has also shown very promising properties, with GDC electrolytes [109]. The partial substitution of Ba^{2+} by Sr^{2+} in $GdBa_{1-x}Sr_xCo_2O_{5+\delta}$ ($0.2 < x < 0.6$) has been found to favor a transformation to a tetragonal phase which exhibits higher activity for oxygen reduction than the orthorhombic phases[110]. The thermal expansion behavior and the electrochemical performance has been found to be further improved for composites with GDC; in the family of $REBaCo_2O_{5+\delta}$ (RE=La, Pr, Nd, Sm, and Eu) composite cathodes, the ASR decreased as the ionic radius decreased from La to Eu, with obtained value of 0.095 $\Omega.cm^2$ and at 600°C for $EuBaCo_2O_{5+\delta}$/GDC on GDC electrolyte[111], which is comparable to the 0.12 $\Omega.cm^2$ at 600°C for 50:50 wt% $SmBa_{0.5}Sr_{0.5}Co_2O_{5+\delta}$/GDC composite on YSZ electrolyte with a GDC interlayer[109].

1.4.3.5. Pyrochlore oxides

Pyrochlore-structured oxides, with general formula $A_2B_2O_7$, are also considered for cathode materials in SOFCs[68, 69, 112]. The most extensively studied family is the pyrochlore ruthenates, due to their high electronic conductivity as well as good catalytic activity towards oxygen reduction; a lot of research has been focused to $Bi_2Ru_2O_7$ showing good chemical compatibility with ceria-based electrolytes and YSZ. The partial substitution of Ru^{4+} with Bi^{3+}, in

$Bi_2Ru_{1.6}Bi_{0.4}O_7$, has been considered to be the reason for the introduction of oxygen vacancies and ASR values lower than 1 $\Omega.cm^2$ at 600°C[113]. The Pb- analogue, $Pb_2Ru_2O_7$, has been found to react with GDC at the operation conditions of IT-SOFCs[112]. Other pyrochlore systems under investigation are Mn-doped ruthenates, with formula R_2RuMnO_7 (R = Tb, Dy, Ho, Er, Tm, Yb, Lu and Y) and $Gd_{2-x}La_xZr_2O_7$ (x = 0–1), both showing acceptable values of ionic conductivity, but thr electronic conductivity is below the desirable values for SOFCs cathodes[68].

1.5. Aim of this work

The work undertaken for this thesis has been focused on the introduction of Mo^{6+} in the B-site of the cubic perovskite $Ba_{0.5}Sr_{0.5}Co_{0.8}Fe_{0.2}O_{3-d}$ (BSCF) and the evaluation of the derived Mo-doped BSCF compounds as cathode materials for IT-SOFCs.

As aforementioned (*Section 1.4.3.1.3*), the structural instability of the cubic perovskite $Ba_{0.5}Sr_{0.5}Co_{0.8}Fe_{0.2}O_{3-d}$ (BSCF) and the high thermal expansion coefficients associated with the Co-containing cathodes limit the applicability for long-term operation. The B-site doping in BSCF, by substituting Co and/or Fe, seems to improve the thermal stability of the cubic forming BSCF derivatives for as low doping levels as 0.2%mol, at extended annealing at the technically useful temperature range for the operation of IT-SOFCs. However, replacing the valent alterable Co in BSCF with more chemically stable ions such as Ti^{4+}[114], Zr^{4+}[115] and Zn^{2+}[116], the electronic conductivity is significantly decreased leading to deterioration of the electrochemical properties of the parent undoped oxide. The good electrochemical performance of BSCF is believed to be due to the relatively high ionic conductivity and the Co catalytic activity [95]. Incorporation of Nb^{5+} and Y^{3+} in $Ba_{0.5}Sr_{0.5}(Co_{0.8}Fe_{0.2})_{1-x}Nb/YO_{3-\delta}$ affording also cubic perovskite compounds showing enhanced stability, but the ionic conductivity is in general decreased at doping levels up to 0.2, measured by oxygen permeation tests[117, 118].

The challenge in doping BSCF is thus to suppress the phase transformation of the cubic phase, lowering the TEC, while retaining the good electrochemical properties. Substituting Mo^{6+} in the place of Co and Fe in the B-site could enhance the stability of BSCF; Mo-containing compounds such as $Ba_2Co(Mo,W)O_6$ [119] and $Ba_2CoMo_{0.5}Nb_{0.5}O_{6-\delta}$[120], are reported to be highly stable compounds. Moreover, molybdenum compounds are well known catalysts with high activity for

selective oxidation of hydrocarbons, for instance, the industrial production of formaldehyde from selective oxidation of methanol and the production of acrolein and acrylonitrile products by propene oxidation are promoted by iron molybdate and bismuth molybdate catalysts respectively[121]. The catalytic activity of molybdenum compounds at these oxidative reactions is believed to depend on the ability of oxomolybdenum species to cycle between the +4 and +6 oxidation states (*Equation 1.15*), in the process releasing and transferring an oxygen atom and the same molybdenum chemistry also operates with oxomolybdenum enzymes, e.g. xanthine oxidase.

$$Mo^{6+}O_2 \rightleftharpoons Mo^{4+}O + O \qquad \textit{Equation 1.15}$$

Hence, the catalytic properties of molybdenum involving dioxygen activation could further promote the electrochemical activity towards the oxygen reduction.

The research in this thesis undertaken can be broadly divided into three areas; the synthesis, stability and properties measurement (Chapter 3), their structural characterization (Chapter 4) and their electrochemical performance with typical IT-SOFC electrolytes measured by electrochemical impedance spectroscopy (Chapter 5).

2. CHAPTER 2- EXPERIMENTAL TECHNIQUES

Experimental Techniques

2.1. Synthesis

The parent BSCF and the Mo-doped BSCF (BSCFM) powders were prepared by ceramic method, which consisted of several steps as illustrated in *Figure 2.1*.

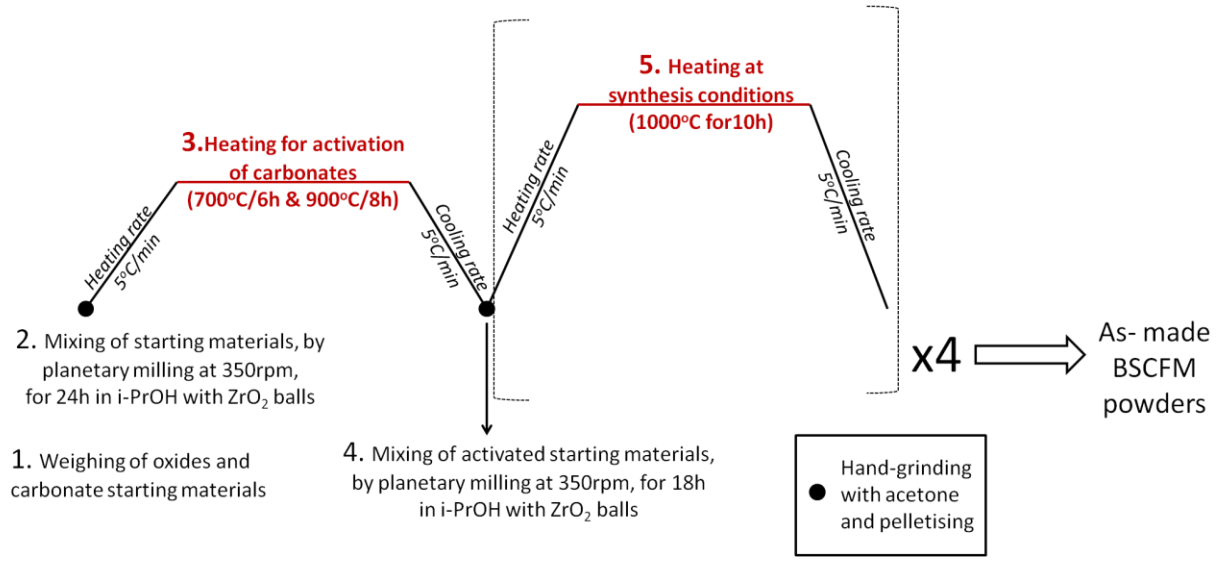

Figure 2.1: Schematic illustration of steps for the synthesis of the Mo-doped BSCF (BSCFM) powders.

According to this, stoichiometric amounts of high purity $BaCO_3$ (99.997%), $SrCO_3$ (99.994%), Co_3O_4 (99.9985%), Fe_2O_3 (99.998%) and MoO_3 (99.95%) were weighted within 0.0005g using a Sartorius balance (*step#1*). The starting materials were then hand-ground in acetone, typically for 15 minutes, using an agate pestle and mortar. However, the homogeneity problems identified

(Chapter 3, *Section 3.1.3*) led to replacement of the hand-grinding by mechanical grinding, using a Pulverisette planenary mill from Fritch. For this, the starting materials were milled for 24 hours in isopropanol (i-PrOH) in ZrO_2 pots using 10 mm ZrO_2 balls at 350rpm and once completed, the powders were left to dry by evaporating the solvent in air (*step#2*). The reactants mixture were then uniaxially pressed into pellets, using a 13 mm stainless steel die in a hand pulled hydraulic piston press at 3tons pressure. The pellets were then fired at 700°C for 6 hours, following by a heating step at 900°C for 8 hours in a chamber furnace in air, for the activation of the carbonate precursors (*step#3*). The heating rate was 5°C/min and after the firing the pellets were cooled to room temperature, with a cooling rate of 5°C/min. The pellets of the activated starting materials were then broken and hand ground with acetone and a second ball-milling step was introduced for 18h at 350rpm, using isopropanol as the solvent (*step#4*). After this, the powders were ground in acetone, repelletised and refired at 1000°C for 10h (*step#5*), using a heating and cooling rate of 5°C/min. The grinding/pelletising/heating steps were repeated a total of four times. During the sinterings, ZrO_2 crucibles were used.

According to the general procedure for ceramic synthesis[27], the reaction between reactants, at appropriate quantities, is achieved when heated at high temperatures (typically in the range 600-1500°C) for several hours or days to overcome the high kinetic barrier, allowing the thermodynamically favoured product to form. The main limitation of this method is that the chemical reactions only take place at the interface of the reactants in contact, and reaction can only continue as reactants diffuse across the interface. Grinding reduces the size of the grains, ensures the thorough mixing of reactants and increases the interface between them and resulting in enhancement of the reaction rate. Similarly, the pelletising maximises the surface contact between the reactants and enhances the reaction rates. The grinding/pelletising steps are usually repeated many times in order to bring fresh interphases in contact and so speed up the reaction.

For quenching experiments (Chapter 4, *Section 4.2.2*), the BSCFM pellets were removed from a furnace at high temperatures of 1000°C or 1200°C and rapidly cooled by placing them onto an aluminium block, which is a good thermal conductor. The pellets reach room temperature within a couple of minutes. Rapid cooling allows for thermodynamically accessible products to be be 'trapped', as low temperature thermodynamic processes are prevented.

2.2. Powder diffraction techniques

2.2.1. Crystal symmetry and diffraction

Powder diffraction is a powerful technique in obtaining information about the crystal structure of crystalline solids and it was extensively used for this thesis. The basics and terminology of crystal structure determination are discussed below.

A crystal structure[27, 122] is made up of regular arrangements of atoms in three dimensions. These arrangements can be represented by the periodic repeat of identical unit cells; the unit cell is defined as the smallest repeating unit in a crystal structure. Crystal lattices can be classified to seven crystal/lattice systems, according to the relation between the edges of the unit cell of length (a, b, c) and the relation between the angles (α, β, γ) between them (*Table 2.1*).

Table 2.1: The seven crystal systems and the lattice characteristics

Crystal system	**Unit cell edges**	**Unit cell angles**
Triclinic	a≠b≠c	α≠β≠γ
Monoclinic	a≠b≠c	α=γ= 90^o, β≠90^o
Orthorhombic	a≠b≠c	α=β=γ= 90^o
Tetragonal	a=b≠c	α=β=γ= 90^o
Hexagonal	a=b≠c	α=β= 90^o, γ= 120^o
Trigonal	a=b=c	α=β=γ≠ 90^o
Cubic	a=b=c	α=β=γ= 90^o

Crystals form lattice planes; these are defined by the three Miller indices (*h*, *k* and *l*) which intersect the unit cell axes at a/h, b/k and c/l respectively. The term of lattice planes is a way to provide a reference grid to which the atoms in the crystal structure may be referred; sometimes this coincides with layers of atoms[27]. However, one atom (or lattice point) can belong to more than one unit cells depending on the centering type, which if combined with the seven possible lattice systems makes 14 possible Bravais lattice types. When the possible Bravais lattice types are used in combination with the internal symmetry operators for the unit cells, 230 space groups are defined.

Powder diffraction can give information about the space group that a crystalline solid adopts and its lattice characteristics, namely the length of lattice edges (usually referred as lattice parameters) and lattice angles. It is a useful technique in the study of solid state chemistry, as it is rapid and non-destructive. Three types of radiation are used for crystal structure diffraction studies: X-rays, neutrons and electrons; all of which were used in this thesis.

2.2.2. Fundamentals of diffraction

When a radiation beam of wavelength λ encounters a crystalline material, diffraction arises from the 'reflection' by the lattice planes within the crystal structure. However, diffraction can be only observed when the scattered beam from one lattice plane is in phase with the scattered beam from other lattice planes and they combine to form an enhanced scattered beam (constructive interference, *Figure* 2.2). If the scattered beams are out of phase, then destructive diffraction occurs, where diffracted beams cancel each other[27].

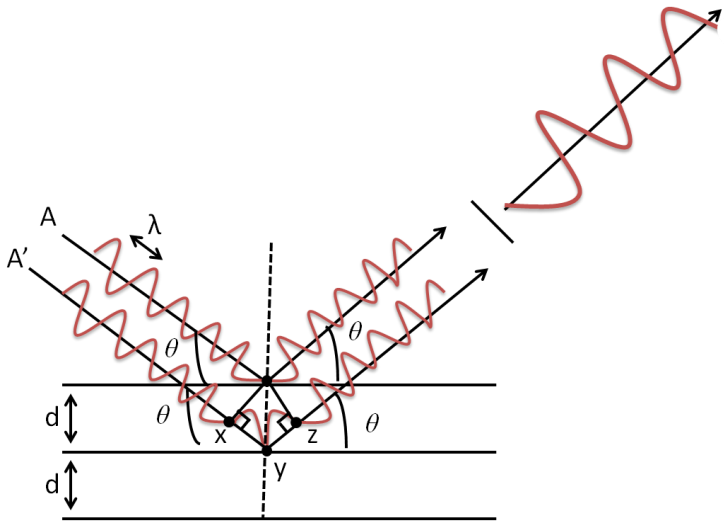

Figure 2.2: Bragg reflection of monochromatic radiation beams A and A', with wavelength λ and incident angle θ, from adjacent crystal lattice planes regularly spaced by d. The labeled distances and points are used to construct the Bragg equation (Equation 2.1).

According to *Figure 2.2*, constructive interference occurs when the difference in path lengths (xyz= xy+yz, and from trigonometry xy=yz= d sinθ) for the beams A and A' is equal to an integer number of wavelengths, $n\lambda$; this is known as the Bragg's law (*Equation 2.1*). When the

Bragg's law is not satisfied, the scattered beams are out of phase and destructive interference occurs.

$$\text{Bragg's law: } n\lambda = 2d \sin\theta \qquad \textit{Equation 2.1}$$

where n is an integer number, λ is the wavelength of the radiation beam, θ is the angle relative to the incident beam at which constructive interference occurs and d is the interplanar distance of the lattice planes, defined by the three Miller indices (*h*, *k* and *l*).

Hence, for a monochromatic beam with a constant wavelength λ, a diffracted beam is only observable at discrete values of θ, which are called Bragg angles and are related to the interplanar spacing *d* according to the Bragg's law. As aforementioned, the interplanar spacing *d* is determined by the lattice characteristics (lattice parameters and angles) of the crystal and the Miller indices (h,k,l) of the planes. The exact relation differs for each of the seven crystal systems in *Table 2.1;* the example of the cubic system, for which a=b=c and $\alpha=\beta=\gamma=90^{o}$, is shown in *Equation 2.2*.

$$\frac{1}{d^2} = \frac{h^2}{a^2} + \frac{k^2}{b^2} + \frac{l^2}{c^2} = \frac{h^2 + k^2 + l^2}{a^2} \qquad \textit{Equation 2.2}$$

Because each crystalline material has a characteristic atomic structure, it will diffract X-rays in a unique characteristic diffraction pattern, showing peaks (Bragg reflections) for each of the allowed Bragg angles. The diffraction pattern can be analysed based on the peak positions, which correspond to the position of the lattice planes. By assigning Miller indices to each observed reflection (a process known 'as indexing' of the diffraction pattern) it is possible to identify the crystal system. Moreover, systematic reflection absences can provide information about the space-group determination; these are the result of destructive interference due to the symmetry of the crystal system.

The intensity of each Bragg reflections can provide information about the position of atoms within the crystal. For a perfect crystal, the intensity I_{hkl} of a reflection with assigned Miller indices h,k,l is described by *Equation 2.3*.

$$I_{hkl} = s\ L\ p\ |\ F_{hkl}\ |^2 \quad \sim |\ F_{hkl}\ |^2 \qquad \textit{Equation 2.3}$$

where s is a scale factor (accounting for factors such as data acquisition time), L is the Lorentz factor (dependent on instrument geometry) and p is the polarisation correction. The factor F_{hkl} is the 'structure factor', which depends on the structure of the crystal and dominates in the intensity equation. For a unit cell containing N unique atoms, F_{hkl} is given by *Equation 2.4*.

$$F_{hkl} = \sum_{n=1}^{N} S_n\ \exp[\ 2\pi i\ (hx_n + ky_n + lz_n)\ ]\exp(-m) \qquad \textit{Equation 2.4}$$

where S_n is the atomic scattering factor of the *n*th atom, x_n, y_n and z_n are the atomic coordinates within the unit cell, and exp(-m) is a thermal motion correction. As temperature increases, the value of m increases and the intensities decrease. For simple isotropic thermal motion of atoms, m is given by *Equation 2.5* and is angle (θ) dependent. This means that with increasing the temperature, the observed intensities at higher θ angles decrease more rapidly than lower θ angles.

$$m = exp\left(\frac{-B_{iso}\ sin^2\theta}{\lambda^2}\right)\ and\ Biso = \ 8\ \pi^2 Uiso \qquad \textit{Equation 2.5}$$

where Biso and Uiso are the experimentally determined isotropic temperature factors.

Hence, in principle, the intensity of the observed Bragg reflections, I_{hkl}, can be used to derive the atomic coordinates within the unit cell, given that the atomic scattering factors S_n of the constituent atoms are known and taking into consideration the thermal correction.

2.2.3. Diffraction techniques

Radiation sources such as X-rays, neutrons and electrons have wavelengths (*Table 2.2*) in the order of the interlattice planar distances (typically in the range of 1.5-3 Å)[27, 123] and are scattered by the lattice planes in crystalline materials; diffraction describes the elastic coherent scattering process.

Table 2.2: Radiation sources beams and their usual values of wavelengths

Radiation	**Wavelength, λ**
X-rays	Order of a few Å[27]
Neutrons	0.5-3 Å[27]
Electrons	0.0087-0.037 Å[123, 124]

The scattering power of an atom, as described by the atomic scattering factor S_n (*Equation 2.4*) varies according to the source of radiation and the interaction with the crystal material (*Table 2.3*). For diffraction of X-rays (XRD) [27], the atomic scattering factor f_n is proportional to the electron number, as expressed by the atomic number (*Z*), of the scattering atom, as the X-rays scattered by an atom are the result of the waves scattered by each electron in the atom. Consequently, heavy elements (high *Z*) are the strongest scatterers of X-rays. Moreover, XRD is inadequate in distinguishing atoms with similar atomic numbers.

Table 2.3: Scattering factors and their origin according to the source of radiation

Radiation	**Scattering factor**	**Scatterer**
X-rays	f_n Proportional to number of electrons (Z)	electrons in atoms[27]
Neutrons	b neutron coherent scattering length	nuclei of atoms[125]
Electrons	σ interaction cross-section Proportional to Z^2	electrons in atoms [123]

The scattering power of neutrons and electrons[123] by an atom is described by the probability of a scattering event, as determined by the interaction cross-section (σ, *Equation 2.6*), defined in Physics as the likelihood of interaction between particles.

$$\sigma = \pi r^2 \qquad \textit{Equation 2.6}$$

For neutron diffraction (ND)[125, 126], neutrons are scattered by the nuclei of the atoms. The cross-section (σ) is equivalent to the effective area presented by the nucleus to the passing neutron. The scattering power of a nucleus is expressed by the neutron coherent scattering length (b_{coh}), as if b_{coh} is the half of the radius of the nucleus as seen by a neutron (*Equation 2.7*) and the incoherent scattering results in general background noise in the data.

$$\sigma = \pi r^2 = \pi (2\, b_{coh})^2 = \pi\, 4\, b_{coh}{}^2 \qquad \textit{Equation 2.7}$$

The scattering power of an atom is thus determined by the interactions of neutrons with atoms in a manner that does not correlate to the atomic number (Z) as in the case of XRD [127]. This makes ND complementary to XRD, giving structural information for isoelectronic atoms and light atoms in the presence of heavier ones[27].

In ED, the electrons are attracted by the positive potential (Coulombic interaction) inside the electron cloud of an atom. The incident electron beam is scattered strongly by the electrons of the atoms, nearly elastically, and the scattering efficiency of electrons is very high, about 10^6-10^7 stronger than XRD. This results in intense diffraction when the scattered electron beams interact constructively (coherent scattering) and accordingly to the Braggs law (*Equation 2.1*). The Bragg-scattering angles of the diffracted electron beams are very small ($0< \theta<2$) compared to XRD and ND, due to the smaller wavelengths (*Table 2.2*).

In the case of elastic scattering of electrons, the interaction cross-section of electrons is:

$$\sigma = \pi r^2 = \left(\frac{Z\, e}{V\, \theta}\right)^2 \qquad \textit{Equation 2.8}$$

where Z is the atomic number, e is the elementary charge, V is the accelerated voltage and θ the scattering angle. Hence, the scattering of electrons by heavier atoms (high Z) is stronger than for lighter atoms (low Z) in a crystalline material, similarly to XRD.

However, the intense diffracted beams in ED can also be diffracted by other lattice planes, resulting in secondary diffraction[27, 123]. As a consequence, the intensities of the diffracted beams

are not reliable and extra reflections may also appear in the diffraction pattern due to secondary diffraction, which makes the structural analysis of a crystalline material more difficult. These difficulties make ED suitable only for samples in small quantities and/or very thin, such as thin films, for which the effect of secondary diffracted beams is moderated. However, ED is strong and the most reliable technique for space group identification, since kinematically forbidden reflections in XRD are also observed[128]; this is possible though for crystals smaller than 0.01 to 0.02 nm in diameter[27]. For this, electron diffraction is often combined with electron microscopy, which is going to be discussed later in *Section 2.3*. Due to the strong scattering of the incident electron beam by the electrons in the atoms, incoherent elastical scattering to high angles or even back-scattering can occur in addition to diffraction; both of these affects are used in electron microscopy studies too[27].

Moreover, it should be noted that the electron radiation can also interact inelastically with matter and cause additional processes, other than diffraction in crystalline materials[27, 123, 124]. The signals caused by inelastical interactions are mainly used in methods of analytical electron microscopy, such as energy dispersive spectroscopy (EDS) which was used in this thesis and is going to be further discussed in *Section 2.3.2.2*.

2.2.4. Radiation sources for diffraction

2.2.4.1. X-ray sources

X-rays are electromagnetic radiation of wavelength ~ 1Å[27]. They can be generated either by laboratory or synchrotron sources through different processes, but in both cases resulting in monochromatic X-rays required for XRD[129]. In XRD experiments, the intensity of the diffracted beam is measured as a function of 2θ, which is the angle between the diffracted and undiffracted beams.

In laboratory based powder X-ray diffractometers[27, 129], electrons are produced by heating a metal filament, usually tungsten, and then accelerated through a voltage of 40 kV to bombard a metal target, usually made of copper, cobalt or molybdenum. The instrument used in this thesis had a cobalt target. The bombardment of high energy electrons causes ionisation of the core K-shell (n=1) electrons of the target anode. Electrons from outer orbitals fill the holes created in the core shell by the ionisation of ions; by this X-rays are emitted with energy corresponding to the energy gap between the two electronic states and hence have different wavelength than the radiation for diffraction. Electrons originating from the L shell (n = 2) give rise to Kα radiation, and electrons from the M shell (n = 3) give rise to Kβ radiation; both comprise of two components: Kα_1 and Kα_2, and Kβ_1 and Kβ_2, respectively, because the transition has a slightly different energy for the two possible spin states of an electron. The Kα radiation is more intense than Kβ, as it occurs more often, and it is the one used in diffraction experiments. Since a monochromatic X-ray beam is desired for the XRD experiments, the Kβ radiation has to be removed; Kβ_1 is absorbed by appropriate filters depending on the target material (Fe filter for Co target) and Kβ_2 can be removed with the use of an appropriate monochromator.

In a synchrotron[19, 130], the electrons are produced in an electron gun where the cathode is under high voltage and heated in a vacuum. The electrons are accelerated to near light-speed by a sequence of particle accelerators and finely tuned bending magnets, producing an extremely intense synchrotron radiation in large storage rings. The synchrotron radiation consists of wavelengths from infra-red to X-rays; a specific X-ray wavelength can be selected by using appropriate monochromators.

2.2.4.2. Neutron sources

Accelerated particles, such as neutrons, possess wave-like characteristics as described by the de Broglie relationship (*Equation 2.9*). The neutrons that are used for diffraction have wavelengths of the order 0.5 to 3 Å[27, 131].

$$\lambda = \frac{h}{p} \qquad \textit{Equation 2.9}$$

where p is momentum and h the Planck constant

The generation of neutrons for diffraction is expensive and hazardous, and is therefore carried out at specialised facilities. There are two types of neutron sources: reactor sources and spallation sources[131]. The reactor source at the Institut Laue-Langevin (ILL) facilities in Grenoble, France, produces neutrons by nuclear fission of ^{235}U. The ND data presented in this thesis were collected at ISIS facility (Rutherford Appleton Laboratory in Oxfordshire, UK) which is a spallation neutron source. The production of neutron by spallation is based on the collision of a high energy proton beam into the nuclei of a heavy-metal target (in ISIS, it is a tungsten target). This results in the destruction of a metal nucleus into two or three smaller nuclei and several neutrons. The spallation process yields about 30 neutrons per proton.

In ISIS, the beam of protons is produced by an 800 MeV proton accelerator, consisting of an injector and a synchrotron, producing intense pulses of protons 50 times a second[132]. This generates high energy neutrons, which are slowed down by moderators to useful speeds for research and directed to the neutron beamlines were experiments are carried out. The detectors are at fixed 2θ scattering angles and the diffracted radiation is recorded as a function of neutron time of flight (t.o.f), which is defined as the time that a neutron needs to reach the detector, and wavelength. Neutron wavelength (λ) is related to its velocity (v) by the de Broglie relationship (Equation 2.9), by expressing the momentum (p) as the multiplication product of velocity and mass of nucleus:

$$\lambda = \frac{h}{p} = \frac{h}{mv} \qquad \textit{Equation 2.10}$$

where p=mv and m the mass of nucleus

By considering a fixed path length (distance, L) of the neutron from moderator to detector and the time of flight (t) taken for a neutron to reach the detector, the relationship gives:

$$\lambda = \frac{h}{mv} = \frac{ht}{mL} \qquad \textit{Equation 2.11}$$

Combining this expression with Bragg's law (*Equation 2.1*), it is possible to relate the neutron time of flight (t) to d-spacing.

$$\lambda = 2d \sin\theta = \frac{ht}{mL} \qquad \textit{Equation 2.12}$$

Hence, by using detectors at fixed 2θ positions and a fixed path length L, the values of interplanar spacing d, defined by the Miller indices, can be determined by using neutron time-of-flight (t.o.f.) as the variable.

The resolution $R(d)$ of ND diffraction data[133], as expressed by the uncertainty in *d*-spacing (Δd), is affected by the uncertainties in timing (Δt), angle ($\Delta\theta$) and path length (ΔL), as given in *Equation 2.13*.

$$R(d) = \sqrt{\Delta\theta^2 \cot^2\theta + \left(\frac{\Delta t}{t}\right)^2 + \left(\frac{\Delta L}{L}\right)^2} = \frac{\Delta d}{d} \qquad \textit{Equation 2.13}$$

The uncertainty in timing (Δt) is mainly influenced by the moderation time of the neutron, during the moderation process. The error in path length (ΔL) originates from the thickness of the moderators and the widths of sample and detectors. As can be deduced from Equation 2.13 the resolution increases when using a long flight path (L) between the moderator and the detector, which also increases the time of flight (t), for a given detector angle ($\Delta\theta=0$). Maximum resolution can be reached when the detector angle are approximately at $2\theta = 180^o$ or $\theta = 90^o$ and the $\cot^2\theta$ factor in *Equation 2.13* becomes zero.

2.2.4.3. Electron sources

Electrons[27, 123, 124] have wave characteristics, usually λ= 0.0087-0.037Å, which allow them to be used for diffraction experiments. As aforementioned ED is usually combined with electron microscopes which operate either in transmission or reflection mode[27]. The principles of electron microscopes are further discussed in *Section 2.3*. In electron microscopes, electron beam is produced by electron guns and are accelerated through a high voltage (usually 50 to 300keV). The electron guns provoke electron emission in two different ways: either heating of a W or LaB_6 filament (thermionic gun) or by applying an extraction voltage (field emission gun).

The wavelength (λ) of the electron beam is related to the accelerating voltage (V):

$$\lambda = \frac{h}{\sqrt{2meV}} \qquad \textit{Equation 2.14}$$

where m and e^- are the mass and charge of the electron and *h* the Planck constant. This relation is derived from combination of the de Broglie relation (λ= h/p= h/mv, *Equation 2.10*, *Section 2.2.4.2*, page 50) where the velocity *v* is related to the kinetic energy of the electrons (E_{kin}= ½ mv^2), which is equal to the energy provided (E= eV).

At the high acceleration voltages reached in electron microscopes, the velocity of electrons reaches the speed of light (c= 2.998 x 10^8 m/s) and relativistic effects have to be taken into account for accurate determination of the wavelength (λ) of the electron beam (*Equation 2.15*).

$$\lambda = \frac{h}{\sqrt{2meV(1+\frac{eV}{2mc^2})}} \qquad \textit{Equation 2.15}$$

2.2.5. Diffraction studies in this thesis

In this study, XRD was used extensively to characterize the BSCFM materials. For the BSCFM composition showing the most promising performance, all diffraction techniques were employed in order to fully characterise its structure. ED was used in combination with electron microscopy to get information related to the space-group and ND data were used in combination with XRD data to obtain structural information about the atomic positions. The scattering factors for XRD and ND of each element in the BSCFM compounds are given in *Table 2.4*.

Table 2.4: Scattering factors for X-ray and Neutron diffraction for the elements used in this study

Element	**Atomic scattering factor (*Z*)**	**Neutron scattering length (*b, fm*)[127]**
Ba	56	5.07
Sr	38	7.02
Co	27	2.49
Fe	26	9.45
Mo	42	6.715
O	8	5.80

As previously mentioned, XRD is not sensitive in locating light atoms in the presence of heavy ones and isoelectronic elements, such as Co (Z= 27) and Fe (Z= 26). However, Co and Fe can be distinguished by ND since the neutron scattering factors are significantly different; *b*(Co)=2.49 fm and *b*(Fe)= 9.45 fm. Moreover, of particular importance is the strong neutron scattering factor of the light (*Z*= 8) oxygen (*b*(O)= 5.80 fm), resulting in greater accuracy by ND compared to XRD data.

All of the samples reported in this thesis were initially characterised using laboratory based powder X-ray diffractometers using a Panalytical X'pert Pro diffractometer. The diffractometer produced X-rays from a cobalt anode operating at 40 kV and 40 mA, producing a monochromatic X-ray beam with Co Kα_1 wavelength λ= 1.7890 Å. The diffractometer was set up in Bragg-Brentano geometry with a fixed X-ray source and a moving detector. Samples were suspended in acetone and mounted on a silicon sample holder, which is cut down to a forbidden

plane so no reflections from silicon were observed in the diffraction pattern. During operation, the samples were rotated to minimize the effect of preferred orientation in the diffraction patterns obtained. Usual diffraction scans were collected at the angular 2θ range between 5-80 degrees, with a step of 0.017 degrees and duration of 15 min; these allowed phase identification and first indexation. Higher quality diffraction data, needed for structural refinements, were collected usually for 6h, covering the angular 2θ range between 5-140 degrees, with a step of 0.017 degrees.

High resolution synchrotron diffraction data were collected at the beamline station I11 [134]of the Diamond Light source (DLS), located at the Harwell Science and Innovation Campus in Oxfordshire- UK, with the guidance of the beamlines scientists Prof. Chiu Tang, Dr. Stephen Thomson and Dr. Julia Parker. The beamline I11 is equipped by a hot air blower, with maximum temperature specification of 1000^{o}C[135], which was used in this thesis in order to collect in-situ diffraction data at variable temperatures. Samples were loaded in capillaries made by quartz of diameter 0.3mm. The wavelength of the X-ray beam was $\lambda = 0.825988$ Å. Scans were collected over a 2θ range of 2 to 150° and a step size of 0.005°, at room temperature, 300°C and from 500 to 900°C in steps of 50°C.

The neutron diffraction (ND) experiments for this thesis were carried out at the HRPD (High Resolution Powder Diffractometer) station in ISIS[136], with the guidance of the instrument scientist Dr. Aziz Daoud- Aladine. HRPD is the highest resolution neutron powder diffractometer of its type in the world; this is due to it being situated 100m away from the target, as resolution increases with distance from the target. HRPD has three fixed detector banks at 30°, at 90° and the highest-resolution back-scattering detector at 168°.

The electron diffraction (ED) work presented in this thesis was carried out by Dr. Jiangling Xu using an electron microscope in transmission mode (TEM) from JEOL; the JEM3010 instrument has a LaB_6 filament and operates at very high voltage 300keV, producing an electron beam with relativistic wavelength 0.0197 Å.

2.2.6. Structural refinement- the Rietveld method

The Rietveld structural refinement is an indirect method to obtain structural information from diffraction data and is based on the comparison between a theoretical pattern obtained from a structural model and the experimental pattern[137]. The refinements in this thesis were carried out by the software TOPAS Academic[138]. The Rietveld method relies on a reasonable accurate starting theoretical model and a close resemble to the actual crystal structure is achieved by refining this model to fit the observed data. The difference S_y between the experimental diffraction pattern and the theoretical pattern is expressed by the residual function (S_y) for an (i) number of steps:

$$S_y = \sum_i w_i \left(y_i^{obs} - y_i^{calc}\right)^2 \text{ and } w_i = {}^1/_{\sigma^2(y_i^{obs})} \qquad \textit{Equation 2.16}$$

where y_i^{obs} and y_i^{calc} are the observed and calculated intensities at the *i*th step, w_i the weight of the squared difference in intensities at the *i*th step and σ the uncertainty estimate[139, 140] (or estimated standard deviation) of y_i^{obs}.

In addition to the intensities of the Bragg reflection, the structural model refines their position, which is dependent on the lattice parameters and the shift from the origin.

There are several factors that can contribute to the observed intensity and they are all considered for the calculated intensity, expressed by the following formula[141, 142]:

$$y_i^{calc} = y_i^b + s \sum_{hkl} L_{hkl}\, P_{hkl}\, A\, |F_{hkl}|^2\, \varphi\, (2\theta_i - 2\theta_{hkl}) \qquad \textit{Equation 2.17}$$

where y_i^b : the background intensity, often generated by a separate polynomial function

s : scale factor

L_{hkl} : a combined Lorenz factor (polarization and multiplicity) for Bragg reflections with Miller indices *hkl* at the *i*th step

P_{hkl} : preferred orientation for Bragg reflections with Miller indices *hkl* at the *i*th step, which is mainly dependent on the experimental set-up

A : absorption factor of the sample, which is mainly dependent on the experimental set-up

$\varphi\,(2\theta_i - 2\theta_{hkl})$: profile function which describes the peak shapes, dependent to the diffractometers to some degree

F_{hkl} : structure factor for the proposed structural model for Bragg reflections with Miller indices hkl at the ith step

In the Rietveld refinement procedure, first all non- structural parameters are considered, such as the shift from the origin, the scale factor, the lattice parameters and the profile function. These preliminary steps may not be easy if the initial starting model is quite far from the experimental data, resulting in poor match. One possible way to overcome this difficulty is to temporarily fit the observed data in the absence of a structural model, by LeBail[143] or Pawley[144] procedures; the latter one was used in this thesis for initial refinements. Provided that the fit is good enough, it can be used as a starting point for refining the structural model. When good convergence between the observed data and the model is reached, the calculated y_i^{calc} is incorporated into the residual function (S_y, *Equation 2.16*), which is then minimised by a least-squares method.

At every step of the refinement procedure, care must be taken regarding the physical meaning of the developed structural model. The quality of the refinement is evaluated by both graphical, close resemblance of the calculated to the observed diffraction pattern, and statistical means, which are known as *R-factors* [141, 145] and should be less than 10% for a complete refinement.

The profile factor (R_p) is defined as:

$$R_p = \frac{\sum_i \left| y_i^{obs} - y_i^{calc} \right|}{\sum_i y_i^{obs}} \qquad \textit{Equation 2.18}$$

The most straightforward statistical parameter, coming directly from the residual function (S_y), is the weighted profile R-factor (R_{wp}):

$$R_{wp} = \sqrt{\frac{\sum_i w_i \left(y_i^{obs} - y_i^{calc}\right)^2}{\sum_i w_i \left(y_i^{obs}\right)^2}} = \sqrt{\frac{S_y}{\sum_i w_i \left(y_i^{obs}\right)^2}} \qquad \textit{Equation 2.19}$$

The expected R-factor (R_{exp}) is the 'lowest possible R_{wp}' for a specific set of data if the refined model was perfect and is given in the following equation:

$$R_{exp} = \sqrt{\frac{N_{obs} - N_{var} + C}{\sum_i w_i \left(y_i^{obs}\right)^2}} \xrightarrow{N_{obs} \gg N_{var,C}} R_{exp} \cong \sqrt{\frac{N_{obs}}{\sum_i w_i \left(y_i^{obs}\right)^2}} \qquad \textit{Equation 2.20}$$

The nominator ($N_{obs} - N_{var} + C$) in *Equation 2.20* refers to the degrees of freedom, where N_{obs}, N_{var} and C are the numbers of observable data points, refined parameters and constraints respectively. For a typical powder diffraction experiment, the number of data points (N_{obs} ~ 2000) is significantly larger than the number of variables and constraints, which can be ignored.

The goodness of fit (χ^2) is defined in terms of R_{exp} and R_{wp} by *Equation 2.21* and can be related to the residual function (S_y) and the degrees of freedom, which as aforementioned are dominated by the number of observable data points (N_{obs}).

$$\chi^2 = \left(\frac{R_{wp}}{R_{exp}}\right)^2 = \left(\frac{S_y}{N_{obs} - N_{var} + C}\right) \xrightarrow{N_{obs} \gg N_{var,C}} \chi^2 \cong \left(\frac{S_y}{N_{obs}}\right) \qquad \textit{Equation 2.21}$$

Since R_{wp} cannot in principle be smaller than R_{exp}, the value of χ^2 should always be ≥1. Abnormal χ^2 values are usually associated to overestimation of the uncertainty estimate σ (*Equation 2.16*). For good quality diffraction data, i.e. sufficient data points and sufficient counting time (such as y_i^{calc} is not dominated by the background intensity (y_i^b, *Equation 2.17*)), the χ^2 value should be between 1 and 2 indicating a good refinement. It should be noted that even if the value of χ^2 is close to 1, there is no guarantee that the structural model is right; the visual evaluation of the calculated pattern compared to the experimental one, as well as the physical meaning of the model should also be taken into account.

Finally, the Bragg-factor (R_{Bragg}, *Equation 2.22*) is a measure of refinement quality based on reflection intensities.s

$$R_{Bragg} = \frac{\sum_K \left| I_K^{obs} - I_K^{calc} \right|}{\sum_K \left| I_K^{obs} \right|} \qquad \textit{Equation 2.22}$$

where I_K^{obs} and I_K^{calc} refer to the observed and calculated intensity of a reflection K respectively.

2.3. Electron Microscopy studies

2.3.1. Fundamentals

Electron microscopy is based on the use of an electron beam to illuminate a specimen and produce a magnified image compared to the image obtained by an optical microscope that uses visible light; this is due to the shorter wavelength of electrons (in the order of 10^{-12}m) compared to visible light ($4\text{-}8x10^{-7}$m). Electron microscopy is a general term describing a wide range of different methods that detect the various signals arising from the interaction of the electron beam with a specimen to obtain information about structure, morphology and composition[124].

When a specimen is exposed to a high energy electron beam, the electrons can be scattered either almost elastically (by diverting the electron beam), or inelastically (by transferring some energy to the specimen). As already discussed in *Section 2.2.3*, electron diffraction detects the elastic interactions of materials with electrons. Signals caused by inelastic interactions include emission of X-rays and ejection of secondary (Auger) electrons as energy releasing mechanisms; many other processes are also possible[123].

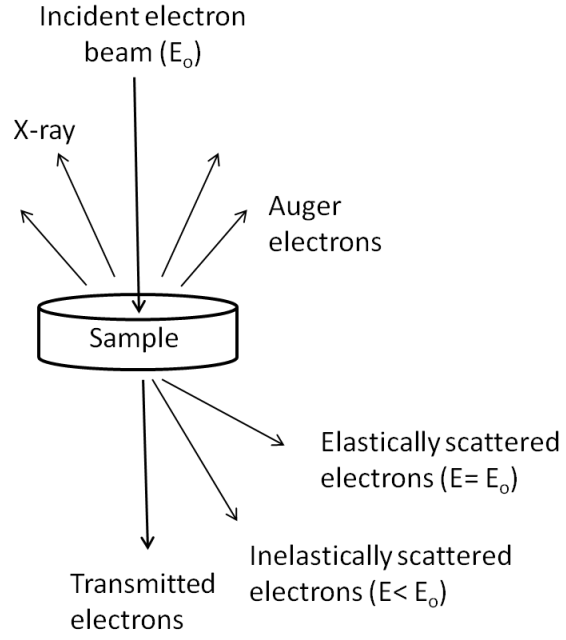

Figure 2.3: Some of the processes that occur when a specimen is exposed to an electron beam with energy E_o.

2.3.2. Types of electron microscopes

Electron microscopes operate either in a transmission mode (TEM) or a reflection mode; the main reflection instrument is the scanning electron microscope (SEM). Often TEM can be equipped with the scanning option and then it can function both as TEM and STEM[27].

2.3.2.1. Transmission electron microscopy (TEM)

Transmission electron microscopy (TEM)[27, 146] detects the elastically scattered electrons when a beam of electrons is transmitted through an ultra thin specimen. As discussed in *Section 2.2.3*, this can give valuable structural information of a crystalline material. The main advantage of TEM is the possibility to obtain information in imaging and diffraction mode almost simultaneously.

In order to use electrons in a microscope it is necessary to be able to focus them; this is achieved by several electromagnetic lenses. The condenser lenses controls the size and angular spread of an incident electron beam. Electrons, coming from the condenser system of the TEM, are scattered by the sample, which is situated in the object plane of the objective lens. The scattered electrons are focalised in the back focal plane of the objective lens and, as a result, a diffraction pattern is formed there.

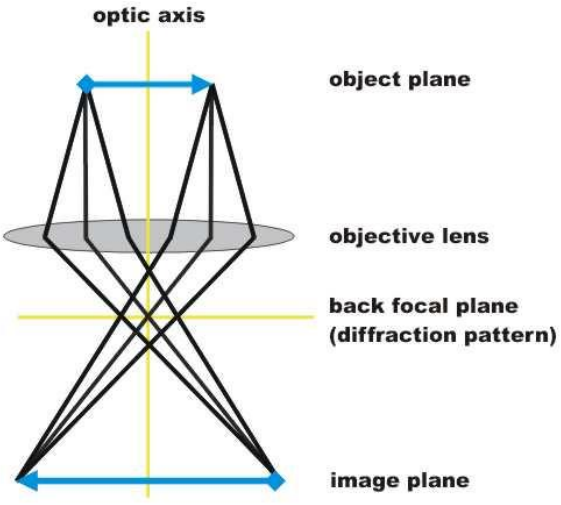

Figure 2.4: Path of electrons in a transmission electron microscope (TEM), adopted from[146]

There are two main ways of imaging the diffraction pattern, called bright field (BF) and dark field (DF) imaging. In bright field (BF) mode, an aperture is placed in the back focal plane of the objective lens allowing only the direct beam to pass. The image then results from the weakening of the direct beam due to interaction with the specimen. In dark field (DF) mode, the direct beam is blocked by an aperture, while one or more diffracted beams are allowed to pass. The diffracted beams which have interacted with the specimen can provide useful structural information.

In addition to the BF and DF imaging, TEM can operate at the high resolution TEM (HRTEM) mode, allowing the imaging of lattice images of a crystalline material oriented along a zone axis. For this, both direct and diffracted beams are allowed through a large objective aperture. The image is formed by the interference of the diffracted beams with the direct beam.

In all TEM modes, the region of the diffraction pattern that is chosen for imaging is controlled by another aperture placed in the intermediate image plane. The first intermediate image is then magnified by further lenses (projective system) and the image of the specimen can be obtained on a fluorescent screen.

2.3.2.2. Scanning Electron Microscopy (SEM)

Scanning electron microscopy (SEM)[27, 147] detects the emissions of X-rays and secondary (Auger) electrons, when a tiny electron beam (covering a spot of 50-100Å in diameter) is focused onto the surface of a specimen.

The energy of the emitted X-rays is characteristic of the elements present and hence qualitative information of the elements present in the specimen can be achieved. This is done by scanning either the wavelength or the energy of the emitted X-rays, by the so called wavelength-dispersive (WDS) and energy-dispersive (EDS) spectroscopy techniques respectively[27]. Quantitative information can also be obtained with suitable calibration. It should be noted that the detection of X-rays can also be done using a TEM instrument.

The detection of secondary (Auger) electrons is used for the imaging of the specimen's surface, providing information about morphology and surface topography. The resolution of the SEM

depends on the size of the electron spot, which is related to the wavelength of the electrons and the electron-optical system that produces the scanning beam. The highest resolution for conventional SEMs is approximately 100 Å, which is lower than the resolution in atomic scale that can be achieved by TEM. However, SEM can provide images of larger areas of a specimen compared to TEM.

2.3.2.3. Scanning transmission electron microscope (STEM)

In scanning transmission electron microscopy (STEM), the surface of a specimen is scanned by a tiny electron beam and the signal is recorded by selected detectors[148]. There are three detectors that can be used to obtain STEM images: (a) a bright field detector (BF), similar to the BF-TEM (Section 2.3.2.1), (b) annular dark field (ADF) and (c) high angle annular dark field (HAADF). The ADF and HAADF detectors are disks with a hole, which use the scattered electrons for image formation. As aforementioned (Section 2.2.3) the electron scattering in crystalline solids is a result of the strong Coulomb interaction of the negatively charged electrons with the positive potential inside the electron cloud in an atom; this interaction leads to high scattering angles. The HAADF disk has larger diameter, with also larger diameter hole, compared to the ADF disk, and hence it is more capable to detect the high-angle scattered electrons[149].

The STEM resolution is similar to the TEM, hence it is capable of giving information in the crystal level. Additionally, it can provide information over a larger area. This makes STEM strong in detection of crystalline areas and defects; when using the HAADF detector it is even possible to detect single atoms in a crystalline material. STEM can also give quantitative information when combined with analytical methods (e.g. EDS, Section 2.3.2.2).

2.3.3. Microscopy studies in this thesis

The BSCFM materials in this thesis, synthesised as described in *Section 2.1*, were characterised by a combination of microscopy techniques. For this, a quantity of the material in powder form was transferred to a copper TEM grid, and this was then transferred to the TEM machine.

Dark field TEM images of the as-made materials were collected by Dr. Jiangling Xu and Dr. Antoine Demont using a JEOL JEM3010 instrument with LaB_6 filament, operating at 300 keV.

Quantitative EDS data for selected samples were collected by Dr. Jiangling Xu using a JEOL JEM2000FX, with a W filament, operating at 200 keV. For the BSCFM composition, showing the most promising performance. High Angle Annular Dark Field (HAADF) images were collected by Dr. Simon Romani using a JEOL JEM 2100FCs, with Schottky Field Emission Gun operating in STEM mode with CEOS aberration corrected probe.

SEM imaging of the symmetrical cells used for electrochemical characterization (*Section2.7.2*), which were placed on a SEM holder, were carried out in the Centre for Materials Discovery (CMD) at Liverpool University by Dr. Christopher I. Ireland and Dr. Xinming Wan. The instrument was a Hitachi S-4800 scanning electron microscope and the analysis of the sample was performed using a low KV electron beam (3 KV).

2.4. Thermogravimetric Analysis (TGA)

Thermogravimetric analysis (TGA) measures weight changes as a function of temperature and/or time[27]. While heating, a material can lose mass due to dehydration. For dry oxide materials, TGA is useful in monitoring weight changes related to changes in oxygen content and oxidation states of the constituent elements. Oxidation of a specimen can lead to weight gain, whilst reduction results in weight loss. In addition, weight loss can indicate decomposition and formation of volatile products.

In this thesis, selected BSCFM compositions were studied by TGA in order to obtain information regarding the oxygen content and the oxidation states of the transition metals. Typically, approximately 0.04 g of the as-made materials (synthesised as described in *Section 2.1*) were placed in a platinum pan. The TGA experiments were performed by heating a sample from room temperature to 750°C in a flowing air atmosphere at a heating and cooling rate of 5°C/min. Each sample was cycled from 50°C to 750°C to 50°C a total of three times (1 cycle is heating and cooling), with a dwell at the maximum and minimum temperatures of 30 minutes on each cycle.

Reduction experiments for selected BSCFM compositions were carried out in 5% H_2/N_2 (50ml/min) with N_2 carrier gas (80ml/min) and heated at 1100^{o}C for 10h with heating and cooling rate of 5^{o}C/min. Before the measurements, the samples were heated to 200^{o}C for 2-3 h, to

ensure moisture removal. The TGA measurements were carried out using a SDT Q600 simultaneous TGA-DSC from TA.

2.5. Mössbauer Spectroscopy

Mössbauer or γ-ray spectroscopy is a technique that measures the absorption of γ-rays by atomic nuclei in a crystalline or amorphous material. The absorption of γ-rays can cause splitting of the nuclear energy levels. The effect can be observed in many nuclei, but sensitive information on the solid state environment can be observed only for a few cases (^{57}Fe, ^{119}Sn, ^{121}Sb) and among them the ^{57}Fe isotope, about 2% in natural iron, is the most sensitive[27].

In ^{57}Fe Mössbauer spectroscopy[150], a beam of ^{57}Fe 14.4 keV γ- rays is produced by a radioactive ^{57}Co source. In a Fe-containing specimen, γ-rays are resonantly absorbed by a ^{57}Fe isotope absorber. The energy of the emitted γ-rays is modified when the source moves with ranging velocity with respect to the absorber, according to the Doppler effect, and this causes splitting of the nuclear energy bands of the absorber, giving a six line spectrum (or 'sextet') in a magnetically ordered sample (*Figure 2.5*). In paramagnetic samples, a characteristic two line spectrum (or 'doublet' is observed).

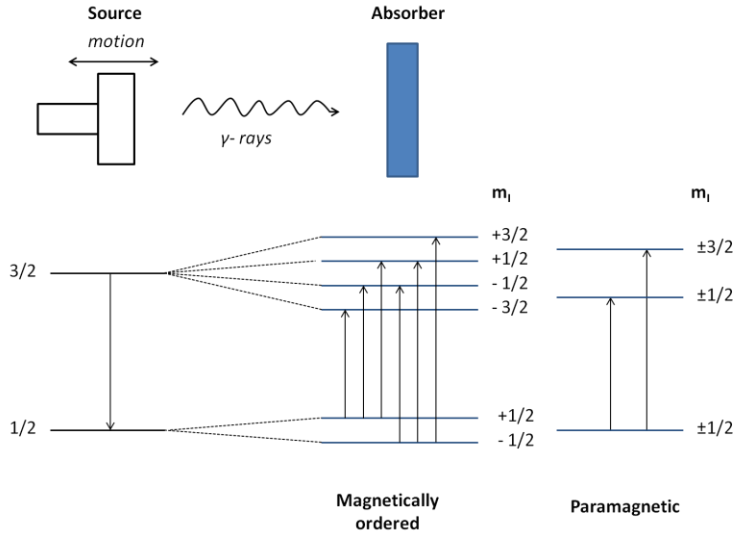

Figure 2.5: Splitting of the nuclear energy bands of a γ-ray absorber, in the cases of magnetically-ordered and paramagnetic materials, measured by Mössbauer spectroscopy.

Mössbauer data can give information regarding the oxidation state and coordination number of Fe-containing samples[151], since the nuclear energy bands differ slightly with the oxidation state and coordination environment of the absorbing atoms.

During this thesis, Mössbauer spectroscopy was used in order to determine the iron oxidation state in the BSCFM materials. Data were collected by Dr. Mike Thomas at 290K using a conventional constant acceleration Mössbauer spectrometer incorporating a ~25mCi source of ^{57}Co in a Rh matrix.

2.6. Iodometric Titrations

Iodometric titrations were performed to determine the oxygen content in the BSCF materials, assuming that all the trivalent transition metals are reduced to their divalent state at the conditions of the titration (*Equation 2.23*). Approximately 40 mg of material was dissolved in 20 ml of 3 M HCl acid with an excess of KI. Upon complete dissolution, the solution was titrated with 0.1 Molar sodium thiosulphate, $Na_2S_2O_3$ (*Equation 2.24*). As $Na_2S_2O_3$ is added the solution turned from orange to straw; starch solution was added just before the end point, where the solution turns dark purple continued titrations leads to the solution turning clear. Titrations were repeated three times to ensure reproducibility.

$$2\ B^{3+} + 2I^- \leftrightarrow 2\ B^{2+} + I_2 \qquad \textit{Equation 2.23}$$

$$I_2 + 2\ S_2O_3^{2-} \leftrightarrow 2I^- + S_4O_6^{2-}, \quad n(S_4O_6^{2-}) = 2\ n(B^{3+}) \qquad \textit{Equation 2.24}$$

Prior to titrations the $Na_2S_2O_3$ solution was standardised by titrating it against potassium iodate (KIO_3), which is a source of I_2 when mixed with potassium iodide (KI) in an acidic solution and for this reason 1 Molar sulphuric acid (H_2SO_4) was used.

$$IO_3^- + 5I^- + 6H^+ \leftrightarrow 3I_2 + 3H_2O$$
$$I_2 + 2\ S_2O_3^{2-} \leftrightarrow 2I^- + S_4O_6^{2-} \qquad \textit{Equation 2.25}$$

The oxygen content ($[O]$) was then calculated according to the following formula:

$$[O] = [\mathrm{Ored}] + \frac{\mathrm{Mw\ (red)}}{\mathrm{mass}\ (1/\mathrm{n(B^{3+})} - 16/\mathrm{mass})} \qquad \textit{Equation 2.26}$$

where [Ored] the oxygen content of the reduced sample, and Mw (red) is its molecular mass, mass (g) is the mass of the sample,16 refers to the atomic weight of oxygen, and $\mathrm{n(B^{3+})}$ is the number of moles of trivalent cations as determined from the titration.

2.7. Electrical characterisation

The electrical properties of the BSCFM materials presented in this thesis were measured by two methods: (a) conductivity measurements by the four-probe direct current (DC) method (b) impedance measurements by alternating current (AC) two-probe impedance spectroscopy; the methods principles are discussed below in *Sections 2.7.1* and *2.7.2* respectively.

2.7.1. Electrical conductivity measurements

2.7.1.1. The four-probe DC method

Electrical conductivity (σ) is defined as the inverse of electrical resistivity (ρ, units: Ω.m), which is the property of a material to oppose the flow of an electric current. The electrical resistivity is dependent on the geometry of a specimen, as expressed by the following equation:

$$\rho = \frac{\mathrm{RA}}{\mathrm{l}} \quad \text{and} \quad \sigma = \frac{1}{\rho} \qquad \textit{Equation 2.27}$$

where A is the cross-sectional area (units: m^2) , l is the length (units: m) and R is the electrical resistance (units: Ω) of the specimen. The electrical resistance (R) is defined as the ratio of the voltage (V) experienced by an electric current (I) that flows through it, according to Ohm's law:

$$\mathrm{R} = \frac{\mathrm{V}}{\mathrm{I}} \qquad \textit{Equation 2.28}$$

The four-probe DC method uses a simple apparatus to measure the voltage generated by a passing current to a specimen. The electrical resistivity and conductivity of the material can be then calculated by *Equation 2.27* and *Equation 2.28*.

The four-probe apparatus (*Figure 2.6*) is constructed by a pair of inner voltage (V) probes and a pair of outer current (I) probes. The separation of current and voltage sensing electrodes eliminates the contribution of the wiring and contact resistances. The inner probes measure the voltage induced by passing a current through the two outer probes.

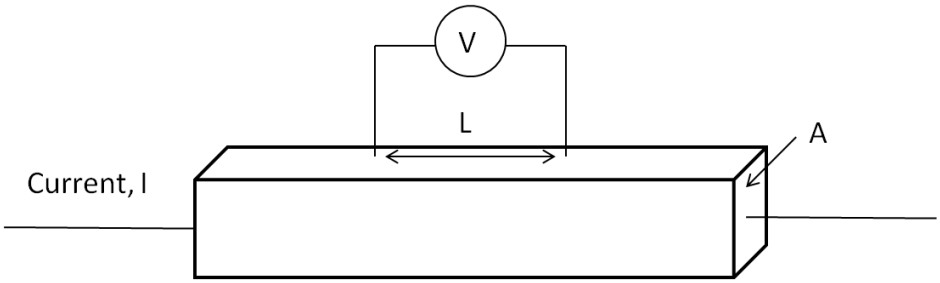

Figure 2.6: Schematic illustration of the arrangement for electrical conductivity measurements using the 4-probe DC technique for a specimen with length L and cross-sectional area A.

The conductivity measurements in this study were done on bars cut from circular 'dense' pellets. The pellets had diameter of 13mm, determining the maximum length of the bar, and thickness approximately 1mm, which controls the cross-sectional area of the bar. The dimensions of the bars were measured carefully with a caliper and recorded. Platinum wires were attached to the bars (held in position with a small amount of platinum paste) to make the I-V probes with four-in-a-line contact geometry. Prior to the DC conductivity measurement, the platinum paste was dried by heating at 800^{o}C for 60 min to achieve good contact. The resistance of the materials was recorded at the temperature range 500-850^{o}C in 50^{o} steps, allowing 90 min for thermal equilibration. The current was provided by a Keithley 220 Current Source and the voltage was measured by a Keithley 2182 Nanovoltameter.

To achieve samples with a high relative density, as-made powders (following the synthesis procedure described in *Section 2.1*) were ballmilled in isopropanol for 12 hours, to reduce the grain size and uniaxially pressed into pellets. The pellets were then isostatically pressed (*Section*

2.7.1.2) to increase the compaction and heated at 1200°C for 24 hours. For all compositions, the relative density was greater than 90% (*Section 2.7.1.3*).

2.7.1.2. Cold Isostatic Pressing

Cold isostatic pressing is a method of applying pressure from multiple directions (hydrostatic pressure) to a molded sample, resulting in great uniformity of compaction over its entire surface[152].

Dense pellets for electrical measurements were made via cold-isostatic pressing (CIP), using an Autoclave Engineers Cold Isostatic Press, under a pressure of 206.85 MPa pressure. Samples are first pelletized as described in *Section 2.7.1.1* then sealed in waterproof bags and lowered into the hydraulic fluid. The system is then sealed and brought up to pressure and left to dwell for five minutes before the pressure is slowly released and the sample bag retrieved.

2.7.1.3. Density measurements

The relative density (ρ_{rel}) of the pellets used for conductivity measurements was calculated as the fraction of the density of the sample (ρ, g/cm^3) to the theoretical crystallographic density (ρ_{theor}, g/cm^3):

$$\rho_{rel}(\%) = \frac{\rho}{\rho_{theor}} \times 100 \qquad \textit{Equation 2.29}$$

The theoretical crystallographic density (ρ_{theor}) is the density of 1 unit cell of the crystalline material, with volume $V_{unit\ cell} = a^2$ for the cubic structures, where a is the lattice parameter coming out from the refinement and differs for each composition. The mass of the unit cell ($m_{unit\ cell}$) is calculated from the molecular mass (M_w) for each composition and the Avogadro number (N_A), assuming packing density (Z) of 1 formula units/ unit cell.

$$\rho_{theor} = \frac{m_{unit\ cell}}{V_{unit\ cell}} = \frac{M_w/N_A\ Z}{V_{unit\ cell}} \qquad \textit{Equation 2.30}$$

The density of the sample (ρ) was measured using an Archimedes balance. According to Archimedes principle when an object is immersed in a fluid, the volume of the displaced fluid is the same as of the object which displaced it. For this measurement, the sample with density was under investigation, was immersed in distilled water to allow for liquid to enter its pores and for

to equilibrate. The weight was recorded before (m_1) and after (m_2) the immersion. The sample was then removed from the distilled water, dried carefully with a non-adsorbing material and the mass of the soaked sample was recorded (m_3). The sample density (ρ) was then calculated according to *Equation 2.31*.

$$\rho = \frac{m_1}{m_3 - m_2} \times \rho_{H_2O} \qquad \textit{Equation 2.31}$$

where ρ_{H_2O} is the density of water which at 20°C is 0.99823 g/cm^3.

2.7.2. AC Electrochemical Impedance Spectroscopy (EIS)

2.7.2.1. Fundamentals

Impedance, defined as the ability of a material to resist the current that passes through it, is a more general term for electrical resistance R (*Equation 2.28, Section 2.7.1.1*) as it takes into account different processes that can affect the passing current in a real electrochemical system.
Electrochemical impedance[35, 153] is usually measured by applying a single frequency sinusoidal AC voltage (*Equation 2.32*) to an electrochemical cell and measuring the current through the cell (*Equation 2.33*).

$$V(t) = V_m \sin(\omega t) \qquad \textit{Equation 2.32}$$

$$I(t) = I_m \sin(\omega t + \theta) \qquad \textit{Equation 2.33}$$

where $V(t)$ and $I(t)$ the signals of voltage and current respectively at time t,
V_m and I_m their magnitude, θ the phase difference between them, and
ω the radial frequency (rad/sec), which is related to the frequency (f, Hz) by: $\omega = 2\pi f$

Impedance (Z) is then defined by the Ohm's law (*Equation 2.34*), similarly to R, as the fraction of voltage (V) to current (I).

$$Z(\omega) = \frac{V(t)}{I(t)} = \frac{V_m \sin(\omega t)}{I_m \sin(\omega t + \theta)} = Z_m \frac{\sin(\omega t)}{\sin(\omega t + \theta)} \qquad \textit{Equation 2.34}$$

where Z_m is the impedance magnitude ($=V_m/I_m$) and θ the phase angle.

It is convenient to express the frequency dependent impedance $Z(\omega)$ as a complex number with real (Re (Z)) and imaginary (Im (Z)) parts.

$$Z(\omega) = |Z_m|\, e^{(-i\theta)} = |Z_m|\cos(\theta) + i|Z_m|\sin(\theta) = Z' + iZ'' \qquad \textit{Equation 2.35}$$

where $\mathrm{Re}\,(Z) = Z' = |Z_m|\cos(\theta)$ and $\mathrm{Im}\,(Z) = Z'' = |Z_m|\sin(\theta)$

with phase angle $\theta = \tan^{-1}\left(\frac{Z''}{Z'}\right)$ and magnitude $|Z_m| = \sqrt{(Z')^2 + (Z'')^2}$

Using this nomenclature, the impedances of the basic electrical elements ohmic resistor (R), inductor (L) and capacitor (C) are defined as follows:

- Ohmic resistor, R: $Z(\omega) = R + i\,0$ *Equation 2.36*
- Inductor, L: $Z(\omega) = 0 + i\omega L$ *Equation 2.37*
- Capacitor , C: $Z(\omega) = 0 + \frac{1}{i\omega C}$ *Equation 2.38*

In addition to the three basic elements, the constant phase element (CPE) is introduced, in order to describe non-ideal processes in real systems.

- CPE: $Z(\omega) = \frac{A}{(i\omega)^n}$ *Equation 2.39*

where A and n constants. Depending on their values, CPE can turn to ideal elements: capacitor if n=1 and A=1/C, ohmic resistance when n=0 and A=R and inductor when n=-1 and A= L.

2.7.2.2. Assignment of impedance response to real processes

When the frequency dependent impedance (Z(ω)), is recorded over a wide range of frequencies, the Re (Z)) and imaginary (Im (Z)) components can be plotted on a Nyquist plot, with a real (Z`) x-axis and imaginary (- Z'') y-axis. This plot displays characteristic impedance arcs which can be modeled by an equivalent circuit, with responses from the defined basic electrical elements connected in parallel or in series. The electrochemical impedance plots of real samples usually contain several arcs. Assignment of the impedance arcs to real physical processes allows the study of the factors and mechanisms associated to the total electrical conductivity.

An example of typical impedance spectrum representing a thick-film solid electrolyte symmetrical cell is shown in Figure 2.7, consisting of three main arcs which were assigned to the electrolyte, grain boundary and the electrode processes[3].

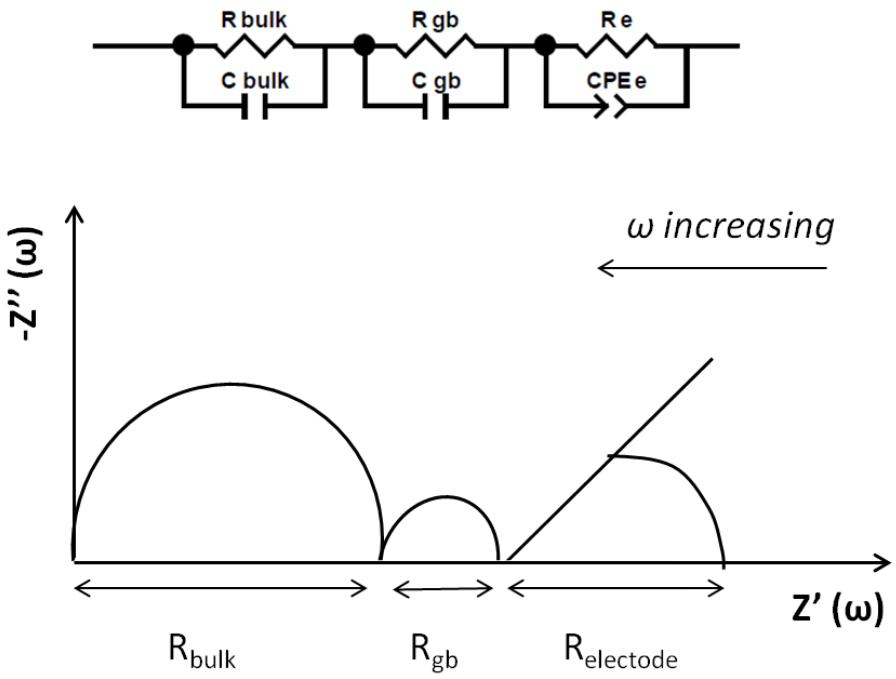

Figure 2.7: Typical Nyquist plot for a thick-film solid electrolyte symmetrical cell and the representative equivalent circuit[3]

The contributions of the electrolyte and the grain boundary were modeled with two RC circuits in series, consisting of a resistor and capacitor in parallel. However, the arc assigned to the

electrode process is depressed and cannot be fitted to a simple RC model; this is due to the large dependence of electrodes resistance on the material and microstructure of the electrode.

In these cases, a CPE is often employed instead of a capacitor in the RC model. The pseudo-capacitance of a CPE is related to the arc depression angle by *Equation 2.40*.

$$C = (R^{1-n} Q)^{1/n} \qquad \textit{Equation 2.40}$$

where R is the element resistance, Q is the pseudo-capacitance and n is the parameter related to the arc depression angle. If n= 1, the CPE behaves as a true capacitor and the arc is a perfect semicircle. If n= 0.5, the impedance spectrum is shown by a straight line, intersecting the real axis by 45^{o}; this can be modeled by a Warburg element and is associated with semi infinite diffusion[3].

The assignment of the arcs to physical processes is based on the fact that different physical phenomena often relax at very different frequencies[3, 153]. Moreover, the fitting of the arcs to equivalent circuits can give very useful information. One of the most useful parameters is the derived capacitance values of each of the arcs present; by using the example of Figure 2.7 the typical capacitance values [154] for the electrolyte, grain boundary and electrode processes differ and this facilitates the assignment to the different contributions.

Table 2.5: Capacitance values and their possible interpretation [154]

Capacitance (F)	**Phenomenon responsible**
10^{-12}	Bulk of electrolyte
10^{-11}-10^{-8}	Grain boundary
10^{-4}	Electrochemical reactions

In the case of cathode materials, different processes involved in the oxygen reduction mechanism can be identified by their dependence on oxygen partial pressure (pO_2); this was used in this study and is discussed in detail in the next section.

2.7.2.3. Assignment of arcs in cathode processes

The most commonly used parameter to determine the species involved in the rate determining step (RDS) of each resistance arc in the impedance response of cathode materials [19, 155] is the power (m) law dependence on pO_2 (*Equation 2.41*) and numerous examples exist in the literature[81, 156-161].

$$R = k\, p_{O_2}^{-m} \qquad \textit{Equation 2.41}$$

As discussed in Chapter 1, (*Section 1.2.2-Insight into the cathode processes*), the reduction of oxygen in a cathode material proceeds through a number of steps including (a) gas phase molecular oxygen diffusion inside the cathode or outside the cathode layer, (b) dissociative adsorption to atomic oxygen species, (c) oxygen exchange redox reaction between the adsorbed oxygen and the bulk cathode material (also called charge transfer) and (d) transport of oxygen species to the cathode-electrolyte interface and (e) finally to the bulk of the electrolyte, which is relative fast and unlikely to be rate controlling. Each of the rest cathode processes displays a different dependence on oxygen partial pressure (pO_2) as shown in *Table 2.6* and explained below.

Table 2.6: Cathode processes and dependence of their resistance values on oxygen partial pressure (pO_2)

Physical process		**pO_2 dependence**
(a) Gas phase diffusion	$O_2(g) \rightleftharpoons O_2(ads)$	$R = k\, p_{O_2}^{-1}$, i.e. m=-1
(b) Dissociative adsorption	$O_2(ads) \rightleftharpoons 2\, O(ads)$	$R = k\, p_{O_2}^{-1/2}$, i.e. m= -1/2
(c) Charge transfer	$O(ads) + Vo^{\bullet\bullet} + 2\, e' \rightleftharpoons O_O^{2-}$	$R = k\, p_{O_2}^{-1/4}$, i.e. m= -1/4

(a) <u>gas phase diffusion</u>

The resistance associated with gas diffusion-limiting step (R_D), as defined from Ohm's law *(Equation 2.28)*, is inversely proportionally to the oxygen gas flux (J_{O_2}, Fick's law (*Equation 1.7*)) assuming that the available current is limited only by the amount of O_2 getting to the reaction sites on the cathode surface. This can be expressed as:

$$R_D = \frac{V}{I} \quad \text{where } I = c\, J_{O_2} \quad \text{and } J_{O_2} = -D\left(\frac{dC}{dx}\right) = -D\, c' pO_2 \qquad \textit{Equation 2.42}$$

where c, c' constants denoting that in diffusion-limiting conditions the current (I) is proportional to the oxygen flux (J_{O_2}). Assuming that the diffusion coefficient (D) is constant over the pO_2 range measured and that the concentration gradients are linear, the oxygen gas flux (J_{O_2}) is proportional to the gas concentration, i.e. pO_2. The exact relation of gas diffusion resistance with pO_2 in diffusion limiting cathode processes is reported [157]to be:

$$R_D = \left(\frac{RT}{4F}\right)^2 L \frac{1}{D}\left(\frac{1}{pO_2} - 1\right)\left(1.0133 \cdot 10^5 \frac{Pa}{atm}\right)^{-1} \qquad \textit{Equation 2.43}$$

where L: thickness of cathode, T is temperature, R and F are the universal gas constant and Faraday constant respectively. Hence, the diffusion resistance is inversely proportionally to partial oxygen pressure, for $pO_2 < 1$ atm.

(b) Dissociative adsorption

The resistance associated with the dissociative adsorption ($R_{dis.ads.}$) can be derived from the resistivity ($\rho_{d.ad.}$), which is given by the complex *Equation 2.44*[161], where k and k' are the adsorption and desorption coefficients assuming Langmuir adsorption, $\left(\frac{l}{\rho_{ion}}\right)$ represents the resistance caused by diffusion of the ion in the bulk cathode and R, T, F have their usual meanings.

$$\rho_{d.ad.} = \left(\frac{RT}{8k'F^2} \times \frac{(B+1)}{B^2}\right) + \left(\frac{l}{\rho_{ion}}\right), \text{where } B = \sqrt{\left(\frac{k}{k'}\right) pO_2} \qquad \textit{Equation 2.44}$$

$$\text{when } \left(\frac{l}{\rho_{ion}}\right) << \left(\frac{RT}{8k'F^2} \times \frac{(B+1)}{B^2}\right)$$

$$\rho_{d.ad.} = \left(\frac{RT}{8k'F^2} \times \frac{(B+1)}{B^2}\right) \xrightarrow{B \gg 1} \rho_{d.ad.} = \left(\frac{RT}{8k'F^2} \times \frac{1}{B}\right) = \frac{RT}{8k'F^2} \times \sqrt{\left(\frac{k'}{k}\right)\frac{1}{pO_2}} = a\, pO_2^{-1/2}$$

When the process is not limited by the ionic diffusion in the bulk and B>>1 (i.e. the rate of adsorption k is greater than the rate of adsorption k'), the resistivity is inversely proportional to the square root of partial oxygen pressure (pO_2). From *Equation 2.44*, it can also be deduced that the oxygen ionic diffusion in the bulk is not dependent on pO_2.

(c) Charge transfer

When charge transfer is the limiting step of the cathode reaction, we assume fast oxygen adsorption (*b*) and transfer of gaseous oxygen into a vacancy $Vo^{\bullet\bullet}$ (*c*), the sum of these reactions is shown in *Equation 2.45*.

$$\tfrac{1}{2}\, O_2(ads) \rightleftharpoons O(ads) \qquad (b)$$

$$+ \qquad O(ads) + Vo^{\bullet\bullet} + 2\, e^- \rightleftharpoons O_O^{2-} \qquad (c)$$

$$\tfrac{1}{2}\, O_2 + Vo^{\bullet\bullet} + 2\, e^- \rightleftharpoons O_O^{2-} \qquad \textit{Equation 2.45}$$

The equilibrium constant of this reaction, is thus given by *Equation 2.46*, which can be rearranged to give the concentration of electrons ([e]) or in other words the current (I) (*Equation 2.47*).

$$K = \frac{[O_O^{2-}]}{pO_2^{\frac{1}{2}}\,[Vo^{\bullet\bullet}][e]^2} \Leftrightarrow \qquad \textit{Equation 2.46}$$

$$I \rightarrow [e] = \sqrt{\frac{[Vo^{\bullet\bullet}]K\, pO_2^{\frac{1}{2}}}{[O_O^{2-}]}} = K' pO_2{}^{1/4} \qquad \text{where } K' = \sqrt{\frac{[Vo^{\bullet\bullet}]\,K}{[O_O^{2-}]}} \qquad \textit{Equation 2.47}$$

In equilibrium, the oxygen vacancies are consumed by the lattice with consequent formation of lattice oxygen ions (O_O^{2-}), and hence their ratio can be assumed to be constant. Under these conditions, the current I is proportional to the fourth root of oxygen partial pressure (pO_2). Combining this information with Ohm's law (*Equation 2.28*), the resistance associated with electronic charge transfer is inversely proportional to $pO_2{}^{1/4}$. If there are is not adequate number of oxygen vacancies in the lattice, the reaction will occur at the opposite direction. In this case, the oxygen ionic transfer in the bulk is the rate determining step and the associated resistance will be proportional to pO_2.

2.7.2.4. Impedance measurements in this thesis

AC impedance was used in order to evaluate the electrochemical behaviour of the BSCF materials as cathode materials for SOFCs. Measurements were performed on samples in the 'symmetrical-cell' configuration, which consists of porous cathode coating on both sides of a dense electrolyte substrate. The preparation procedure is illustrated in Figure 2.8. The electrolyte substrate was obtained by pressing approximately 0.8g powder $Ce_{0.8}Sm_{0.2}O_{2-d}$ (SDC, from FuelcellMaterials.com) into pellets with a diameter of 10 mm and sintering at 1400^{o}C for 8h. The density of the SDC electrolyte was in the range of 90-95%, measured as described in Section *2.7.1.3*. Symmetrical cells were fabricated by screen-printing a BSCFM ink, consisting of a mixture of the BSCFM powder with a commercially provided organic pore-former in an appropriate ratio.The BSCFM powder used in the preparation of the ink was ball-milled from the as-made material in order to reduce particle size leading to enlargement of the active area. The particle size measured by BET, as will be discussed in *Section 2.8*, was about 190 nm. Before the printing, the electrolyte substrate was polished with SiC grinding papers (first use No.240, then No.320 and finally No.600) to thickness 1.5-2.0 mm and washed with acetone. The printing of the BSCFM ink was performed with an AccuCoat Screen Printer (model 3230) from Aremco.

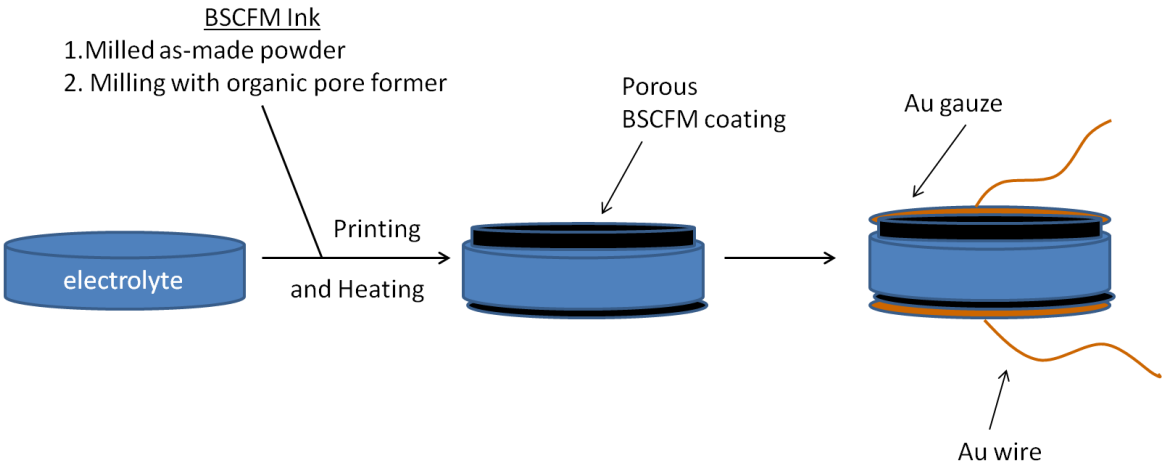

Figure 2.8: Schematic illustration of the preparation of BSCFM specimens in the 'symmetrical-cell' configuration for AC impedance measurements

The symmetrical cell was then heated slowly to 950^{o}C (heating rate: 1.5^{o}C/min) allowing the organic pore-former to burn-off resulting in the required cathode porous structure and the

adhesion of the cathode layer onto the electrolyte substrate. The morphology of the cathode is an important factor affecting the cathode performance and the fabrication procedure has been studied in detail in Chapter 5. Before the measurement, contacts were made by gold wire attached to a piece of gold gauze, placed to both sides of the symmetrical cell with small amount of gold paste applied to ensure good contact, when slowly heated at 600^{o}C for 2h (heating rate: 1.5^{o}C/min).

The measured resistance for the cathode was converted to area specific resistance (ASR) by normalising and dividing by two to take into account the symmetry of the cell.

$$\text{Area Specific resistance (ASR)} = R\ A/2 \qquad \textit{Equation 2.48}$$

AC impedance measurements in air were recorded over the temperature range of 600-800^{o}C every 50°C and the symmetrical cell was held for 90 minutes at each temperature to allow thermal equilibration.

For the AC impedance measurements in variable gas environment, the gas flows were controlled by mass flow controllers. The oxygen partial pressure was recorded by an oxygen gas sensor, which was located in the furnace and connected to a Keithley 617 programmable electrometer. The signal (E, in V) was then converted to pO_2 (atm) by *Equation 2.49*. Measurements were collected at the pO2 range 0.21-0.0028 atm over the temperature range 600-850^{o}C.

$$E = \frac{-RT}{4F} \ln \frac{pO_2}{pO_2, ref} \text{ where } pO_2, ref = 0.21 \text{ atm} \qquad \textit{Equation 2.49}$$

All impedance data were collected over the frequency range 1 MHz to 0.01 Hz using a Solartron 1260 FRA with a modulation potential of 10 mV, and measurements were made using ZPlot v.2.9b (Scribner Associates).The impedance arcs were modeled using equivalent circuit models (ECM) with ZView v.3.2b (Scribner Associates).

2.8. BET surface area measurements

2.8.1. Fundamentals

Surface area measurements of a specimen are based on gas sorption. The Brunauer-Emmet-Teller BET) theory[162] is an extension of the classical Langmuir monolayer adsorption theory assuming that gas molecules physically adsorb on a solid in layers infinitely, there is no interaction between each adsorption layer, and Langmuir theory can be applied to each layer. The limiting case of an infinite number of adsorbate layers, which provides a reasonable approximation for multilayer adsorbates with more than four layers[163], can be expressed by the BET equation:

$$\frac{\mathrm{P}}{\mathrm{V}(\mathrm{P_o}-\mathrm{P})} = \frac{1}{\mathrm{V_m C}} + \frac{\mathrm{C}-1}{\mathrm{V_m}-\mathrm{C}}\left(\frac{\mathrm{P}}{\mathrm{P_o}}\right) \qquad \textit{Equation 2.50}$$

$$\text{intercept: } \frac{1}{\mathrm{V_m C}} \quad \text{gradient: } \frac{\mathrm{C}-1}{\mathrm{V_m}-\mathrm{C}}$$

where V is the gas uptake, $\mathrm{V_m}$ is volume of monolayer adsorbed gas quantity, P and P_o stand for the equilibrium and saturation pressure of the adsorptive gas and C is the BET constant which should be positive. The values of V_m and C can be derived from the BET isotherm, i.e. plotting $\frac{\mathrm{P}}{\mathrm{V}(\mathrm{P_o}-\mathrm{P})}$ against $\left(\frac{\mathrm{P}}{\mathrm{P_o}}\right)$, from the gradient and intercept (*Equation 2.50*).

The calculation of the BET surface area (S_{BET}, $\mathrm{m^2/g}$) can then be calculated according to:

$$\mathrm{S_{BET}} = \frac{\mathrm{V_m\, N_A\, s}}{\mathrm{V\, m}} \qquad \textit{Equation 2.51}$$

where $\mathrm{N_A}$ is Avogadro's number, $\boldsymbol{s}$ is the adsorption cross section of the adsorbing species and m is the mass of absorbent.

2.8.2. BET measurements in this thesis

In this thesis, the BET method was used in order to measure the surface area of the porous BSCFM coating in the symmetrical cells used for electrochemical measurements (Section 2.7.2.4). For this study, the BSCFM coating was supported on a thin Pt foil, instead of the dense electrolyte substrate, in order to increase the relative weight of the cathode in the cell and maximise the gas uptake. The Pt-supported cells were prepared by applying the cathode inks on the surface of the Pt foil, which was glued with the Pt in order to support it during the printing process. The glue was burned off upon heating, allowing the cathode coating (*ca*. 10 mg) to adhere on the Pt foil (*ca*. 40 mg) and separate the Pt- supported cathode from the SDC substrate. The preparation of the Pt-supported cathode is illustrated in *Figure 2.9*, including the measurement procedure.

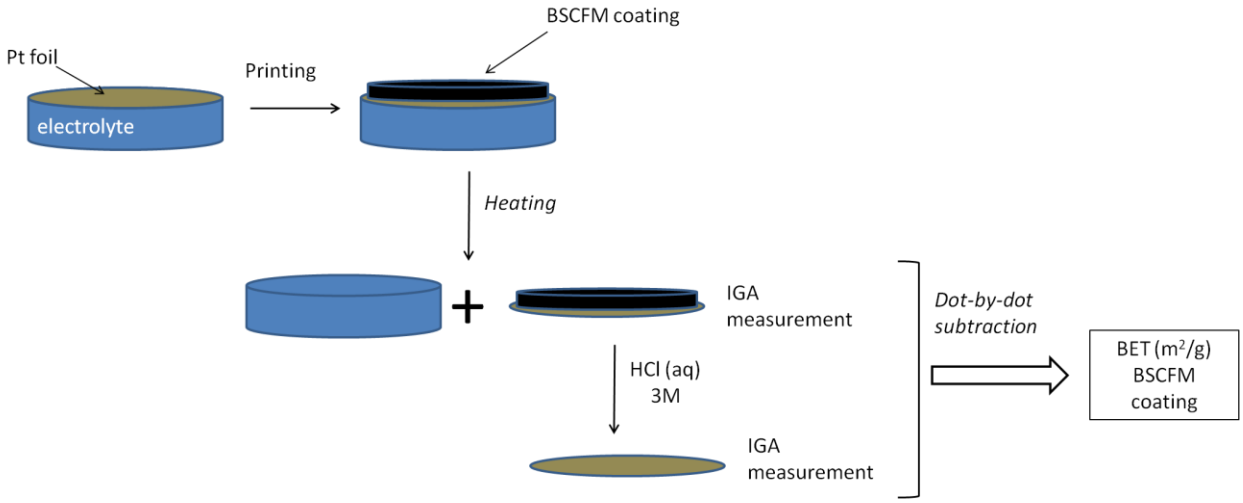

Figure 2.9: Schematic illustration for the preparation and BET measurement of the BSCFM coating in the symmetrical-cells configuration.

The porosity of the Pt-supported cathode coating was evaluated by Dr. Carlos Martí-Gastaldo with gravimetric sorption measurements by using an Intelligent Gravimetric Analyzer (IGA) from Hiden. N_2 isotherms were collected at 77K up to 1 bar. Before data collection, the samples were evacuated overnight at 10^{-6} mbar and heated at 80ºC for 2 hours. A measurement "time-out" of 40 minutes was used for all measurements, this being the maximum time allowed for the measurement of a single data point.

The response of the Pt foil was removed by a using a dot-by-dot subtraction protocol, so that the weight difference could be solely ascribed to the N_2 uptake for the cathode coating. This involved the collection of an additional isotherm with response solely from the Pt foil. For this, the cathode coating was removed by soaking the cell in 10ml of HCl(aq) 3M for 2 hours. The bare substrate was thoroughly washed with water, acetone and left to dry in the oven at 100ºC. Next, it was transferred to the IGA and measured by following the same protocol used for the coated cell. Finally, the BET surface area of the cathode coating was calculated by fitting the dependence of the N_2 uptake with the pressure to the BET equation (*Equation 2.51*) at $0.05 \leq (\frac{P}{P_o}) \leq 0.35$.

3. CHAPTER 3-SYNTHESIS AND PROPERTIES OF BSCFM OXIDES

Synthesis and properties of BSCFM oxides

This chapter focuses on the preparation of BSCFM compounds, with general formula $Ba_{0.5}Sr_{0.5}Co_{0.8-x}Fe_{0.2-y}Mo_{x+y}O_{3-\delta}$, and their evaluation as cathode materials for IT-SOFCs. The synthesis and phase identification are described in *Section 3.1*, including the synthetic approach (*Section 3.1.1*), characterisation by X-ray diffraction (XRD, *Section 3.1.2*), elemental analysis by energy dispersive spectroscopy (EDS, *Section 3.1.3*) and microscopy studies (*Section 3.1.4*); all information obtained are summarised in *Section 3.1.5*.

Investigations of the long-term stability in air are discussed in *Section 3.2*. This is followed by properties characterisation of selected compositions (*Section 3.3*), classified in measurements of electrical conductivity (*Section 3.3.1*), thermogravimetric analysis (*Section 3.3.2*) and electrochemical measurements (*Section 3.3.3)*.

3.1. Synthesis and structural characterisation

3.1.1. Synthesis

3.1.1.1. Synthetic strategy

In order to investigate the effect of Mo introduction into the B-site of the perovskite structure (ABO_3), adopted by the parent $Ba_{0.5}Sr_{0.5}(Co_{0.8}Fe_{0.2})O_{3-\delta}$ (BSCF) compound, a range of $Ba_{0.5}Sr_{0.5}(Co_{0.8-x}Fe_{0.2-y}Mo_{x+y})O_{3-\delta}$ specimens was synthesised, denoted with numbers in *Figure 3.1*, by varying the molar ratios of Co, Fe and Mo in the B-site. The undoped BSCF is represented with a black star. The synthetic attempts were limited at the B-site compositional region above the auxiliary (blue) line, which indicates a boundary for the formation of the perovskite structures due to mass and charge balance considerations (*Table 3.1*).

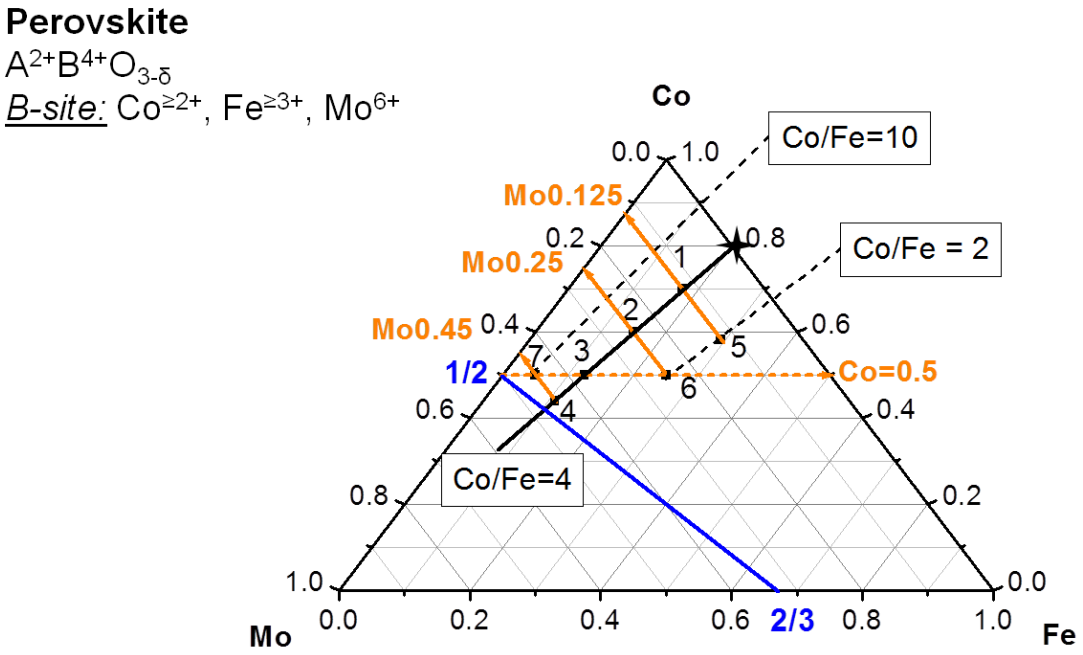

Figure 3.1: Ternary diagram representing the molar ratios of the B-site cations in $Ba_{0.5}Sr_{0.5}(Co_{0.8-x}Fe_{0.2-y}Mo_{x+y})O_{3-\delta}$ perovskite specimens (abbreviated as BSCFMox+y(Co/Fe=0.8-x/0.2-y) in Table 3.2), denoted with numbers, whilst the parent compound $Ba_{0.5}Sr_{0.5}(Co_{0.8}Fe_{0.2})O_{3-\delta}$ (BSCF) is shown as a black star. The synthetic attempts were limited to the area above the blue line. The compositions having the same Co/Fe ratio= 4, as BSCF, lie on the black solid line, whilst dashed black lines indicate the ratios studied for which Co/Fe≠4. Iso-Mo containing compositions lie on orange solid lines, whilst specimens with B-site half-filled with Co represented on the orange dash line.

The B-site of the Mo-doped BSCF perovskite compounds should have an overall charge of 4+, induced by the stable divalent state in air of both the A site cations (Ba^{2+} and Sr^{2+}). Lower B-site valence than 4+ can be compensated by the formation of oxygen vacancies (δ) in the perovskite structure, whilst higher overall oxidation state on the B-site will not favor the formation of cubic perovskite structures[164]. Molybdenum is usually encountered at its highest possible oxidation state (Mo^{6+}) in oxide compounds made in air, whilst the commonly oxidation states of cobalt and iron can vary, with Co^{2+} and Fe^{2+}, Fe^{3+} being the lowest possible valences in air [148, 165, 166]. In the Fe case it is considered mainly Fe^{3+}, since oxidation of Fe^{2+} to Fe^{3+} is preferable due to the oxygen content in air; however it should be mentioned that Fe^{2+} presence is also possible[167].

Table 3.1: Mass and charge balance for the Mo-Fe (x- axis) and Mo-Co (z-axis) regions in the ternary diagram (Figure 3.1), indicating the limit in Co, Fe and Mo contents in the B-site of the Mo-doped BSCF compositions that perovskite phases can be formed, assuming that Mo is in its hexavalent state whilst Co and Fe are in their lowest possible common oxidation states in air (Co^{2+} and Fe^{3+}).

	x axis: Mo-Fe region	z axis: Mo-Co region
Mass balance	Fe + Mo= 1	Mo + Co= 1
Charge balance	3 Fe + 6 Mo ≤ 4	2 Co + 6 Mo ≤ 4
Conditions	Mo≤ 1/3 and Fe≥ 2/3	Mo≤ 1/2 and Co≥ 1/2

The Mo-doped BSCF samples are abbreviated as $BSCFMo_{x+y}$-(Co/Fe=0.8-x/0.2-y) to signify the two factors investigated; the Mo content and the Co/Fe ratio in the B-site (*Table 3.2*). The effect of increasing the Mo content was studied for a series of $BSCFMo_{x+y}$-(Co/Fe=4) compounds with increasing amount of Mo^{6+} , whilst keeping the Co/Fe ratio constant to 4 as the parent undoped material. These lie on the black solid line in *Figure 3.1* and the numbering follows the increase in Mo content, for the abbreviated compositions BSCFMo0.125-(Co/Fe=4) (#1), BSCFMo0.25-(Co/Fe=4) (#2), BSCFMo0.375-(Co/Fe=4) (#3) and BSCFMo0.45-(Co/Fe=4) (#4). Compositions with with Co/Fe≠4 are set on the black dashed lines. The compounds with abbreviated compositions BSCFMo0.125-(Co/Fe=2) (#5) and BSCFMo0.25-(Co/Fe=2) (#6), both have Co/Fe=2. The orange solid lines indicate the Mo content for the iso-Mo containing compositional pairs, differing in the Co/Fe ratio, such as BSCFMo0.125-(Co/Fe=4) (#1) with BSCFMo0.125-(Co/Fe=2) (#5) and BSCFMo0.25-(Co/Fe=4) (#2) with BSCFMo0.25-(Co/Fe=2)

(#6). The orange dashed line connects the compositions for which the B-site is half-filled with Co; these are BSCFMo0.25-(Co/Fe=2) (#5), BSCFMo0.375-(Co/Fe=4) (#3) and BSCFMo0.45-(Co/Fe=10) (#7). The latter is a compositional pair with BSCFMo0.45-(Co/Fe=4) (#4), both containing Mo0.45 in their B-site.

Table 3.2: Summary of the B-site information of the $Ba_{0.5}Sr_{0.5}Co_{0.8-x}Fe_{0.2-y}Mo_{x+y}O_{3-\delta}$ compositions studied and represented as numbers in Figure 3.1.

Composition reference	Abbreviation	Co	Fe	Co/Fe	Mo
star	BSCF	0.80	0.2	4	0
1	BSCFMo0.125-(Co/Fe=4)	0.70	0.175	4	0.125
2	BSCFMo0.25-(Co/Fe=4)	0.60	0.150	4	0.250
3	BSCFMo0.375-(Co/Fe=4)	0.50	0.125	4	0.375
4	BSCFMo0.45-(Co/Fe=4)	0.44	0.110	4	0.450
5	BSCFMo0.125-(Co/Fe=2)	0.583	0.292	2	0.125
6	BSCFMo0.25-(Co/Fe=2)	0.50	0.25	2	0.250
7	BSCFMo0.45-(Co/Fe=10)	0.50	0.050	10	0.450

3.1.1.2. Synthesis protocol

The parent BSCF and the Mo-doped BSCF specimens were prepared by solid-state synthesis. Stoichiometric amounts of high purity $BaCO_3$, $SrCO_3$, Co_3O_4, Fe_2O_3 and MoO_3 were mixed and ground with acetone in an agate mortar. The powders were then pelletised and heated at 700°C for 6 hours and 900°C for 8 hours for the activation of carbonates and then cooled to room temperature. After breaking the pellets, the powders were hand-ground thoroughly and heated at 1000°C for 24h. Homogeneity problems were identified for the resulting products (*Section 3.1.3*). This led to the replacement of the two hand grinding steps by mechanical ball-milling. According to the established optimised synthesis protocol, which is described in detail in *Section 2.1*, the powders were heated for four times at 1000°C for 10h, with three intermediate hand grinding-pelletising steps. The phase identification of the as-made powders was performed by powder X-ray diffraction which is discussed in the following section.

3.1.2. Characterisation by X-ray diffraction

3.1.2.1. Parent undoped BSCF

The parent undoped BSCF material was confirmed as phase pure from Pawley fit against XRD data collected at room temperature (*Figure 3.2*), crystallising in $Pm\bar{3}m$ with lattice parameter 3.98538(3) Å (*Table 3.3*), which is in good agreement with previous report for BSCF (3.9830 Å)[168].

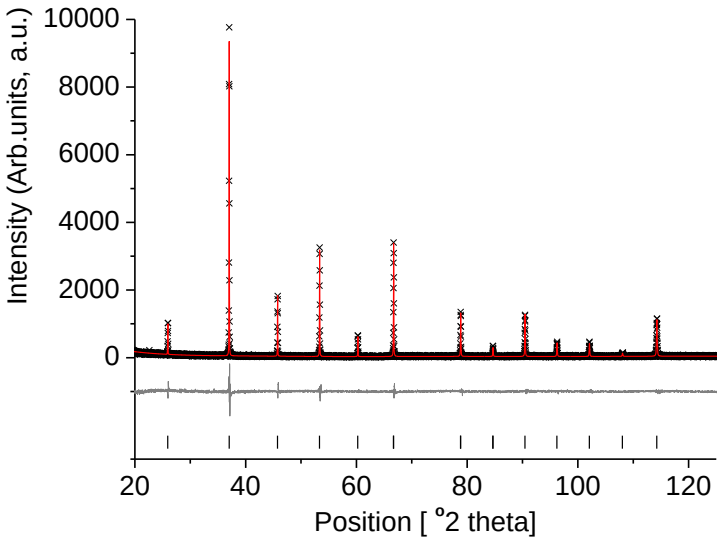

Figure 3.2: Observed (black), calculated (red) and difference (grey) plots of Pawley fit of room temperature XRD data from $Ba_{0.5}Sr_{0.5}Co_{0.8}Fe_{0.2}O_{3-\delta}$ (BSCF) in $Pm\bar{3}m$ symmetry, with the black tick marks showing the allowed reflections. Normalised to 10,000 a.u.

Table 3.3: Refined lattice parameters and goodness of fit parameters for Pawley fit of $Ba_{0.5}Sr_{0.5}Co_{0.8}Fe_{0.2}O_{3-\delta}$ (BSCF) against XRD data collected at room temperature.

Lattice Parameters		**Fit Parameters**	
Space Group	$Pm\bar{3}m$	R_{wp} / %	21.325
a / Å	3.98538(3)	R_{exp} / %	16.588
		χ^2	1.65

3.1.2.2. Effect of Mo content

The effect of Mo doping in the perovskite structure of BSCF is discussed below, and classified as low (Mo< 0.2) (*Section 3.1.2.2.1*), intermediate (0.2<Mo<0.4) (*Section 3.1.2.2.2*) and high Mo content (Mo>0.4) (*Section 3.1.2.2.3*).

3.1.2.2.1. Low Mo content (Mo< 0.2)

The small amount of Mo in BSCFMo0.125-(Co/Fe=4) (composition #1 on the ternary diagram, *Figure 3.1*), favors the formation of an isostructural compound with the un-doped single perovskite (SP) material. Superimposing the normalised XRD patterns of BSCF and BSCFMo0.125-(Co/Fe=4) (*Figure 3.3*), shows that there are no extra reflections of the latter and makes clear that there is a shift in reflection positions to higher 2theta angles, highlighted in the inset for the most intense peak at ca. 37 degrees. This indicates a decrease in lattice parameters upon substitution of the cations in first transition series Co and Fe, for the smaller Mo in the second series.

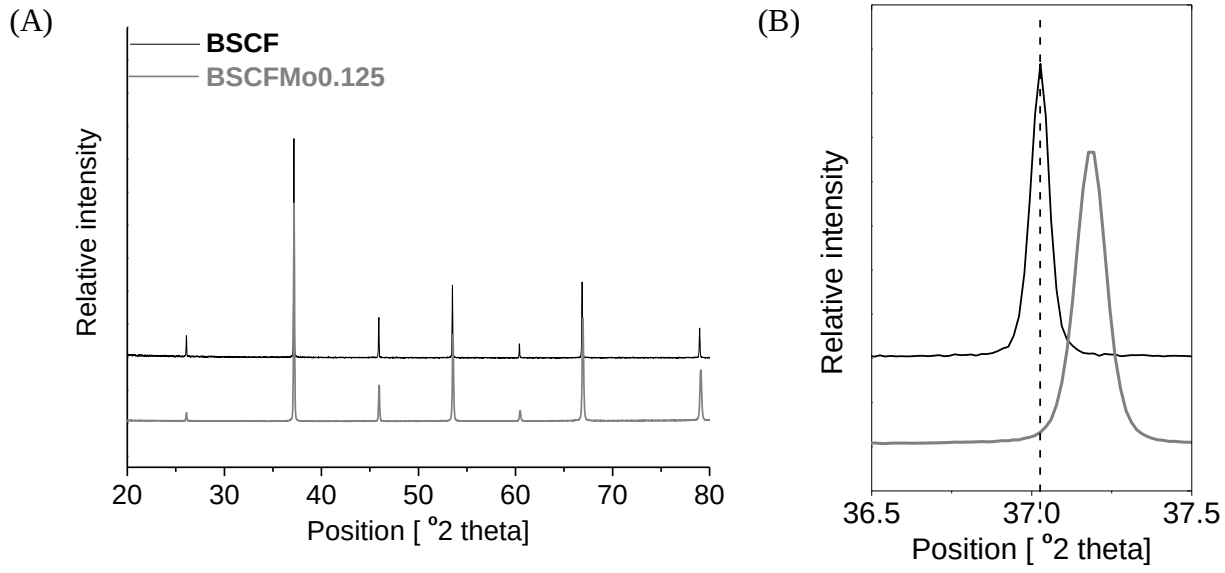

Figure 3.3: (A) Superimposing the normalized XRD patterns of BSCF (black) and BSCFMo0.125-(Co/Fe=4) (grey), in (B) magnification of the 2theta range 36.6-37.5, focusing on the main perovskite peak, revealing the shift in reflection positions.

Pawley fitting of the XRD data of this sample (*Figure 3.4*) in $Pm\bar{3}m$, confirms that BSCFMo0.125(Co/Fe=4) crystallises in the same space group as the parent undoped material, with lattice parameters of 3.97736(2) Å (*Table 3.4*) indicating a decrease by 0.00802 Å compared to the parent undoped BSCF (3.98538 Å from *Section 3.1.2.1*).

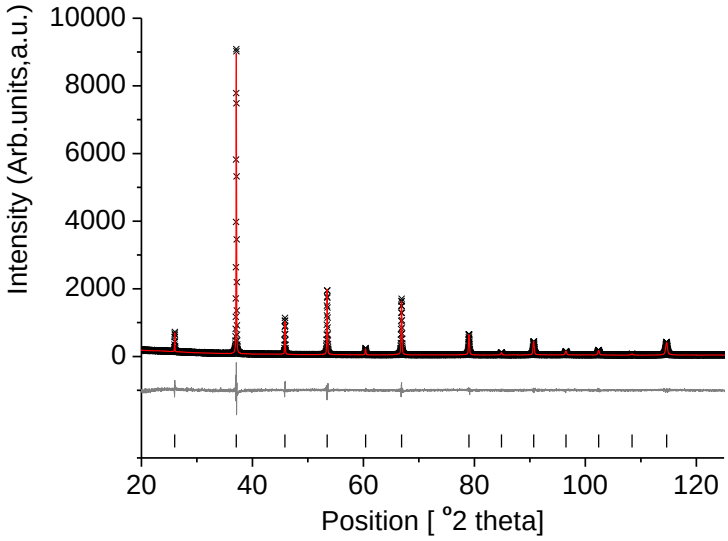

Figure 3.4: Pawley fitting of PXRD pattern for $Ba_{0.5}Sr_{0.5}Co_{0.78}Fe_{0.175}Mo_{0.125}O_{3-\delta}$ (BSCFMo0.125-(Co/Fe=4)) in $Pm\bar{3}m$ space group, with black showing the allowed reflections. Normalised to 10,000 a.u.

Table 3.4: Refined lattice parameters and goodness of fit parameters for Pawley fit of BSCFMo0.125-(Co/Fe=4) against PXRD data collected at room temperature.

Lattice Parameters		**Fit Parameters**	
Space Group	$Pm\bar{3}m$	R_{wp} / %	6.291
a / Å	3.97736(2)	R_{exp} / %	4.712
		χ^2	1.78

3.1.2.2.2. Intermediate Mo content (0.2<Mo<0.4)

The increased amount of Mo in BSCFMo0.25-(Co/Fe=4) (composition #2 on the ternary diagram, *Figure 3.1*) has a clear effect on the XRD patterns of the BSCFM compounds, compared to the un-doped material (*Figure 3.5)*. Low intensity additional reflections appear, as highlighted in the inset in *Figure 3.5*A for the ^{o}2theta range 20-35. Another interesting feature coming out by observing the diffraction pattern corresponding to BSCFMo0.25-(Co/Fe=4) sample is the splitting of all the reflections, as shown in *Figure 3.5B* for the main perovskite peak at 37 ^{o}2theta, manually shifting the pattern to lower angles to allow direct superimpose and comparison with the peakshape of the XRD corresponding to the undoped parent BSCF.

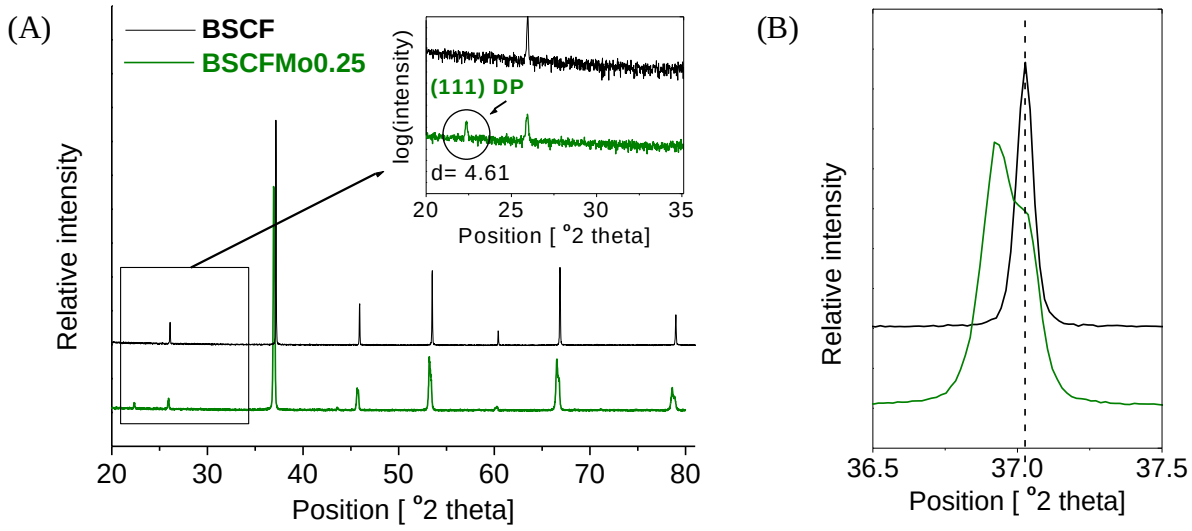

Figure 3.5: (A) Superimposing the normalized XRD patterns of BSCF (black) and BSCFMo0.25-(Co/Fe=4) (green). In the inset, magnification of the 2theta range 20-35 in logarithmic intensity scale, indicating the low angle reflection at d= 4.61 Å of the latter (B) magnification of the 2theta range 36.5-37.5, revealing splitting of the main perovskite reflection for BSCFMo0.25-(Co/Fe=4), manually shifted to lower angles to allow direct superimpose and comparison with the peakshape of BSCF.

The most valuable information can be extracted from the positions of the low angle reflections, which can indicate possible multiplications of the unit cell parameters and ordering[164, 169]. For BSCFMo0.25-(Co/Fe=4), the first and most intense additional peak compared to BSCF is at about 22 degrees, corresponding to d spacing= 4.61 Å. Calculation of the lattice parameter agrees with the formation of a double perovskite (DP) with lattice parameter ca. 7.98 Å, which is

double than the typical unit cell of a simple perovskite (a_{SP}= 3.99Å), and with the first reflection corresponding to (111) Miller indices. Fitting of the XRD pattern (*Figure 3.6A*) agrees well to a double perovskite (DP) formation (crystallising in $Fm\bar{3}m$), with lattice parameters 7.98416(17) Å (*Table 3.5*). The main misfitting is due to the splitting of the peaks, highlighted for the main perovskite reflection at approximately 37 degrees *(Figure 3.6B*).

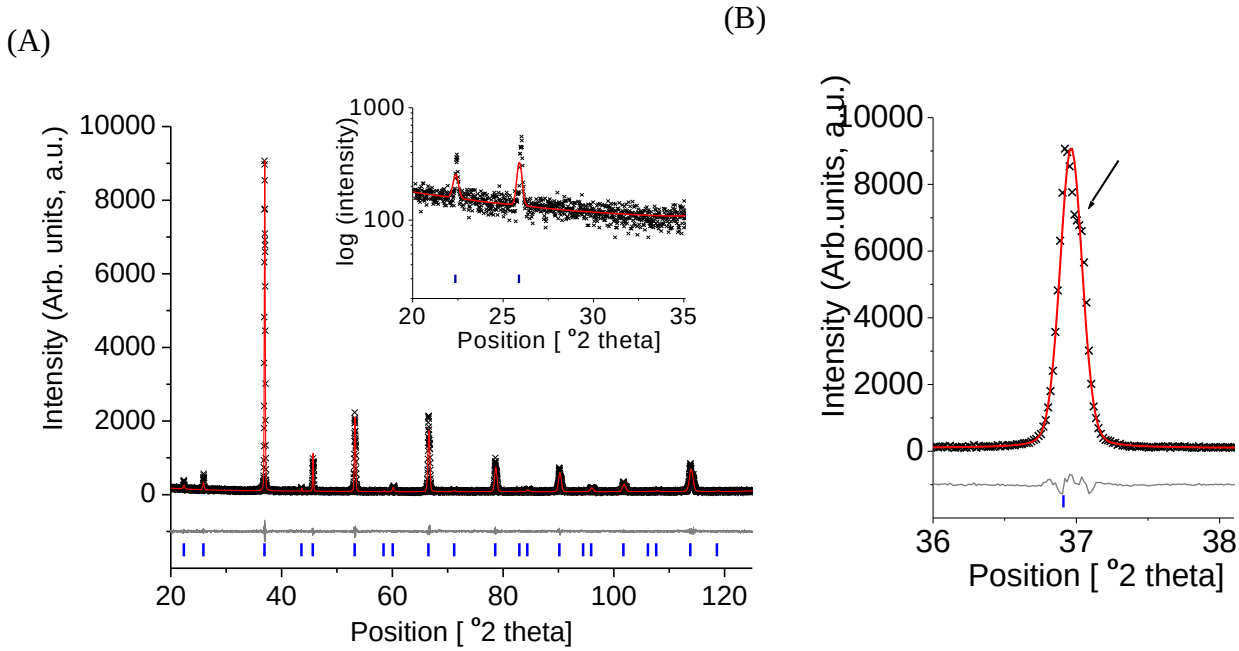

Figure 3.6: (A) Observed (black), calculated (red) and difference (grey) plots of Pawley fit of room temperature XRD data $Ba_{0.5}Sr_{0.5}Co_{0.6}Fe_{0.15}Mo_{0.25}O_{3-\delta}$ (BSCFMo0.25-(Co/Fe=4)) in $Fm\bar{3}m$ space group, with the blue tickmarks showing the allowed reflections. In the inset, magnification of the 2theta range 20-35 in logarithmic intensity scale indicating the characteristic (111) DP reflection at ca. 22 degrees. (B) magnification of the 2theta range 36-38° focusing on the fit of the main perovskite reflection. The Pawley plot is normalized to 10,000 a.u.

Table 3.5: Refined lattice parameters and goodness of fit parameters for Pawley fit of BSCFMo0.25-(Co/Fe=4) against PXRD data collected at room temperature.

Lattice Parameters		**Fit Parameters**	
Space Group	$Fm\bar{3}m$	R_{wp} / %	16.868
a / Å	7.98416(17)	R_{exp} / %	11.735
Volume / Å^3	508.96	χ^2	2.065

The splitting of the peaks could be an indication of the formation of lower-symmetry structures, due to distortion of the ideal cubic unit cell. According to the literature, when all reflection types of ordered perovskite are split, as in the case of BSCFMo0.25-(Co/Fe=4), crystallising in the monoclinic space group $P2_1/n$ or P-1 is expected [170-172]. Other possible explanations for the splitting of the reflections could be the formation of phases with very close reflection positions, such as a second DP phase with very small difference in lattice parameters or an SP unit giving overlapping reflections.

Three different models were tested and the fitting of the PXRD pattern to (i) monoclinic unit cell ($P2_1/n$) (ii) two different DP unit cells with slightly different lattice constants and (iii) a SP and a DP unit cell. The splitting of the reflections is well fitted in all models; a representative fit for the SP/DP model is shown in *Figure 3.7*.

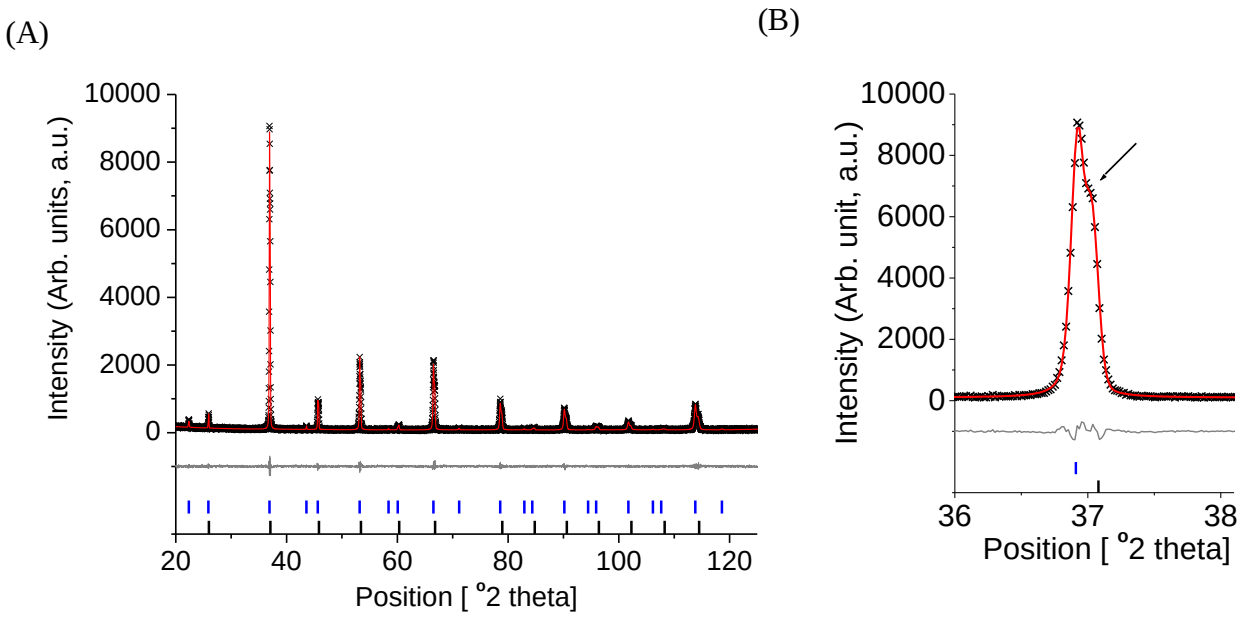

Figure 3.7: (A)Observed (black), calculated (red) and difference (grey) plots of Pawley fit of room temperature XRD data from $Ba_{0.5}Sr_{0.5}Co_{0.6}Fe_{0.15}Mo_{0.25}O_{3-\delta}$ (BSCFMo0.25-(Co/Fe=4)) using the structural model the structural model of a SP and a DP phase crystallizing in space groups $Pm\bar{3}m$ and $Fm\bar{3}m$ with the blue and black tick marks showing the allowed reflections respectively and in (B) magnification of the 2theta range 36.5-37.5, focusing on the fitting of the main perovskite reflection. The plots are normalized to 10,000 a.u.

The structural information and quality of Pawley fits obtained for BSCFMo0.25-(Co/Fe=4) using the three different structural models are shown in *Table 3.6* and are compared with the DP model. There is a clear improvement in the reliability factors compared to the DP model (R_{wp}= 16.868, χ^2= 2.07), but there is no significant difference between the three models (R_{wp}= 13.045-13.395, χ^2= 1.28-1.34). However, the outcome of the microscopy studies (*Section 3.1.4*) agrees with the SP/DP model and hence the splitting of the diffraction reflections is the effect of its biphasic nature.

Table 3.6: Comparison of refined lattice parameters and goodness of fit parameters for Pawley fits of BSCFMo0.25-(Co/Fe=4) using the three different structural models, against XRD data collected at room temperature.

$Ba_{0.5}Sr_{0.5}Co_{0.6}Fe_{0.15}Mo_{0.25}O_{3-\delta}$ Models	**Space group**	**Lattice information**	**R_{wp}/%**	**R_{exp}/%**	**χ^2**
DP	$Fm\bar{3}m$	a (Å) = 7.9842(2)	16.868	11.735	2.07
monoclinic	$P2_1/n$	a (Å) =7.9915(4) b (Å) = 7.9811(6) c (Å) = 7.9639(3) β(°)= 89.785(3)	13.045	11.252	1.34
DP/DP	$Fm\bar{3}m$ $Fm\bar{3}m$	a_{DP1}(Å) =7.9699(2) a_{DP2} (Å) =7.9921(2)	13.269	11.707	1.28
SP/DP	$Pm\bar{3}m$ $Fm\bar{3}m$	a_{SP} (Å) = 3.9839(1) a_{DP}(Å) =7.9906(2)	13.395	11.718	1.31

When introducing more Mo, reaching to 37.5% of Mo in the B-site, the XRD pattern of BSCFMo0.375-(Co/Fe=4) (composition #3 on the ternary diagram, *Figure 3.1*) still shows the characteristic first (111) DP reflection at about 22 degrees and d= 4.61 Å (inset in *Figure 3.8A*), confirming the existence of the DP phase. When superimposing and shifting the XRD pattern of BSCFMo0.375-(Co/Fe=4) to lower angles to allow direct superimpose and comparison with the peakshape of the parent undoped BSCF, the existence of an asymmetric broadening on the right of all the reflections becomes evident *(Figure 3.8B* for the main perovskite peak at 37 degrees). It is worth noticing that no clear splitting of all the peaks was observed for this specimen, in contrast with the lower Mo containing BSCFMo0.25-(Co/Fe=4) composition.

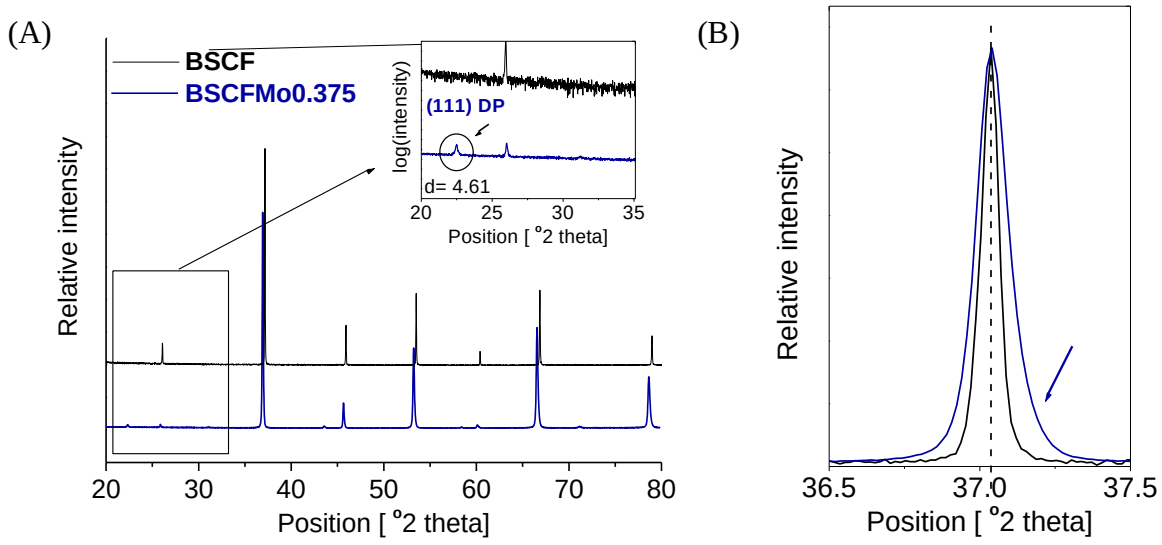

Figure 3.8: (A) Superimposing the normalised XRD patterns of BSCF (black) and BSCFMo0.375-(Co/Fe=4) (blue). In the inset, magnification of the 2theta range 20-35^o in logarithmic intensity scale indicating the low angle reflection at ca. 22^o of the latter (B) magnification of the 2theta region 36.5-37.5 revealing asymmetry of the main perovskite reflection for BSCFMo0.375-(Co/Fe=4)), when manually shifted to lower angles to allow direct superimpose and comparison with the peakshape of BSCF.

The asymmetry of the most intense reflection is fitted when using the SP/DP model (*Figure 3.9*), giving improved goodness of fit parameters compared to the DP model (*Table 3.7)*.

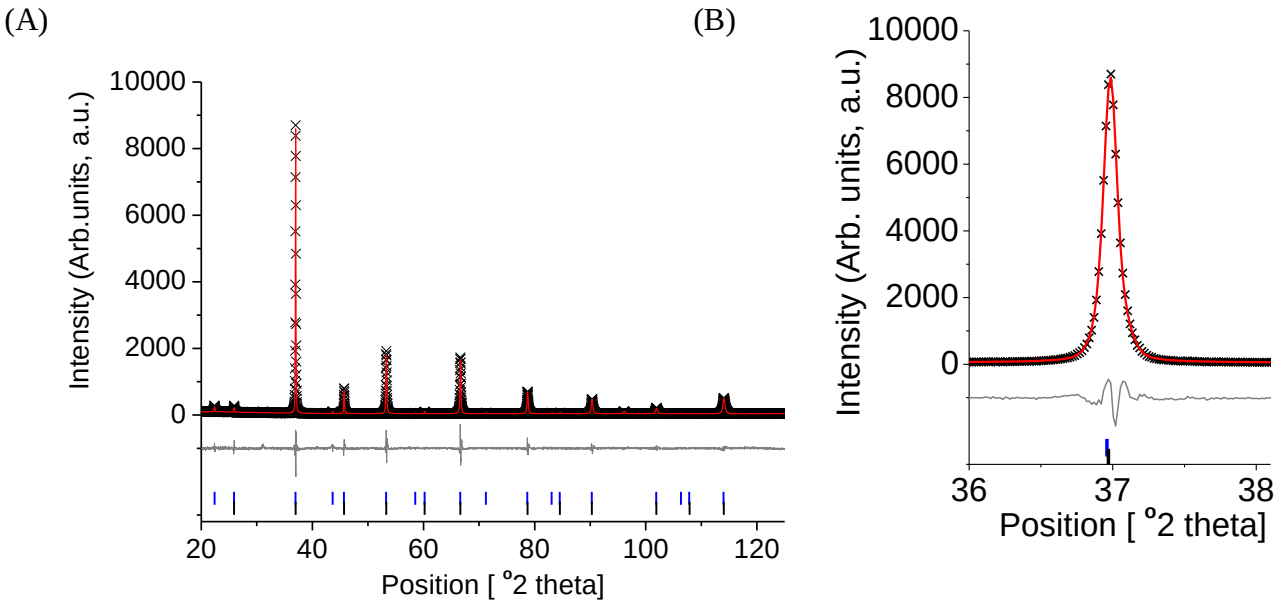

Figure 3.9: (A) Observed (black), calculated (red) and difference (grey) plots of Pawley fit of room temperature XRD data $Ba_{0.5}Sr_{0.5}Co_{0.5}Fe_{0.125}Mo_{0.375}O_{3-\delta}$ (BSCFMo0.375-(Co/Fe=4)) using the structural model of a SP and a DP phase crystallizing in space groups $Pm\bar{3}m$ and $Fm\bar{3}m$, with the black and blue tickmarks showing the allowed reflections and in (B) magnification of the 2theta range 36-38°, focusing on the fit of the main perovskite reflection. The plots are normalized to 10,000 a.u.

Table 3.7: Comparison of refined lattice parameters and goodness of fit parameters for Pawley fits of BSCFMo0.375-(Co/Fe=4) using the two different structural models, against XRD data collected at room temperature.

$Ba_{0.5}Sr_{0.5}Co_{0.5}Fe_{0.125}Mo_{0.375}O_{3-\delta}$ Models	**Space group**	**Lattice information**	**R_{wp} / %**	**R_{exp}/ %**	**χ^2**
DP	$Fm\bar{3}m$	7.97934(6)	9.567	5.603	2.91
SP/DP	$Pm\bar{3}m$ $Fm\bar{3}m$	3.98956(4) 7.98169(12)	8.673	5.595	2.40

3.1.2.2.3. High Mo content (Mo> 0.4)

The XRD analysis for the BSCFMo0.45-(Co/Fe=4) specimen (composition #4 on the ternary diagram, *Figure 3.1*), containing 45% Mo in the B-site, is very informative at the low °2theta angle range 20-35 (inset in *Figure 3.10*). There are clearly four reflections, whilst the parent simple perovskite BSCF shows only one reflection at about 26 degrees. The first peak (at 22 degrees) is at the same position as in the case of the intermediate Mo containing BSCFMo0.25-(Co/Fe=4) and BSCFMo0.375-(Co/Fe=4) discussed in *Section 3.1.2.2.2* and attributed to the formation of a double perovskite (DP). The extra two reflections at the °2theta range 30-32 were indexed to $BaMoO_4$ impurity phase[173].

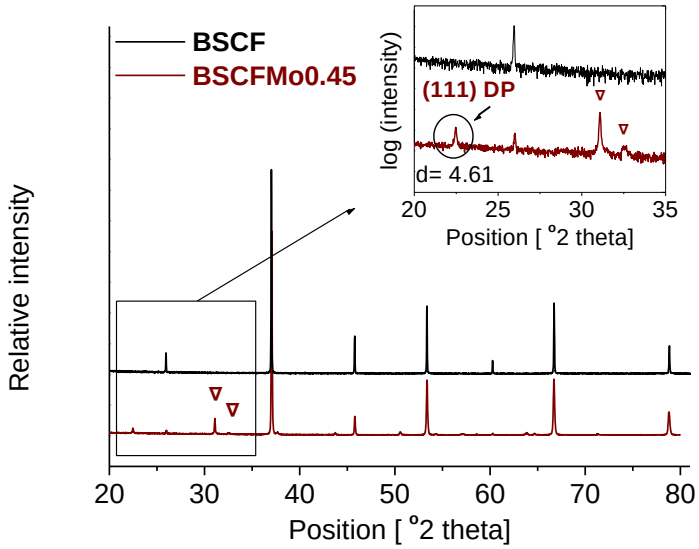

Figure 3.10: Superimposing the normalized XRD patterns of BSCF (black) and BSCFMo0.45-(Co/Fe=4) (red). In the inset, magnification in logarithmic intensity scale of the 2theta range 20-35, focusing on existence of the (111) DP reflection at ca. 22 degrees but also the most intense reflections for the impurity phase $BaMoO_4$, denoted with red upturned triangles.

The fitting agrees well with a DP model plus $BaMoO_4$ (R_{wp}= 13.305, χ^2= 1.31). However the reliability factors are just slightly improved (R_{wp}= 12.870, χ^2= 1.23) when adding a small SP component (*Table 3.8*) which is in agreement with the microscopy study (*Section 3.1.4*). The actual fit for the SP/DP model is shown in *Figure 3.11*.

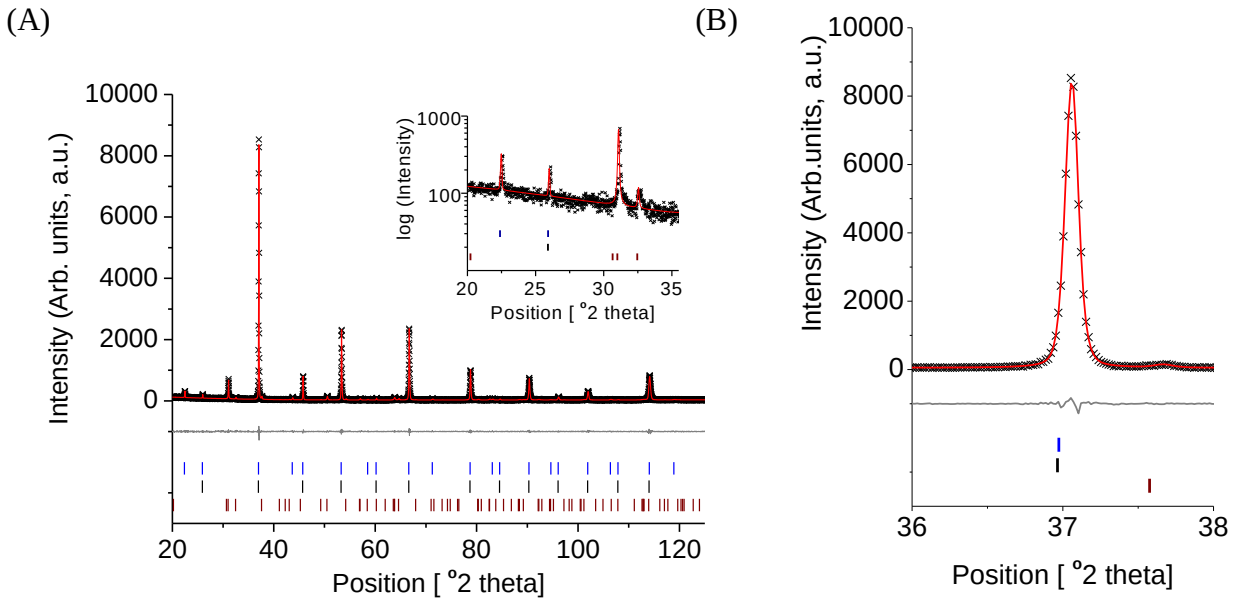

Figure 3.11: (A) Observed (black), calculated (red) and difference (grey) plots of Pawley fit of room temperature XRD data for $Ba_{0.5}Sr_{0.5}Co_{0.44}Fe_{0.11}Mo_{0.45}O_{3-\delta}$ (BSCFMo0.45-(Co/Fe=4)) in the structural model of a SP and a DP phase crystallizing in space groups $Pm\bar{3}m$ and $Fm\bar{3}m$ respectively, with the black and blue tickmarks showing the allowed reflections for the SP and DP phase and red tickmarks indicating the $BaMoO_4$ impurity phase. In the inset, magnification of the 2theta range 20-35^o in logarithmic intensity scale indicating the positions of the DP and $BaMoO_4$ reflections(B) magnification of the 2theta range 36-38^o focusing on the fit of the main perovskite reflection. The plots are normalized to 10,000 a.u.

Table 3.8: Comparison of refined lattice parameters and goodness of fit parameters for Pawley fits of BSCFMo0.45-(Co/Fe=4) under the two different structural models, against PXRD data collected at room temperature.

Models $Ba_{0.5}Sr_{0.5}Co_{0.44}Fe_{0.11}Mo_{0.45}O_{3-\delta}$	**Space group**	**Lattice information**	**R_{wp}/ %**	**R_{exp}/%**	**χ^2**
DP+$BaMoO_4$	$Fm\bar{3}m$ $I\,4_1/a$	a(Å)$_{DP}$= 7.98041(6) a(Å)$_{BaMoO4}$=5.55129(30) c(Å)$_{BaMoO4}$=12.82695(47)	13.305	11.605	1.31
SP/DP+$BaMoO_4$	$Pm\bar{3}m$ $Fm\bar{3}m$ $I\,4_1/a$	a(Å)$_{SP}$= 3.98929(19) a(Å)$_{DP}$= 7.98148(15) a(Å)$_{BaMoO4}$= 5.55158(33) c(Å)$_{BaMoO4}$= 12.82(1)	12.870	11.587	1.23

3.1.2.3. Effect of Co/Fe ratio

3.1.2.3.1. Low Co/Fe (<4)

The introduction of Mo in BSCFMo0.125-(Co/Fe=2), (composition #5 on the ternary diagram, *Figure 3.1*), having lower Co/Fe ratio than 4, affords the formation of an SP phase crystallizing in Pm3m, as demonstrated by the Pawley fit (*Figure 3.12*), isostructural to the parent BSCF compound (*Section 3.1.2.1*) and the iso-Mo containing BSCFMo0.125-(Co/Fe=4) (*Section 3.1.2.2.1*). As evidenced at low angles (inset in *Figure 3.12*) the absence of the characteristic (111) DP reflection at ca. 22 ^{o}2theta, indicates that the double perovskite formation is not favored, similarly to the case of the iso-Mo containing composition BSCFMo0.125-(Co/Fe=4).

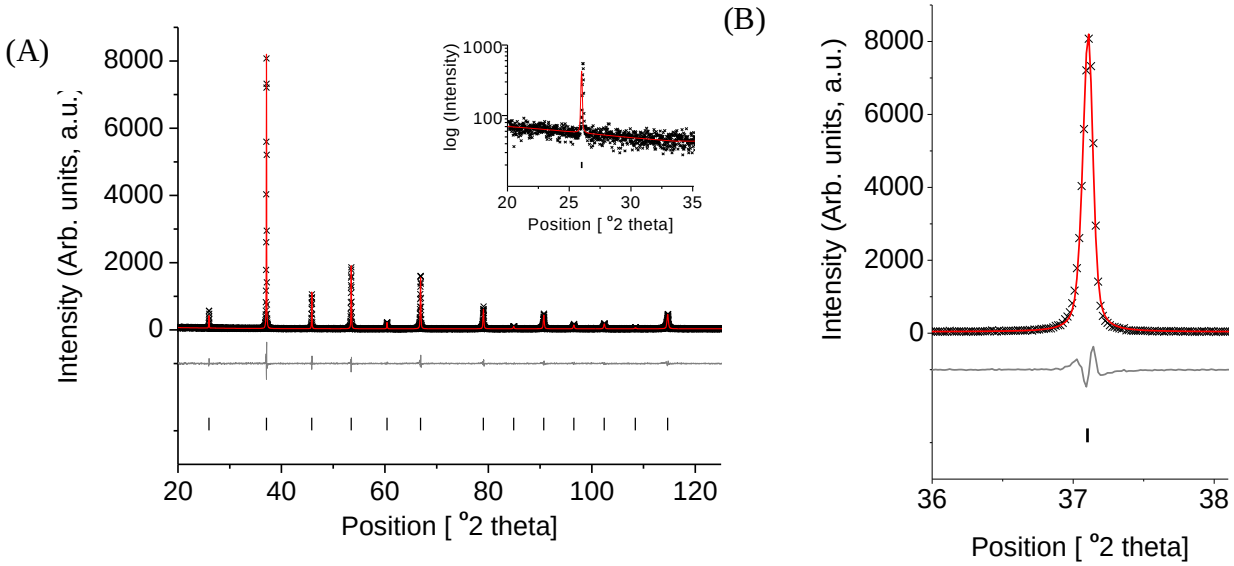

Figure 3.12: (A) Observed (black), calculated (red) and difference (grey) plots of Pawley fit of room temperature PXRD data for $Ba_{0.5}Sr_{0.5}Co_{0.583}Fe_{0.292}Mo_{0.125}O_{3-\delta}$ (BSCFMo0.125-(Co/Fe=2)) crystallizing in space group $Pm\bar{3}m$, with black showing the allowed reflections. In the inset, magnification of the 2theta range 20-35^{o} in logarithmic intensity scale, indicating the absence of additional phases. (B) Magnification of the 2theta range 36-38^{o} focusing on the fit of the main perovskite reflection. The plots are normalized to 10,000 a.u.

The refined lattice constant of 3.97613(4) Å for BSCFMo0.125-(Co/Fe=2) (*Table 3.9*) is smaller than for BSCF (a_P=3.98538(3) Å, *Section 3.1.2.1*), indicating that the incorporation of the small Mo^{6+} in the perovskite structure leads to the contraction of the perovskite unit cell. Moreover, this is slightly smaller than the refined lattice constant for BSCFMo0.125-(Co/Fe=4) (3.97736(2)

Å, *Section 3.1.2.2.1*), possibly related to the different molar ratios of Co and Fe ions in the two compositions.

Table 3.9: Refined lattice parameters and goodness of fit parameters for Pawley fit of $Ba_{0.5}Sr_{0.5}Co_{0.583}Fe_{0.292}Mo_{0.125}O_{3-\delta}$ (BSCFMo0.125-(Co/Fe=2)) against PXRD data collected at room temperature.

Lattice Parameters		**Fit Parameters**	
Space Group	$Pm\bar{3}m$	R_{wp} / %	16.341
a / Å	3.97613(4)	R_{exp} / %	12.902
		χ^2	1.61

When the Co/Fe ratio is kept to 2, increasing the Mo content to 25% for BSCFMo0.25-(Co/Fe=2) (composition #6 on the ternary diagram, *Figure 3.1*), results in the formation of DP phase showing the characteristic DP reflection at 22 °2theta (inset in *Figure 3.13*). Moreover, the formation of $BaMoO_4$ impurity phase is favored as indicated by the most intense reflections at about 30-32 degrees. The fit against the SP/DP+$BaMoO_4$' model (*Figure 3.13*) shows better reliability factors (R_{wp}= 11.100, χ^2= 1.21) compared to the 'DP+$BaMoO_4$' (R_{wp}= 13.639, χ^2= 1.82), demonstrating the coexistence of an SP with a DP phase and $BaMoO_4$ for this composition (*Table 3.10*).

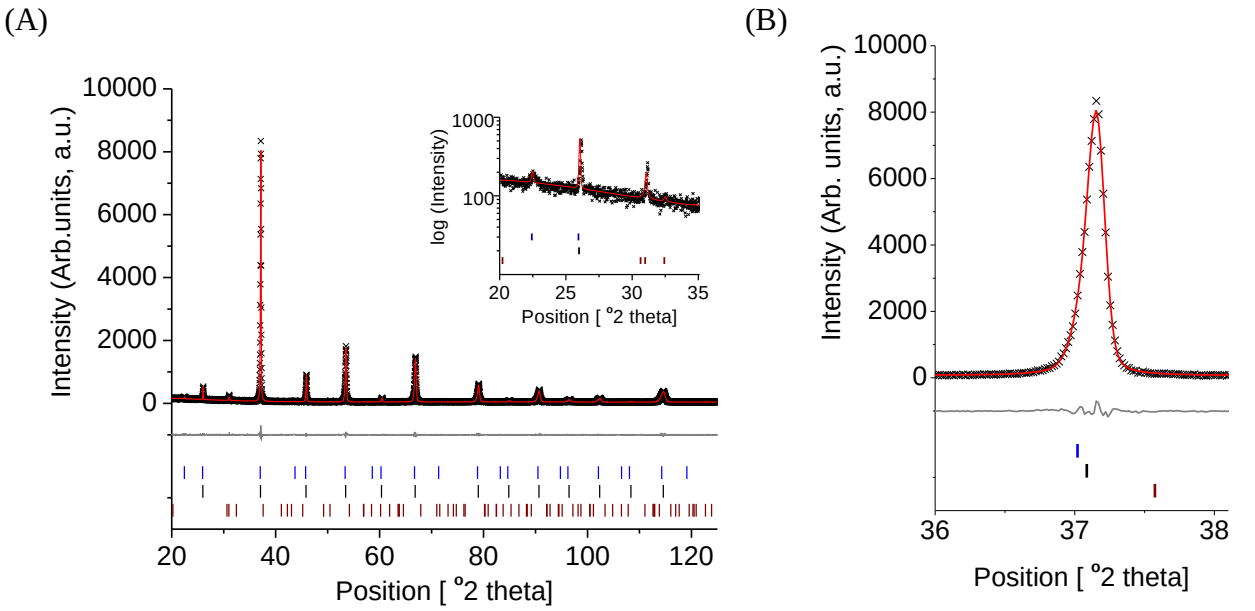

Figure 3.13: (A) Observed (black), calculated (red) and difference (grey) plots of Pawley fit of room temperature XRD data $Ba_{0.5}Sr_{0.5}Co_{0.5}Fe_{0.25}Mo_{0.25}O_{3-d}$ (BSCFMo0.25-(Co/Fe=2)) in the structural model of a SP and a DP phase crystallizing in space groups $Pm\bar{3}m$ and $Fm\bar{3}m$, with the black and blue tickmarks showing the allowed reflections and red tickmarks indicating the $BaMoO_4$ impurity phase. In the inset, magnification of the 2theta range 20-35° in logarithmic intensity scale and (B) magnification of the 2theta range 36-38° focusing on the fit of the main perovskite reflection. The plots are normalized to 10,000 a.u.

Table 3.10: Comparison of refined lattice parameters and goodness of fit parameters for Pawley fits of BSCFMo0.25-(Co/Fe=2) under the two different structural models, against XRD data collected at room temperature

$Ba_{0.5}Sr_{0.5}Co_{0.5}Fe_{0.25}Mo_{0.25}O_{3-\delta}$ Models	**Space group**	**Lattice information**	**R_{wp}/ %**	**R_{exp}/%**	**χ^2**
DP+$BaMoO_4$	$Fm\bar{3}m$	$a(Å)_{DP}$= 7.9604 (2)			
	$I\,4_1/a$	$a(Å)_{BaMoO4}$= 5.557(2)	13.639	10.120	1.82
		$c(Å)_{BaMoO4}$= 12.79115(5)			
SP/DP+$BaMoO_4$		$a(Å)_{SP}$= 3.9777 (2)			
	$Pm\bar{3}m$	$a(Å)_{DP}$= 7.9692 (8)			
	$Fm\bar{3}m$	$a(Å)_{BaMoO4}$= 5.555 (2)	11.100	10.104	1.21
	$I\,4_1/a$	$c(Å)_{BaMoO4}$= 12.82 (8)			

The formation of DP phases with increasing the Mo content from 0.125 to 0.25 for the compositions with the same Co/Fe=2 <4, is in agreement with the outcome of the effect of Mo content on compositions with Co/Fe=4 (*Section 3.1.2.2*). However, for this series of Mo-doped BSCF compounds, the expulsion of $BaMoO_4$ phase is observed for Mo≥ 0.45. On the contrary, the $BaMoO_4$ impurity is present for as low Mo content as 0.25 in BSCFMo0.25-(Co/Fe=2) composition, whilst not evident for the BCFMo0.25-(Co/Fe=4) counterpart (*Figure 3.5, Section 3.1.2.2.2*). This demonstrates that the Mo limit for $BaMoO_4$ impurity-free compounds is clearly lowered when the Co/Fe ratio is lowered. Moreover, both SP and DP unit cells are smaller for BSCFMo0.25-(Co/Fe=2) (a_{SP}= 3.97773 Å, a_{DP}= 7.96922 Å) compared to BCFMo0.25-(Co/Fe=4) (a_{SP}= 3.98389Å, a_{DP}= 7.99057 Å), which is in agreement with the observation for lower Mo containing compositions as aforementioned for the SP forming BSCFMo0.125-(Co/Fe=2). This evidence suggests compositional differences of the perovskite components depending on the Co/Fe ratio and the actual Co and Fe amounts.

3.1.2.3.2. High Co/Fe ratio(>4)

The high Mo containing BSCFMo0.45-(Co/Fe=10) (composition #7 on the ternary diagram, *Figure 3.1*), results in a very intense DP reflection at about 22 °2theta, whilst there is no evidence for $BaMoO_4$ formation (inset in *Figure 3.14*). The Pawley fit for the 'SP+DP' model (*Figure 3.14*), shows improved goodness of fit factors (R_{wp}= 8.475, χ^2= 1.37), compared to the 'DP' model (R_{wp}= 12.345, χ^2= 2.90), suggesting that the main phase is DP but coexisting with small amounts of SP phases (*Table 3.11*).

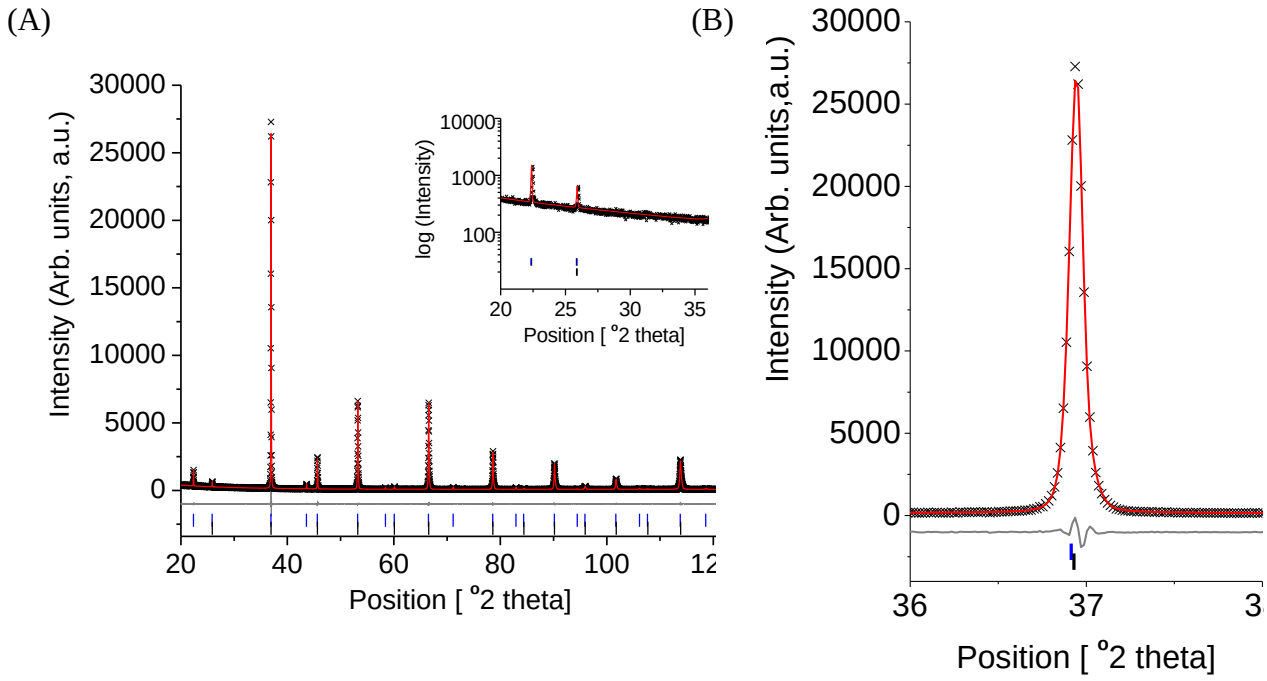

Figure 3.14: (A) Pawley fitting of PXRD pattern for $Ba_{0.5}Sr_{0.5}Co_{0.5}Fe_{0.05}Mo_{0.45}O_{3-d}$ (BSCFMo0.45-(Co/Fe=10)) in the structural model of a SP and a DP phase crystallizing in space groups $Pm\bar{3}m$ and $Fm\bar{3}m$ respectively. In the inset, magnification of the 2theta region 20-35 in logarithmic intensity scale, indicating the existence of the (111) DP reflection and (B) magnification of the 2theta range 36.5-37.5 focusing on the fitting of the main perovskite reflection. The plots are normalized to 10,000 a.u.

Table 3.11: Comparison of refined lattice parameters and goodness of fit parameters for Pawley fits of BSCFMo0.45-(Co/Fe=10) under the two different structural models, against PXRD data collected at room temperature.

$Ba_{0.5}Sr_{0.5}Co_{0.5}Fe_{0.05}Mo_{0.45}O_{3-\delta}$ **Models**	**Space group**	**Lattice information**	R_{wp}/ %	R_{exp}/%	χ^2
DP	$Fm\bar{3}m$	$a(Å)_{DP}$= 7.98984(5)	12.345	7.244	2.90
SP/DP	$Pm\bar{3}m$ $Fm\bar{3}m$	$a(Å)_{SP}$= 3.99397(5) $a(Å)_{DP}$= 7.99121(6)	8.475	7.234	1.37

As aforementioned for BSCFMo0.45-(Co/Fe=4) (*Section 3.1.2.2.3*), the high amount of Mo favors the formation of DP compounds, accompanied by the formation of the undesired impurity $BaMoO_4$ phase. However, the introduction of equal amount of Mo in BSCFMo0.45-(Co/Fe=10), having overall higher Co/Fe ratio, suppresses the expulsion of Mo as $BaMoO_4$, demonstrating that the higher Co/Fe ratio favors the incorporation of higher amount of Mo. For comparison, the formation of $BaMoO_4$ impurity in the low Co/Fe classified BSCFMo0.25-(Co/Fe=2) (*Section 3.1.2.3.1*) is favored for as low Mo content as Mo0.25 content. These suggest that the maximum amount of Mo that can be introduced in the impurity-free Mo-doped BSCFM materials increases with increasing the Co/Fe ratio.

3.1.3. Energy-dispersive X-ray analysis (EDS)

As aforementioned (*Section 3.1.1.2*), the first synthetic approach of the BSCFM materials involved grinding of the starting materials, heating for activation of the carbonates followed by grinding and finally heated at the synthesis temperature 1000^{o}C for 24h. After this step, compositional analysis was carried out by using energy-dispersive X-ray analysis (EDS) which showed inhomogeneity of the resulting products and hence an optimised synthesis protocol was established; this investigation is described in detail herein.

The EDS analysis for the example of BSCFMo0.375-(Co/Fe=4), synthesised according to first synthetic approach, is shown in *Figure 3.15*, separately for the A- and B-site cations. The composition of each of the crystals measured is shown in black squares, whilst the nominal composition is represented by a red star. The Ba:Sr ratio on the A-site (*Figure 3.15*A) showed a deviation from the nominal 50:50 ratio, with the majority of the crystals having Ba:Sr= 40:60 and hence revealing loss of Ba on the A-site. Moreover, the random distribution of the crystal's composition on the B-site (*Figure 3.15B*), indicates inhomogeneity problems.

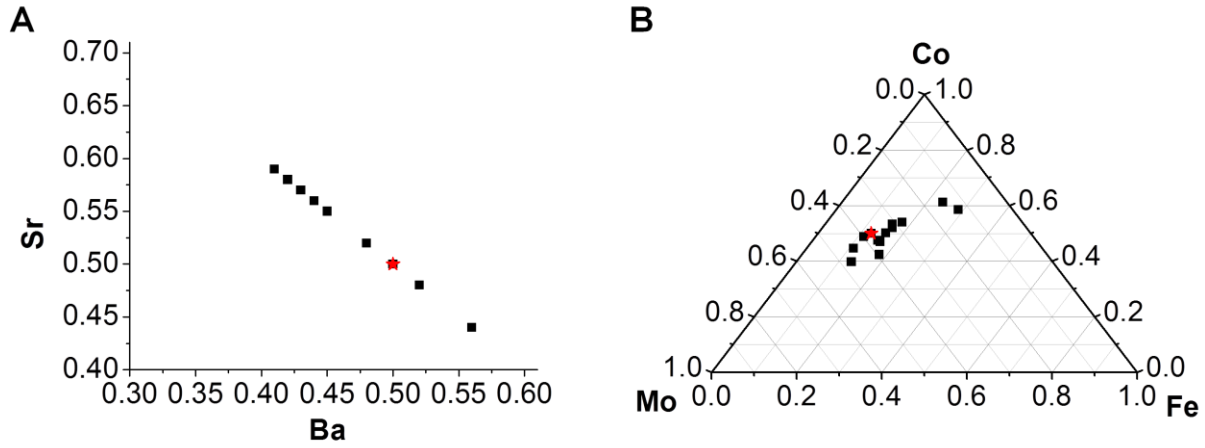

Figure 3.15: (A) A-site and (B) B-site cations distribution in BSCFMo0.375-(Co/Fe=4) with nominal composition $Ba_{0.5}Sr_{0.5}Co_{0.5}Fe_{0.125}Mo_{0.375}O_{3-\delta}$, synthesised at 1000^{o}C/24h, provided by EDS analysis. The black squares represent the compositions of the measured crystals, whilst the red star indicates the nominal composition.

Focusing on BSCFMo0.375-(Co/Fe=4), further regrindings and refirings at the same temperature were tried in an effort to improve the homogeneity. Heating at 1000^{o}C for another 24h with an

intermediate regrinding, seems to limit the compositional distribution on the B-site (*Figure 3.15B*), but still the A-site was richer in Sr than Ba cations (*Figure 3.15A*). Annealing at the higher temperature of 1150^{o}C for 8h, seems to degrade the homogeneity of the sample in both A (*Figure 3.15C*) and B-sites (*Figure 3.15D*) compared to both aforementioned synthesis procedures.

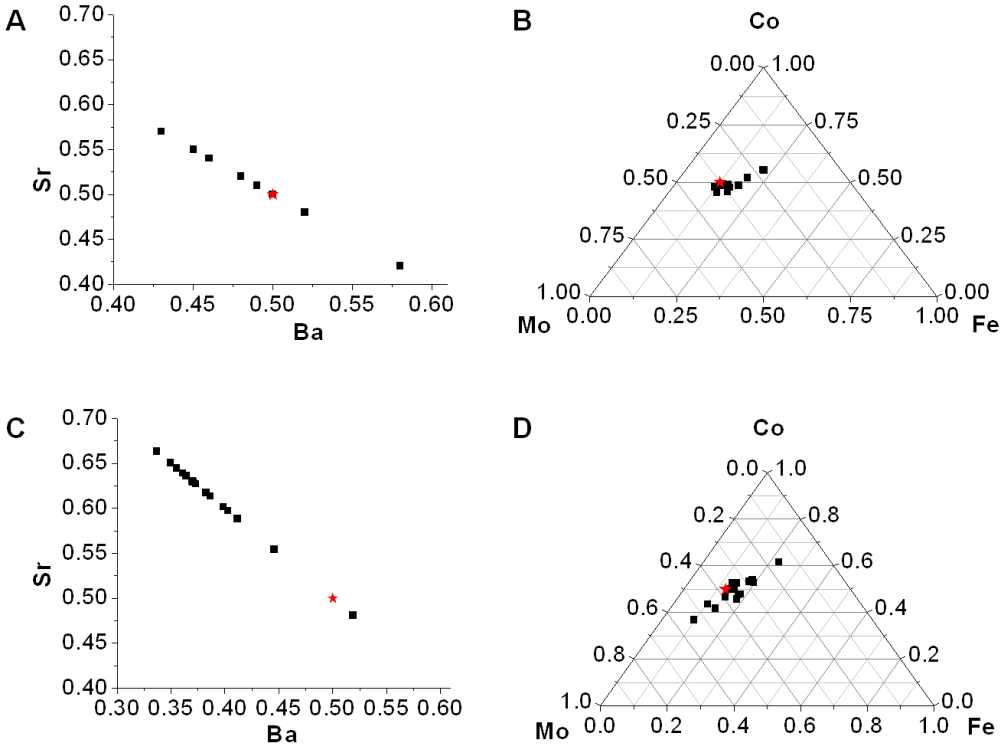

Figure 3.16: A-site and B-site cations distribution, provided by EDS analysis, for BSCFMo0.375-(Co/Fe=4) with nominal composition $Ba_{0.5}Sr_{0.5}Co_{0.5}Fe_{0.125}Mo_{0.375}O_{3-\delta}$, synthesised at 1000^{o}C/24h, followed by further firing at 1000^{o}C/24h ((A) and (B) respectively) and followed by firing step at 1150^{o}C/8h ((C) and (D) respectively). The black squares represent the compositions of the measured crystals, whilst the red star indicates the nominal composition.

The compositional analysis, for all the synthetic approaches described so far, showed some Ba loss in the A-site with the Ba/Sr ratio being approximately 60:40 for the majority of crystals measured. However, there was no evidence for phases containing the 'missing' amount of Ba^{2+} by XRD (*Section 3.1.2.2.2*) resulting in Sr excess. A possible explanation could be that barium reacts with the alumina crucibles, used for the synthesis, forming barium aluminate ($BaAl_2O_4$) which is reported to start forming from 900^{o}C[174], which is very close to the synthesis

temperature of 1000°C for the BSCFM materials. Moreover, the blue color observed at the bottom of the alumina crucibles could be due to the formation of cobalt aluminate ($CoAl_2O_4$), also known as 'cobalt-blue', and the presence of molybdenum oxide is reported to enhance the cobalt aluminate formation[175].

The synthetic approach was then modified in order to solve the problems of Ba loss on the A-site and inhomogeneity on the B-site, by avoiding the alumina containers and by introducing ball-milling for the mixing of the starting materials and between intermediate heating steps. According to this optimised synthetic procedure, stoichiometric amounts of the starting materials were mixed together by planetary ball milling for 24 hours in isopropanol with ZrO_2 balls, followed by drying, grinding, pressing in to pellets and calcining at 700°C for 6 hours and finally heating to 900°C for 8 hours. The resulting pellets were hand ground in an agate mortar and the powder was ball milled further for 18 hours in isopropanol. After milling the powder was dried, ground, pressed into pellets and subsequently sintered in air at 1000°C for 10 hours the grinding/pellet pressing/heating step was repeated a total of four times. During the sinterings, zirconia crucibles were used. The resulting compositions possessed the desired compositional homogeneity distributed over the sample grains, verified by EDS (*Figure 3.17*).

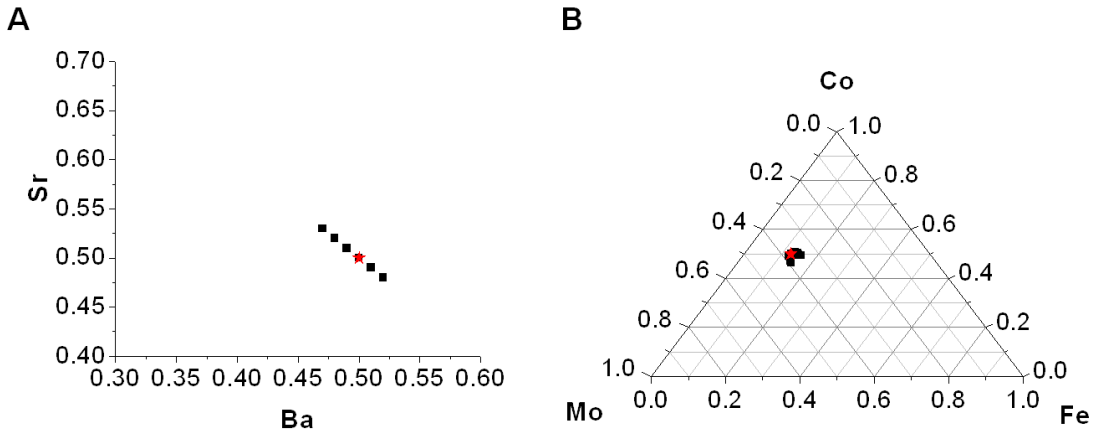

Figure 3.17: (A) A-site and (B) B-site cations distribution in BSCFMo0.375-(Co/Fe=4), with nominal composition $Ba_{0.5}Sr_{0.5}Co_{0.5}Fe_{0.125}Mo_{0.375}O_{3-\delta}$, synthesised by ballmilling and fired at 1000°C/10h with three intermediate regrindings, provided by EDS analysis. The black squares represent the compositions of the measured crystals, whilst the red star indicates the nominal composition.

3.1.4. Microscopy studies

3.1.4.1.Dark field imaging[*]

Microscopy techniques were used in order to better understand the nature of the BSCFM samples and complement the PXRD data. Dark field imaging (DF) in the transmission electron microscope (TEM) was performed on $[1\bar{1}0]$ oriented grains. The [111]* superstructure reflections, denoting the double perovskite (DP), were selected by the objective aperture.

The DF/TEM image for BSCFMo0.375-(Co/Fe=4) composition reveals that a single grain actually consists of two crystallite domains with coherent boundaries between them (*Figure 3.18*). The light areas correspond to the DP structure, for which the diffraction conditions allow the [111] superstructure reflections, while the dark regions correspond to structures (such as the SP or incorrectly oriented crystallites) for which the diffraction conditions are not met.

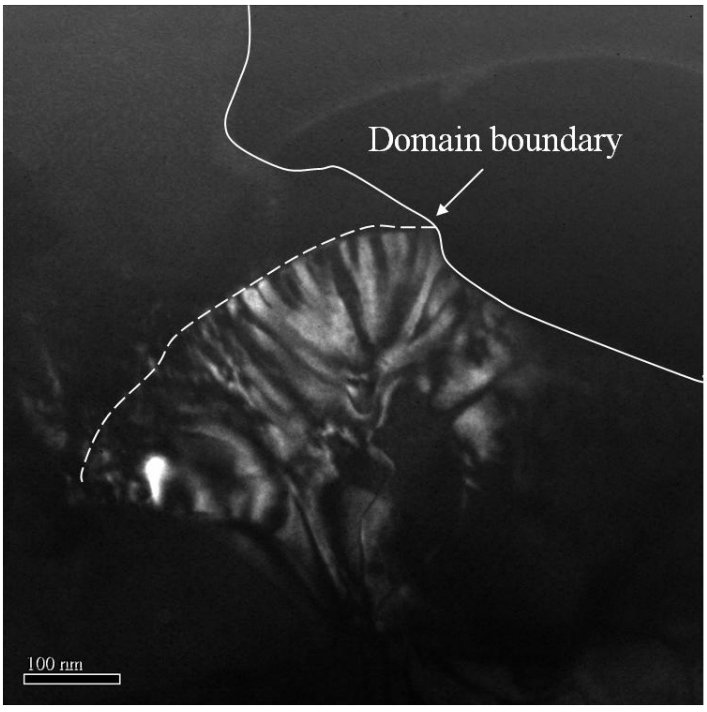

Figure 3.18: DF/TEM of a single grain for BSCFMo0.375-(Co/Fe=4). Domain boundaries are highlighted as solid and dashed lines.

∗ The DF-TEM work presented herein was done by Dr. J. Xu.

3.1.4.2.High Resolution Transmission Electron Microscopy (HRTEM)[*]

The different crystallite domains seen in a single grain of BSCFMo0.375-(Co/Fe=4) (*Figure 3.18*) were analysed by HRTEM, moving across the boundary in *Figure 3.18*, showing the two different diffraction patterns indicated by white circles (*Figure 3.19A*). Fourier Transforms (FT) of the top left area (*Figure 3.19B*) and bottom right area (*Figure 3.19C*) demonstrate additional diffraction spots in the latter which are not present for the former; in both cases indicated by white arrows.

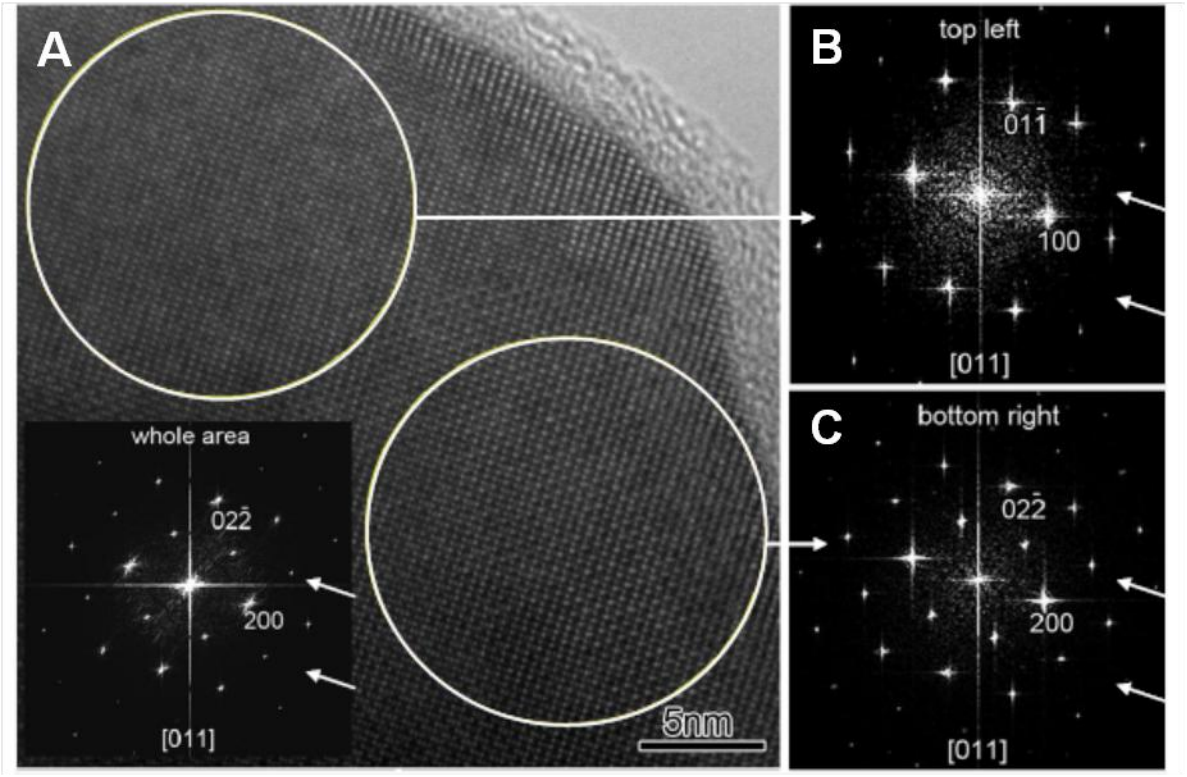

Figure 3.19: (A) HRTEM image of a $[1\bar{1}0]$ *oriented area and its diffraction pattern for a single grain BSCFMo0.375-(Co/Fe=4). The FT pattern is indexed as a double perovskite with the DP superstructure reflections indicated by white arrows. The FT of different sections in the same image (indicated by white circles) show (B) the absence and (C) presence of DP superstructure reflections, indicated by white arrows.*

The difference between the diffraction spots, which defines the unit cell, is half in *Figure 3.19C* corresponding to the compared to *Figure 3.19B*. As the electron diffraction pattern shows the unit cell in reciprocal space, when transformed to the real space, the unit cell agrees well with a

∗ The HRTEM-ED work was done by Dr. J. Xu

superstructure with double unit cell for the bottom right compared to the top left area of the HRTEM image (*Figure 3.19A*). In combination with the XRD analysis (*Section 3.1.2*), the diffraction pattern in *Figure 3.19B* corresponds to a single perovskite (SP) formation, whilst the superstructure diffraction spots in *Figure 3.19C* demonstrate the existence of the superstructure unit cell with double lattice parameters than the SP, and hence it is referred to as double perovskite (DP). The whole pattern was indexed as a DP (inset in *Figure 3.19*), with the superstructure reflections indicated by white arrows, demonstrating that the DP diffraction spots are intense for the total area of the single grain.

3.1.4.3.Prevalence of SP/DP microstructure *

A selection of DF images (*Figure 3.20*) shows the prevalence of the SP/DP microstructure coexistence of SP and DP throughout the BSCFM phase diagram. The majority of the grains are SP (dark areas) for BSCFM compositions with low Mo contents, here shown for BSCFMo0.125-(Co/Fe=4) (*Figure 3.20*A) and BSCFMo0.125-(Co/Fe=2) (*Figure 3.20*B) specimens. Small 5-10 nm domains of the DP phase are present as light areas in the DF images, which are too small to be observed by XRD. It should be noted that the parent BSCF is reported to be a pure SP based on DF/TEM[176].

The volume of the DP domains increases when the Mo content is increased, here shown for BSCFMo0.375-(Co/Fe=4) in *Figure 3.20*C. Higher magnification data of this sample (*Figure 3.20*D) reveal that the individual grains actually consist of an intergrowth of the two phases with multiple size domains, some reaching the order of a hundred nanometres, while other areas have a complex arrangement of smaller domains of a few tens of nanometres in size. The introduction of increased amount of the Mo^{6+} in the place of the Co and Fe seems to be the driving force for the formation of almost pure DP phases with small SP domains, in BSCFMo0.45-(Co/Fe=4) and BSCFMo0.45-(Co/Fe=10) compositions shown in *Figure 3.20E* and *Figure 3.20F* respectively.

∗ The DF-TEM images presented herein were taken by Dr. A. Demont.

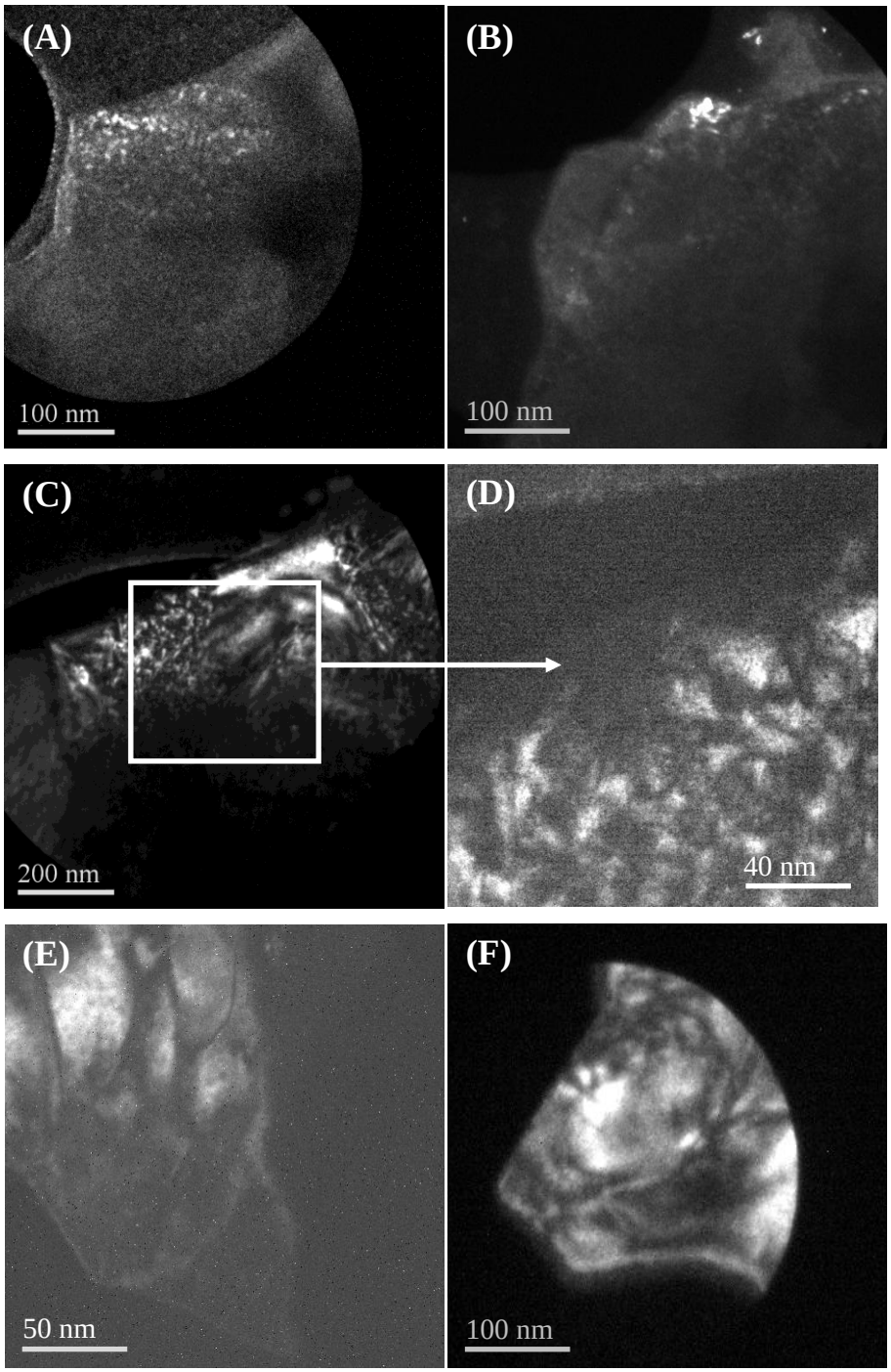

Figure 3.20: Dark field images based on the double perovskite superstructure reflections showing DP (white) and SP (black) domains for a range of compositions:

(A) BSCFMo0.125-(Co/Fe=4), (B) BSCFMo0.125-(Co/Fe=2), (C) and (D) BSCFMo0.375-(Co/Fe=4), (E) BSCFMo0.45-(Co/Fe=4) and (F) BSCFMo0.45-(Co/Fe=10).

3.1.5. Overview of phase assemblage and microstructure

A range of $Ba_{0.5}Sr_{0.5}(Co_{0.8-x}Fe_{0.2-y}Mo_{x+y})O_{3-\delta}$ samples was synthesised in order to find the compositional limits for the formation of the different phases. Three phase regions were clearly identified which are marked in different colours on the pseudo-phase ternary diagram (*Figure 3.21*), where the parent un-doped BSCF is represented as a black star. The compositions that were discussed in *Section 3.1.2* are represented in larger symbols on the phase diagram and numbered according to *Table 3.2*. The optimisation of the first synthetic approach (close symbols), by introducing ball-milling (open symbols), did not change the compositional limits of the phase areas.

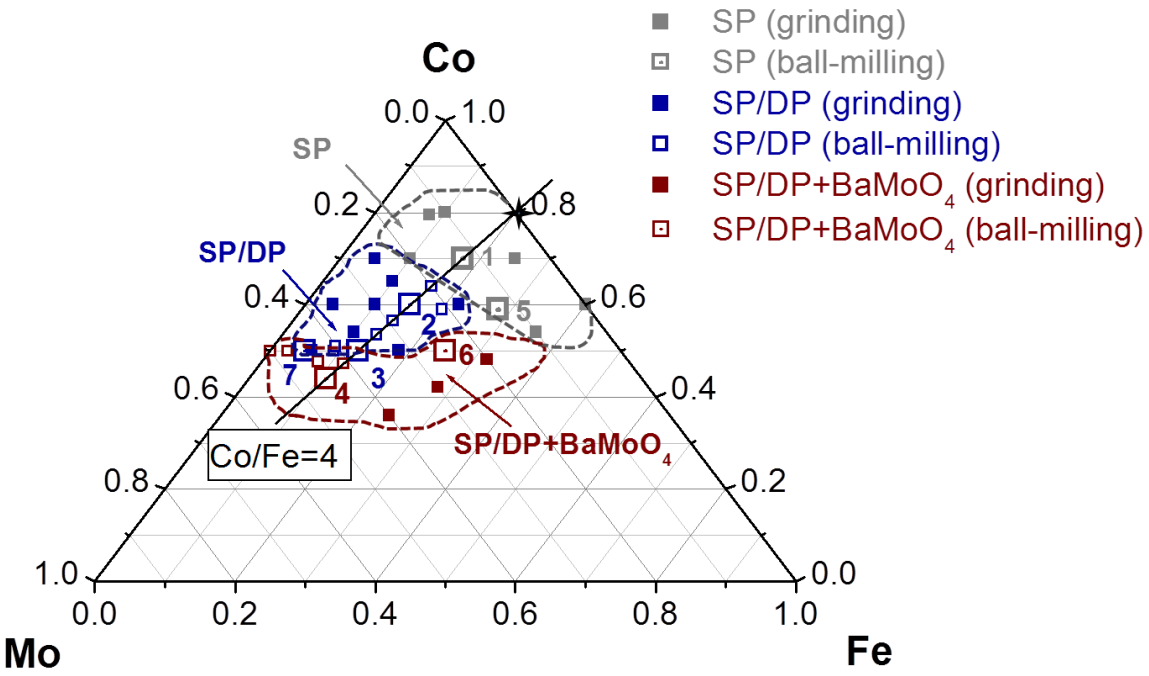

Figure 3.21: Phase Diagram of the $Ba_{0.5}Sr_{0.5}Co_{0.8-x}Fe_{0.2-y}Mo_{x+y}O_{3-\delta}$ compositions studied showing the three different phase regions identified, in different colours, and their compositional boundaries. The parent BSCF is shown as a black star, whilst the BSCFM compositions made are represented as squares in open and close cymbols corresponding to specimens prepared by hand-grinding and ball-milling respectively. The compositions discussed in Section 3.1.2, are shown in bigger symbols and are numbered according to Table 3.2.

Low Mo contents (Mo<0.2) afford a single perovskite (SP) phase isostructural with BSCF (ABO_3, cell parameter $a_p \sim 3.99$Å), marked in the 'SP' (grey) phase region, as evidenced by XRD. However, small DP domains of 5-10 nm were manifested the DF/TEM images, illustrating the higher sensitivity of the microscopy techniques. At increased Mo content (Mo ≥0.2, into the blue region denoted 'SP/DP'), a second perovskite phase coexists with the SP, with a doubled perovskite (DP) unit cell ($A_2BB'O_6$, cell parameter $2a_p \sim 7.98$Å), with increased volume of the DP domains compared to the 'SP' phase region, as seen by DF/TEM. The existence of DP phase was also evidenced by X-ray diffraction, showing the characteristic first DP reflection at about 22 degrees. The biphasic nature on the XRD patterns resulted in the splitting or broadening of the perovskite. Further increase in Mo content resulted in the expulsion of $BaMoO_4$ (marked as SP/DP + $BaMoO_4$ in the red phase region) coexisting with the SP/DP mixture and the maximum Mo content for impurity-free compounds depends strongly on the Co/Fe ratio.

The full structural characterisation of these biphase compounds was a great challenge and is further analysed in Chapter 4, whilst the focus of this chapter remains the description of the phase regions and the effect of this two phase coexistence on the stability and physical properties.

3.2. Long-term phase stability

The long-term phase stability of the BSCFM specimens was evaluated by annealing the synthesised powders at 750^{o}C for 120h (5days) in air, imitating the conditions of operation of an IT-SOFC. The phases before and after the treatment were characterised by X-ray diffraction.

3.2.1. Stability of 'SP' classified BSCFM compositions

The long-term stability of the parent BSCF and representative 'SP' classified BSCFM compositions is shown and compared in *Figure 3.22*. Plot (A) in black shows the as-made BSCF material, representative of the SP diffraction pattern, whilst plot (B) corresponds to BSCF after the stability test. The partial decomposition of the cubic to lower symmetry hexagonal perovskite phase of the parent un-doped BSCF is evidenced by the broad additional reflections[177], denoted with star symbols, after the long thermal treatment at 750^{o}C, showing the most intense at the 2theta range 20-55 (inset in *Figure 3.22*, in logarithmic scale). It is worth mentioning that only a few reflections can be attributed solely to either the hexagonal phase or to the cubic phase due to the close structural relationship between them.

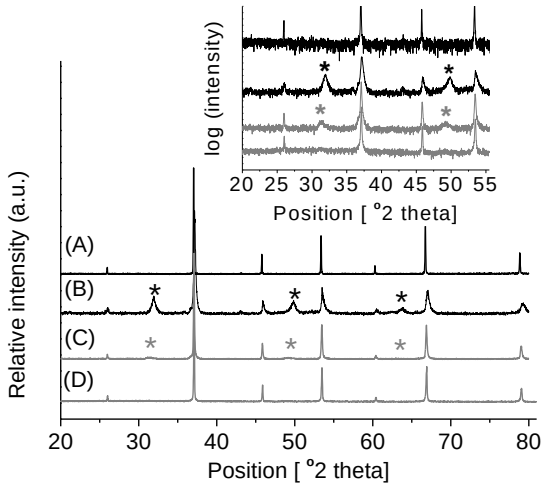

Figure 3.22: XRD of BSCF (A) before and (B) after thermal stability test at 750℃ for 120 hours in air, compared with the XRD of (C) BSCFMo0.125-(Co/Fe=4) and (D) BSCFMo0.125-(Co/Fe=2) after the same thermal treatment. The appearance of hexagonal perovskite decomposition products are indicated by star symbols and the inset shows in greater detail the 2theta range 20-55, in logarithmic intensity scale.

The BSCFM compositions with 12.5%Mo in their B-site show improved stability compared to BSCF. The specimen with abbreviated composition BSCFMo0.125-(Co/Fe=4) (composition #1 in *Figure 3.1*), shows some decomposition under the conditions tested (plot C), but less severe compared to BSCF based on the relative intensities of the reflections corresponding to the hexagonal phase formation. All compositions classified as SP with Co/Fe>4, show similar instability behavior with BSCFMo0.125-(Co/Fe=4). On the contrary, the iso-Mo containing BSCFMo0.125-(Co/Fe=2) (composition #5 in *Figure 3.1)*, located on the boundary with the other phase regions, was found stable under the same conditions (plot D), as evidenced by the lack of additional peaks and was an exception among the compositions marked in the SP region on the pseudo-phase diagram. This demonstrates that the stability of the SP forming BSCFM compounds is enhanced for the compositions having lower Co/Fe ratio and related with the actual amounts of Co and Fe.

The driving force for the decomposition of the cubic BSCF, is believed to be the cobalt preference to low-spin configuration in the Co^{3+} (d^6) oxidation state, which is favored at temperatures below 900^{o}C due to oxidation of Co^{2+} (d^7) present in the BSCF cubic structure[94, 178]. When reducing the Co content by introducing the bigger Mo^{6+} (0.59Å (HS)) in the B-site (compared to Co^{3+}(LS), 0.545Å), it is anticipated that the cubic phase would be favored for the Mo-doped BSCF compositions under the same conditions that the cubic BSCF is partially decomposed to the hexagonal polymorph.

The actual Co content for the stable BSCFMo0.125-(Co/Fe=2) and the unstable BSCFMo0.125-(Co/Fe=4) are 0.58 and 0.7 respectively, leading to considerations about the maximum Co content leading to the stability of the SP cubic phase after the prolonged thermal treatment. This observation is in agreement with previous reports in the $Ba_{0.5-x}Sr_{0.5+x}Co_{0.8-y}Fe_{0.2+y}O_{3-\delta}$ family. The stability of the cubic phases is enhanced when the Co content is 0.4[179] showing no secondary phases after prolonged heating at 750^{o}C for 500h for $Ba_{0.5}Sr_{0.5}Co_{0.4}Fe_{0.6}O_{3-\delta}$ and $Ba_{0.45}Sr_{0.5}Co_{0.4}Fe_{0.6}O_{3-\delta}$ compositions[180]. Focusing on other B-site dopings in BSCF in the literature, information about the stability of the cubic derived phases after prolonged thermal treatment at the operation temperature of IT-SOFCs is rather scarce. Interestingly, substitution with Nb^{5+} in $Ba_{0.5}Sr_{0.5}(Co_{0.8}Fe_{0.2})_{1-x}Nb_xO_{3-\delta}$, x= 0.05- 0.20, has been found to retain the cubic

structure for as high Co contents as 0.76 for x=0.05 and higher doping levels after firing at 750°C/ 240h[181].

3.2.2. Stability of 'SP/DP' classified BSCFM compositions

The XRD patterns for the representative BSCFMo0.25-(Co/Fe=4) composition (#2 in *Figure 3.1*), marked in the 'SP/DP' phase region, before (plot A) and after ageing for 120 hours at 750°C (plot B) are shown in *Figure 3.23* and compared with the XRD pattern of BSCFMo0.375-(Co/Fe=4) (#3 in *Figure 3.1*) after the same stability test (plot C). The inset provides magnification in logarithmic intensity scale of the 2theta region 20-55 degrees where the most intense peaks corresponding to the hexagonal perovskites are expected. The position of the characteristic (111) DP reflection is also marked to indicate that these compositions belong to the SP/DP phase region. For BSCFMo0.25-(Co/Fe=4), the diffraction pattern show small, almost negligible, hexagonal reflections after the long thermal treatment, whilst no decomposition was observed for BSCFMo0.375-(Co/Fe=4) after the same stability test.

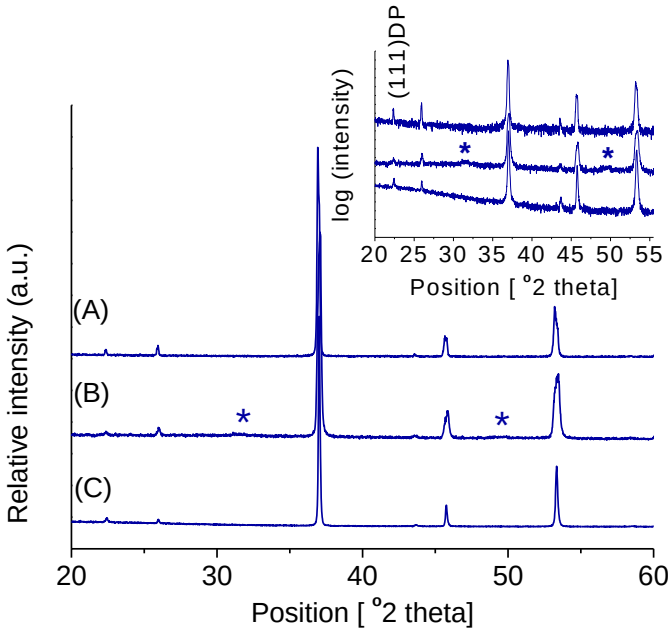

Figure 3.23: XRD of BSCFMo0.25-(Co/Fe=4) (A) before and (B) after thermal stability test at 750℃ for 120 hours in air, compared with the XRD of (C) BSCFMo0.375-(Co/Fe=4) after the same thermal treatment. The appearance of hexagonal perovskite decomposition products are indicated by star symbols and the inset shows in greater detail the 2theta range 20-55. The appearance of hexagonal perovskite decomposition products are indicated by star symbols.

The enhanced stability of the BSCFM compounds classified in the 'SP/DP' phase region compared to the SP counterparts, is extended to compositions with varying Co/Fe ratio, as for instance for BSCFMo0.45-(Co/Fe=10) *(#7* in *Figure 3.1)*. The stability of the SP/DP biphase compounds can be attributed to their overall Co content, in agreement with the outcome of the stability of SP classified compounds showing improved stability for compositions with maximum Co content up to 0.58, as in BSCFMo0.125-(Co/Fe=2). The overall Co content in BSCFMo0.375-(Co/Fe=4) and BSCFMo0.25-(Co/Fe=4) is 0.5 and 0.6 respectively, with the latter being at the Co maximum limit.

The presence of the DP component in the SP/DP classified BSCFM compounds may also be an additional stabilisation factor. Cubic double perovksites are reported to be very stable compared to the cubic simple perovskite coutnerparts. For instance, the cubic structure in the Mo-containing double perovskite $Ba_2CoMo_{0.5}Nb_{0.5}O_{6-\delta}$[182], crystallising in $Fm\bar{3}m$, is retained after long annealing at 750^{o}C for 10 days. Moreover, the Co-free double perovskite $Sr_2Fe_{1.5}Mo_{0.5}O_{6-\delta}$, showing good redox stability, has been applied as both anode and cathode of SOFCs[183, 184].

3.2.3. Stability of 'SP/DP + $BaMoO_4$' classified BSCFM compositions

The stability of compositions classified in SP/DP+ $BaMoO_4$ phase region was also tested under the same prolonged heating stability test at 750°C/120h (*Figure 3.24*), here shown for the representative BSCFMo0.45-(Co/Fe=4) (composition #4 in *Figure 3.1*). There are no changes in the XRD patterns corresponding to the as-made (plot A) and the specimen after the prolonged heating (plot B); for which the $BaMoO_4$ impurity phases are denoted by upturned triangles. Moreover, compared to the XRD pattern of BSCF under the same stability test (plot C), it becomes obvious than no hexagonal perovskite formation is favoured for these compounds. This indicates that the formation of the undesirable impurity $BaMoO_4$, doesn't affect the enhanced stability of the SP/DP composites.

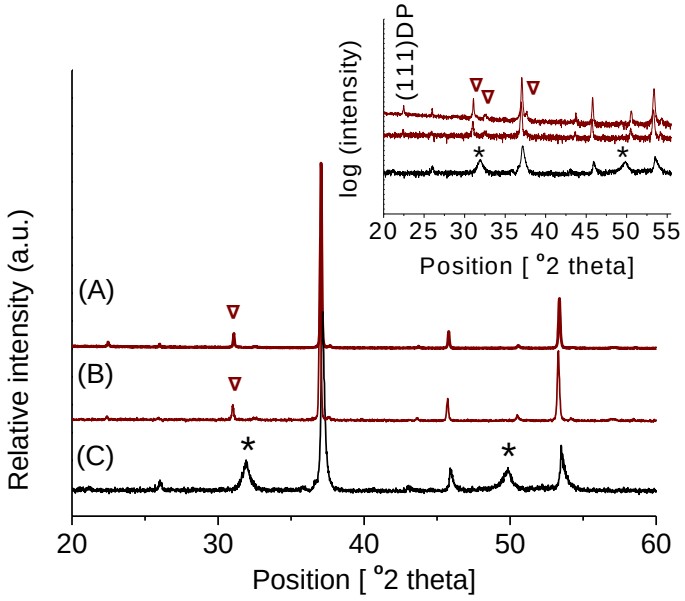

Figure 3.24: XRD of BSCFMo0.45-(Co/Fe=4) (A) before and (B) after ageing at 750℃ for 120 hours in air; the reflections corresponding to the $BaMoO_4$ impurity phase are denoted by upturned triangle symbols. (C) Comparison with XRD of BSCF after the stability test, for which the hexagonal perovskite decomposition products are indicated by star symbols.

3.3. Electrical and electrochemical properties

The electrical and electrochemical properties of four key selected BSCFMo$_{x+y}$(Co/Fe=0.8-x/0.2-y) compositions were studied in detail and are listed in *Table 3.12*. BSCFMo0.125-(Co/Fe=4) is classified in the SP phase region (#1 in *Figure 3.1* and *Figure 3.21*) whilst BSCFMo0.375-(Co/Fe=4) is a representative composition for the SP/DP phase region (#3 in *Figure 3.1* and *Figure 3.21*). Both specimens have Co/Fe ratio equal to 4, as the undoped parent BSCF material, allowing comparisons between Mo-poor SP compositions and Mo-rich SP/DP biphase compounds. BSCFMo0.45-(Co/Fe=10) (#7 in *Figure 3.1*and *Figure 3.21*) is the compound that had successfully incorporated the highest Mo content, resulting in a highest DP-rich compound achieved in this study, without the formation of the $BaMoO_4$ impurity phase. The Co content is the same (Co0.50) for both BSCFMo0.375-(Co/Fe=4) and BSCFMo0.45-(Co/Fe=10), hence the differences in their properties will reflect the differences in the Co/Fe ratio and actual Mo content. Both SP/DP compounds were found stable, whilst BSCFMo0.125-(Co/Fe=4) shows some decomposition to hexagonal perovskite similarly to the BSCF undoped material, under the same stability test (*Section 3.2*).

Table 3.12: Summary of B-site information for BSCF and key-selected BSCFM compositions chosen for the study, following the same classification, numbering and colour code introduced in Figure 3.1and Figure 3.21.

Abbreviation	Phase region	Code (#)	Co	Fe	Mo
BSCF	SP	star	0.8	0.2	0
BSCFMo0.125-(Co/Fe=4)	SP	1	0.7	0.175	0.125
BSCFMo0.375-(Co/Fe=4)	SP/DP	3	0.5	0.125	0.375
BSCFMo0.45-(Co/Fe= 10)	SP/DP	7	0.5	0.05	0.45

3.3.1. Electrical properties-electrical conductivity

The electrical conductivity of the key selected compositions was measured over the temperature range 500-850^{o}C, by the standard DC four-probe method on highly dense bars. The relative density was greater than 90% for all specimens, measured using an Archimedean balance. Platinum wires were attached to the bars to make the I-V probes with four-in-a-line contact geometry.

The electrical conductivity σ of all the Mo-BSCF compositions studied, increases with temperature (*Figure 3.25*), demonstrating semiconducting behaviour over the temperature range measured. BSCF, made at this study, affords a total conductivity of 47.3 S.cm^{-1} at 500^{o}C and displays a metallic like behavior between 500^{o}C to 700^{o}C, where the conductivity decreases gradually with temperature to 44.9 S.cm^{-1} (*Table 3.13*). At 700^{o}C it undergoes a transition to semiconducting behavior and the conductivity increases with temperature reaching 46.4 S.cm^{-1} at 850^{o}C, which is in agreement with previous reports [95, 185].

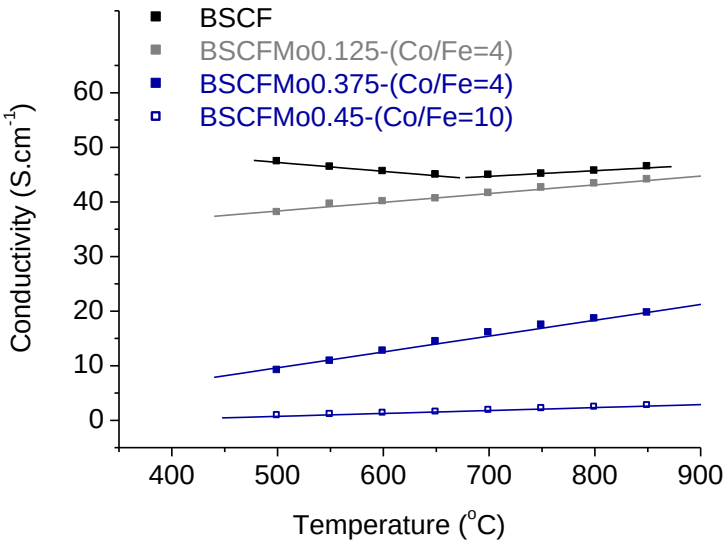

Figure 3.25: Electrical conductivity data for BSCF and the key-selected BSCFM compositions.

The transition from metallic to semiconductor is suppressed even for isostructural SP compounds to the parent BSCF with low Mo contents (e.g. BSCFMo0.125-(Co/Fe=4)), which display a total conductivity of 38 S.cm^{-1} at 500^{o}C, 41.5 S.cm^{-1} at 700^{o}C and 44 S.cm^{-1} at 850^{o}C (*Table 3.13*).

The electrical conductivity decreases more significantly on increasing further the Mo content to compositions classified to the SP/DP phase region. The maximum conductivity of BSCFMo0.375-(Co/Fe=4) is 15.97 $S.cm^{-1}$ at 700°C, which is more than half than for of un-doped BSCF and BSCFM0.125-(Co/Fe=4) at the same temperature. Increasing the amount of Mo and the relative amount of DP, leads to further decrease in the total conductivity of BSCFMo0.45-(Co/Fe=10) by almost an order of magnitude, reaching 1.78$S.cm^{-1}$ at 700^{o}C.

The measured values for the BSCFM materials mainly refer to the electronic conductivity part ($\sigma_{electronic}$) of the total conductivity (σ_{total}), as generally the ionic conductivity part (σ_{ionic}) in MIECs is usually one to two orders of magnitudes lower[186, 187], due to the lower mobility of the bulkier and higher charged oxygen ions (O^{2-}) compared to the more mobile electron holes ($h^{\bullet}$).

$\sigma_{total} = \sigma_{electronic} + \sigma_{ionic} \sim \sigma_{electronic}$

For BSCF, the ionic conductivity has been calculated to be 0.53–1.17 $S.cm^{-1}$ in the temperature range 700–850^{o}C by using data from oxygen permeation measurements[188],which is about ten times lower than its electronic conductivity as found in this study (σ = 44.83 S. cm^{-1} at 700^{o}C).

Table 3.13: Electrical conductivity data at 550^{o}C, 700^{o}C and 800^{o}C of the key-selected BSCFM compositions and the calculated activation energy over the whole temperature range measured (500-800^{o}C), showing clearly a decrease in the performance with increasing Mo content.

Abbreviation Nominal composition	**Phase region**	**σ (550^{o}C)**	**σ (700^{o}C)**	**σ (800^{o}C)**	**Ea (eV)**
BSCF $Ba_{0.5}Sr_{0.5}Co_{0.8}Fe_{0.2}O_{3-\delta}$	SP	46.31	44.83	45.61	0.074
BSCFMo0.125-(Co/Fe=4) $Ba_{0.5}Sr_{0.5}Co_{0.7}Fe_{0.175}Mo_{0.125}O_{3-\delta}$	SP	39.5	41.5	43.25	0.110
BSCFMo0.375-(Co/Fe=4) $Ba_{0.5}Sr_{0.5}Co_{0.5}Fe_{0.125}Mo_{0.375}O_{3-\delta}$	SP/DP	10.78	15.97	18.53	0.246
BSCFMo0.45-(Co/Fe= 10) $Ba_{0.5}Sr_{0.5}Co_{0.5}Fe_{0.05}Mo_{0.45}O_{3-\delta}$	SP/DP	1.00	1.79	2.35	0.339

The thermally activated electronic conductivity ($\sigma_{electronic}$) for perovskites containing transition metals is usually described by the small polaron hopping mechanism and expressed by the Arrhenius relationship[165]:

$$\sigma = \left(\frac{A}{T}\right) \exp\ \left(-\frac{Ea}{kT}\right) \qquad \textit{Equation 3.1}$$

where Ea is the activation energy for the polaron hopping, k is the Boltzmann constant, T is the absolute temperature and A is a material dependent constant related with the collisions frequency. The activation energy for conduction of the small polarons in BSCF above 400^{o}C and at $pO_2 \geq 0.1$ has been reported to be 0.07 eV[185], which is in good agreement with the finding in this work (Ea= 0.074eV), as shown in Table 3.13. The associated activation energy (Ea), determined by the plots ln(σT) against 1/T, increases with increasing the Mo content from 0.110 eV for the BSCFMo0.125-(Co/Fe=4) representative composition for the SP phase region to 0.246 eV and 0.339 eV for BSCFMo0.375-(Co/Fe=4) and BSCFMo0.45-(Co/Fe=10) respectively classified in the SP/DP phase area.

The electrical conductivity of the BSCFM oxide series can be explained in terms of the presence of the valent-alterable Co and Fe cations. Upon heating, the transition metals are reduced followed by creation of holes and can be described by *Equation 3.2* and *Equation 3.3*, according to the Kröger–Vink defect notation[187, 189]:

$$Co^{x}_{Co} \leftrightarrow Co'_{Co} + h^{\bullet} \qquad \textit{Equation 3.2}$$

$$Fe^{x}_{Fe} \leftrightarrow Fe'_{Fe} + h^{\bullet} \qquad \textit{Equation 3.3}$$

where M'_M (M: Co or Fe) refers to $M^{(x-1)}$ localized on $M^{(x)}$ site, M^{x}_M stands for $M^{(x)}$ and $h^{\bullet}$ for holes.

In the case of BSCF, data of thermopower and oxygen nonstoichiometry confirm p-type small polaron hopping between $(Co, Fe)^{4+}$ to $(Co, Fe)^{3+}$ cations upon heating up to 900^{o}C[190, 191] . The further reduction of $(Co, Fe)^{3+}$ to $(Co, Fe)^{2+}$ could produce additional charge carriers[187], however higher temperatures are needed. The reduction of Co^{3+} to Co^{2+} is reported to become significant for temperatures above 900^{o}C and further reduction to Fe^{2+} requires temperatures of ca. 1560^{o}C [192]and hence is not possible to be observed at the temperature range (500-850^{o}C) used for this study. The average oxidation state of Co and Fe at room temperature in BSCF was

determined to be near 3+ with some amount of 4+ from Mössbauer data in air (in Appendix A), which is consistent with findings from soft XAS of BSCF powders quenched from 250 and 900^{o}C[192]. Hence, at the temperature range used for our experiment, it is mostly the small proportion of M^{4+} cations being reduced to M^{3+} that occurs, where M: Co, Fe. In the case of BSCFM materials, the substitution of Co and Fe by the highly charged and chemically stable d0 Mo^{6+}, results in direct decrease in the concentration of M species, but also forces the oxidation states of Co and Fe to decrease to maintain the electrostatic neutrality. Since the concentration of tetravalent cations is reduced, the number of mobile charge carriers produced upon heating is decreased, leading to lower values of electrical conductivity.

The decrease in conductivity values with decreasing the concentration and overall charge of the valent-alterable transition metals by introducing reduction-tolerant dopants has been widely reported for perovskite compounds compositionally close to BSCF. The Nb^{5+} doping in $Ba_{0.5}Sr_{0.5}(Co_{0.8}Fe_{0.2})_{1-x}Nb_xO_{3-\delta}$ (x=0-0.2), showing decreased conductivity with increasing the Nb content[181]. The conductivity of $Ba_{0.5}Sr_{0.5}Co_{0.6}Fe_{0.2}Zr_{0.2}O_{3-\delta}$, where Zr^{4+} partially substitutes Co, shows a maximum of 16.9 S.cm^{-1} at 540^{o}C [193]. When Ti^{4+} fully substitutes Fe by forming $Ba_{0.5}Sr_{0.5}Co_{0.8}Ti_{0.2}O_{3-\delta}$, the total conductivity drops to about 10 S.cm^{-1} at 550^{o}C[194], highlighting the lack in concentration of tetravalent Fe cations. Reduced Ti^{4+} content in $Ba_{0.5}Sr_{0.5}Co_{0.85}Ti_{0.15}O_{3-d}$ results in slightly improved conductivity values, reaching about 18 S.cm^{-1} at 550^{o}C [194] highlighting the role of Co^{4+} species. The Ba-free $Sr_2Fe_{1-x}Mo_xO_3$ system, crystallizing also in Pm-3m, shows an abrupt decrease in the conductivity values from 165 S.cm^{-1} to 85 S.cm^{-1}and 20 S.cm^{-1} at 550^{o}C as the Mo content increases from x=0, to x=0.1 and x=0.25 respectively[195].

Overall, the electrical conductivity of the BSCFM materials studied herein is considered relatively low, noting that conductivities of at least 100 S.cm^{-1} [69]are required for use as cathodes in IT- SOFCs, to support the flow of charged particles during operation. For instance, the common IT-SOFC cathode $La_{0.6}Sr_{0.4}Co_{0.2}Fe_{0.8}O_{3-\delta}$, displays an electrical conductivity of 333 S.cm^{-1} at 800°C[196].

3.3.2. Thermogravimetric Analysis (TGA)

Thermogravimetric analysis (TGA) was performed for BSCF and the key selected doped BSCFM compositions, heating from room temperature to 750°C in a flowing air atmosphere at a heating and cooling rate of 5°C/min. Each sample was cycled from 50°C to 750°C to 50°C a total of three times (1 cycle is heating and cooling), with a dwell at the maximum and minimum temperatures of 30 minutes on each cycle and the relative weight (w%) as a function of temperature was recorded. The first cycle was not taken into account, as moisture removals can lead to artifacts. After the initial heat up, the TGA curves showed good reproducibility as the powder was thermally cycled, indicating that the powder was able to equilibrate with its surroundings (gaining or losing oxygen) on the time scale of the measurement. The data plotted in *Figure 3.26* are from the third cycle, with solid and dash lines corresponding to the heating and cooling respectively.

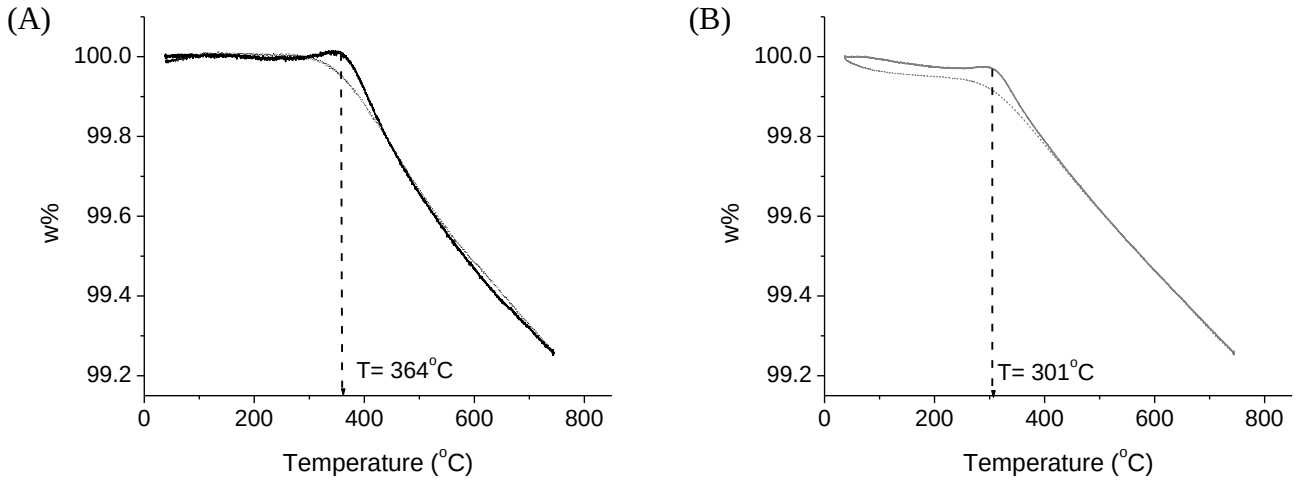

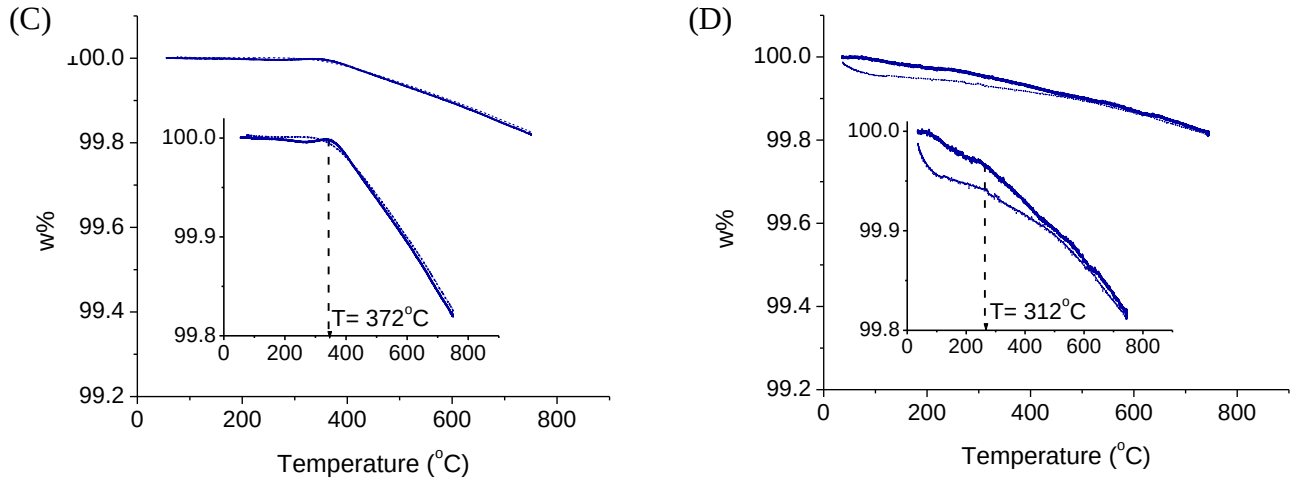

Figure 3.26: Thermogravimetric analysis (TGA) data for (A) BSCF, (B) BSCFMo0.125-(Co/Fe=4), (C) BSCFMo0.375-(Co/Fe=4) and (D) BSCFMo0.45-(Co/Fe=10) showing the weight loss (w%) upon heating up to 750°C and cooling back to room temperature, in solid and dash lines respectively. The arrows indicate the temperature that the weight loses commence.

Upon initial heating in air to about 300-400 °C the specimens did not exhibit any significant weight changes. Continued heating from 300-400 to 750°C resulted in a steady weight loss (*Table 3.14*). The total weight loss for BSCF (*Figure 3.26A*) and the isostructural BSCFMo0.125-(Co/Fe=4) (*Figure 3.26B*) is the most significant of all the compositions with both losing 0.74%. On increasing Mo content and entering the SP/DP phase region, there is a dramatic reduction in the amount of weight loss at 750°C of 0.17% and 0.18% for BSCFMo0.375-(Co/Fe=4) (*Figure 3.26C*) and BSCFMo0.45-(Co/Fe=10) (*Figure 3.26D*) respectively. The exact temperature value (T) where the weight loss commences varied slightly for each composition. No trend of the T value was observed with increasing the Mo content, as for the undoped BSCF the weight loss starts at 364°C, with obtained values of 301°C, 372°C and 312°C for BSCFMo0.125-(Co/Fe=4), BSCFMo0.375-(Co/Fe=4) and BSCFMo0.45-(Co/Fe=4) respectively. Cooling the samples back to 300-400°C resulted in a steady weight gain. There is a small hysteresis during cooling, compared to heating, which is expected due to the slower kinetics involved in oxygen gain. Further cooling did not result in significant weight changes.

The relative weight (w) % change as a function of temperature in air corresponds to the concentration of mobile oxygen species in the crystal lattices. Upon heating, the sample looses oxygen while the valent-alterable transition metals (M: Co, Fe) are reduced (*Equation 3.3*). The holes created by the reduction of the transition metals are consumed by the lattice reaction by increasing the number of oxygen vacancies ($V_o^{\bullet\bullet}$) into the lattice, as the sample loses oxygen during the heating process [187, 189] (*Equation 3.4*).

$$O_O^x + 2\,h^{\bullet} \leftrightarrow \tfrac{1}{2}\,O_2\,(g) + V_o^{\bullet\bullet} \qquad \textit{Equation 3.4}$$

where O_O^x is the lattice oxygen and $V_o^{\bullet\bullet}$ refers to the oxygen vacancies with an effective charge of +2q.

Table 3.14: Thermogravimetric analysis (TGA) data for BSCF and the key-selected BSCFM compositions, showing the weight loss corresponding to the oxygen loss from the lattice, upon heating at 750^{o}C for 30 min.

Abbreviation Nominal composition	**Phase region**	**Weight loss (%)**	**Change in Oxygen stoichiometry**
BSCF $Ba_{0.5}Sr_{0.5}Co_{0.8}Fe_{0.2}O_{3-\delta}$	SP	0.74	0.092
BSCFMo0.125-(Co/Fe=4) $Ba_{0.5}Sr_{0.5}Co_{0.7}Fe_{0.175}Mo_{0.125}O_{3-\delta}$	SP	0.74	0.092
BSCFMo0.375-(Co/Fe=4) $Ba_{0.5}Sr_{0.5}Co_{0.5}Fe_{0.125}Mo_{0.375}O_{3-\delta}$	SP/DP	0.17	0.021
BSCFMo0.45-(Co/Fe= 10) $Ba_{0.5}Sr_{0.5}Co_{0.5}Fe_{0.05}Mo_{0.45}O_{3-\delta}$	SP/DP	0.18	0.022

The total weight loss for BSCF and the isostructural BSCFMo0.125-(Co/Fe=4) corresponds to an oxygen loss of 0.092 (*Table 3.14*), where $ABO_{3-\delta}$ is the general perovskite formula unit and δ the number of oxygen vacancies. This change in oxygen stoichiometry is smaller than reported for BSCF from 200°C to 750°C (oxygen loss%= 0.18)[197]. This discrepancy may be associated with differences in the thermal history of the samples. It is interesting to note that the introduction of 12.5%Mo on the B-site does not have a significant effect on the oxygen loss compared with undoped BSCF, where it would be anticipated that the addition of Mo^{6+} on the B-site would reduce the number of oxygen vacancies to maintain charge balance. The observations here

indicate that in small quantities of Mo-doping this may not be the case, suggesting that the metal charge states are lowered compared with BSCF in the BSCFM materials.

The oxygen losses for the higher Mo containing specimens were calculated to 0.021 and 0.022 for the biphase compounds BSCFMo0.375-(Co/Fe=4) and BSCFMo0.45-(Co/Fe=10) respectively (*Table 3.14*). This demonstrates that on increasing the Mo^{6+} content the number of oxygen vacancies is significantly reduced compared to the undoped BSCF and the Mo-poor BSCFMo0.125-(Co/Fe=4), as charge balance requires an increase in the oxygen content to compensate for increased charge on the B-site. However, the formation of DP seems to be the main driving force for the reduction in oxygen vacancy concentration compared to the parent BSCF, since the oxygen content for these compositions is very close even if the relative Mo content differs.

3.3.3. Electrochemical properties

The electrochemical performance of the parent BSCF and the key-selected Mo-doped BSCF compositions was evaluated by measuring their resistance with impedance spectroscopy (*Section 3.3.3.1*) in the 'electrolyte-supported symmetrical cells configuration', consisted of a dense electrolyte substrate and porous cathode ink deposited onto both surfaces. The electrolyte for this study was SDC ($Sm_{0.2}Ce_{0.8}O_{1.9}$). The area specific resistance (ASR) of the cathode was calculated by normalising the measured resistance for the electrode area and dividing by two to take into account the symmetry of the cell.

According to the protocol established by the optimisation study (described in detail in Chapter 5, *Section 5.1.1*), the cathode inks were prepared by mixing with ball-milling BSCFM powders with an organic pore-former, in the weight ratio of 60:40 powder to binder. The electrode ink was applied to both surfaces of the SDC dense electrolyte substrate (98-99%) via screen printing. The cell was heated in air at 950°C for 3 hours to achieve good adherence of the electrodes to the electrolyte surface. Each cathode was manufactured by the same protocol (milling regime, ink processing, screen printing parameters and thermal treatment) to minimize variations in porosity, tortuosity and surface area. The cells morphology was evaluated by SEM (*Section 3.3.3.2*). The compatibility of the BSCFM materials with the SDC electrolyte was tested with reactivity experiments, discussed in *Section 3.3.3.3*.

3.3.3.1. Electrochemical performance

The cathode polarisation resistance for BSCF and the BSCFM symmetrical cells was measured at the temperature range 600-800^{o}C in 50^{o} steps, allowing 90 min for thermal equilibration at each temperature. The measurements were repeated for all the compositions for validating the reproducibility (*Table 3.15*) and the ones corresponding to the lowest values are plotted in *Figure 3.27A*. The lowest measured ASR value for the parent BSCF was 0.16 Ω.cm^2 at 650^{o}C, which is equal to the value obtained for the isostructural BSCFMo0.125-(Co/Fe=4) at the same temperature. The polarization resistance of BSCFMo0.375-(Co/Fe=4), having SP/DP biphase microstructure, was the lowest from the compositions studied with an ASR (650^{o}C) value of 0.13 Ω.cm^2. However, the cathode properties were found to be much worse for the BSCFMo0.45-(Co/Fe=10) composition, also classified in the 'SP/DP' phase region, since the associated ASR (0.51 Ω.cm^2, at 650^{o}C) was about four to five times higher than for the rest of the compositions.

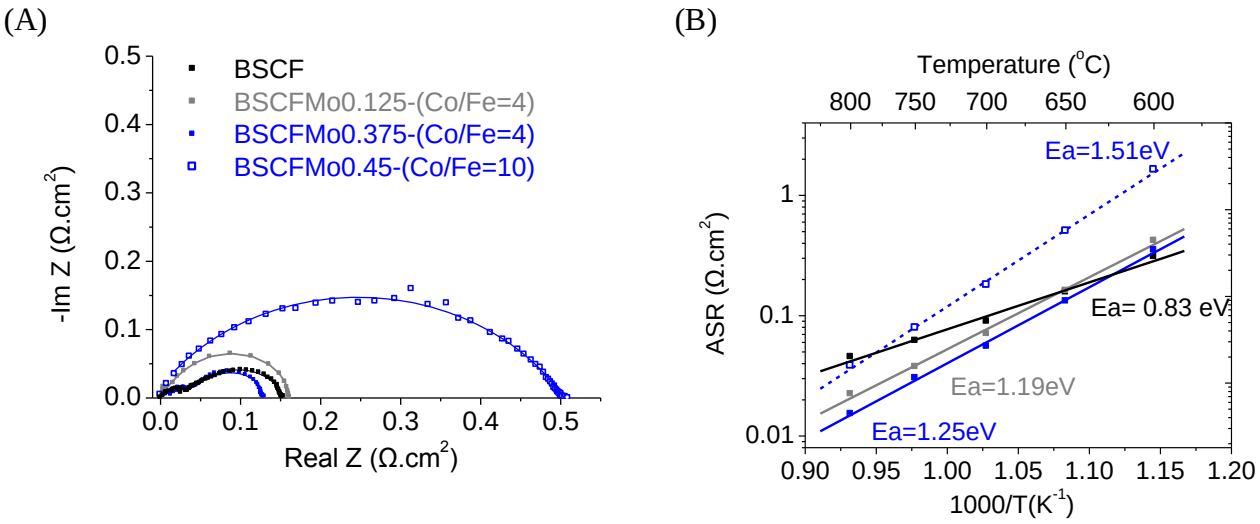

Figure 3.27: (A) Electrochemical impedance arcs (EIS) for BSCF, BSCFMo0.125-(Co/Fe=4), BSCFMo0.375-(Co/Fe=4) and BSCFMo0.45-(Co/Fe=10) at 650^{o}C, normalised to zero on the x-axis to remove electrolyte contribution (B) Arrhenius plots of ASR against temperature at the range 600-800^{o}C and calculated activation energy (Ea) for the oxygen reduction reaction (ORR) derived from the slope of the curves.

The ASR values for all the specimens decrease linearly with the temperature, allowing the estimation of the activation energies (*E*a) calculated from the slope of the curves (*Figure 3.27B*). The energy barrier for the oxygen reduction reaction (ORR) increases linearly with the Mo

content from 0.83 eV for BSCF to 1.19 eV for BSCFMo0.125-(Co/Fe=4), 1.25 eV for BSCFMo0.375-(Co/Fe=4) and 1.51 eV for BSCFMo0.45-(Co/Fe=10) and show no dependence on the phases present.

Table 3.15: Summary of information obtained from the electrochemical measurements of BSCF and the Mo-doped BSCF compositions, classified according to the phase diagram in Figure 3.21, showing the area specific resistance (ASR) at the temperature range 600-800^{o}C for two replicates for each composition and the associated activation energy (Ea). The measurements giving the lowest ASR for each sample are plotted in Figure 3.27 and are shown in bold.

Abbreviation Nominal composition	**Phase region**	**ASR (600^{o}C)**	**ASR (650^{o}C)**	**ASR (700^{o}C)**	**Ea (eV)**
BSCF	SP	**0.30**	**0.16**	**0.09**	**0.83**
$Ba_{0.5}Sr_{0.5}Co_{0.8}Fe_{0.2}O_{3-\delta}$		0.51	0.17	0.08	1.31
BSCFMo0.125-(Co/Fe=4)	SP	**0.42**	**0.16**	**0.08**	**1.19**
$Ba_{0.5}Sr_{0.5}Co_{0.7}Fe_{0.175}Mo_{0.125}O_{3-\delta}$		0.45	0.20	0.10	1.13
BSCFMo0.375-(Co/Fe=4)	SP/DP	**0.35**	**0.13**	**0.06**	**1.25**
$Ba_{0.5}Sr_{0.5}Co_{0.5}Fe_{0.125}Mo_{0.375}O_{3-\delta}$		0.46	0.21	0.10	1.18
BSCFMo0.45-(Co/Fe= 10)	SP/DP	**1.63**	**0.51**	**0.18**	**1.51**
$Ba_{0.5}Sr_{0.5}Co_{0.5}Fe_{0.05}Mo_{0.45}O_{3-\delta}$		1.74	0.63	0.26	1.38

According to the literature, BSCF itself displays a range of ASR values from 0.13 to 2.1 cm^2 at 600^{o}C, depending on processing conditions and electrolytes [69, 198-205]. Here, the lowest ASR value measured at 600˚C was 0.30 Ω.cm^2. Lower ASR values by almost an order of magnitude are obtained when pure ionic conductors are used either as a porous layer between BSCF and the electrolyte or for composites with BSCF[95, 206-208]. The activation energy for the ORR in the literature varies between 0.85- 1.48 eV for both BSCF bulk and composites [69, 95, 198-208], which is in good agreement with the 0.83 eV that was achieved under this study.

It is hard to comment whether Mo enhances the cathode performance. The good electrochemical properties of BSCF are reported to result from high oxygen ionic conductivity, originated by the high oxygen non-stoichiometry and concentration of oxygen vacancies [69, 206]. On substituting Co and Fe by Mo^{6+}, the oxygen content is decreased to balance the increased charge on the B-

site (*Section 3.3.2*) and this can explain the slightly larger ASR obtained for the SP classified BSCFMo0.125-(Co/Fe=4).

The increased amount of Mo in the SP/DP biphase BSCFMo0.375-(Co/Fe=4) shows enhanced cathodic performance compared to both BSCF and BSCFMo0.125-(Co/Fe=4), although the total conductivity and oxygen vacancy concentration decreases significantly (*Section 3.3.1* and *Section 3.3.2*). This supports the catalytic activity of Mo and suggests that the observed SP/DP intragrain microstructure in BSCFMo0.375-(Co/Fe=4) is beneficial for the cathode performance. However, the increased DP and total Mo content character in BSCFMo0.45-(Co/Fe=10) results in deterioration of the electrochemical properties, implicating different mechanism for the ORR, likely linked to structural differences with the rest of the compositions discussed herein that have lower Co/Fe =4. The evolution of electrochemical performance with Mo at the constant Co/Fe=4 and the effect of Co/Fe ratio at constant Mo content are further discussed in Chapter 5 in *(Section 5.2.1* and *Section 5.2.3*) respectively.

According to the literature, the partial substitution of Co by more chemically stable ions results clearly in deterioration of the cathode performance. For instance, when Zr^{4+} replaces Co in $Ba_{0.5}Sr_{0.5}(Co_{0.6}Zr_{0.2})Fe_{0.2}O_{3-\delta}$, which crystallizes in $Pm\bar{3}m$ as the parent compound, exhibits an activation energy of 1.18eV and ASR value of 0.255 at 650^{o}C[193]. Moreover, the lowest ASR values for the $Ba_{0.5}Sr_{0.5}Co_{0.2-x}Zn_xFe_{0.8}O_{3-\delta}$ (x= 0, 0.05, 0.1, 0.15, 0.2) family, are reported for the lowest Zn^{2+} doping. The polarization resistance of $Ba_{0.5}Sr_{0.5}Co_{0.15}Zn_{0.05}Fe_{0.8}O_{3-\delta}$ is reported to be 0.28 $\Omega.cm^2$ at 650^{o}C, which is about half than the corresponding ASR for end member $Ba_{0.5}Sr_{0.5}Zno_{0.2}Fe_{0.8}O_{3-\delta}$ (0.64 $\Omega.cm^2$) [116]. On the contrary, the A-site doping with trivalent cations in the place of Ba^{2+} and Sr^{2+}, results in enhanced electrochemical performance for the systems $(Ba_{0.5}Sr_{0.5})_{1-x}A_xCo_{0.8}Fe_{0.2}O_{3-\delta}$, for A^{3+}: Sm[198, 199], Pr[209], Nd [202]. This was attributed to the combined effect of increased electrical conductivity, due to reduction of the M^{4+} (M: Co,Fe) ions to their trivalent state followed by charge disproportionation of Co^{3+}(HS) to Co^{3+} (LS), and the enhanced oxygen diffusion, due to the weakening of the coulombic attraction of M^{3+} to oxygen compared to M^{4+}. The best performance is reported for $(Ba_{0.5}Sr_{0.5})_{0.8}Pr_{0.2}Co_{0.8}Fe_{0.2}O_{3-\delta}$ with obtained ASR at 600^{o}C of 0.108 $\Omega.cm^2$ [209] and $(Ba_{0.5}Sr_{0.5})_{0.9}Sm_{0.1}Co_{0.8}Fe_{0.2}O_{3-\delta}$ showing an activation energy for ORR of 0.69 eV [198].

Overall, the best electrochemical performance obtained under this study was for the compound with abbreviation composition BSCFMo0.375-(Co/Fe=4) with ASR of 0.132 $\Omega.cm^2$ at 650^oC and associated activation energy of 1.25 eV over the temperature range measured. This is still higher than the target value of 0.15 $\Omega.cm^2$ for cathodes, for temperatures below 600^oC[210], but better than the commonly used LSCF ($La_{0.6}Sr_{0.4}Co_{0.2}Fe_{0.8}O_{3-\delta}$) on SDC with ASR in the range of around 1.3 $\Omega.cm^2$ at 600^oC under similar processing conditions [211, 212] and activation energy in the range of 1.36-1.43 eV[81, 213]. The electrochemical performance of BSCFMo0.375-(Co/Fe=4) is comparable with the double perovskite $GdBaCo_2O_{5+\delta}$ reported to exhibit an ASR of 0.25 $\Omega.cm^2$ at 625^oC on GDC[214]; however ASR of 0.15 $\Omega\ cm^2$ at 750 °C and 1.11 $\Omega\ cm^2$ at 600 °C are reported when SDC is used as the electrolyte [215].

In order to give more insight on the compositional parameters affecting the cathode polarisation resistance, cells corresponding to different compositions were fabricated and measured following identical protocol and are further discussed in Chapter 5.

3.3.3.2. Morphology of cells[*]

The morphology of the symmetrical cells for the parent undoped BSCF and the Mo-doped symmetrical, fabricated and measured under identical conditions, was visualized by SEM (*Figure 3.28*) and the pore accessible volume was measured by sorption studies in N_2 and the calculated surface area for each sample is given in *Table 3.16*.

As can be seen in *Figure 3.28A*, the morphology of the BSCF cell differs that for the Mo-doped BSCF compositions, due to the existence of large agglomerates compared to smaller particles observed for BSCFMo0.125-(Co/Fe=4) (*Figure 3.28B*), BSCFMo0.375-(Co/Fe=4) (*Figure 3.28C*) and BSCFMo0.45-(Co/Fe=10) (*Figure 3.28D*). This accompanied by a significant decrease in the measured surface area from 3 m^2/g for the Mo-doped compositions to 0.70 m^2/g for BSCF.

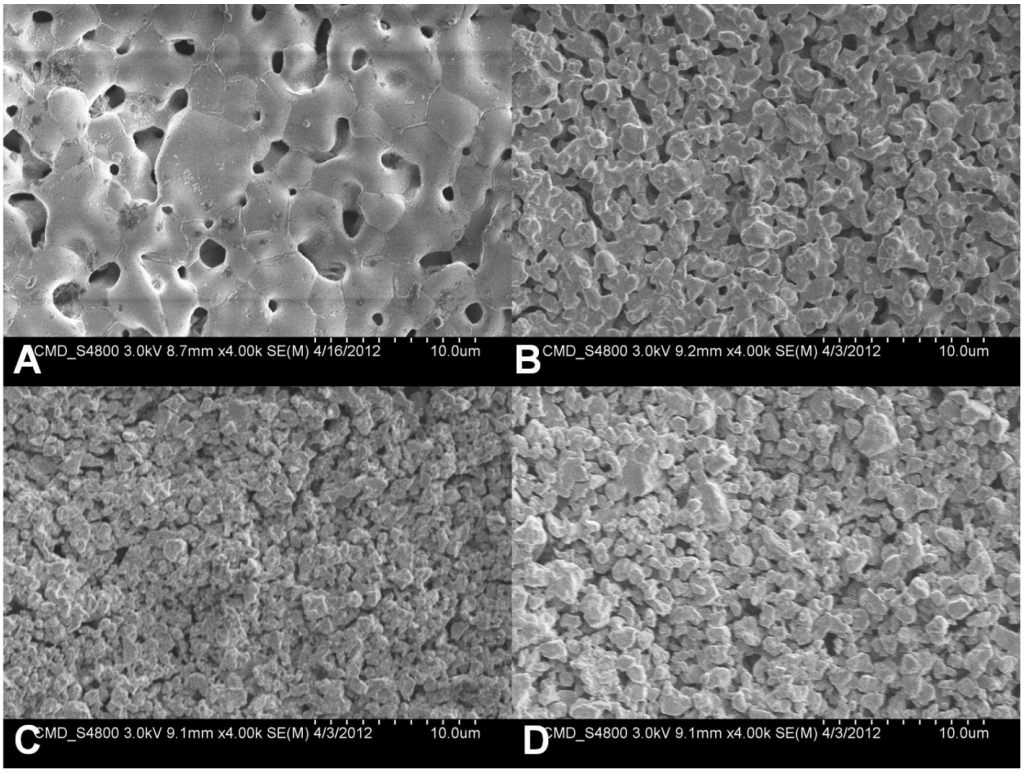

Figure 3.28: SEM on the cathode surface of the symmetrical cells for (A) BSCF, (B) BSCFMo0.125-(Co/Fe=4), (C) BSCFMo0.375-(Co/Fe=4) and (D) BSCFMo0.45-(Co/Fe=10).

∗ The SEM images were taken by Dr. X.Wang and the sorption study was done by Dr. C. Martí- Gastaldo.

Since all the symmetrical cells were fabricated under identical procedure and hence heated at the same temperature for adhesion to the electrolyte (950^{o}C for 3h), the difference in morphology could be related to different melting points. The melting point of BSCFMo0.125-(Co/Fe=4) and the 'SP/DP' classified compositions BSCFMo0.375-(Co/Fe=4) and BSCFMo0.45-(Co/Fe=10) is above 1200^{o}C as established from this study, whilst the melting point of the parent un-doped BSCF, is reported be in the range of 1130-1180^{o}C[216]. Hence, the low surface area measured for BSCF is likely to influence its electrochemical performance, due to limited diffusion, bigger particles and decreased number of active sites for ORR compared to the Mo-doped materials. Lower adhesion temperature of the BSCF cell would favor smaller particles sizes and possibly enhance the cathode performance. According to the literature, the ASR values for BSCF on CGO electrolyte (isostructural to the fluorite SDC used herein) are two times lower when the adhesion temperature was kept to 900^{o}C compared to 950^{o}C[217], which is a result of optimised morphology but could also be associated with higher reactivity with the electrolyte[218].

Table 3.16: BET surface area as determined by sorption measurements for BSCF and the Mo-doped BSCF symmetrical cells.

Abbreviation Nominal composition	**BET (m^2/g)**
BSCF $Ba_{0.5}Sr_{0.5}Co_{0.8}Fe_{0.2}O_{3-\delta}$	0.70
BSCFMo0.125-(Co/Fe=4) $Ba_{0.5}Sr_{0.5}Co_{0.7}Fe_{0.175}Mo_{0.125}O_{3-\delta}$	3.19
BSCFMo0.375-(Co/Fe=4) $Ba_{0.5}Sr_{0.5}Co_{0.5}Fe_{0.125}Mo_{0.375}O_{3-\delta}$	3.18
BSCFMo0.45-(Co/Fe= 10) $Ba_{0.5}Sr_{0.5}Co_{0.5}Fe_{0.05}Mo_{0.45}O_{3-\delta}$	3.02

Overall, the morphology and the surface area of the Mo-doped BSCF cells are very close and thus the differences observed for the ASR (*Section 3.3.3.1*) are mostly affected by their compositional differences.

3.3.3.3. Compatibility with electrolyte materials

The BSCFM compositions and the parent undoped BSCF were tested towards reactivity with the SDC electrolyte used for the fabrication of the symmetrical cells. For this experiment: (1) the powders, prior fabrication of symmetrical cells, were mixed by hand-grinding with 20%SDC ($Sm_{0.2}Ce_{0.8}O_2$, surface area: $20m^2/g$) in 1:1 ratio by weight, (2) uniaxially pressed of diameter 5mm into pellets and (3) the mixture was co-fired at 950°C/3h, imitating the thermal conditions for the preparation of the cells (*Section3.3.3.1*). The mixtures were then characterized by XRD and compared to the diffraction profiles of the raw BSCFM and SDC powders, also fired at the same conditions, in order to identify any reactivity products (*Figure 3.29*).

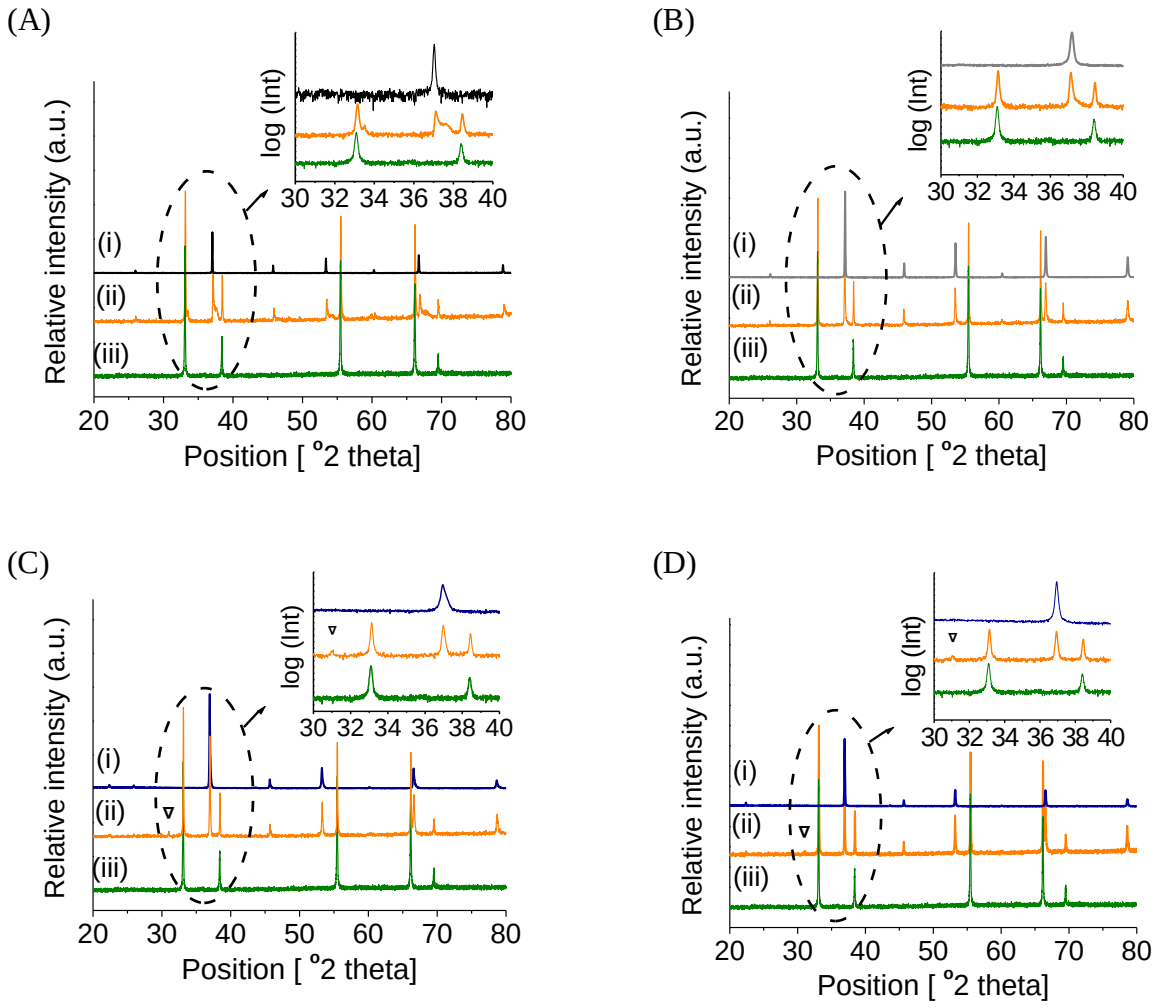

Figure 3.29: Reactivity study with the SDC electrolyte for (A) BSCF, (B) BSCFMo0.125-(Co/Fe=4), (C) BSCFMo0.375-(Co/Fe=4) and (D) BSCFMo0.45-(Co/Fe=10), showing XRD patterns at the 2theta range 20-80 of (i) the starting powders, (ii) the powder-SDC 1:1 mixtures,

in orange and (iii) SDC, in green, all fired at 950^{o}C for 3h imitating the conditions for fabrication of the symmetrical cells in this study. The insets provide magnification of the 2theta range 30-40 degrees, where the most significant changes in the XRD patterns appear.

The parent undoped BSCF compound was found clearly reacting with the electrolyte under the conditions tested (*Figure 3.29*A). The XRD pattern corresponding to the BSCF: SDC mixture after the thermal treatment (plot (ii) in orange) shows significant change in shape of the perovskite reflections compared to BSCF fired at the same conditions (plot (i), in black), here highlighted in the inset for the most intense perovskite peak at about 37 degrees. However, the perovskite phase is still present indicating just partial reactivity. Moreover, the shoulder in (ii) of the reflection corresponding to SDC at about 33 degrees compared to the raw SDC powder under the same thermal treatment (plot (iii), in green), demonstrates the change in the electrolyte pattern. Studies on mechanically mixed powders and co-fired at temperatures 900-1100^{o}C, have shown that the solid-state phase reaction between BSCF and SDC was negligible at 900^{o}C and becomes more significant at temperatures above 900 ^{o}C, which are necessary in order to obtain a compact attachment of a cathode material on the electrolyte. The reactivity of BSCF is limited at the interphase with the SDC electrolyte, forming (Ba,Sr,Sm,Ce)(Co,Fe)$O_{3-\delta}$ perovskite phases and becomes severe at T≥1100^{o}C and the perovskite phase is almost completely destroyed[219].

The reactivity of the 'SP' representative composition BSCFMo0.125-(Co/Fe=4) (*Figure 3.29B*) is improved compared to the undoped parent compound, as demonstrated by the lineshape of the most intense reflections corresponding to the perovskite and SDC patterns at about 37 and 33 degrees respectively. The dual 'SP/DP' compositions BSCFMo0.375-(Co/Fe=4) (*Figure 3.29*C) and BSCFMo0.45-(Co/Fe=10) (*Figure 3.29D*) do not show the reactivity products present when BSCF is reacting with SDC, but they show a low intensity $BaMoO_4$ impurity phase, which is not evidenced at the compounds heated at the same conditions without the SDC. The amount of $BaMoO_4$ present in the reactivity products of BSCFMo0.375-(Co/Fe=4) and BSCFMo0.45-(Co/Fe=10) was determined by Rietveld refinement to about 2% and 1% respectively. It is worth noticing though that the formation of $BaMoO_4$ was not observed for the actual BSCFMo0.375-(Co/Fe=4) cell heated at the same conditions (Chapter 5, *Section 5.1.1.4*), suggesting that the conditions of the reactivity test were more extreme. This indicates that at the actual symmetrical cells, the reactive sites are limited at the interface of the porous BSCFM cathode layer and the

dense SDC electrolyte and hence not affecting the bulk of the cathode material as in the case of the BSCFM: SDC mixtures studied during the reactivity experiments. However, in the long-term operation, the interface reactivity with the electrolyte might significantly affect the cathode performance.

3.4. Summary and Conclusions

As coming out from the study of a range of $Ba_{0.5}Sr_{0.5}Co_{0.8-x}Fe_{0.2-y}Mo_{x+y}O_{3-\delta}$ compositions, abbreviated as $BSCFMo_{x+y}$-(Co/Fe=0.8-x/0.2-y), when Mo^{6+} substitutes the valent-alterable transition metals Co and Fe the BSCF in the single perovskite (SP) structure, the SP phases were found to coexist with double perovskite (DP) domains, with increasing volume as the Mo content increases. The presence of the highly stable DP component in the SP/DP biphase compounds and the decrease in the overall Co content, are believed to result in the enhanced structural stability of the cubic phases in the Mo-doped BSCF compositions, compared to the parent un-doped compound and Co-containing cathodes, at conditions mimicking the long-term operation in a SOFC. The study of the effect of Mo incorporation in the BSCF series oxides on the cathode properties was based on four key selected BSCFM compositions. The properties of the Mo-doped BSCF compositions, abbreviated as BSCFMo0.125-(Co/Fe=4), BSCFMo0.375-(Co/Fe=4) and BSCFMo0.45-(Co/Fe=10) were studied thoroughly in order to establish the compositional and structural requirements for both good stability and performance as cathodes in SOFCs.

In the low Mo containing specimens (Mo, the introduction of Mo in the place of Co and Fe was accompanied with a decrease in the SP lattice parameters compared to the parent BSCF, as coming out from Pawley fits of the XRD patterns. For instance, the lattice parameters of BSCFMo0.125-(Co/Fe=4 with nominal composition $Ba_{0.5}Sr_{0.5}Co_{0.7}Fe_{0.175}Mo_{0.125}O_{3-\delta}$, is 3.97736(2), which is smaller than the refined value of 3.98538(3) Å for the parent un-doped BSCF, as expected by the substitution of the second-series transition metal Mo in the place of the first-series transition metals Co and Fe. The oxygen content in BSCFMo0.125-(Co/Fe=4) is approximately the same as the parent BSCF material, as established by the oxygen loss upon heating at 750^{o}C for 30min of 0.092 for both specimens. This demonstrates that the metal (Fe, Co) charge states are lowered compared to BSCF, due to charge balance considerations, upon substitution with the reduction tolerable d0 Mo^{6+}. The decrease in the oxidation states of the

valent-alterable transition metals Co and Fe causes the decrease in charge carriers, induced by the polaron-hopping between $(Co,Fe)^{4+}$ to $(Co/Fe)^{3+}$ upon heating. This results in the suppression of the metallic to semiconductor transition encountered in the BSCF at 650^{o}C and BSCFMo0.125-(Co/Fe=4) shows clearly semiconductor behavior at the temperature range 500-850^{o}C with associated activation energy for the polaron-hopping of 0.11 eV, which is larger than 0.074eV for the un-doped material. The decrease of the electrical conductivity in BSCFMo0.125-(Co/Fe=4) does not affect significantly the cathode properties compared to the parent BSCF, showing ASR values of 0.161 and 0.156 cm^{-2} respectively at 650^{o}C. However, this could be just an artifact, due to the limited porosity of the BSCF symmetrical cell compared to BSCFMo0.125-(Co/Fe=4) and the rest the Mo-doped BSCF cells, as determined by sorption measurements, and likely affecting the obtained ASR of the undoped compound.

Further increase in the Mo-content, with concomitant increase of the DP volume, results in an abrupt decrease of the oxygen content from 0.092 for the SP classified (BSCF and BSCFMo0.125-(C/Fe=4)) to 0.021 and 0.022 for BSCFMo0.375-(Co/Fe=4) and BSCFMo0.45-(Co/Fe=10) respectively, as established by the thermogravimetric analysis. This demonstrates that the number of mobile oxygen species is significantly reduced due to the presence of the DP, and demonstrates that the overall metal charge for Co and Fe in the 45% Mo^{6+} containing BSCFMo0.45-(Co/Fe=10), is lower compared to the Mo-poorer BSCFMo0.375-(Co/Fe=4). The reduced metal charges in BSCFMo0.45-(Co/Fe=0.45), leading to decreases number of metal charge carriers (M^{4+}/M^{3+}, where M: Co, Fe), seems to be the main reason for the decrease in the electrical conductivity of the BSCFMo0.45-(Co/Fe=10) to the very low values of 1.79 $S.cm^{-1}$ compared to the 15.97 $S.cm^{-1}$ obtained for BSCFMo0.375-(Co/Fe=4) at 700^{o}C. The conductivity values decrease linearly with the Mo content, including the 44.83 $S.cm^{-1}$ for the parent un-doped BSCF to 41.5 $S.cm^{-1}$ for BSCFMo0.125-(Co/Fe=4) at 700^{o}C. Hence no deviation was observed for BSCFMo0.45-(Co/Fe=10), which differs in Co/Fe ratio compared to the rest of the compositions studied, demonstrating no strong dependence on the Co/Fe ratio. On the contrary, the effect of the Co/Fe ratio seems to be important for the electrochemical properties, as measured by the ASR of symmetrical cells. The measured polarization resistance of BSCF, BSCFMo0.125-(Co/Fe=4) and BSCFMo0.375-(Co/Fe=4) area is in the range of 0.1-0.2 $\Omega.cm^{2}$ at 650^{o}C for all of them, whilst BSCFMo0.45-(Co/Fe=10) clearly stands out with observed ASR of

0.6 $\Omega.cm^2$ at 650^oC, that is three-times larger than the rest of the compositions studied. This suggests that the Co/Fe ratio affects more significantly the electrochemical performance than the overall Mo content, suggesting similar mechanism ORR for compositions with the same Co/Fe ratio, but different for compositions with differing Co/Fe, likely related to structural differences.

Overall, the compound with abbreviated composition BSCFMo0.375-(Co/Fe=4) shows the best electrochemical performance among the compositions studied, comparable with BSCF and better than LSCF and the GBCO, composites excluded. Moreover, BSCFMo0.375-(Co/Fe=4) does not suffer from the decomposition to hexagonal phases, encountered in the parent undoped BSCF and highly Co-containing cathodes, at conditions mimicking the long-term operation of IT-SOFC cathodes. Both these observations suggest that the SP and DP phases evidenced in BSCFMo0.375-(Co/Fe=4) act synergically to combine both good reactivity and stability. The optimal behavior of this composition compared to the rest of the Mo-BSCF specimens studied must be the interplay of the phases ratio, their composition and spatial arrangement. The structural analysis of the biphasic microstructure in BSCFMo0.375-(Co/Fe=4) is covered in Chapter 4 and more detail regarding its electrochemical performance is given in Chapter 5. In both cases, this is followed by a discussion about the main factors controlling the structure-properties relation; this is based on the rest of the BSCFM compounds and overall aims in getting a better understanding of the Mo-doped BSCF system.

4. STRUCTURAL CHARACTERISATION OF BSCFM OXIDES

Structural characterisation of BSCFM oxides

In order to understand better the structural features of the BSCFM system controlling the stability under conditions simulating the IT-SOFCs operation and electrochemical performance over oxygen reduction, the structural characterisation was primarily focused on the BSCFMo0.375-(Co/Fe=4) composition (*Section 4.1*), a biphasic SP/DP compound, which showed combined properties of enhanced stability and high activity as coming out from Chapter 3. The structural refinement of BSCFMo0.375-(Co/Fe=4) is discussed in Sections *4.1.1 to 4.1.3*. The refinement outcomes were correlated with information regarding Fe oxidation state by Mössbauer spectroscopy (*Section 4.1.4)* and oxygen content determination (*Section 4.1.5*), allowing derivation of Co oxidation state (*Section 4.1.6*). In addition, the evolution of the SP/DP biphasic assemblage with temperature is demonstrated in *Section 4.2*, based on variable temperature in-situ Synchrotron X-ray data (*Section 4.2.1*), allowing also the calculation of the thermal expansion coefficient of BSCFMo0.375-(Co/Fe=4) (*Section 4.2.3*). Quenching studies (*Section 4.2.2*) helped to obtain more information regarding the behavior of the SP and DP phases in BSCFMo0.375-(Co/Fe=4) with temperature.

The structural model developed for BSCFMo0.375-(Co/Fe=4) was used for the structural analysis of the rest BSCFM compounds (*Section 4.3)* in order to get some more understanding into the two phase segregation mechanism, with variables the Mo content (*Section 4.3.3*) and the Co/Fe ratio (*Section 4.3.4*). Finally, synthetic efforts to obtain a pure DP structure are covered in *Section 4.3.5*.

4.1. Structural analysis of BSCFMo0.375-(Co/Fe=4)

4.1.1. Difficulties

The main obstacle for the structural characterisation of BSCFMo0.375-(Co/Fe=4) is its biphasic nature. An additional degree of difficulty is introduced when considering the high overlapping Bragg reflections in the X-ray diffraction data, corresponding to the single (SP) and double (DP) perovskite phase components (Chapter 3, *Section 3.1.2.2.2*).

A joint Rietveld refinement using both X-ray (XRD) and Neutron (ND) diffraction data was performed for the structural analysis of BSCFMo0.375-(Co/Fe=4), in order to best combine the strengths of each diffraction technique. Given that the scattering power in XRD (scattering factor, *f*) is a simple function of atomic number (Z)[148, 220], this leads to the intrinsic difficulty to clearly distinguish between Co and Fe in the Ba-Sr-Co-Fe-Mo (BSCFM) system, as they have only one electron difference between them (*Table 4.1*). On the contrary, the neutron scattering factors (neutron scattering length, *b*) are a property of the atomic nucleus and do not vary in the systematic way that the equivalent *f* values do in the X-ray case[148, 220]. Hence ND is advantageous when aiming to distinguish atoms that have similar X-ray scattering powers, such as Co and Fe in the BSCFM system.

Table 4.1: Scattering factors of the B-site elements and oxygen in the BSCFM system, by X-ray (XRD) and neutron (ND) diffraction.

Element/ Scattering factor	**Bsite**			**O**
	Co	**Fe**	**Mo**	
XRD: atomic number (*Z*) [221]	26	27	42	8
ND: coherent scattering length (*b*, fm) [222]	2.49	9.450	6.715	5.803

However, the average scattering length of these elements (<*b*(Co,Fe>= 5.97 fm) is very close to the corresponding scattering length of Mo (*b*= 6.715 fm) (*Table 4.1*), which makes XRD data necessary for an accurate determination of the Mo content in each of the SP and DP phases. Moreover, ND is advantageous in locating light atoms which diffract X-rays weakly[148]. In the case of the BSCFM oxide materials, this becomes particularly useful for determining the oxygen

content. Oxygen, having atomic number Z=8, is a weak scatterer of X-rays but a relatively strong scaterrer of neutrons (b= 5.803 fm). The oxygen content in the each phase of the SP/DP biphase BSCFM materials could provide information about the functional role of each phase, as it could be related to the concentration of oxygen vacancies and the ionic conductivity. Despite the advantages of ND over XRD in the crystal structure refinement, the calibration of neutron diffractometers is much more complicated than for the X-ray diffractometers due to the instrumental setup[220]. This makes XRD stronger in the determination of accurate lattice parameters.

4.1.2. Model

The combined Rietveld analysis of ND and XRD data from BSCFMo0.375-(Co/Fe=4) was performed with a model of two discrete single (SP) and double (DP) perovskite crystallites in a single grain, as evidenced by dark field imaging TEM (Chapter 3, *Section 3.1.4.1*). This is an approximation as it averages over the interphase boundary volume between the two components.

Selective peak size broadening for the DP superstructure reflections, corresponding to odd combination of the Miller indices: h+k+l=2n+1, led to an improved agreement of the calculated profile with the observed data (*Figure 4.1*). The DP crystallites having the 'supercell' dimensions (lattice parameters $2a_p$), are double in unit cell compared to the SP crystallites for which the unit cell is also be referred to 'subcell' (lattice parameters a_p). The common reflections between the subcell and supercell, called fundamental reflections, overlapping strongly in the case of the biphasic SP/DP materials resulting from the substitution of Mo into the BSCF structure, as discussed in *Section 4.1.1*.

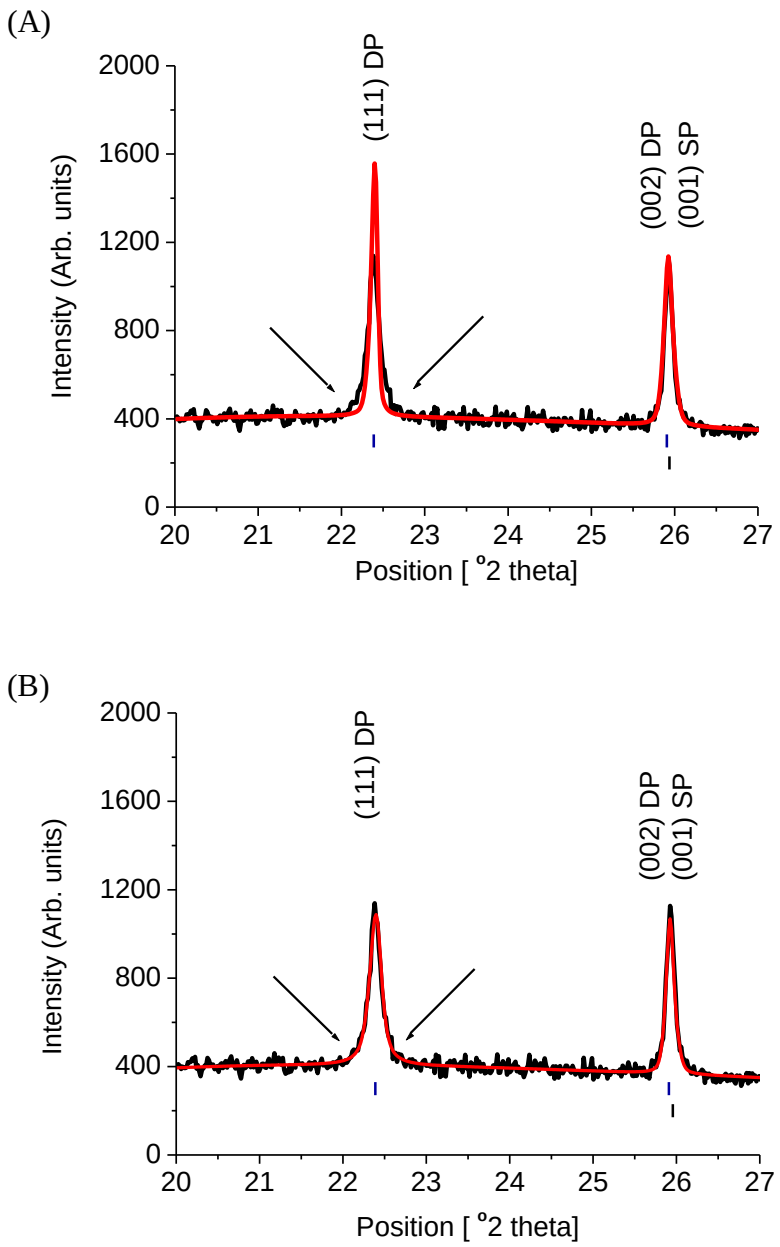

Figure 4.1: PXRD diffraction patterns of BSCFMo0.375-(Co/Fe=4), at the 2theta range 20-27°, highlighting the fitting of the reflections (A) without and (B) with applying selective peak broadening on the characteristic superstructure odd DP reflections, here shown for the (111)DP reflection. The blue and black tick marks show the allowed reflections for the DP and SP crystallites respectively.

The anisotropic line broadening of the diffraction data has been reported previously for pure double perovskite structures, such as Sr_2FeMoO_6[223], and has been associated with antiphase boundaries which are likely present in the highly DP containing BSCFMo0.375-(Co/Fe=4). The antiphase domain boundaries are three-dimensional lattice imperfections, such as stacking faults and twins[224], typical of several intermetallic systems undergoing disorder/order transformations[225], and separate incoherently diffracting domains within a DP crystal. These domain boundaries have a characteristic effect on the peak profiles, as they only broaden the fundamental reflections, whereas the superstructure reflections are unaffected[223, 225]. This can be explained by the allowed reflections of the DP model, as the characteristic odd superstructure peaks correspond only to the few coherently reflecting DP crystallites, free of antiphase boundaries, in the total volume of DP crystallites. According to the schematic illustration (*Figure 4.2*), a single grain of BSCFMo0.375-(Co/Fe=4) consists of SP and DP crystallites, with single and double unit cell respectively. Each DP crystallite may consist of either one coherently reflecting domain, or multiple incoherently reflecting domains, depending on the presence of antiphase boundaries.

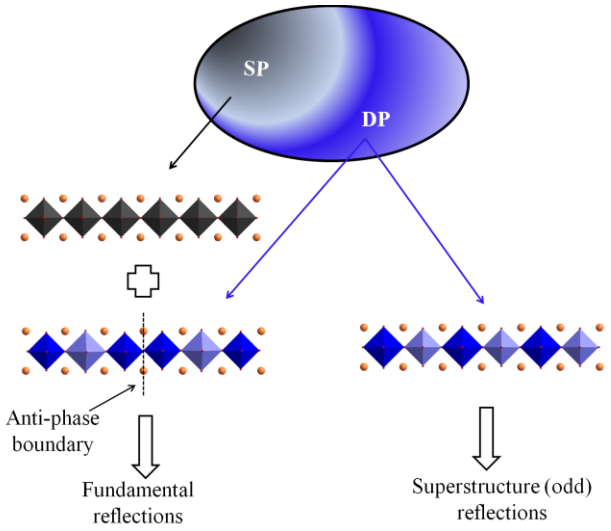

Figure 4.2: Schematic illustration of the adopted model for the Rietveld refinements, based on a single grain consisting of both simple (SP) and double perovskites (DP) units. The B-site in each SP crystallite consists of disordered BO_6 octahedra (dark grey), where B: Co, Fe and Mo and red spheres represent the oxygen atoms. The DP crystallites are B-site ordered with alternating B_1O_6 (blue) and B_2O_6 (light blue) octahedra of different compositions. For all, the A cations: Ba, Sr (yellow spheres), occupy the center positions created by the corner sharing octahedra.

The line broadening induced by the instrument was refined with a Silicon (Si SRM 640c) standard, providing the measured instrumental profile function consisiting of Lorentzian, Gaussian and axial divergence components. Standard pseudo-Voigt profile functions were used to determine the crystallite size of the fundamental reflections corresponding to the SP and DP phases respectively. For the latter, the profile parameters for the superstructure odd reflections were selectively refined and represent the coherent volume weighted size of the DP crystallites free of antiphase boundaries.

4.1.3. Outcomes of the joint refinement*

Combined Rietveld refinement for BSCFMo0.375-(Co/Fe=4) was performed on XRD data collected on the Panalytical X-pert Pro and ND data from the backscattering and 90° banks of HRPD, with the model of two discrete simple (SP) and double (DP) perovskite phases, crystallizing in Pm3m and Fm3m respectively, as described in *Section 4.1.2*. The nominal cation composition, as confirmed by EDS (Chapter 3, *Section 3.1.3*), was used to restrain the refinement with penalties applied if the total B site composition (summed over the SP and DP phases) deviated from the given value of $Co_{0.5}Fe_{0.125}Mo_{0.375}$. The weighting of the penalty was significantly reduced, but not completely removed, during the final stages of the refinement which produced a refined global composition of $Ba_{0.5}Sr_{0.5}Co_{0.500(3)}Fe_{0.125(1)}Mo_{0.375(3)}O_{2.94(1)}$.

The occupancy of the SP B-site and the two DP B-sites were initially refined allowing for simultaneous occupation by Co, Fe and Mo with penalties introduced for total site occupancies ≠ 1. For the DP, one site refined to mainly Co, with some Fe, while the other site refined to mainly Mo, with some Fe. For the final refinement, the site occupancy penalties were removed and site mixing of the form $Co_{1-x}Fe_x$ and $Mo_{1-y}Fe_y$ were refined for the two DP-B sites, whereas a three-way hard constraint [226] was used for the SP B-site occupancies. The occupancies of the A-site cations in both phases were not refined and fixed to the nominal values of $Ba_{0.5}Sr_{0.5}$. The thermal displacement parameters for cations occupying the same site within a phase were constrained to be equal.

∗ This work would not have been possible without help from Dr. P. Chater, Dr.Y. Breard and Dr.A. Demont.

Final refinements and reliability factors for all histograms are shown in *Figure 4.3*(XRD) and *Figure 4.4* (ND-backscattering bank); the ND-90^{o} bank is shown in Appendix B. Refined parameters and bond lengths for both perovskite phases are given in *Table 4.2*.

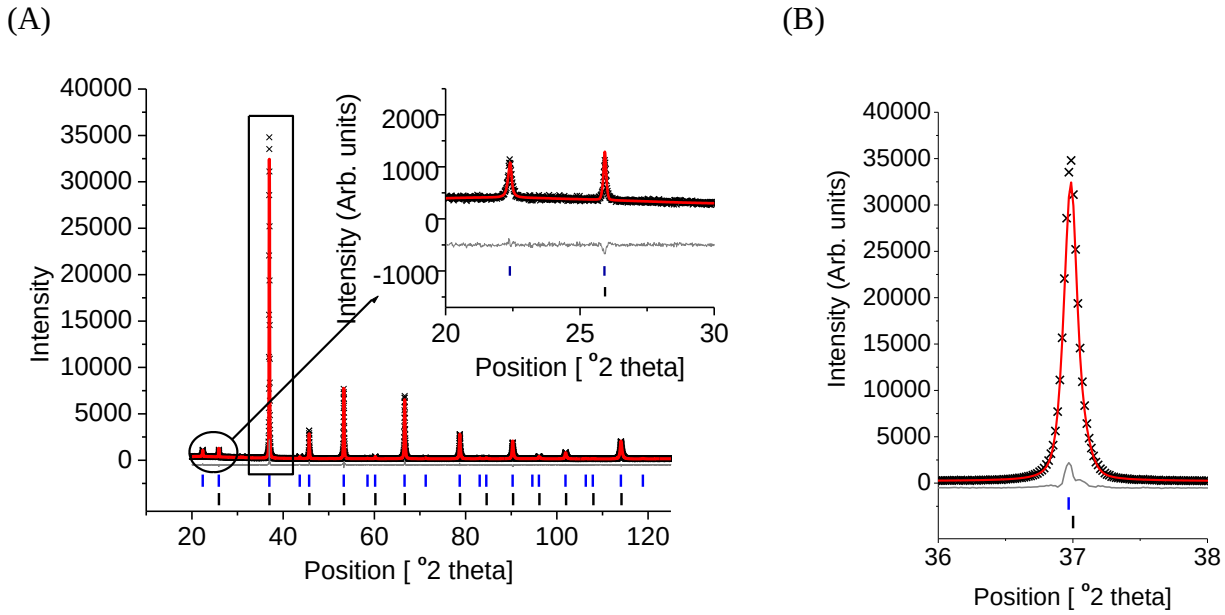

χ^2= 2.02, R_{exp}= 5.602%, R_{wp}= 7.960%, R_{Bragg}(SP)=3.80%, R_{Bragg}(DP)= 4.62%

Figure 4.3: (A) Observed (black), calculated (red) and difference (grey) plots of Rietveld fit against room temperature XRD data for $Ba_{0.5}Sr_{0.5}Co_{0.5}Fe_{0.125}Mo_{0.375}O_{3-d}$ (BSCFMo0.375-(Co/Fe=4)) using the structural model the structural model of a SP and a DP phase crystallising in space groups $Pm\bar{3}m$ and $Fm\bar{3}m$, with the black and blue tick marks showing the allowed reflections respectively. In the inset, magnification of the 2theta range 20-30, (B) magnification of the 2theta range 36-38^{o} focusing on the fit of the main perovskite reflection.

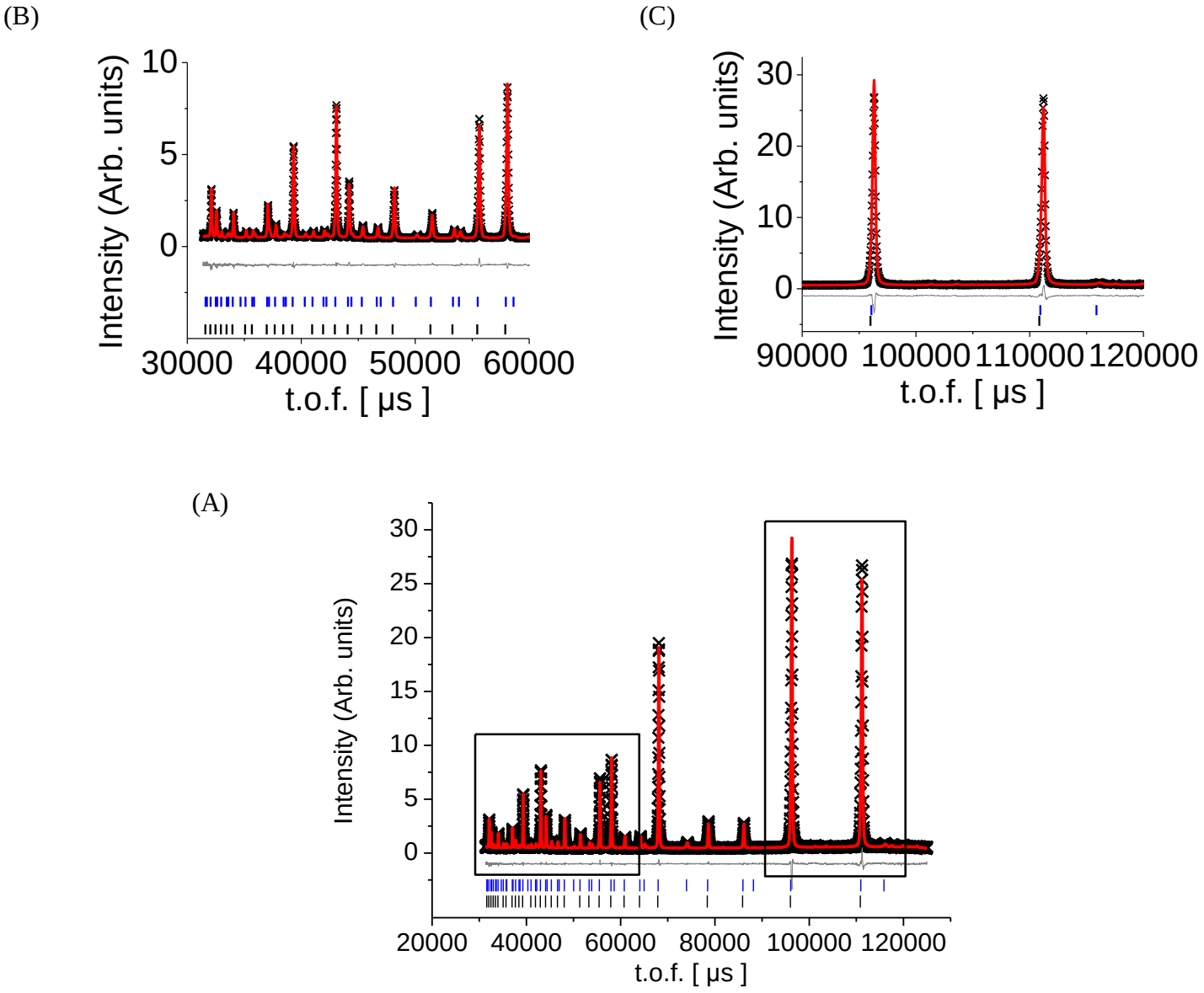

χ^2= 1.82, R_{exp}= 2.798%, R_{wp}= 6.643% , R_{Bragg}(SP)=1.30%, R_{Bragg}(DP)= 1.97%

Figure 4.4: (A) Observed (black), calculated (red) and difference (grey) plots of Rietveld fit against room temperature ND data at the backscattering bank for $Ba_{0.5}Sr_{0.5}Co_{0.5}Fe_{0.125}Mo_{0.375}O_{3-d}$ *(BSCFMo0.375-(Co/Fe=4) using the structural model the structural model of a SP and a DP phase crystallizing in space groups* $Pm\bar{3}m$ *and* $Fm\bar{3}m$*, with the black and blue tick marks showing the allowed reflections respectively, (B) magnification of the t.o.f. range 30,000-60,000 μs, showing the fit of lower intensity reflections and (C) magnification of the t.o.f. range 90,000-120,000 μs, focusing on the fit of the most intense perovskite reflections.*

Table 4.2: *Atomic coordinates and metal-oxygen (M-O) bond lengths from Rietveld refinement of BSCFMo0.375-(Co/Fe=4) with nominal composition* $Ba_{0.5}Sr_{0.5}Co_{0.5}Fe_{0.125}Mo_{0.375}O_3$.

Phase 1 – DP:
$BaSrCo_{0.961(2)}Fe_{0.142(2)}Mo_{0.897(3)}O_{5.95(3)}$
$Fm\bar{3}m$ (space group number 225)

Weight fraction 70.81(10) %
a = 7.9812(2) Å

Atom	multiplicity	x	y	z	B_{iso} (Å^2)	occupancy
Ba	8c	0.25	0.25	0.25	0.57(2)	0.5
Sr	8c	0.25	0.25	0.25		0.5
Mo	4b	0.5	0.5	0.5	0.08(2)	0.897(2)
Fe1	4b	0.5	0.5	0.5		0.103(2)
Co	4a	0	0	0	0.41(6)	0.961(1)
Fe2	4a	0	0	0		0.039(1)
O	24e	0.2585(8)	0	0	0.62(2)	*0.991(3)*

Phase 2 – SP:
$Ba_{0.5}Sr_{0.5}Co_{0.547(9)}Fe_{0.253(2)}Mo_{0.200(8)}O_{2.81(3)}$
$Pm\bar{3}m$ (space group number 221)

Weight fraction: 28.13 (9) %
a =3.9844(1) Å

Atom	multiplicity	x	y	z	B_{iso} (Å^2)	occupancy
Ba	1a	0	0	0	0.69(5)	0.5
Sr	1a	0	0	0		0.5
Mo	1b	0.5	0.5	0.5	0.60(6)	0.200(8)
Fe	1b	0.5	0.5	0.5		0.253(1)
Co	1b	0.5	0.5	0.5		0.547(8)
O	3c	0.5	0.5	0	0.98(6)	0.936(7)

Phase 1 – DP

Bond	n × bond length (Å)	B.V.S.
(Ba/Sr) - (O)	11.892 × 2.82243(4)	Ba / Sr : 2.78 / 1.77
(Mo/Fe1) - (O)	5.946 × 1.9353(11)	Mo / Fe1 : 5.51 /3.69
(Co/Fe2) - (O)	5.95 × 2.0553(11)	Co / Fe2 : 2.22 / 2.67

Phase 2 – SP

Bond	n × bond length (Å)	B.V.S.
(Ba/Sr) - (O)	11.232 × 2.81743(5)	Ba / Sr : 2.66 / 1.70
(Co/Fe/Mo) - (O)	5.616 × 1.99222(2)	Co / Fe / Mo : 2.49/ 2.99 / 4.46

Global refined composition: $Ba_{0.5}Sr_{0.5}Co_{0.500(3)}Fe_{0.125(1)}Mo_{0.375(3)}O_{2.94(1)}$

Global Rietveld Statistics: $\chi^2 = 2.28$, $R_{exp}=2.285\%$, $R_{wp}= 3.456\%$

The refinement (*Table 4.2*) shows that BSCFMo0.375-(Co/Fe=4) is higher in DP content, with 70.81(10) % DP by weight compared to 28.13(9) % for the SP component. In addition to the main two perovskite phases, 1.06(8) % weight fraction $BaMoO_4$ is present. The SP and DP have closely related a_p and $2a_p$ unit cell parameters with derived a_p = 3.9844(1) Å and 3.9906(1) Å ($2a_p$ = 7.9812(2) Å) respectively. The SP, with refined composition $Ba_{0.5}Sr_{0.5}Co_{0.547(9)}Fe_{0.253(2)}Mo_{0.200(8)}O_{2.81(3)}$ is Mo-deficient and Fe-rich with respect to the global composition, with a significant O vacancy concentration. The refined DP composition of $BaSrCo_{0.961(2)}Fe_{0.142(2)}Mo_{0.897(3)}O_{5.95(3)}$, which can also be written as $Ba_{0.5}Sr_{0.5}Co_{0.480(1)}Fe_{0.071(2)}Mo_{0.449(2)}O_{2.98(2)}$ according to the ABO_3 general perovskite formula, is enriched in Mo compared to the global composition and stoichiometric in oxygen. There are two B- antisites in the DP component; a Mo-rich and a Co-rich site with site compositions $Mo_{0.897(2)}Fe_{0.103(2)}$ and $Co_{0.961(1)}Fe_{0.039(1))}$ respectively (*Figure 4.5*).

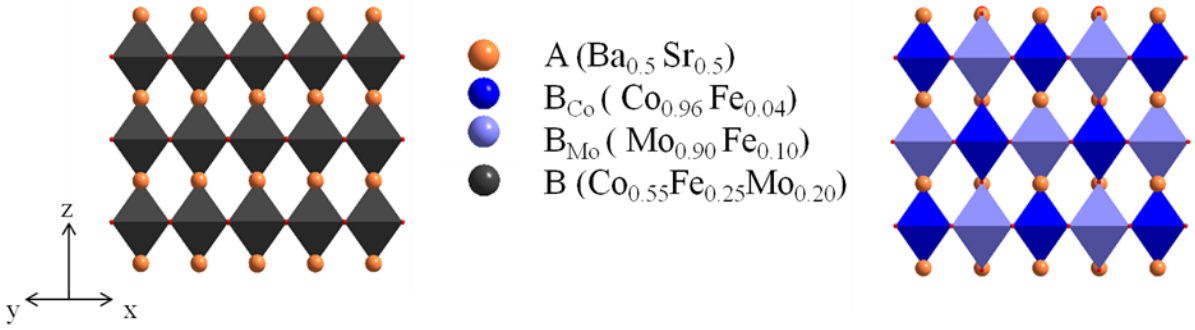

Figure 4.5: The structure of (A) the SP phase with refined composition $Ba_{0.5}Sr_{0.5}Co_{0.547(9)}Fe_{0.253(2)}Mo_{0.200(8)}O_{2.81(3)}$, viewed along the [11 □0] direction, highlighting that there is a single octahedral site (dark grey) and (B) the DP phase with refined composition $BaSr(Co_{0.961(1)}Fe_{0.039(1)})(Mo_{0.897(2)}Fe_{0.103(2)})O_{5.95(3)}$ as established from the combined refinements, viewed along the same [1$\bar{1}$0] direction showing the cation ordering on the octahedral B sites, which produces separate columns of distinct composition (Co-rich site (dark blue) and Mo-rich site(light blue)).

The analysis of the metal-oxygen (M-O) bond lengths and derived bond valence sum (B.V.S.) (*Table 4.2*) gives more insight in the segregation mechanism at a crystallographic level. In the DP Mo-rich B-site, the short bond lengths of 1.9353(11) Å favours the incorporation of the small and highly oxidized Mo^{6+} with bond valence sum (B.V.S.) calculations giving a formal oxidation state of 5.51. The other DP B-site, with six longer M-O distances of 2.0553(11) Å favours the incorporation of the largest and most reduced Co^{2+} with a B.V.S. of 2.22. From these calculations, interatomic distances on these two DP sites would require the presence of iron

either on a highly oxidized state (3.69) for the smallest Mo-rich site or in a reduced state (2.67) not favourable under ambient conditions on the Co-rich site, leading to the Fe-poor content in the DP. In contrast, on the unique B-site of the SP, the metal-oxygen distance of 1.99222(2) Å lead to a B.V.S. of 2.99 for Fe, favouring the incorporation of Fe^{3+}, hence the observation of a richer content relative to the nominal and DP compositions. In comparison, this SP site is less favourable to Mo^{6+}, with a B.V.S. of 4.46, in agreement with the poor Mo content while the value of 2.49 suggest the presence of Cobalt in a 2+/3+ mixed valence state.

The combination of both perovskite structures also generates two different A-sites. The SP hosts a mixture of Ba and Sr with metal-oxygen distances of 2.81743(5) Å that is very close to the 2.82273(4) Å observed in the equivalent DP site, demonstrating that the Ba/Sr composition is very similar in the two perovskite structures. The valence states for Ba/Sr are 2.66 / 1.70 and 2.78 / 1.77 for SP and DP respectively, by resulting formally in an over bonded Ba^{2+} and an under bonded Sr^{2+} on the average structures, as mixed valence is not expected.

The diffraction-derived SP and DP volume weighted crystallite sizes for BSCFMo0.375-(Co/Fe=4) were 144(6) nm and 217(9) nm respectively. The size of the DP crystallites, free of anti-phase boundaries, was refined to 66(9) nm, as derived from the odd superstructure reflections. These diffraction-derived values are in the nanometer scale as seen in DF TEM. However, given that the crystallite size estimation by diffraction is related to the volume of matter that scatters, the direct correlation with the number weighted derived TEM crystallite sizes (Chapter 3, *Section 3.1.4.3, Figure 3.20*), is not possible without knowing the exact crystallite shape.

4.1.4. Determination of Fe oxidation state by Mössbauer spectroscopy*

The estimated Fe valence state in BSCFMo0.375-(Co/Fe=4) was verified with ^{57}Fe Mössbauer spectroscopy (MS, *Figure 4.6*). The observed spectrum was fitted with two Fe^{3+} components, both with an isomer shift of 0.389(2) mm s^{-1}. No evidence for the presence of Fe^{2+} or Fe^{4+} valence states was observed above the detection limit of the apparatus (~2%). The major component (77(2) %) was fitted to a quadrupole-split doublet, consistent with a Fe^{3+} ion without magnetic ordering. The minor component (23(2) %) was fitted to a relatively broad sextet, consistent with a magnetically ordered Fe^{3+} state. The broadness of the peaks due to the minor magnetic Fe^{3+} state is indicative of small magnetically ordered regions.

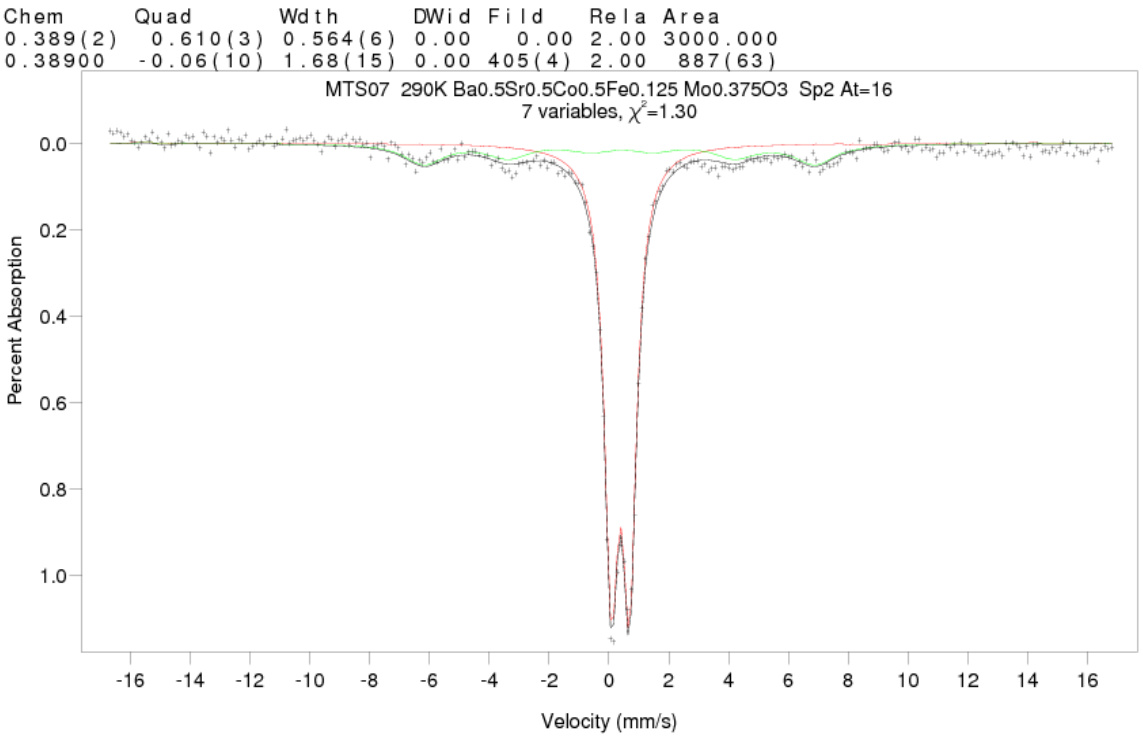

Figure 4.6: ^{57}Fe Mössbauer spectrum (MS) of BSCFMo0.375-(Co/Fe=4) showing the observed data (black crosses) and calculated fit (black line). Individual components of the calculated fit corresponding to the majority (77(2)%) Fe^{3+} quadrupole-split doublet (non magnetically ordered) and to the minority (23(2)%) Fe^{3+} sextet (magnetically ordered) are shown in red and green, respectively. These Mössbauer data show the Fe in BSCFMo0.375-(Co/Fe=4) is present as Fe^{3+}.

∗ The Mössbauer work was done by Dr. M.Thomas.

The determination of the overall Fe charge in BSCFMo0.375-(Co/Fe=4) as Fe^{3+} is thus lower than the Mössbauer determined charge for the BSCF parent compound (Appendix A), for which Fe was found in a mixed valence of approximately 61%Fe^{3+} and 39% Fe^{4+}, giving overall valence of +3.3, in agreement with the literature for BSCF[227]. The Fe distribution within BSCFMo0.375-(Co/Fe=4), as determined by Rietveld refinement (*Section 4.1.3*), is 52 mol_{Fe}% SP ($Ba_{0.5}Sr_{0.5}Co_{0.547(9)}Fe_{0.253(2)}Mo_{0.200(8)}O_{2.81(3)}$, 28.13(9) weight%) and 48 mol_{Fe}% DP ($BaSrCo_{0.961(2)}Fe_{0.142(2)}Mo_{0.897(3)}O_{5.95(3)}$, 70.81(10) weight%). The low Fe concentration of the DP phase means that the DP is unlikely to be magnetically ordered, and so contributes only to the non-magnetic component of the MS(77(2)% quadrupole-split doublet). The higher Fe concentration within the SP phase means that the SP can be attributed to the minority (23(2)%) magnetic Fe environment observed in the MS. The magnetic component of the MS (23(2)%) alone cannot account for all of the SP present in the sample (52 mol_{Fe}%). The SP phase is therefore assigned as consisting of both small magnetically ordered Fe^{3+} clusters and non-magnetic, independent Fe^{3+} environments, which is consistent with Fe^{3+} making up only 25.3(2)% of the B-site cations. The information obtained from the MS spectrum are summarised in *Table 4.3*.

Table 4.3: Information obtained from the ^{57}Fe Mössbauer spectrum (MS) of BSCFMo0.375-(Co/Fe=4) including the isomer shift, fit components, fit area, calculated % fit areaand assignment to the fitting components.

Isomer shift ($mm\ s^{-1}$)	**Fit**	**Area**	**Area (%)**	**Assigned to**
0.389(2)	quadrupole-split doublet (non magnetically ordered)	3000	77(2)	Fe^{3+} in DP and SP
0.38900	Sextet (magnetically ordered)	887(63)	23(2)	Fe^{3+} in SP

4.1.5. Oxygen content

The determination of the oxygen content of a solid is not easy and the most accurate methods for establishing precisely the initial oxygen contents of oxides at room temperature are based on redox reactions. A generally applicable indirect method is the 'hydrogen reduction thermogravimetric analysis', which is based on heating a specimen in a reducing atmosphere and, provided that the products are known, determine the oxygen content from the weight change in reduction. Moreover, iodometric titrations are often used for substances containing mixed valence elements, such as cobalt and iron in our case. [148, 228]

4.1.5.1. Reduction in hydrogen

The total reduction of the transition metals in BSCFMo0.375-(Co/Fe=4) to metals with oxidation state of (0), was studied by thermogravimetric analysis by heating at 1100°C/10h in a mixture of 50ml/min 5% H_2/N_2 and 80ml/min N_2 as the carrier gas. The sample was initially heated at 150°C/3h for the removal of moisture.

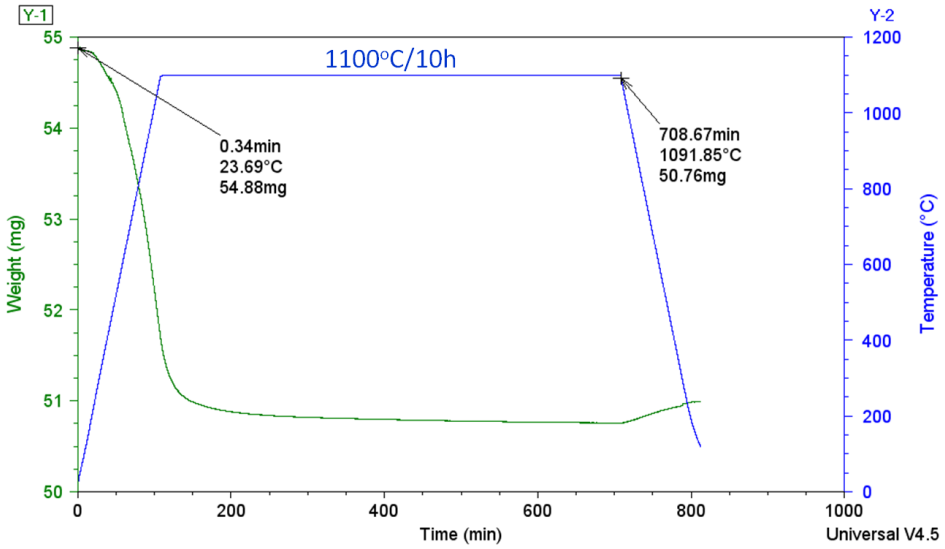

Figure 4.7: Thermogravimetric analysis (TGA) showing the weight loss of BSCFMo0.375-(Co/Fe=4) after heating at 1100°C for 10h in reducing conditions (in a mixture of 50ml/min 5% H_2/N_2 and 80ml/min N_2 as the carrier gas)

After the annealing at the reduced atmosphere (*Figure 4.7*), there was 4.12 mg of weight loss for initial mass of m_o= 54.88mg, corresponding to the reduction reaction of $Ba_{0.5}Sr_{0.5}Co_{0.5}Fe_{0.125}Mo_{0.375}O_{3-\delta}$ to $Ba_{0.5}^{2+}Sr_{0.5}^{2+}Co_{0.5}^{x}Fe_{0.125}^{y}Mo_{0.375}^{z}O_{red}^{2-}$, where $[O_{red}]$ is

calculated according to charge balance. For total reduction of all transition metals to their metal state, i.e. x= y=z=0, the oxygen content of the reduced sample ([O_{red}]) is calculated to be 1.

The oxygen content [O] of $Ba_{0.5}Sr_{0.5}Co_{0.5}Fe_{0.125}Mo_{0.375}O_{3-\delta}$ (BSCFMo0.375-(Co/Fe=4)) at room temperature in air is calculated according to *Equation 4.1*.

$$[O] = [Ored] + \left(\frac{m_o - m_{red}}{16}\right) \Big/ \frac{m_{red}}{Mw_{red}} \qquad \textit{Equation 4.1}$$

where [Ored] the oxygen content of the reduced sample $Ba^{2+}_{0.5}Sr^{2+}_{0.5}Co^{x}_{0.5}Fe^{y}_{0.125}Mo^{z}_{0.375}O_{red}^{2-}$ with x=y=z=0 for total reduction, $\left(\frac{m_o - m_{red}}{16}\right)$ denotes the number of moles that are reduced normalised by the number of moles ($\frac{m_{red}}{Mw_{red}}$) of the reduced material.

However, according to the XRD analysis (*Figure 4.8*) of the post-reduction specimen, complete reduction of BSCFMo0.375-(Co/Fe=4) was not achieved.

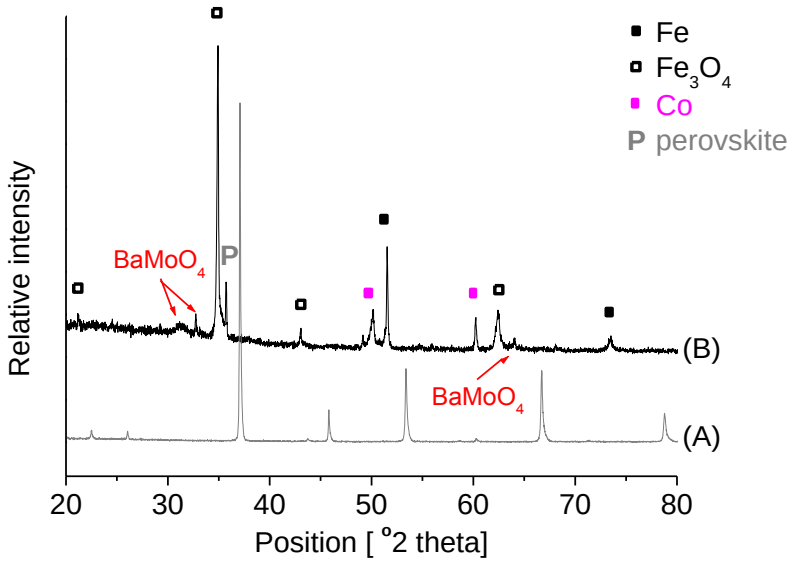

Figure 4.8: XRD pattern of BSCFMo0.375-(Co/Fe=4) sample (A) before and (B) after annealing at 1100°C for 10h in 5%H_2/N_2, showing the decomposition products.

The oxidation states of the transition metals vary, with cobalt mostly found as Co (0) and Fe in the form of Fe_3O_4 and Fe (0). The most intense reflection of a perovskite phase is still present but shifted indicating change in the lattice parameters due to compositional changes, whilst there is also some small amount of amorphous $BaMoO_4$, which is the evidence of some amount of Mo^{6+}. There is no evidence of the Ba, Sr binary oxides, suggesting that they are either in the form of amorphous hydroxides as the alkalines in BSCF have great tendency to absorb moisture[69], or that they occupy the A-site of the survived perovskite phase. The remaining amount of Mo is likely to form the B-site of the perovskite phase with oxidation state of Mo^{4+}, since $BaMo(IV)O_3$ and $Sr(IV)O_3$ are reported to be very stable compounds in reduced atmospheres[229] .

According to thermodynamic analysis, the reduction of the transition metals, occurs only if $\Delta G_{reaction} < O$, where $\Delta G_{reaction}$ is the calculated free Gibbs energy for the reduction reactions by oxidization of H_2 (*Table 4.4*). The data for free energy of reduction of the binary oxides were derived from Ellingham diagrams [230]at the temperature of the reduction experiment (1100^{o}C).

Table 4.4: Calculation of the free Energy Gibbs ($\Delta G_{reaction}$) for the reduction reactions of the transition metal oxides in BSCFMo0.375-(Co/Fe=4), in the form of binary oxides, by H_2 ($2\ H_2 + O_2 \leftrightarrow 2\ H_2O$, ΔG_f = 342.37 kJ) at 1100^{o}C and 0.21 atm. The thermodynamic data were derived from Ellingham diagrams[230].

Reduction	Reaction	$\Delta G_{reaction}$(kJ/mol)
$Co^{3+/4+} \rightarrow Co^{2+}$	$2\ Co_3O_4 + 2\ H_2 \leftrightarrow 6\ CoO + 2\ H_2O$	-382.57
$Co^{2+} \rightarrow$ Co (0)	$2\ CoO + 2\ H_2 \leftrightarrow 2\ Co + 2\ H_2O$	-68.77
$Co^{3+/4+} \rightarrow$ Co (0)	$Co_3O_4 + 4\ H_2 \leftrightarrow 3\ Co + 4\ H_2O$	-588.88
$Fe^{3+} \rightarrow Fe^{2+/3+}$	$6\ Fe_2O_3 + 2\ H_2 \leftrightarrow 4\ Fe_3O_4 + 2\ H_2O$	-229.74
$Fe^{2+/3+} \rightarrow Fe^{2+}$	$2\ Fe_3O_4 + 2\ H_2 \leftrightarrow 6\ FeO + 2\ H_2O$	-61.48
$Fe^{3+} \rightarrow Fe^{2+}$	$2\ Fe_2O_3 + 2\ H_2 \leftrightarrow 4\ FeO + 2\ H_2O$	-352.7
$Fe^{2+} \rightarrow$ Fe(0)	$2\ FeO + 2\ H_2 \leftrightarrow 2\ Fe + 2\ H_2O$	+5.1
$Fe^{3+} \rightarrow$ Fe(0)	$Fe_2O_3 + 6\ H_2 \leftrightarrow 6\ Fe + 6\ H_2O$	-322.1
$Mo^{6+} \rightarrow Mo^{4+}$	$2\ MoO_3 + 2\ H_2 \leftrightarrow 2\ MoO_2 + 2\ H_2O$	-242.57
$Mo^{4+} \rightarrow$ Mo(0)	$MoO_2 + 2\ H_2 \leftrightarrow Mo + 2\ H_2O$	+6.14
$Mo^{6+} \rightarrow$ Mo(0)	$2\ MoO_3 + 6\ H_2 \leftrightarrow 2\ Mo + 6\ H_2O$	*-230.4*

The reduction of $Co^{3+/4+}$ to Co (0) is thermodynamically favourable (ΔG = -588.88 kJ/mol), with the intermediate step to Co^{2+} also favored under the conditions of the experiment. The total

reduction of $Fe^{3+}$to Fe(0), with intermediate reductions to $Fe^{2+/3+}$ and Fe^{2+} , also gives negative value of $\Delta G_{reaction}$ (ΔG = -322.1 kJ/mol) and explains the fact that Fe(0) is observed in the PXRD pattern of BSCFMo0.375-(Co/Fe=4) after the reduction experiment. The relatively low energy barrier for the thermodynamically disfavored reduction of Fe^{2+} to Fe (0) (ΔG = +5.1 kJ/mol > O) in the case of binary oxides can differ in the case of perovskite oxides and become even favorable. Another possible explanation for the observed Fe(O) content in the XRD pattern of the reduced material could be that the highly favorable reaction of Fe^{3+} to Fe^{2+} (ΔG = -352.7 kJ) promotes the reduction of Fe^{2+} to Fe (0).

One might expect that the total reduction of Mo^{6+} to Mo (0) (ΔG = -230.4 kJ/mol) would also occur similarly to the Fe case, by surpassing the energy barrier for the slightly thermodynamically disfavored reduction of $Mo^{4+}$to Mo(0) (ΔG = +6.14 kJ). However, reduction to Mo(0) was not observed, suggesting that the Mo^{4+}-containing perovskite phase formed at the end of the reduction has a very high lattice energy and the energy released by the reduction to Mo^{4+} is not sufficient to overcome this energy barrier and promote the reduction to Mo(0). Whilst in the diffraction pattern there are also reflections indexed to (Ba,Sr)MoO_4, where Mo is in its hexavalent state, the relative intensities suggest that amount of this phase is small and hence Mo is considered to exist mostly as Mo^{4+} in the perovskite phase surviving after the reduction experiment. Finally, the fact that both $Fe^{2+/3+}{}_3O_4$ and Fe (0) are indexed in the PXRD pattern, with no evidence of the intermediate $Fe^{2+}O$, suggests that the highly stable Mo containing perovskite phase might also consist of some amount of $Fe^{2+/3+}{}_3O_4$ which cannot obtain the required energy for reduction to Fe(0). The oxygen content of BSCFMo0.375-(Co/Fe=4) was then calculated (*Equation 4.1*), based on the identified oxidation states by XRD and confirmed by the thermodynamic considerations, of Co(0), Mo^{4+} and a mix valence of Fe between Fe_2O_3 and Fe(0).

Table 4.5: Oxygen content ([O]) based on the reduction experiment of BSCFMo0.375-(Co/Fe=4) in 5%H_2/N_2 at 1100^oC for 10h, using oxidation states of Co(0), Mo^{4+} and considering different cases for the Fe charge, as coming out from the concordant outcomes of XRD analysis of the post-reduction sample and thermodynamic considerations.

Case	Co(x)	Fe(y)	Mo(z)	**[O]**
1	0	2+/3+	4+	2.998
2	0	0	4+	2.830
3	0	2+/3+ 0	4+	2.914

Three different cases of the oxidation state of Fe (y) were considered, $Fe^{2+/3+}$ (case 1), Fe (0) (case 2) and a 1:1 mixture of $Fe^{2+/3+}$ and Fe (0) (case 3), giving oxygen contents of 2.998, 2.830 and 2.914 respectively. Case 3 is more consistent with the observations from the diffraction pattern as both $Fe^{2+/3+}{}_3O_4$ and Fe (0) were identified and gives an oxygen content of 2.914.

4.1.5.2. Iodometric titration

Iodometric titrations were also performed to determine the oxygen content in BSCFMo0.375-(Co/Fe=4). Approximately 40 mg of material was dissolved in 20 ml of 3M HCl with an excess of KI. Upon complete dissolution, the solution was titrated with 0.1M sodium thiosulphate ($Na_2S_2O_3$). Prior the titrations, the $Na_2S_2O_3$ solution was standardised by titrating it against potassium iodate (KIO_3) dissolved in distilled water with potassium iodide (KI) and 1 Molar sulphuric acid (H_2SO_4) and its normality was calculated to 0.10105(8) N *(Table 4.6)*. As Na_2S_2O3 is added the solution turned from orange to colourless; starch solution was added just before the end point, where the solution turns from dark purple to clear. Titrations were repeated three times to ensure an accurate and reproducible result. The method is described in more detail in Chapter 2, *Section 2.6*.

Table 4.6: Calculations for determination of the normality of the standardised $Na_2S_2O_3$ solution used for the iodometric titration of BSCFMo0.375-(Co/Fe=4). The mean normality value was calculated to be 0.10105±0.00008N.

Titration	**m (KIO_3)**	**m (KI)**	**V($Na_2S_2O_3$)**	**Normality (N)**
1	0.0485	0.5138	13.45	0.10110
2	0.0442	0.522	12.25	0.10116
3	0.0493	0.5264	13.7	0.10089

The oxygen content ([O]) of BSCFMo0.375-(Co/Fe=4) is directly linked with the oxidation states of the multivalent transition metals (Co and Fe). Iron is in its trivalent state as coming out from the Mossbauer determination, whilst cobalt in the parent BSCF is in a mixture of $Co^{3+/4+}$ (Appendix A and [227]) and is expected to contain more divalent character due to the reduction imposed by the presence of Mo^{6+}. Under the conditions of the titration, all the trivalent cations (Co and Fe) get reduced to 2+ according to *Equation 4.2*. Under the mild reducing conditions of the iodometric titration, the divalent cations, are not further reduced[228], as well as Mo^{6+} ions remain in the hexavalent state[135]. Hence, $Ba_{0.5}Sr_{0.5}(B^{3+})_{0.625}Mo_{0.375}O_y$ is reduced to $Ba_{0.5}Sr_{0.5}(B^{2+})_{0.625}Mo_{0.375}O_{red}$, where [Ored] the oxygen content of the reduced sample which according to charge balance is equal to 2.75. According to stoichiometry (*Equation 4.3* and *Equation 4.4*), the number of moles of the reducing trivalent cations (n_{B3+}) corresponds to the half of the $S_4O_6^{2-}$moles titrated (n ($S_4O_6^{2-}$) = CxV= 2 n_{B3+}). The oxygen content ([O]) of the sample is then given by *Equation 4.5*.

BSCFMo0.375-(Co/Fe=4) = $Ba_{0.5}Sr_{0.5}Co_{0.5}Fe_{0.125}Mo_{0.375}O_{3-\delta}$

$$Ba_{0.5}Sr_{0.5}(B^{3+})_{0.625}Mo_{0.375}O_y \rightarrow Ba_{0.5}Sr_{0.5}(B^{2+})_{0.625}Mo_{0.375}O_{red} \qquad \textit{Equation 4.2}$$

$$2\ B^{3+} + 2I^- \leftrightarrow 2\ B^{2+} + I_2 \qquad \textit{Equation 4.3}$$

$$I_2 + 2\ S_2O_3^{2-} \leftrightarrow 2I^- + S_4O_6^{2-} \qquad \textit{Equation 4.4}$$

where n n_{B3+} = n ($S_4O_6^{2-}$) = C ($Na_2S_2O_3$) x V ($Na_2S_2O_3$)

$$[O] = [Ored] + \frac{Mw\ (red)}{mass\ (^1/_{n_{B3+}} - {}^{16}/_{mass})} \qquad \textit{Equation 4.5}$$

where [Ored] the oxygen content of the reduced sample with composition $Ba_{0.5}Sr_{0.5}(B^{2+})_{0.625}Mo_{0.375}O_{red}$, which according to charge balance is 2.75, and Mw(red) is its molecular mass (calculated to be 228.8984 g/mol). Mass (g) is the mass of the sample as given in *Table 4.7* and 16 is the atomic weight of oxygen.

Table 4.7: Calculations for determination of the oxygen content ([O]) for BSCFMo0.375-(Co/Fe=4) by titration against the standardised $Na_2S_2O_3$ solution with normality 0.10105(8)N.

Titration	Sample Mass (g)	Titre (ml) $Na_2S_2O_3$	Calculated Oxygen content [O]
1	0.0439	0.8	2.964
2	0.0441	0.9	2.963
3	0.0459	0.9	2.981

The titrations, repeated three times, produced an average value of oxygen content of 2.969(6) in BSCFMo0.375-(Co/Fe=4).

4.1.6. Comments on oxidation states of the transition metals

The overall refined composition $Ba_{0.5}Sr_{0.5}Co_{0.500(3)}Fe_{0.125(1)}Mo_{0.375(3)}O_{2.94(1)}$ is in agreement with the nominal composition, which was confirmed by EDS. The overall refined oxygen content of 2.94(1) is in good agreement with the outcomes of the total reduction experiment (2.91) and iodometric titrations (2.96(9)). The overall oxygen content is thus confirmed to be higher than +2.71 for BSCF (Appendix A), as derived from oxygen reduction experiment in this study and in agreement with the 2.4-2.75 range quoted for BSCF[89, 227, 231, 232].

The refined oxygen content of 2.94(1) and the stability of Mo^{6+} in air allow the overall mean Co/Fe oxidation state to be calculated as +2.58. With the Mössbauer determination of the overall Fe oxidation state as +3 gives an overall Co oxidation state of +2.47. Hence, they are both much lower than the Fe+3.36 and Co+3.44 as established for BSCF under this study, based on the combination of Mössbauer and oxygen reduction experiments (Appendix A) and consistent with the literature[227].

Table 4.8: Summary of derived overall and individual Co and Fe oxidation states in the SP and DP phases in BSCFMo0.375-(Co/Fe=4) (Section 4.1.3), based on Mössbauer data and the refined oxygen content. The B.V.S. produced from the joint refinement (Table 4.2), also included for comparison reasons.

Composition	Fe	Co
Global: $Ba_{0.5}Sr_{0.5}Co_{0.500(3)}Fe_{0.125(1)}Mo_{0.375(3)}O_{2.94(1)}$	3+	2.47+
SP: $Ba_{0.5}Sr_{0.5}Co_{0.547(9)}Fe_{0.253(2)}Mo_{0.200(8)}O_{2.81(3)}$	3+ B.V.S.= 2.99	3.04+ B.V.S.= 2.49+
DP: $Ba_{0.5}Sr_{0.5}Co_{0.480(1)}Fe_{0.071(1)}Mo_{0.449(2)}O_{2.98(2)}$	3+ B.V.S.= 3.18	2.18+ B.V.S.= 2.22

According to the Mössbauer data, the Fe ions are in their trivalent state in both phases, which is in good agreement with the estimated B.V.S. values from the joint refinement, giving +2.99 and +3.18 for the SP and DP respectively (*Table 4.2*, in *Section 4.1.3*). The stability of Mo^{6+}, the determination of Fe in its trivalent state in both phases and the refined oxygen content of 2.81(3) in the SP and 2.92(2) in the DP, gives a Co oxidation state of +3.04 in the SP and +2.18 in the DP. This is in agreement with the derived B.V.S. values from the joint refinement, showing that Co is in higher oxidation state in the SP (B.V.S.=2.49), whilst Co^{2+} is favored in the DP component (B.V.S.=2.22).

4.1.7. Reproducibility

The reproducibility of the synthesis and the structure of BSCFMo0.375-(Co/Fe=4), with nominal composition $Ba_{0.5}Sr_{0.5}Co_{0.5}Fe_{0.125}Mo_{0.375}O_{3-\delta}$, was evaluated for another three samples made independently by following exactly the same synthetic protocol and characterized by lab XRD data. The structural parameters determined for the DP and SP phases from combined powder X-ray and neutron Rietveld refinement (*Section 4.1.3*) were used without further refinement. No compositional restraint was applied. Lattice parameters, phase fractions and a Thompson-Cox-Hastings pseudo-Voigt peak shape were refined for each phase, as described in *Section 4.1.2*. The refinement outcomes are given in *Table 4.9* including the information coming out from the combined refinement, whilst the refinement plots are shown in Appendix E.

The Rietveld refinements of the three samples agree that BSCFMo0.375-(Co/Fe=4) is a biphase SP/DP compound consisting of 71.2(7)-75.5(9) % DP and 24.5(9)-28.8(7) % SP by weight, and are consistent with the outcome of the combined refinement. There is a small amount of $BaMoO_4$ (1.06(8)%) detectable only for the sample for which the combined XRD-ND refinement was performed. This could be due to lower background, better counting statistics and resolution of ND data collected in HRPD, which is one of the highest resolution diffractometers available, compared to the lab XRD data.

Table 4.9: Summary of structural parameters extracted from Rietveld refinements against XRD data for three BSCFMo0.375-(Co/Fe=4) samples with nominal composition $Ba_{0.5}Sr_{0.5}Co_{0.500}Fe_{0.125}Mo_{0.375}O_{3-\delta}$, showing phase fractions (Phase %), lattice parameters (Lat.par.), crystallite sizes (Cry.sz) and refined composition. The information from the joint ND/XRD refinement is also included for comparison reasons.

Abbreviation	**Phase (%)** SP% DP% $BaMoO_4$%	**Lat.par. (Å)** a (SP) a (DP) a, c ($BaMoO_4$)	**Cr.sz.(nm)** SP DP *DP-odd*	Refined composition
BSCFMo0.375- (Co/Fe=4) Sample 1	28.8(7) 71.2(7) 0	3.98476(14) 7.98108(8) ----------	98(3) 403(41) *70(4)*	$Ba_{0.5}Sr_{0.5}Co_{0.500(4)}Fe_{0.125(5)}Mo_{0.376(2)}O_{2.93(5)}$
BSCFMo0.375- (Co/Fe=4) Sample 2	27.9(8) 72.1(8) 0	3.98434(16) 7.98049(10) ----------	131(8) >800nm *53(3)*	$Ba_{0.5}Sr_{0.5}Co_{0.500(8)}Fe_{0.123(8)}Mo_{0.376(4)}O_{2.93(1)}$
BSCFMo0.375- (Co/Fe=4) Sample 3	24.5(9) 75.5(9) 0	3.98445(1) 7.98011(12) ----------	261(42) 298(22) *65(4)*	$Ba_{0.5}Sr_{0.5}Co_{0.497(5)}Fe_{0.117(4)}Mo_{0.385(1)}O_{2.93(7)}$
BSCFMo0.375- (Co/Fe=4) Combined	28.13 (9) 70.81(10) 1.06(8)	3.9844(1) 7.9812(2)	144(6) 217(9) *66(9)*	$Ba_{0.5}Sr_{0.5}Co_{0.500(3)}Fe_{0.125(1)}Mo_{0.375(3)}O_{2.94(1)}$

The lattice parameters of the SP are in the range of 3.98434(16) - 3.98476(14) Å whilst the lattice constants of the DP vary slightly between 7.98011(12) - 7.98108(8) Å for the three samples, which is in good agreement with the outcome of the XRD-ND refinement (a_{SP}= 3.9844(1) Å and a_{DP}= 7.9812(2) Å). The refined composition was in very good agreement with

the $Ba_{0.5}Sr_{0.5}Co_{0.500(3)}Fe_{0.125(1)}Mo_{0.375(3)}O_{2.94(1)}$ from the joint refinement, considering that no compositional restraint was applied.

As coming out from the microstructural analysis, the sizes of the different crystallites vary more significantly in absolute values. However, it becomes clear that the size of the SP crystallites (range: 98(3) - 261(42) nm) is smaller than the corresponding for the DP crystallites (298(22) - 403(41) nm) for all specimens, including the outcome from the combined refinement. This shows that the DP crystallites occupy more volume than the SP counterparts for all specimens, in agreement with the higher weight derived DP% content. The difficulty of estimating accurately the DP crystallites sizes, due to the significant overlap of all the fundamental reflections (*Section 4.1.1*) with those of the subcell, is clearly evidenced for sample #2 for which no broadening was refined. The size of the DP crystallites, free of antiphase boundaries and corresponding to the DP superstructure (odd) reflections, is the smallest (53(3) – 70(4) nm), supporting the fact that the coherently diffracting DP crystallites are just a part of the total number the DP crystallites. This shows that the presence of these three-dimensional lattice imperfections, often encountered in ordered-disordered systems, is highly favored and suggest that the DP crystallites in BSCFMo0.375-(Co/Fe=4) are in an intermediate state of ordering.

4.1.8. Microscopy studies*

4.1.8.1. HRTEM simulations

The microstructural nature of BSCFMo0.375-(Co/Fe=4), based on the structural models refined for each phase by the means of the combined refinement, was also simulted by HRTEM (*Figure 4.9*). The generation of a homogeneous distribution of grey dots contrast along two perpendicular directions in Region 1 agrees with the formation of simple perovskite (SP). On the contrary, the neighboring area (Region 2) shows white and grey dots alternated along the same two directions, in agreement with the ordering in the double perovskite (DP) structure. The simulation confirms the epitaxial intergrowth nature of the phases in a single grain shown in (Chapter 3, *Section 3.1.4.2*).

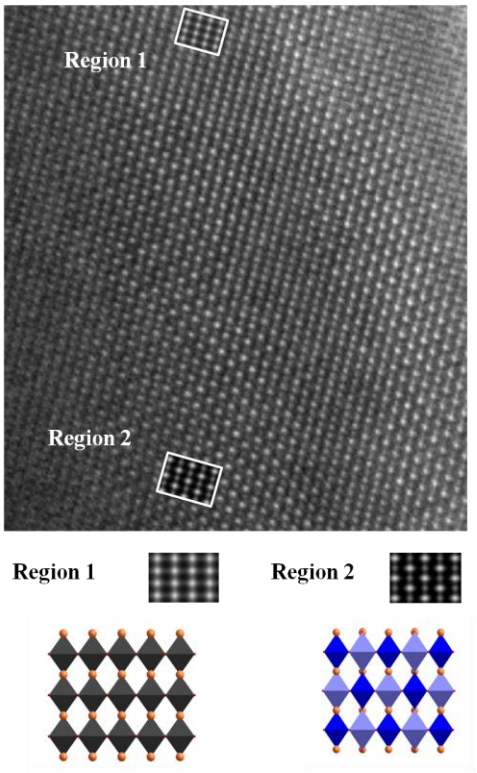

Figure 4.9: HRTEM simulation of SP and DP regions, from calculations based on the refined structural models discussed in section 4.1.3.

∗ All the microscopy work presented in this chapter was done by Dr. S. Romani.

4.1.8.2. High Angle Annular Dark Field (HAADF)

High Angle Annular Dark Field (HAADF) imaging performed on different regions of the HRTEM image (Chapter 3) of a $[1\bar{1}0]$ oriented single grain. As HAADF is sensitive to electron count[149], it is not possible to distinguish Co (Z=26) and Fe (Z=27) which differ by one electron, but the intensities of the atomic columns corresponding to Mo (Z= 42) are significantly higher.

The blue rectangles (*Figure 4.10B* and *Figure 4.10E*) correspond to the horizontal direction in the SP (*Figure 4.10A*) and DP (*Figure 4.10D*) structures respectively.

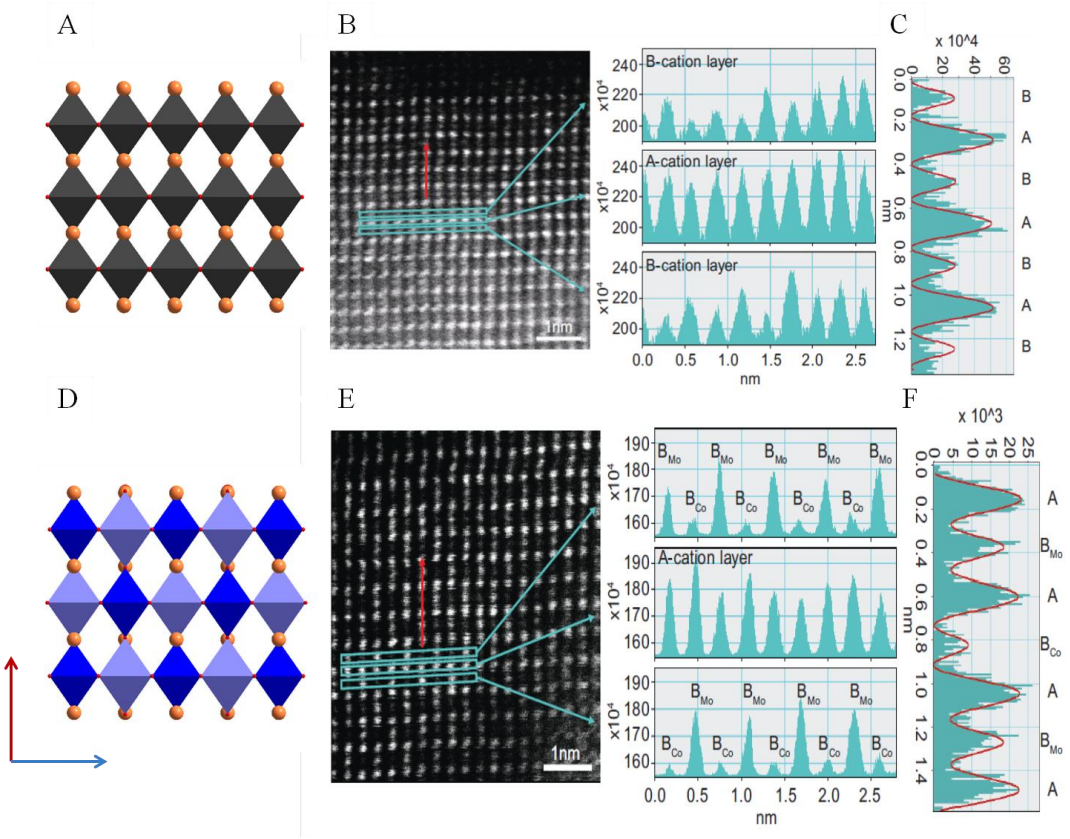

Figure 4.10: Schematic representation of a (A) BO_6 (dark grey) octahedra in the SP structure and (B) alternating B^1O_6 (dark blue) and B^2O_6 (light blue) octahedra in the double perovskite (DP) structure with different B-site compositions, where yellow spheres represent the A cations, as coming out from the refinement of BSCFMo0.375-(Co/Fe=4) (Section 4.1.3). HAADF images for a $[1\bar{1}0]$ oriented (B) SP and (E) DP region in the simulated HRTEM images (Section 4.1.8.1). The blue rectangles indicate three lines of cations along which the variation of the intensity is shown for the SP and DP respectively. The top and bottom rows correspond to B sites whilst the middle row corresponds to A sites.

The variation of intensities along three cation lines, where the top and bottom rows correspond to the B sites and the middle one to the A cations, indicate that there is clearly alternation between Co- and Mo-rich sites in the B-sites, which is not observed for the SP counterpart. The intensities of the atomic columns correposponding to Mo (Z=42) are bigger than the relatively electron poor Co,Fe cations. Moreover, for both perovkite regions, no long-range ordering between Ba (Z= 56) and Sr (Z= 38) was observed, indicating homogeneous cation distribution in their A sites.

The red arrows (*Figure 4.10B* and *Figure 4.10*E), corresponding to vertical line scans which traverse through the A and B sites in the SP and DP perovskite units, generate the observed potential curves (highlighted by red lines) in *Figure 4.10*C and *Figure 4.10*F respectively. The variation of the cations intensities clearly distinguishes the A and B cations and confirms the Co-Mo ordering for the DP in three dimensions, in contrast to the disorderd B-site in the SP.

4.1.9. Targeting isolated SP and DP phases

Attempts to make pure SP and DP compounds, with the compositions coming out from the combined Rietveld refinement, were investigated in order to evaluate whether the two perovskite components in the nanoscale biphase assemblage in BSCFMo0.375-(Co/Fe=4) could be isolated, When targeting the individual SP ($Ba_{0.5}Sr_{0.5}Co_{0.547(9)}Fe_{0.253(2)}Mo_{0.200(8)}O_{2.81(3)}$) and DP ($Ba_{0.5}Sr_{0.5}Co_{0.480(1)}Fe_{0.071(1)}Mo_{0.449(2)}O_{2.98(2)}$) compositions, the biphasic SP/DP microstructure was observed (shown in Dark field TEM images in *Figure 4.11*) for both specimens.

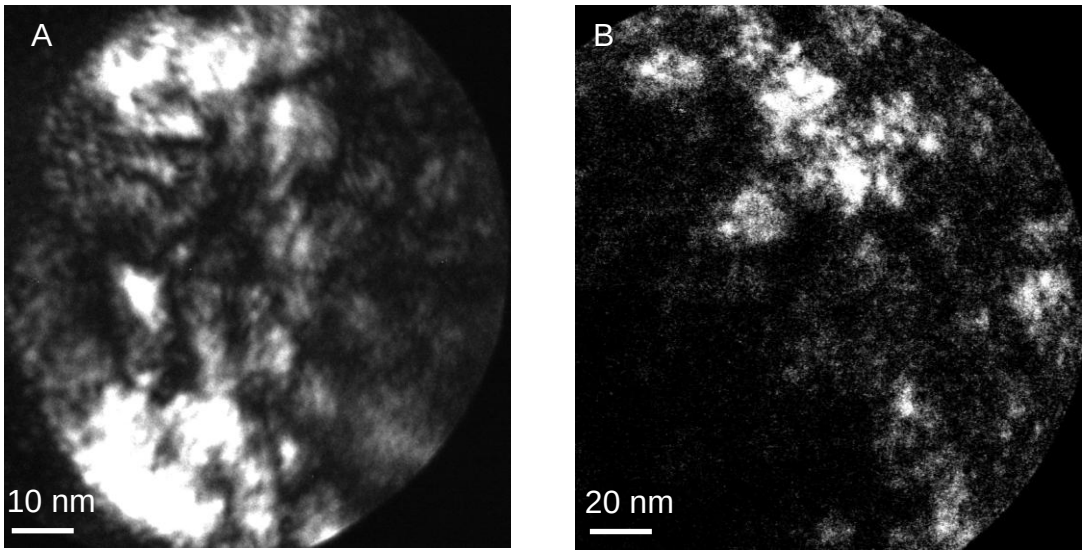

Figure 4.11: Dark field TEM of BSCFM on [110] oriented grains for the compositions coming out from the refinement of BSCFMo0.375-(Co/Fe=4) (A) targeted SP phase $Ba_{0.5}Sr_{0.5}Co_{0.547(9)}Fe_{0.253(2)}Mo_{0.200(8)}O_{2.81(3)}$ and (B) targeted DP composition $Ba_{0.5}Sr_{0.5}Co_{0.480(1)}Fe_{0.071(1)}Mo_{0.449(2)}O_{2.98(2)}$ indicating the biphase nature in both, as DP (white) and SP (black) areas were present in both specimens.

The Rietveld refinement protocol described in *Sections 4.1.2* and *4.1.7* was adopted. The parameters from Rietveld refinement of the targeted SP and DP compositions are given in *Table 4.10* and the refinement plots can be viewed in Appendix E. The targeted DP phase yielded 98.5% perovskite structure with total composition $Ba_{0.5}Sr_{0.5}Co_{0.484(6)}Fe_{0.082(3)}Mo_{0.433(1)}O_{2.96(3)}$ where the majority (93.7(2)%) were DP crystallites, whilst small amount of $BaMoO_4$ of 1.5% was also refined. The refinement of the targeted SP composition gave a SP/DP biphase compound which

consists of 86.5(2) % SP and 13.5(2) % DP, with total composition $Ba_{0.5}Sr_{0.5}Co_{0.54}Fe_{0.23}Mo_{0.23}O_{3-\delta}$. Moreover, the volume weighted DP crystallite sizes are relatively larger (169(2) nm) for the target DP composition compared to the targeted SP counterpart (61(2) nm), indicating the higher weight DP% content of the former. The volume weighed crystallite size of the DP crystallites, free of antiphase boundaries and corresponding to the superstructure odd reflections, is smaller in both cases than the total DP crystallite size, corresponding to 44% (27(4)nm of 61(2)nm) and 67% (114(5) over 169(2) nm) respectively.

Table 4.10: Summary of structural parameters extracted from Rietveld refinements of PXRD data for targeted SP and DP phases, showing phase fractions (Phase %), lattice parameters (Lat.par.), crystallite sizes (Crys.sz), nominal and refined compositions.

	Phase (%)	**Lat.par. (Å)**	**Cr.sz.(nm)**	
	SP	a (SP)	SP	**Nominal composition**
	DP	a (DP)	DP	Refined composition
	$BaMoO_4$	a, c ($BaMoO_4$)	*DP-odd*	
Target SP phase	86.5(2)	3.97603(3)	> 800[(i)]	**$Ba_{0.5}Sr_{0.5}Co_{0.547(9)}Fe_{0.253(2)}Mo_{0.200(8)}O_{2.81(3)}$**
	13.5(2)	7.97768(34)	61(2)	$Ba_{0.5}Sr_{0.5}Co_{0.538(4)}Fe_{0.229(5)}Mo_{0.232(1)}O_{2.83(2)}$
	0	----------	*27(4)*	
Target DP phase	4.8(2)	3.98314(20)	169(2) [(ii)]	**$Ba_{0.5}Sr_{0.5}Co_{0.480(1)}Fe_{0.071(1)}Mo_{0.449(2)}O_{2.98(2)}$**
	93.7(2)	7.98470(4)	169(2) [(ii)]	98.5% $Ba_{0.5}Sr_{0.5}Co_{0.484(6)}Fe_{0.082(3)}Mo_{0.433(1)}O_{2.96(3)}$
	1.5(1)	5.549(1), 12.766(6)	*114(5)*	+1.5% $BaMoO_4$

(i) No broadening of the diffraction peaks was observed. The limit of the measureable crystallite size is in the region of 800 nm.

(ii) A single broadening and strain term was refined for the fundamental reflections, corresponding to both SP and DP phases, since the amount of SP is too small to allow accurate estimation.

The lattice parameters of the perovskite components in the targeted SP and DP phases are adequately different, implicating differences in compositions which were not refined according to the protocol used. The perovskite unit cells in the target DP phase are larger compared to the corresponding unit cell of the target SP phase. However, overall, both refined compositions are in good agreement with the nominal targeted compositions and showing good reliability factors at

the Rietveld plots, indicating that the strategy for the refinement of the SP/DP biphase compounds is a good approximation.

4.2. Evolution of the biphasic assemblage with temperature

4.2.1. Variable temperature in-situ X-ray diffraction

Variable temperature in-situ X-ray diffraction data were collected at synchrotron facilities in order to monitor the evolution of the SP:DP assemblage in BSCFMo0.375-(Co/Fe=4) during the last heating step at 1000^{o}C of the synthesis process (decribed in detail in *Section 2.1*) and evaluate any possible structural changes over the temperature range measured. The specimen was heated from room temperature (RT) to 300^{o}C and from 500^{o}C to 900^{o}C. Data were collected over a 2theta range of 2 to 150° (λ = 0.825988 Å) and a step size of 0.005. It should be noted that the 2theta position of the reflections in the synchrotron data is different compared to the rest of the XRD data presented in this thesis, due to the different wavelength.

As the temperature increases, the position of the reflections shift to lower angles (*Figure 4.12*), indicating the increase in size of the unit cell, due to the net broadening of the atoms' electron clouds induced by the atomic thermal motion. There is no change in the structure of BSCFMo0.375-(Co/Fe=4) up to 850^{o}C. Small intensity $BaMoO_4$ peaks are observed at the diffraction pattern at 900^{o}C, refined to 1.04(8) % weight $BaMoO_4$ phase in the sample. Temperature has also effect on the intensities of the reflections, here highlighted for the high angle peaks were the effect is more significant. As the temperature increases, the intensities of all the reflections decrease, due to the enhanced destructive scattering of the atoms induced by thermal motion. This becomes most obvious at the high angle reflections, here highlighted for the 2theta range 65-95^{o}.

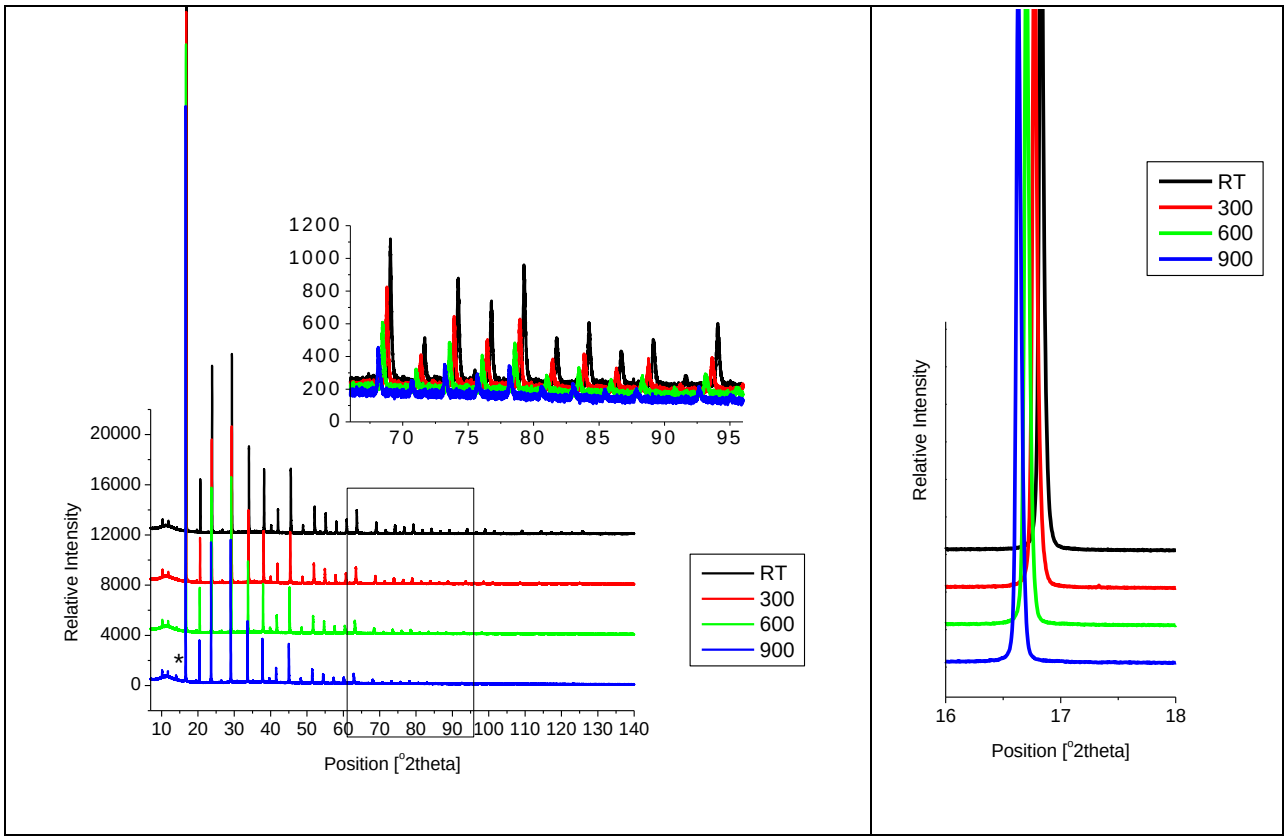

Figure 4.12: (A) In-situ X-ray Synchrotron diffraction data at room temperature (RT), 300, 600 and 900°C, showing the decrease in intensities upon heating, most evident at the high angles reflections as indicated in the inset which is a magnification of the 2theta range 65-95°. (B) shift of the reflections to lower angles, focusing on the most intense perovskite reflection, indicating the expansion of the unit cell upon heating. The star in (A) represents the $BaMoO_4$ impurity forming at 900°C.

The Rietveld refinements (appendices) were performed based on the model (described in more detail in *Sections 4.1.2*) and the compositions of the DP and SP phases were used without further refinement from the outcome of the combined refinement (*Section 4.1.3*), whilst the peakshape, lattice parameters, phase percentages and thermal displacement parameters were refined. The results are tabulated in Appendix B and the refinement plots are shown in Appendix E.

Upon heating, the relative weight phase fractions of BSCFMo0.375-(Co/Fe=4) vary slightly, with the SP phase fraction increasing slightly at temperatures above 500°C, whilst the DP phase fraction decreases (*Figure 4.13*). Heating a sample containing 22.0 (4) %SP and 78.0 (4)% DP at room temperature resulted in a sample containing 27.2 (3)% SP and 72.8(3)% DP at 850°C.

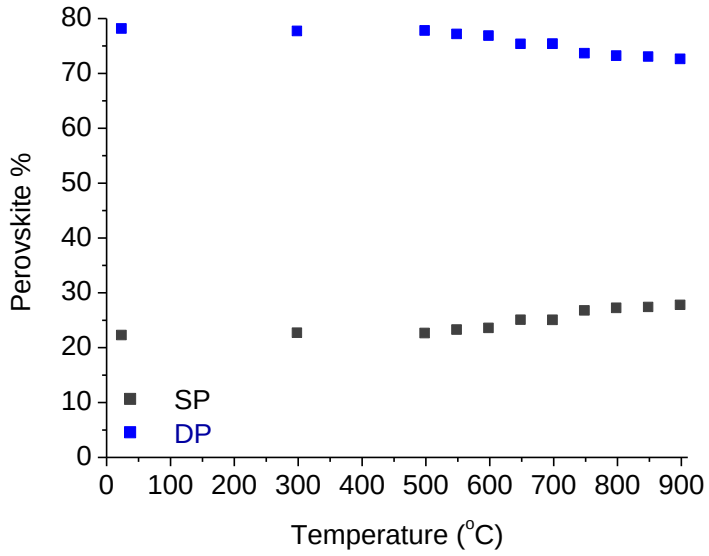

Figure 4.13: Perovskite (SP, DP) phase fractions from Rietveld refinements of synchrotron X-ray diffraction, coming out from Rietveld refinements of synchrotron X-ray diffraction data for BSCFMo0.375-(Co/Fe=4) at room temperature, 300°C and from 500 to 900°C in steps of 50°.

As coming out from the microstructural analysis (*Figure 4.14*), from room temperature up to 500°C there are no significant changes in the crystallites. In the temperature range 500-900°C, the SP crystallites expand slightly with temperature from 80(1) nm to 107(1) nm, whilst the DP crystallites size vary slightly from 182(2) to 173(2) nm. The sizes of the completely ordered DP crystallites, which are free of antiphase boundaries and correspond to the DP-odd reflections, remain intact to 58(2) -63(3) nm, with no obvious trend over the temperature range measured. This suggests that the slight decrease in size of the total number of the DP crystallites is related to the decrease in the DP phase (DP%) upon heating.

It is hard to say definitely what the driving force for this behavior is. One possible explanation could be that the thermal energy provided by heating could cause the breaking of the antiphase boundaries, connecting the incoherently diffracting domains in the DP structure, resulting in an apparent increase in the size and volume of the entropically favored disordered SP crystallites and concomitant decrease of the DP crystallite size.

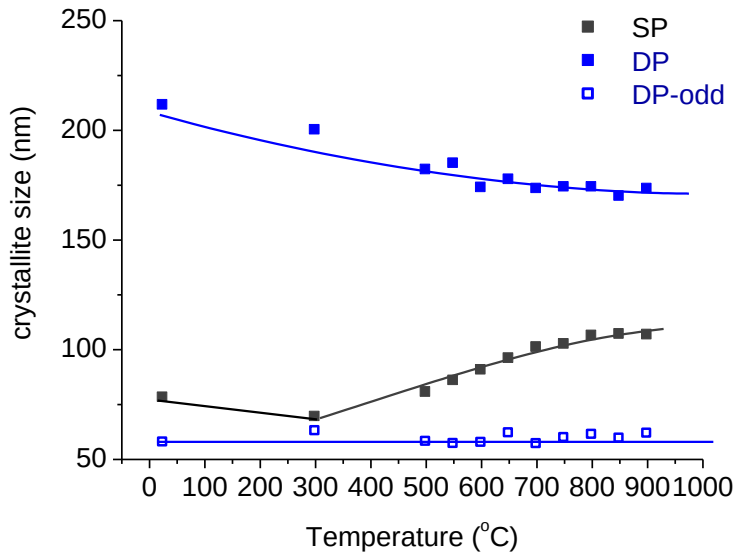

Figure 4.14: Crystallite size evolution upon heating as coming out from the microstructure analysis of Rietveld refinements of synchrotron X-ray diffraction data for BSCFMo0.375-(Co/Fe=4) at room temperature, 300°C and from 500 to 900°C in steps of 50°.

The lattice parameters of the SP and DP phases increase linearly with temperature (*Figure 4.15*) from 500-800^{o}C and the lattice parameter difference between the phases remains unaltered throughout the temperature range measured. The smooth separate (rather than converging) thermal evolution of the cell parameters for both SP and DP phases, is consistent with a mechanism based on nucleation and growth process, rather than spinodal decomposition for which metastable structures result in a single phase at high temperature.

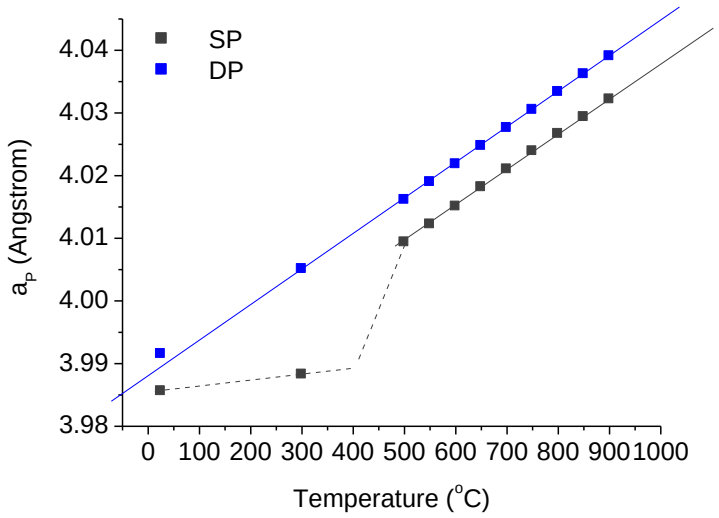

Figure 4.15: Perovskite lattice parameters evolution upon heating for the SP ($a_P=a_{SP}$) and DP ($a_p=a_{DP}/2$), coming out from Rietveld refinements of Synchrotron X-ray diffraction data for BSCFMo0.375-(Co/Fe=4) at room temperature, 300°C and from 500 to 900°C in steps of 50°.

Another interesting feature from *Figure 4.15* is the different behavior observed only for the SP lattice parameters from room temperature to approximately 300-500^{o}C compared to the linear part of the higher temperature range 500-800^{o}C. The exact temperature where this change occurs is not clear due to the limited number of data at this temperature range; a suggested plot is represented by the dashed lines. Similar behavior has been observed for the isostructural parent undoped BSCF [90]from thermal expansion curves collected with a dilatometer at 50-900^{o}C in 20^{o}C steps over the whole temperature range of the experiment, showing a curve with a turning point at approximately 382^{o}C. This was attributed to the loss of lattice oxygen resulting in electrostatic repulsion between the cations and abrupt increase of the lattice parameters.

The loss of oxygen by BSCFMo0.375-(Co/Fe=4) was studied by thermogravimetric analysis (TGA) in Chapter 3, *Section 3.3.2* and it was identified to occur at about 372^{o}C, which is in close agreement with the observation herein. This demonstrates that the SP, with refined composition $Ba_{0.5}Sr_{0.5}Co_{0.547(9)}Fe_{0.253(2)}Mo_{0.200(8)}O_{2.81(3)}$ has mobile oxygen atoms; this is related with the significant number of oxygen vacancies. On the contrary, the DP with refined composition $Ba_{0.5}Sr_{0.5}Co_{0.480(1)}Fe_{0.071(2)}Mo_{0.449(2)}O_{2.98(2)}$, is oxygen stoichiometric and hence the oxygen atoms are not mobile resulting in steady increase of the lattice constants.

The information obtained from the evolution of the lattice parameters with temperature allowed the estimation of the linear thermal expansion coefficient at the temperature range 500-800^{o}C, as discussed further in *Section 4.2.3*.

4.2.2. Quenching (rapid cooling) experiments

Quenching experiments were performed in order to complement the in-situ diffraction study, which was limited to temperatures up to 900^{o}C. When a specimen is cooling rapidly to room temperature, low-temperature processes are prevented by providing a narrow window of time in which the reaction is both thermodynamically favorable and kinetically accessible. In this way, it became possible to monitor the changes of the biphasic SP:DP compound during the last heating step, from the synthesis temperature (1000^{o}C) but also from higher temperatures after annealing for 10h. For the quenching, the specimens were taken out of the furnace and immediately placed on an aluminium block, which is a good thermal conductor, and left in air.

4.2.2.1.Quenching from the synthesis temperature

Quenching a sample containing 22.2(4) % SP:77.8(4)% DP, from the last heating step at 1000°C after annealing for 10h, affords a material with 96% perovskite, with the same biphasic phase assemblage (22.2(6)% SP:77.8(6)% DP) and 4.0(4) % $BaMoO_4$ (*Table 4.11*). According to the in-situ diffraction experiment (*Section 4.2.1*), $BaMoO_4$ starts forming already from 900^{o}C (1.04(8) %) and its content is further increased at 1000^{o}C 'trapped' by rapid cooling, but not observed at the slowly cooled specimen with cooling rate 5^{o}C/min for equivalent XRD data (*Section 4.1.7*). This indicates that the slow cooling favors the incorporation of the $BaMoO_4$ in the biphase SP/DP assemblage. It is likely though that $BaMoO_4$ is still present in BSCFMo0.375-(Co/Fe=4) at the synthesis conditions but in an amorphous phase. When monitoring the reaction in situ and quenching at high temperatures, $BaMoO_4$ becomes more crystalline and hence detectable by XRD. This is also supported by the outcome of the combined XRD-ND diffraction study, (*Section 4.1.3*) where the XRD data are combined with the high resolution ND data and ca. 1% $BaMoO_4$ was refined.

The SP lattice parameters are equal within error for the specimens before (3.9810(2) Å) and after quenching (3.9811(2) Å) from 1000^{o}C, whilst there is slight contraction of the major DP phase

form 7.9858(1) to 7.98152(8) Å respectively (*Table 4.11*). In contrast with the VT in-situ experiment, the atomic thermal motion 'freezes' by the quenching and hence no thermal expansion effect is observed. This suggests slight changes in the SP and DP components, which were not refined according to the model used. Nevertheless, the refined compositions are in good agreement with the nominal composition, indicating that the model used is a good approximation.

Table 4.11: Summary of structural parameters extracted from Rietveld refinements against XRD data for BSCFMo0.375-(Co/Fe=4) before and after the last heating step of the synthesis procedure at 1000°C for10h, followed by rapid cooling (quenching), showing phase fractions (Phase %), lattice parameters (Lat.par.), crystallite sizes (Crys.sz), nominal and refined compositions.

	Phase (%)	**Lat.par. (Å)**	**Cr.sz.(nm)**	
	SP	a (SP)	SP	**Nominal composition**
	DP	a (DP)	DP	Refined composition
	$BaMoO_4$	a, c ($BaMoO_4$)	*DP-odd*	
Before last heating step	22.2(4) 77.8(4) 0	3.9810(2) 7.9858(1) ----------	49(1) 181(5) *54(4)*	**$Ba_{0.5}Sr_{0.5}Co_{0.5}Fe_{0.125}Mo_{0.375}O_{3-\delta}$** $Ba_{0.5}Sr_{0.5}Co_{0.495(9)}Fe_{0.113(1)}Mo_{0.391(8)}O_{2.93(6)}$
After last heating step and quenching	21.3(5)* 74.7(6)* 4.0(4)	3.9811(2) 7.98152(8) 5.27(1), 14.36(9)	54(7) 83(1) *59(3)*	**$Ba_{0.5}Sr_{0.5}Co_{0.5}Fe_{0.125}Mo_{0.375}O_{3-\delta}$** 96%$Ba_{0.5}Sr_{0.5}Co_{0.495(9)}Fe_{0.113(2)}Mo_{0.433(1)}O_{2.93(5)}$ +4.0% $BaMoO_4$

**Excluding the $BaMoO_4$ impurity phase, there is 96% perovskite in this sample with phase assemblage of 22.2(6)% SP:77.8(6)% DP.*

According to the microstructural analysis, the apparent volume weighted SP crystallite size is equal within error before and after the last heating step at 1000°C of the synthetic procedure 'trapped' by quenching, with refined values of 49(1) nm to 54(7) nm respectively (*Table 4.11*). Similarly, the size of DP crystallites, free of antiphase boundaries and corresponding to the odd reflections, is within error equal for the samples before and the last heating step of the synthesis procedure, corresponding to 30% and 71% of the total volume of the DP crystallites (54(4) nm over 181(5) nm and 59(3) nm over 83(1) nm for DP-odd and DP reflections respectively). The increase is consistent with the in-situ diffraction experiment's outcomes, where the DP crystallites at 900°C are 37% ordered (62(2) nm over 171(1) nm, *Section 4.2.1*). This shows

clearly that the DP crystallites, free of antiphase boundaries are not affected but represent higher volume of the DP crystallites as the temperature reaches the synthesis conditions, likely related to the breaking of the antiphase boundaries with temperature. The breaking of these 3D lattice imperfections seems to be thermodynamically favored but kinetically limited at temperatures below the synthesis temperature (1000^{o}C). It would be interesting to observe the evolution of the DP crystallite size over time; presumably if kept for longer at 1000^{o}C, the antiphase boundaries would be completely broken leading to equal broadening of all the DP reflections, corresponding to both DP crystallites free and non-free of antiphase boundaries.

4.2.2.2.Quenching from higher than the synthesis temperature

A quench following an annealing for 10 hours at 1200°C (i.e. above the synthesis temperature and very close to the melting point found out to be ca.1250^{o}C) resulted in an increase of the DP weight based content from 77.8(4)% DP to 86.0(1)% DP, with consequent increase in the SP% content from 22.2(4)% to 13.9(1)% (*Table 4.12*). The quenched sample consisted of 96.5(2) % perovskite phases and 3.5(1) % $BaMoO_4$, which is equal within error to the 4.0(4) % refined for the quenched sample from the synthesis temperature (*Section 4.2.2.1*).

Table 4.12: Summary of structural parameters extracted from Rietveld refinements against XRD data for BSCFMo0.375-(Co/Fe=4) before and after heating at 1200^{o}C for 10h followed by rapid or slowly cooling (cooling rate 5 ^{o}C/min), showing phase fractions (Phase %), lattice parameters (Lat.par.), crystallite sizes (Cr..sz) and refined composition.

	Phase (%)	**Lat.par. (Å)**	**Cr. sz.(nm)**	
	SP	a (SP)	SP	**Nominal composition**
	DP	a (DP)	DP	Refined composition
	$BaMoO_4$	a, c ($BaMoO_4$)	*DP-odd*	
Before last heating step	22.2(4) 77.8(4) 0	3.9810(2) 7.9858(1) ----------	49(1) 181(5) *54(4)*	$Ba_{0.5}Sr_{0.5}Co_{0.5}Fe_{0.125}Mo_{0.375}O_{3-\delta}$ $Ba_{0.5}Sr_{0.5}Co_{0.495(9)}Fe_{0.113(1)}Mo_{0.391(8)}O_{2.93(6)}$
After last heating step at 1200^{o}C and quenching	13.5(1)* 83.0(3)* 3.5(1)	3.9830(4) 7.9799(1) 5.5524(5), 12.7180(2)	69(4) 175(6) *66(5)*	**$Ba_{0.5}Sr_{0.5}Co_{0.5}Fe_{0.125}Mo_{0.375}O_{3-\delta}$** 96.3%$Ba_{0.5}Sr_{0.5}Co_{0.491(3)}Fe_{0.100(5)}Mo_{0.418(3)}O_{2.94(7)}$ +3.5% $BaMoO_4$
After last heating step at 1200^{o}C and slow cooling	14.9(8)* 81.4(8)* 3.7(1)	3.9820(4) 7.9794(1) 5.5520(7), 12.719(3)	64(3) 161(4) *70(5)*	**$Ba_{0.5}Sr_{0.5}Co_{0.5}Fe_{0.125}Mo_{0.375}O_{3-\delta}$** 96%$Ba_{0.5}Sr_{0.5}Co_{0.495(9)}Fe_{0.113(2)}Mo_{0.433(1)}O_{2.93(5)}$ +4.0% $BaMoO_4$

**Excluding the $BaMoO_4$ impurity phase, there is 96.5(2)% perovksite in the quenched sample from 1200°C, with phase assemblage of 13.9(8)% SP:86.0(1)% DP. Similarly, the slowly cooled specimen consists of 96.3(2) % perovskite with 15.4(7) % SP and 84.5(6)% DP.*

This demonstrates that the main effect of increasing the temperature above the synthesis temperature is the increase in DP% content, implying that the B-site ordering is favored. The cooling procedure does not affect significantly the perovskite constituents, since the slowly cooled specimen (containing 96.3(2)% of perovskite phases) consists of equal within error perovskite assemblage (15.4(7) % SP and 84.5(6) % DP) with the quenched sample from the same temperature.

The increase in the DP% content is accompanied by a slight increase of the volume weighted crystallite size of the antiphase-boundary-free DP crystallites, as derived from the odd superstructure reflections, from 54(4) to 66(5) for the quenched sample, which is equal within error for the specimen cooled down with 5°/min cooling rate (70(5) nm). The total volume of the DP crystallites is not significantly affected by the annealing at 1200°C/10h, with refined values of and for the sample before (181(5) nm) and after the heat treatment followed by rapid cooling 175(6) nm and for cooled slowly (161(4) nm). However, these are significantly larger than the 83(1) nm refined DP crystallite size for the specimen undergone the last heating step at 1000°C/10h followed by quenching (*Section 4.2.2.1*). This suggests that different processes are favored at the synthesis temperature compared to higher temperatures, which are related to the DP crystallites. However, the increase in the SP crystallite size from 49(1) nm to 69(4) nm and 64(3) nm for the quenched and slowly cooled specimens respectively, is consistent with the refined SP crystallite size of 54(7) nm from the quenching experiment from 1000°C (*Section 4.2.2.1*). This is in agreement with the outcome of the in-situ diffraction experiment (*Section 4.2.1*) showing increase of the SP crystallite size with temperature (*Figure 4.14*). As aforementioned, this is likely associated with the breaking of antiphase boundaries in the DP due to heating resulting in an apparent increase of the SP volume.

The DP unit cell contracts when heated at 1200°C/10h followed by quenching or slow cooling, from 7.98581 Å to 7.9799(1) Å and 7.9794(1) Å respectively, whilst the minor SP phase expands slightly from 3.9810(2) Å to 3.9830(4) Å and 3.9820(4) Å accordingly. This is consistent with

the decreased refined DP lattice constant of 7.98152(8) Å for the sample quenched from 1000°C/10h (*Section 4.2.2.1*) compared to the sample before the heating. As aforementioned, this suggests slight changes in the SP and DP components, which were not refined according to the model used, but likely related to the increased DP% content upon heating to 1200°C. The B-site ordering favored at high temperature could indicate that heating favors the incorporation of more Mo^{6+} in the B-site of the DP component, resulting in smaller DP lattices and consequently bigger SP unit cells, due to its smaller size compared to Co and Fe ions.

4.2.3. Thermal Expansion Coefficient

The in-situ variable temperature experiment allowed also the calculation of the linear thermal expansion coefficient of BSCFMo0.375-(Co/Fe=4), given by the formula:

$$TEC = \frac{dL/dT}{Lo} \qquad \textit{Equation 4.6}$$

where L: the perovskite lattice parameter (Å), T the temperature (K), dL/dT the gradient of the graph a_P against T and L_o the lattice parameters at 500°C (*Figure 4.15*).

According to the refinements at room temperature, BSCFMo0.375-(Co/Fe=4) contains 78.0(4)% DP and 22.0(4)% SP at with lattice parameter a_p (500°C) = 4.00932(7) Å and a_p (500°C) = 8.03219(3) Å respectively (from Appendix B). The thermal expansion coefficient of the biphasic SP/DP sample was then calculated according to the formula at the temperature range 500-900°C.

$$TEC\ (BSCFMo0.375\text{-}(Co/Fe=4)) =$$
$$DP\%\ TEC\ (DP) + SP\%\ TEC\ (SP) = 13.87\ x10^{-6}\ K^{-1} \qquad \textit{Equation 4.7}$$

Table 4.13: Calculations of the thermal expansion coefficient (TEC) for BSCFMo0.375-(Co/Fe=4), at 500-900°C, for each of the two perovskite components (SP, DP) by the evolution of lattice parameters with temperature (dL/dT) and the perovskite lattice parameter at RT (Lo). Each phase contributed to the TEC of the biphase BSCFMo0.375-(Co/Fe=4) compound according to each phase percentage (phase%).

	Phase% (500°C)	dL/dT	a_p(500°C), Å	Lo, Å	TEC ($x10^{-6}$ K^{-1})
SP	22.4(3)	$5.87.10^{-5}$	4.00932(7)	4.00932(7)	14.64
DP	77.6(3)	$5.48.10^{-5}$	8.03219(3)	4.01609(5)	13.65

The linear TEC of BSCFMo0.375-(Co/Fe=4), calculated to 13.87 x10^{-6} K^{-1}, is hence smaller than the reported values for BSCF of 19.0(5)–20.8(6) ×10−6 K^{-1}[89] between 600-900^{o}C, measured by in-situ neutron diffraction. It is generally accepted that cobalt-based perovskite oxides exhibit large TEC values, which is mainly attributable to the electronic spin state transitions associated with the Co^{3+}[233-237], from the larger high-spin state Co^{3+} ions (0.61Å) to the smaller low-spin state Co^{3+} ions (0.545 Å) upon heating[236, 237], which leads to the increase of the TEC[233, 238, 239]. Moreover, the TEC for perovskite-type oxides is closely related to the oxide vacancies [90, 240], which inducing a reduction in the electrostatic bond strength, result in increase of the metal-oxygen bonds[241]. Hence, the decreased TEC value for BSCFMo0.375-(Co/Fe=4) compared to BSCF, can be attributed to the overall lower Co content (refined to 0.500(3), *Section 4.1.3*), charge (+2.47, *Section 4.1.6*) and number of oxygen vacancies (δ= 0.06) compared to BSCF (Co content 0.8, overall charge: +3.44, δ= 0.29, *Section 4.1.6*).

When comparing with the state-of-the art cathodes, the TEC of BSCFMo0.375-(Co/Fe=4) is comparable with the Co-poor LSCF ($(La_{0.6}Sr_{0.4})_{1-x}Co_{0.2}Fe_{0.8}O_{3-\delta}$, for x = 0.00–0.15) series, exhibiting a TEC of 13.8-14.2×10−6 K^{-1} [242, 243]at the temperature range 25-700^{o}C. The TEC for the Co-free Sr-doped $LaMnO_3$ series (LSM, $La_{1-x}Sr_xMnO_{3-\delta}$) is reported to be in the range of 11.7- 13.1 K^{-1}[13, 244, 245], with the minimum at x =0.15-0.20, at the temperature range 20-1100^{o}C[246]. Moreover, the TEC of BSCFMo0.375-(Co/Fe=0.375) is the lowest compared to other reports for B-site doping in the BSCF series of oxides, as for instance the Nb^{5+}-BSCF system ($Ba_{0.5}Sr_{0.5}(Co_{0.8}Fe_{0.2})_{1-x}Nb_xO_{3-\delta}$ (with x=0-0.2)) with reported TEC of 16- 19×10^{-6} K^{-1}[181], and the $Ba_{0.6}Sr_{0.4}Co_{0.8}Ti_{0.2}O_{3-\delta}$ system, where Ti^{4+} fully substitutes Fe in the parent BSCF[247], with TEC= 13.6×10^{-6} K^{-1}.

The thermal expansion behavior of BSCFMo0.375-(Co/Fe=4) (TEC= 13.87 x10^{-6} K^{-1}) matches well with ceria based electrolytes as SDC ($Sm_{0.2}Ce_{0.8}O_{1.9}$, TEC= 12.7 K^{-1}), used for this study, and GDC ($Gd_{0.2}Ce_{0.8}O_{1.9}$, TEC= 13.4 K^{-1})[248]. It is also in good match with the lanthanum gallate family of electrolytes (LSGM: $La_{0.8}Sr_{0.2}Ga_{1-x}Mg_xO_{3-d}$) with reported TEC= 10.4 - 10.5x10^{-6} K^{-1} and YSZ (8YSZ: $Zr_{0.85}Y_{0.15}O_{1.93}$ and 10YSZ: $Zr_{0.82}Y_{0.18}O_{1.91}$) with TEC= 10.5 and 10.6 x10^{-6} K^{-1} respectively[245].

4.3. Structural characterisation of other BSCFM compositions

4.3.1. Refinement protocol

The structural characterization of other BSCFM compositions, following identical synthetic protocol, was based on the Rietveld refinement of lab-XRD data. Given the difficulties of the BSCFM system (*Section 4.1.1*), the SP and DP structural parameters (occupancies and displacement parameters) determined from the combined XRD/ND refinement for BSCFMo0.375-(Co/Fe=4) (*Section 4.1.3*) were used without any further refinement. Lattice parameters, phase fractions and a Thompson-Cox-Hastings pseudo-Voigt peak shape were refined for each phase, as described in *Section 4.1.2*. This simplified model allowed estimating the phases ratio, profile functions and lattice constants, whilst deviation in the composition of the individual phases was not refined and no compositional restraint was applied.

A modified protocol was established for the refinement of compounds, forming SP single phases and containing less Mo than the SP structure determined in *Section 4.1.3* ($Mo_{0.200(8)}$). In these cases, the B-site Mo occupancy, $(Co,Fe)_{(1-x)}Mo_x$, was refined for a global (Co,Fe) content. The distinction of Co and Fe cations and theoxygen determination are not possible with non-resonant XRD (*Section 4.1.1*).

All refinement plots are shown in Appendix E.

4.3.2. Structural information for BSCF and selected BSCFM compositions

The structural outcomes for the parent undoped BSCF and the selected BSCFM compositions, for which the properties were analysed in detail in Chapter 3, Section 3.3 are summarised in *Table 4.14* and discussed below. The structural information of equivalent XRD data for BSCFMo0.375-(Co/Fe=4) (*Section 4.1.7*) are also included in the table for comparison reasons.

The parent BSCF and the low Mo containing BSCFMo0.125-(Co/Fe=4) are purely SP compounds and no DP was observed in the XRD patterns. When partially substituting Co and Fe in the perovskite BSCF structure by a small amount of the smaller Mo^{6+} (BSCFMo0.125-(Co/Fe=4), this is accommodated in the SP by causing a decrease in lattice parameters from 3.98505(3) Å to 3.97711(3) Å. The volume weighted SP crystallite size for both samples was above the measurable range (>800 nm).

Table 4.14: Summary of structural outcomes extracted from Rietveld refinements against XRD data for the parent undoped BSCF and the key selected compositions, for which the properties were discussed in detail in Chapter 3 (Section 3.3), showing phase fractions (Phase %), lattice parameters (Lat.par.), crystallite sizes (Crys.sz), nominal and refined compositions.

Abbreviation	**Phase (%)** SP DP	**Lat.par. (Å)** a (SP) a (DP)	**Cr.sz.(nm)** SP DP , *DP-odd*	**Nominal composition** Refined composition
BSCF	100 0	3.98505(3) ----------	> 800[(i)] ----------	**$Ba_{0.5}Sr_{0.5}Co_{0.8}Fe_{0.2}O_{3-\delta}$** $Ba_{0.5}Sr_{0.5}(Co,Fe)_1O_{3-\delta}$
BSCFMo0.125-(Co/Fe=4)	100 0	3.97711(3) ----------	>800[(i)] ----------	**$Ba_{0.5}Sr_{0.5}Co_{0.7}Fe_{0.175}Mo_{0.125}O_{3-\delta}$** $Ba_{0.5}Sr_{0.5}(Co,Fe)_{0.876(4)}Mo_{0.124(2)}O_{3-\delta}$
BSCFMo0.375-(Co/Fe=4) *(#1)**	28.8(7) 71.2(7)	3.98476(14) 7.98108(8)	98(3) 403(41), *70(4)*	**$Ba_{0.5}Sr_{0.5}Co_{0.500}Fe_{0.125}Mo_{0.375}O_{3-\delta}$** $Ba_{0.5}Sr_{0.5}Co_{0.497(5)}Fe_{0.117(4)}Mo_{0.385(1)}O_{2.93(7)}$
BSCFMo0.45-(Co/Fe=10)	8.7(3) 91.2(3)	3.98671(13) 7.98940(4)	317(79) >800[(i)], *>800*[(i)]	**$Ba_{0.5}Sr_{0.5}Co_{0.50}Fe_{0.05}Mo_{0.45}O_{3-\delta}$** $Ba_{0.5}Sr_{0.5}Co_{0486(6)}Fe_{0.087(8)}Mo_{0.425(5)}O_{2.95(8)}$

[(i)] No broadening of the diffraction peaks was observed. The limit of the measureable crystallite size is in the region of 800 nm.

**This is just one representative sample for BSCFMo0.375-(Co/Fe=4) from equivalent XRD data as for the rest of the compositions presented herein (Section 4.1.7).*

With increasing Mo content and regardless the Co/Fe ratio, the DP% component is increasing, from 71.2(7) % DP to 91.2(3)% DP for BSCFMo0.375-(Co/Fe=4) and BSCFMo0.45-(Co/Fe=10) respectively. The increased DP character of BSCFMo0.45-(Co/Fe=10) compared to BSCFMo0.375-(Co/Fe=4) has been demonstrated previously by the DF/TEM *(Chapter 3, Section 3.1.4.3*). The DP crystallite size of the DP-rich BSCFMo0.45-(Co/Fe=10) was above the measurable range (>800 nm) and the measured crystallite size for the SP phase (317(79) nm) is significantly lower than for the purely SP phases, but its exact value is debatable due to the very low weight SP%. For BSCFMo0.375-(Co/Fe=4), the volume weighted DP crystallite size (403(41) nm) in BSCFMo0.375-(Co/Fe=4) is larger than the SP counterpart, in agreement with the high weight weighted DP%. As coming out from the reproducibility study (*Section 4.1.7*), the size of SP (range: 98(3) - 261(42) nm) and DP (217(9) - 403(41) nm) crystallites vary significantly, due to the highly overlap of all fundamental subcell and supercell reflections. The DP odd superstructure peaks are broader than the fundamental Bragg reflections, corresponding to smaller DP crystallites free of antiphase boundaries ((53(3) – 70(4) nm)).

Both SP and DP unit cell in BSCFMo0.375-(Co/Fe=4) are smaller than in BSCFMo0.45-(Co/Fe=10), with refined lattice parameters of a_{SP}=3.98476(14) Å, a_{DP}= 7.98108(8) Å and a_{SP}=3.98671(13), a_{DP}=7.98940(4) Å respectively. This suggests differences in the composition of the individual phases, however limited by the Rietveld protocol used for this study. However, the refined compositions are in good agreement with the nominal composition and the fits are good, indicating that the model used is a good approximation.

The comparable electrochemical properties of BSCF, BSCFMo0.125-(Co/Fe=4) and BSCFMo0.375-(Co/Fe=4) (Chapter 3, *Section 3.3.3.1*) suggest tentatively similarities in the mechanism of the oxygen reduction reaction, which is likely related to structural features of the perovskite components. More detailed analysis in the BSCFMo$_x$(Co/Fe=4) oxides series is given in *Section 4.3.3*. The compound with abbreviated compositions BSCFMo0.45-(Co/Fe=10), for which the B-site is half-filled with Co as in BSCFMo0.375-(Co/Fe=4), shows much worse cathode properties. It is believed that the good properties of the high Co-containing cathodes, including BSCF, are due to the good Co catalytical properties. The marginally different cathode response of these iso-Co containing compositions, demonstrate that the functionality of the Mo-

doped BSCF materials is not a simple relation with the Co content. This indicates that the Co/Fe ratio is an important factor affecting the electrochemical performance, likely linked to different structural features from the BSCFMo$_{x+y}$ (Co/Fe=4) oxides series and is further discussed in Section 4.3.4.

4.3.3. Effect of Mo content

To understand the effect of introducing Mo in the structure, a range of BSCFMo$_{x+y}$-(Co/Fe=4) compositions with differing Mo content ($0<x+y<0.45$), but all having Co/Fe ratio equal to 4, were studied. The refinement protocol described in Section 4.3.1 was adopted. The refinement outcomes of BSCF, BSCFMo0.125-(Co/Fe=4) and BSCFMo0.375-(Co/Fe=4) (*Section 4.3.2*) are also included in this study to provide an overall picture.

According to the outcomes from the Rietveld refinements (*Table 4.15*), there is a clear evolution of the phase % by weight with increasing the Mo content (*Figure 4.16*). The weight SP% decreases from 100% for BSCF and BSCFMo0.125-(Co/Fe=4) to 6.8(8) % for the end member with Mo=0.45. The weight DP% increases from 20.9(7) % for BSCFMo0.20-(Co/Fe=4) to 71.2(7)% for BSCFMo0.375-(Co/Fe=4) and 85.7(7)% for BSCFMo0.45-(Co/Fe=4). The introduction of higher Mo content than 0.375, results in the expulsion of BaMoO4 impurity phase, which was refined to 1.6(1)% for BSCFMo0.409-(Co/Fe=4) and 7.5(1)% for BSCFMo0.45-(Co/Fe=4).

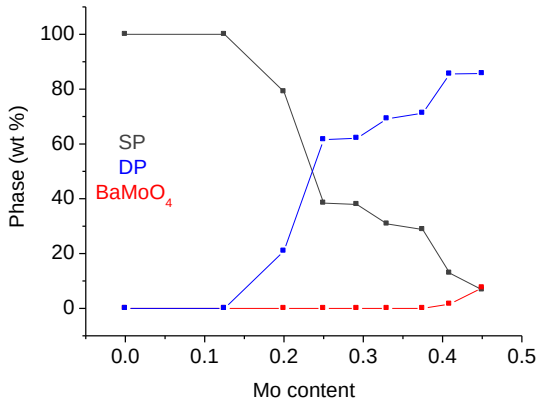

Figure 4.16: Evolution of % phase by weight with increasing the Mo content, based on Rietveld refinements against XRD data for the series of BSCFMo$_{x+y}$-(Co/Fe=4) compounds, where

$0 \leq (x+y) \leq 0.45$. The SP and DP contents are represented by black and blue symbols lines respectively, whilst the formation of $BaMoO_4$ is shown in red.

This demonstrates that the B-site ordering is favored with increasing the Mo content resulting in richer DP compounds and the high DP% content is accompanied by the presence of $BaMoO_4$, as also summarised in the pseudo-phase ternary diagram in Chapter 3 (*Section 3.1.5*). It is hard to comment on the mechanism of accommodating the increasing amount of Mo since no deviation for the SP and DP compositions was refined by the adopted model. However, the changes in lattice parameters of the two phases with varying the Mo content (*Figure 4.17*) could tentatively suggest a preference of Mo incorporation to the SP or DP phase.

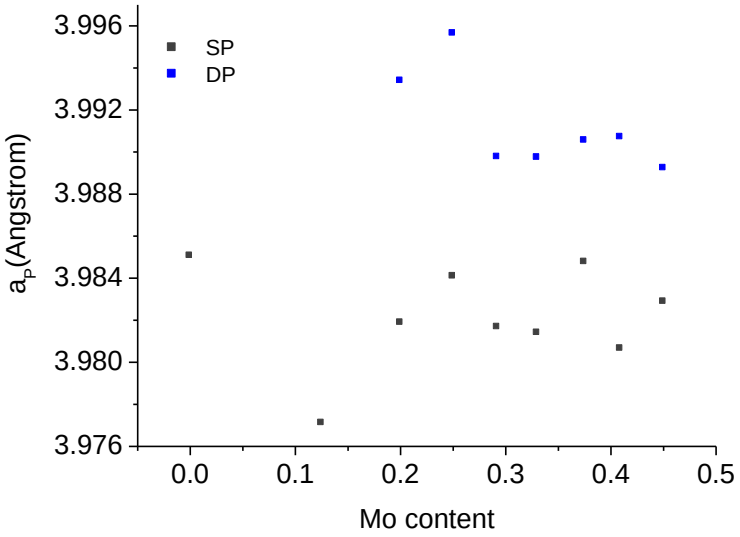

Figure 4.17: Evolution of lattice parameters for the SP ($a_P = a_{SP}$) and DP ($a_P = a_{DP}/2$) phases with increasing Mo content.

The gradual increase in the lattice parameters of the major SP phase from Mo=0.125 (a_{SP}= 3.97711(3) Å) to Mo=0.25 (a_{SP}= 3.98408(8) Å) could indicate the expulsion of Mo from the SP. The lattice parameter of the SP for BSCFMo0.25-(Co/Fe=4) reaches the lattice parameter of the undoped BSCF (a_{SP}= 3.98505(3) Å), suggesting that Mo is preferably accommodated in the DP structure. The DP phase becomes the major phase for the compositions having total Mo content higher than 0.292. This is accompanied by a dramatic decrease in the DP lattice parameters from 7.99126(13) Å to 7.98083(12) Å for BSCFMo0.25-(Co/Fe=4) and BSCFMo0.292-(Co/Fe=4)

respectively. At global Mo content 0.292≤Mo≤0.45, the DP lattice parameters are pretty much stable to 7.981(1) Å, suggesting that the DP composition doesn't change significantly with increasing the Mo content. This suggests that the main effect of increasing the amount of Mo in the $BSCFMo_{Mo}$-(Co/Fe=4) series is the enhancement of the B-site ordering, resulting in increasing DP% fraction, where the DP has a global composition for all in the 0.292≤Mo≤0.45 range. On the contrary, there is slight fluctuation in the lattice parameters of the minor SP phase from the highest point corresponding at Mo=0.250 (a_{SP}= 3.98408(8) Å) to the lowest at Mo= 0.33 (a_{SP}= 3.97979(21) Å). This implies that the amount of Mo in the SP phase varies, but no clear trend could be established.

Overall, the refined compositions are in quite good agreement with the nominal compositions, showing increased amount of Mo and decreased amount of Co, Fe in the perovskite assemblage as the total Mo content increases. At a closer look, it becomes evident that the largest errors are encountered in the Co and Mo sites for the compositions further situated in composition from BSCFMo0.375-(Co/Fe=4) on which the model was based. This implies that the adopted model is inadequate in refining accurately the phase fractions and cation occupancies for the biphase compounds, but works well for limiting cases containing mainly SP or DP as demonstrated previously (*Section 4.3.2*).

Table 4.15: Summary of structural parameters extracted from Rietveld refinements against XRD data for the $BSCFMo_{x+y}$-(Co/Fe=4) series with 0≤x+y≤0.45, showing phase fractions (Phase %), lattice parameters (Lat.par.), crystallite sizes (Cr.sz), nominal and refined compositions.

Abbreviation	**Phase (%)** SP DP $BaMoO_4$	**Lat.par. (Å)** a (SP) a (DP) a, c ($BaMoO_4$)	**Cr.sz. (nm)** SP DP *DPodd*	**Nominal composition** Refined composition
BSCF*	100 0 0	3.98505(3) ---------- ----------	> 800[(i)] ---------- ----------	**$Ba_{0.5}Sr_{0.5}Co_{0.8}Fe_{0.2}O_{3-\delta}$** $Ba_{0.5}Sr_{0.5}(Co,Fe)_1O_{3-\delta}$
BSCFMo0.125-(Co/Fe=4)*	100 0 0	3.97711(3) ---------- ----------	>800[(i)] ---------- ----------	**$Ba_{0.5}Sr_{0.5}Co_{0.700}Fe_{0.175}Mo_{0.125}O_{3-\delta}$** $Ba_{0.5}Sr_{0.5}(Co,Fe)_{0.876(4)}Mo_{0.124(2)}O_{3-\delta}$

BSCFMo0.20-(Co/Fe=4)	79.1(7) 20.9(7) 0	3.98187(9) 7.98676(60) ----------	>800[(i)] 83.7(5) *34.9(7)*	**$Ba_{0.5}Sr_{0.5}Co_{0.640}Fe_{0.160}Mo_{0.200}O_{3-\delta}$** $Ba_{0.5}Sr_{0.5}Co_{0.533(7)}Fe_{0.216(5)}Mo_{0.249(8)}O_{2.84(5)}$
BSCFMo0.25-(Co/Fe=4)	38.4(4) 61.6(4) 0	3.98408(8) 7.99126(13) ----------	>800[(i)] 200(15) *109(13)*	**$Ba_{0.5}Sr_{0.5}Co_{0.600}Fe_{0.150}Mo_{0.250}O_{3-\delta}$** $Ba_{0.5}Sr_{0.5}Co_{0.507(9)}Fe_{0.143(3)}Mo_{0.350(8)}O_{2.84(5)}$
BSCFMo0.292-(Co/Fe=4)	37.9(6) 62.1(6) 0	3.98167(12) 7.98083(12) ----------	50.4(6) 61.5(5) *28 (2)*	**$Ba_{0.5}Sr_{0.5}Co_{0.566}Fe_{0.142}Mo_{0.292}O_{3-\delta}$** $Ba_{0.5}Sr_{0.5}Co_{0.507(6)}Fe_{0.142(3)}Mo_{0.351(1)}O_{2.91(1)}$
BSCFMo0.33-(Co/Fe=4)	30.8(6) 69.2(6) 0	3.97979(21) 7.98108(8) ----------	35.2(5) 52.9(4) *32.9(2)*	**$Ba_{0.5}Sr_{0.5}Co_{0.536}Fe_{0.134}Mo_{0.330}O_{3-\delta}$** $Ba_{0.5}Sr_{0.5}Co_{0.502(8)}Fe_{0.129(2)}Mo_{0.369(1)}O_{2.92(2)}$
BSCFMo0.375-(Co/Fe=4) ***(#1)***** **$Ba_{0.5}Sr_{0.5}Co_{0.500}Fe_{0.125}Mo_{0.375}O_{3-\delta}$** $Ba_{0.5}Sr_{0.5}Co_{0.500(4)}Fe_{0.125(5)}Mo_{0.376(2)}O_{2.93(5)}$	28.8(7) 71.2(7) 0	3.98476(14) 7.98108(8) ----------	98(3) 403(41) *70(4)*	
BSCFMo0.409-(Co/Fe=4)	12.9(7) 85.5(7) 1.6(1)	3.98087(44) 7.98115(12) Bamoo4	67(4) 382(74) *84(6)*	**$Ba_{0.5}Sr_{0.5}Co_{0.473}Fe_{0.118}Mo_{0.409}O_{3-\delta}$** 98.6%$Ba_{0.5}Sr_{0.5}Co_{0.490(6)}Fe_{0.096(1)}Mo_{0.414(4)}O_{2.95(1)}$ + 1.6 (1)%$BaMoO_4$
BSCFMo0.45-(Co/Fe=4)	6.8(8) 85.7(8) 7.5(1)	3.98287(46) 7.97845(9) Bamoo4	131(19) 258(12) *81(5)*	**$Ba_{0.5}Sr_{0.5}Co_{0.440}Fe_{0.110}Mo_{0.450}O_{3-\delta}$** 92.5%$Ba_{0.5}Sr_{0.5}Co_{0.486(6)}Fe_{0.085(1)}Mo_{0.429(3)}O_{2.96(1)}$ +7.5(1)%$BaMoO_4$

(i)No broadening of the diffraction peaks was observed. The limit of the measureable domain size is in the region of 800 nm.
**As from Section 4.3.2*
***This is just one representative sample for BSCFMo0.375-(Co/Fe=4) from equivalent XRD data as for the rest of the compositions presented herein. The range of structural parameters values for this sample can be found in Section 4.1.7.*

The information that we can obtain from the microstructural analysis for the BSCFMo_x-(Co/Fe=4), is rather limited, since there is no clear evolution of the volume weighted crystallite sizes with the Mo content. The volume weighted SP crystallite sizes for the Mo poor (up to Mo0.25) are above the detection limit of 800nm, due to the high fraction of the SP phase. For the compositions that DP is the major phase (Mo0.25- Mo0.45), the SP crystallite sizes become measurable but smaller than for the DP counterparts in all cases, demonstrating the high DP%

content. The size of the DP crystallites free of antiphase boundaries and corresponding to the superstructure odd reflections, is progressively increasing with the Mo content from 32.9(2) nm for BSCFMo0.33 to 84(6)nm for BSCFMo0.409 and 81(5) nm for BSCFMo0.45.

4.3.4. Effect of Co/Fe ratio

As demonstrated in Chapter 3, varying the Co/Fe ratio can affect the structure and properties of the BSCFM compounds. Here, it is discussed in terms of lower (*Section 4.3.4.1*) and higher Co/Fe ratio (*Section 4.3.4.2*) than 4 of the parent undoped BSCF material.

4.3.4.1. Low Co/Fe

The effect of Co/Fe ratio was primarily studied for two compositional pairs, with Mo contents 0.125 and 0.25 (*Table 4.16*), classified in the SP and SP/DP phase region respectively, for Co/Fe ratio 4 and 2. The effect of the intermediate Co/Fe ratio=3 was also investigated for the iso-Mo compositions containing Mo=0.20. The refinement outcomes of BSCFMo0.125-(Co/Fe=4), BSCFMo0.20-(Co/Fe=4) and BSCFMo0.25-(Co/Fe=4) (*Section 4.3.3*) are also tabulated for comparison reasons.

For the low Mo content compositional pair (Mo0.125), the lowering of the Co/Fe ratio doesn't seem to have any effect on the phases present, since both BSCFMo0.125-(Co/Fe=4) and BSCFMo0.125-(Co/Fe=2) are pure SP compounds according to the XRD analysis. The lattice constant is lowered for lower Co/Fe ratio by 0.00112, with refined values 3.97711(3) Å and 3.97599(4) Å for Co/Fe=4 and Co/Fe=2 respectively, demonstrating that the lower Co/Fe ratio favors the formation of slightly smaller perovskite structure.

Table 4.16: Summary of structural parameters extracted from Rietveld refinements against XRD data for iso-Mo containing compositional pairs with differing Co/Fe (≤4), showing phase fractions (Phase %), lattice parameters (Lat.par.), crystallite sizes (Cr.sz), nominal and refined compositions.

Abbreviation	**Phase (%)** SP DP $BaMoO_4$	**Lat.par. (Å)** a (SP) a (DP) a, c ($BaMoO_4$)	**Cr. sz.(nm)** SP DP *DP-odd*	**Nominal composition** Refined composition
BSCFMo0.125-(Co/Fe=4)*	100 0 0	3.97711(3) ---------- ----------	>800[(i)] ---------- ----------	**$Ba_{0.5}Sr_{0.5}Co_{0.7}Fe_{0.175}Mo_{0.125}O_{3-\delta}$** $Ba_{0.5}Sr_{0.5}(Co,Fe)_{0.88(4)}Mo_{0.124(2)}O_{3-\delta}$
BSCFMo0.125-(Co/Fe=2)	100 0 0	3.97599(4) ---------- ----------	>800[(i)] ---------- ----------	**$Ba_{0.5}Sr_{0.5}Co_{0.583}Fe_{0.292}Mo_{0.125}O_{3-\delta}$** $Ba_{0.5}Sr_{0.5}(Co,Fe)_{0.879(7)}Mo_{0.121(7)}O_{3-\delta}$
BSCFMo0.20-(Co/Fe=4)*	79.1(7) 20.9(7) 0	3.98187(9) 7.98676(60) ----------	>800[(i)] 83.7(5) *34.9(7)*	**$Ba_{0.5}Sr_{0.5}Co_{0.640}Fe_{0.160}Mo_{0.200}O_{3-\delta}$** $Ba_{0.5}Sr_{0.5}Co_{0.533(7)}Fe_{0.216(5)}Mo_{0.249(8)}O_{2.84(5)}$
BSCFMo0.20-(Co/Fe=3)	68.4(4) 31.6(4) 0	3.97730(8) 7.98035(28) ----------	>800[(i)] 136(11) *32(3)*	**$Ba_{0.5}Sr_{0.5}Co_{0.600}Fe_{0.200}Mo_{0.200}O_{3-\delta}$** $Ba_{0.5}Sr_{0.5}Co_{0.526(8)}Fe_{0.197(6)}Mo_{0.275(7)}O_{2.86(3)}$
BSCFMo0.25-(Co/Fe=4)*	38.4(4) 61.6(4) 0	3.98408(8) 7.99126(13) ----------	>800[(i)] 200(15) *109(13)*	**$Ba_{0.5}Sr_{0.5}Co_{0.600}Fe_{0.150}Mo_{0.250}O_{3-\delta}$** $Ba_{0.5}Sr_{0.5}Co_{0.507(9)}Fe_{0.143(3)}Mo_{0.350(8)}O_{2.84(5)}$
BSCFMo0.25-(Co/Fe=2)	80.2(6) 18.5(6) 1.3(1)	3.97726(8) 7.97945(60) 5.549(1), 12.824(5)	>800[(i)] 79(5) *46(11)*	**$Ba_{0.5}Sr_{0.5}Co_{0.500}Fe_{0.250}Mo_{0.250}O_{3-\delta}$** 98.7%$Ba_{0.5}Sr_{0.5}Co_{0.535(1)}Fe_{0.220(4)}Mo_{0.244(6)}O_{2.84(1)}$ +1.3% $BaMoO_4$

(i)No broadening of the diffraction peaks was observed. The limit of the measureable domain size is in the region of 800 nm.

**As from Section 4.3.3.*

However, for higher Mo contents forming biphase SP/DP compounds, the Co/Fe ratio seems to affect the phase fractions, but not in a controlled way. For the compositional pair with Mo0.25, there is increased DP content when increasing the Co/Fe ratio from 2 to 4. The major phase in BSCFMo0.25-(Co/Fe=4) is DP with 61.6(4) %, which is significantly higher than the 18.5(6) DP% refined for the iso-Mo containing composition with Co/Fe ratio equal to 2. BSCFMo0.25-(Co/Fe=2) is a SP-rich sample with 80.2(6) % weight fraction and 1.3(1) % $BaMoO_4$ impurity phase, which implies that the perovskite assemblage cannot incorporate the whole amount of Mo up to 0.25 for the Co/Fe=2 case whilst successfully introduced into the structure of BSCFMo0.25-(Co/Fe=4). This demonstrates that lower Co/Fe ratio in BSCFMo0.25-(Co/Fe=2) favors the formation of SP phases, whilst the B-site ordering is enhanced resulting in predominance of the DP in BSCFMo0.25-(Co/Fe=4), which is the higher Co/Fe member in this compositional pair. On the contrary, the DP content is lower for BSCFMo0.20-(Co/Fe=4) compared to BSCFMo0.20-(Co/Fe=3), with refined values 20.9(7)% and 31.6(4)% accordingly, which are both impurity-free biphase compounds. The SP composition coming out from the refinement of BSCFMo0.375-(Co/Fe=4) (*Section 4.1.9*), which can be abbreviated as BSCFMo0.2-(Co/Fe=2.62) and can also be included in the study of iso-Mo=0.2 containing compositions, contains 13.5(2)% DP, which is less than for both BSCFMo0.20-(Co/Fe=3) and BSCFMo0.20-(Co/Fe=2). Hence, it is ambiguous if increasing the Co/Fe ratio favors the B-site ordering, in this series of iso-Mo=0.20 containing samples, implicating limitations of the refinement protocol used.

The microstructural analysis agrees with the relative phase fractions, showing larger volume weighted DP crystallites size for the compound with the higher DP% content within the BSCFM compositional pairs consisting of Mo=0.2 and Mo=0.25. The volume weighted DP crystallite size is larger for the higher DP% containing BSCFMo0.25-(Co/Fe=4) compared to the lower DP% BSCFM0.25-(Co/Fe=2) with refined values of 200(15) nm and 79(5) nm respectively. Similarly, the DP crystallites in the higher DP% containing BSCFMo0.2-(Co/Fe=3) (136(11) nm) are larger than the refined size for the DP crystallites in BSCFMo0.2-(Co/Fe=4) (83.7(5) nm) and BSCFMo0.20-(Co/Fe=2.62) (61(2) nm), which is the lowest DP% containing member of the compositional pair with Mo=0.2. This demonstrates that the DP% phase fraction and DP crystallite sizes are interdependent. The volume weighted SP crystallite size was above the

detection limit for all the samples discussed herein, in agreement with their high SP% content and as demonstrated previously (*Section 4.3.2*). The DP crystallites free of antiphase boundaries and corresponding to the superstructure odd reflections, were also found to be larger for the iso-Mo=0.25 containing compositions with Co/Fe=4 (109(13) nm) compared to the Co/Fe=2 counterpart and 46(11) nm accordingly), but approximately equal for the DP-richer BSCFMo0.2-(Co/Fe=3) (32(3) nm) compared to BSCFMo0.20-(Co/Fe=4) (34.9(7) nm) and BSCFMo0.2-(Co/Fe=2.62) (27(4) nm). This shows that the variation of Co/Fe ratio in compositions of containing equal amount of Mo affects more the total size of the incoherently diffracting DP crystallites than the size of the coherently scattering domains in the DP crystallites.

It is difficult to comment on the variation in composition with the Co/Fe ratio, since according to the refinement protocol adopted, the SP and DP compositions were not refined. As aforementioned, the lattice parameter information could tentatively give some insight on the derivation from the fixed SP and DP compositions. For the BSCFM compositional pairs having Mo=0.20, there is a decrease in the SP unit cell by 0.00457 for Co/Fe=4 to Co/Fe=3 (3.98187(9) to 3.97730(8) Å). Moreover, the DP unit cell for BSCFMo0.20-(Co/Fe=4) is smaller than the DP unit cell of BSCFMo0.20-(Co/Fe=3) with refined lattice parameters of 7.98867(60) Å and 7.98035(28) Å respectively. This demonstrates that the Co/Fe ratio has the same effect on the DP phase, as for the SP component, resulting in smaller DP unit cells when comparing compositions with the same Mo content and decreased Co/Fe ratio. The same trend is also observed for the compositional pair of BSCFMo0.25-(Co/Fe=4) and BSCFMo0.25-(Co/Fe=2), with lattice constants a_{SP}= 3.98408(8) Å, a_{DP}= 7.99126(13) Å and a_{SP}= 3.97726(8) Å, a_{DP}= 7.97945(5) respectively. Hence there is a clear tendency to smaller biphase perovskite unit cells when comparing BSCFM compounds containing the same amount of Mo as decreasing the Co/Fe ratio, possibly due to the relative higher concentration of the smaller Fe cations, similarly to the case of the SP-pure compounds consisting Mo0.125, which suggests similar mechanism for the incorporation of Mo into the perovskite components.

4.3.4.2. High Co/Fe

The effect of higher Co/Fe ratio than 4 for the parent material was studied for three compositional pairs, with Mo contents 0.125, 0.375 and 0.45, for Co/Fe ratios of 4 and 10 (*Table 4.17*). The effect of the intermediate Co/Fe ratio=6 was also investigated for the iso-Mo compositions containing Mo0.409. The refinement outcomes of BSCFMo0.125-(Co/Fe=4), BSCFMo0.409-(Co/Fe=4), BSCFMo0.45-(Co/Fe=4) (*Section 4.3.3*) and BSCFMo0.45-(Co/Fe=10) (*Section 4.3.2*) are also tabulated for comparison reasons.

The introduction of Mo=0.125 in the compound with Co/Fe=4 results in the formation of a pure SP, whilst the iso-Mo containing composition with Co/Fe ratio=10 has clearly a biphasic nature, consisting of 87.3(3) % SP and 12.7(3) % DP. The B-site ordering is thus more favored for compositions with high Co content and Co/Fe ratio, resulting in the formation of DP phase for as low Mo content as 0.125 in its B-site in BSCFMo0.125-(Co/Fe=10).

The main observation for the compositional pair with Mo0.45 is that BSCFMo0.45-(Co/Fe=10) is impurity-free, whilst the iso-Mo containing BSCFMo0.45-(Co/Fe=4) contains 7.5(1)% $BaMoO_4$ impurity phase. The DP composition coming out from the refinement of BSCFMo0.375-(Co/Fe=4) (*Section 4.1.9*), which can also be abbreviated as BSCFMo0.45-(Co/Fe=6.77), lying between BSCFMo0.45-(Co/Fe=4) and BSCFMo0.45-(Co/Fe=10), also contains small amount of $BaMoO_4$ refined to 1.5(1)%. The BSCFMo0.45-(Co/Fe=10) composition results in the formation of a highly DP rich (91.2(3) % DP) biphase compound consisting of only 8.7(3) % SP. Excluding the $BaMoO_4$ amount, the biphase assemblage in BSCFMo0.45-(Co/Fe=4) (consisting of 92.6% DP and 7.4% SP) is slightly higher in DP% content than BSCFMo0.45-(Co/Fe=10). The DP% content seems to be higher for the compositions with lower Co/Fe ratio in the case of Mo0.375 and Mo0.409 compositional pairs too. The refined DP% amount in BSCFMo0.375-(Co/Fe=4) (71.2(7) %) is significantly higher than the 55.9(4) % in BSCFMo0.375-(Co/Fe=10). The high DP nature in BSCFMo0.409-(Co/Fe=4), consisting of 85.5(7) % DP, is decreased for the iso-Mo containing in the case of BSCFMo0.409-(Co/Fe=6) with refined 77.3(12) % DP amount.

Table 4.17: Summary of structural parameters extracted from Rietveld refinements against XRD data for iso-Mo containing compositional pairs with differing Co/Fe (≥4), showing phase fractions (Phase %), lattice parameters (Lat.par.), crystallite sizes (Cr.sz), nominal and refined compositions.

Abbreviation	**Phase (%)** SP DP $BaMoO_4$	**Lat.par. (Å)** a (SP) a (DP) a, c ($BaMoO_4$)	**Cr.sz.(nm)** **SP** **DP** ***DP-odd***	**Nominal composition** Refined composition
BSCFMo0.125-(Co/Fe=4)*	100 0 0	3.97711(3) ---------- ----------	>800[(i)] ---------- ----------	**$Ba_{0.5}Sr_{0.5}Co_{0.7}Fe_{0.175}Mo_{0.125}O_{3-\delta}$** $Ba_{0.5}Sr_{0.5}(Co,Fe)_{0.876(4)}Mo_{0.124(2)}O_{3-\delta}$
BSCFMo0.125-(Co/Fe=10)	87.3(3) 12.7(3) 0	3.98167(4) 7.98727(43) ----------	>800[(i)] 70(3) *49(14)*	**$Ba_{0.5}Sr_{0.5}Co_{0.795}Fe_{0.080}Mo_{0.125}O_{3-\delta}$** $Ba_{0.5}Sr_{0.5}Co_{0.538(9)}Fe_{0.231(1)}Mo_{0.230(1)}O_{2.83(1)}$
BSCFMo0.375-(Co/Fe=4)*(#1)*	28.8(7) 71.2(7) 0	3.98476(14) 7.98108(8) ----------	98(3) 403(41) 70(4)	**$Ba_{0.5}Sr_{0.5}Co_{0.500}Fe_{0.125}Mo_{0.375}O_{3-\delta}$** $Ba_{0.5}Sr_{0.5}Co_{0.500(4)}Fe_{0.125(5)}Mo_{0.376(2)}O_{2.93(5)}$
BSCFMo0.375-(Co/Fe=10)	44.1(4) 55.9(4) 0	3.98504(8) 7.99625(14) ----------	89(2) 87(2) *81(10)*	**$Ba_{0.5}Sr_{0.5}Co_{0.582}Fe_{0.043}Mo_{0.375}O_{3-\delta}$** $Ba_{0.5}Sr_{0.5}Co_{0.510(6)}Fe_{0.153(5)}Mo_{0.335(8)}O_{2.89(9)}$
BSCFMo0.409-(Co/Fe=4)*	12.9(7) 85.5(7) 1.6(1)	3.98087(44) 7.98115(12) Bamoo4	67(4) 382(74) *84(6)*	**$Ba_{0.5}Sr_{0.5}Co_{0.473}Fe_{0.118}Mo_{0.409}O_{3-\delta}$** 98.6%$Ba_{0.5}Sr_{0.5}Co_{0.490(6)}Fe_{0.096(1)}Mo_{0.414(4)}O_{2.95(1)}$ + 1.6%$BaMoO_4$
BSCFMo0.409-(Co/Fe=6)	22.7(12) 77.3(12) 0	3.98778(24) 7.98275(9) ----------	38(3) 133(4) *49(3)*	**$Ba_{0.5}Sr_{0.5}Co_{0.500}Fe_{0.091}Mo_{0.409}O_{3-\delta}$** $Ba_{0.5}Sr_{0.5}Co_{0.496(2)}Fe_{0.114(1)}Mo_{0.389(7)}O_{2.93(5)}$
BSCFMo0.45-(Co/Fe=4)*	6.8(8) 85.7(8) 7.5(1)	3.98287(46) 7.97845(9) Bamoo4	131(19) 258(12) *81(5)*	**$Ba_{0.5}Sr_{0.5}Co_{0.440}Fe_{0.110}Mo_{0.450}O_{3-\delta}$** 92.5%$Ba_{0.5}Sr_{0.5}Co_{0.486(6)}Fe_{0.085(1)}Mo_{0.429(3)}O_{2.96(1)}$ +7.5%$BaMoO_4$
BSCFMo0.45-(Co/Fe=10)**	8.7(3) 91.2(3) 0	3.98671(13) 7.98940(4) ----------	317(79) >800[(i)] *>800[(i)]*	**$Ba_{0.5}Sr_{0.5}Co_{0.50}Fe_{0.05}Mo_{0.45}O_{3-\delta}$** $Ba_{0.5}Sr_{0.5}Co_{0486(6)}Fe_{0.087(8)}Mo_{0.425(5)}O_{2.95(8)}$

*(i) No broadening of the diffraction peaks was observed. The limit of the measureable domain size is in the region of 800 nm.*As from Section 4.3.3, ** As from Section 4.3.2.*

The SP unit cell of BSCFMo0.125-(Co/Fe=10) is bigger than the iso-Mo-containing single SP phase of BSCFMo0.125-(Co/Fe=4) composition, with refined values of 3.98167(4) and 3.97711(3) Å respectively. This is further demonstrated by the even smaller lattice parameters for the SP forming BSCFMo0.125-(Co/Fe=2) (*Section 4.3.4.1*) of 3.97599(4) Å. Similarly, both SP and DP unit cells increase when the Co/Fe increases from 4 to 10 for the iso-Mo=0.375 and Mo=0.45 containing compositions. The BSCFMo0.375-(Co/Fe=4) compound (a_{SP}= 3.98476(14) Å, a_{DP}= 7.98108(8) Å) affords the formation of smaller perovskite unit cells than BSCFMo0.375-(Co/Fe=10) with refined values of a_{SP}= 3.98504(8) Å and a_{DP}= 7.99625(14) Å. For the compositional pair of Mo0.45, the SP lattice parameters increase from 3.98287(46) to 3.98671(13) and the DP lattice constants from 7.97845(9) Å, 7.98940(4) Å for BSCFMo0.45-(Co/Fe=4) and BSCFMo0.45-(Co/Fe=10) respectively. The same trend was also observed for the intermediate Co/Fe ratio of 6 for BSCFMo0.409-(Co/Fe=6) (a_{SP}= 3.98778(24) Å, a_{DP}= 7.98275(9) Å), forming bigger unit cells than its BSCFMo0.409-(Co/Fe=4) pair (a_{SP}= 3.98087(44) Å, a_{DP}= 7.98115(12) Å). This demonstrates a general tendency to bigger perovskite cells for compositions with higher Co/Fe ratio in an iso-Mo containing compositional pair, in agreement with the outcome of *Section 4.3.4.1* for both SP-pure and SP/DP biphasic compounds.

4.3.4.3. Discussion for effect of Co/Fe ratio

It is difficult to comment about the mechanism of Mo incorporation into the distinct perovskite phases for compositions with varying the Co/Fe ratio, since variations in the SP and DP compositions were not refined according to the refinement protocol adopted due to the difficulties of the BSCFM system. According to the refinements for a range of BSCFM compositions with Co/Fe≠ 4, there is a prevailing tendency to larger SP and DP unit cells as Co/Fe increases for all compositional pairs studied (BSCFMo0.125, BSCFMo0.20, BSCFMo0.25, BSCFMo0.375, BSCFMo0.409 and BSCFMo0.45 in *Sections 4.3.4.1* and *4.3.4.2*), regardless of the overall Mo content and the formation of the $BaMoO_4$ impurity phase. This is likely due to the higher relative concentration of the bigger Co^{2+} (0.745 Å) compared to the smaller Fe^{3+} (0.645 Å) ions, where Co^{2+} and Fe^{3+}represent the lowest possible oxidation state of the valent-alterable transition metals in a perovskite structure upon reduction by Mo^{6+}. This suggests very tentatively that compositions having lower overall Co/Fe form SP or SP/DP biphase compounds which have analogically lower Co/Fe ratio in each of the perovskite phases compared to BSCFM compounds with higher overall Co/Fe ratio. Consequently, this implies that the amount of Mo incorporated in each phase is also dependent on the Co/Fe ratio.

Compositions with higher Co/Fe ratio (and hence overall amount of Co) are more prone to B-site ordering between Co-Mo and hence less Mo would be adequate for phase segregation to SP and DP components with Co/Fe ratio close to the overall. This has been demonstrated for the iso-Mo=0.125 compositions, for which it becomes clear though that the higher Co/Fe ratio in BSCFMo0.125-(Co/Fe=10) favors the formation of the DP phase (12.7%DP), whilst absent in the case of the compositions with lower Co/Fe ratio (BSCFMo0.125-(Co/Fe=2) and BSCFMo0.125-(Co/Fe=4). This is also observed in the case of BSCFMo0.25 compositional pairs with Co/Fe=2 and 4. BSCFMo0.25-(Co/Fe=4) affords the formation of significantly more DP (61.6(4) % DP) compared to BSCFMo0.25-(Co/Fe=2) which is a SP-rich compound with only 18.5(6)% refined amount of DP.

Even if higher Co/Fe ratio favors the DP formation for low Mo content compositions (Mo0.125, Mo0.25), the opposite occurs for higher Mo contents (Mo0.375, Mo0.409 and Mo0.45). For instance, the refined DP% content for BSCFMo0.375-(Co/Fe=10) is less than for

BSCFMo0.375-(Co/Fe=4), with 71.2(7) % and 55.9(4) % DP respectively, likely due to the entropically favored disordered competing SP phase. This suggests that the incorporation of Mo in the SP/DP biphase compounds occurs either in the SP or in the DP phase, via competing processes.

The maximum limit for impurity-free biphasic compounds seems to be strongly dependent on the Co/Fe ratio, being as low as Mo0.25 for Co/Fe=2 but increasing to Mo0.409 for Co/Fe=4. For compositions with Co/Fe ratio > 4, the formation of the undesirable $BaMoO_4$impurity phase is suppressed for as high Mo content as 0.45 as for instance BSCFMo0.45-(Co/Fe=10) which is an impurity-free compound. Hence, the expulsion of $BaMoO_4$ impurity phase indicates that the biphasic system cannot afford the incorporation of the increasing amount of Mo^{6+}.As discussed in Chapter 3, *Section 3.3.1*, the incorporation of Mo^{6+} induces the reduction of the valent-alterable metals to their lowest possible oxidation states of Co^{2+} and Fe^{3+}, for charge balance reasons. This means that the total charge in Fe-rich (low Co/Fe ratio) compositions would be higher than in Co-rich (high Co/Fe) BSCFM specimens. Therefore, the B-site ordering is favored for compositions with increasing Co/Fe ratio, whilst the formation of $BaMoO_4$ becomes favorable for the compositions with high total charge and Fe content. This is further discussed in *Section 4.3.5* aiming for a pure-DP compound.

4.3.5. Synthetic efforts for a pure double perovskite (DP)

The aim of the experiment described in this section was to obtain a pure DP forming composition, without any SP content and free of $BaMoO_4$ impurity phase. For all compositions presented herein (*Table 4.18*), their B-site is half-filled with Co, and the Mo content varies inversely from the Fe content. The BSCFMo0.25-(Co/Fe=2) (*Section 4.3.4.1*), BSCFMo0.375-(Co/Fe=4) (*Section 4.3.3*) and BSCFMo0.45-(Co/Fe=10) (*Section 4.3.4.2*) compositions, which have also Co=0.5 content, are included in this study for comparison reasons.

As can be seen in *Figure 4.18* and, there is a clear tendency to higher DP% as the Mo content increases and Fe decreases. Taken as the starting point the BSCFMo0.25-(Co/Fe=2) biphase compound, consisting of 80.2(6) % SP and 18.5(6)% DP, further addition of Mo results in gradually higher DP% content in the biphasic assemblages, as for instance BSCFMo0.375-(Co/Fe=4) and BSCFMo0.45-(Co/Fe=10) specimens containing 71.2(7) % DP and 91.2(3) % DP respectively.

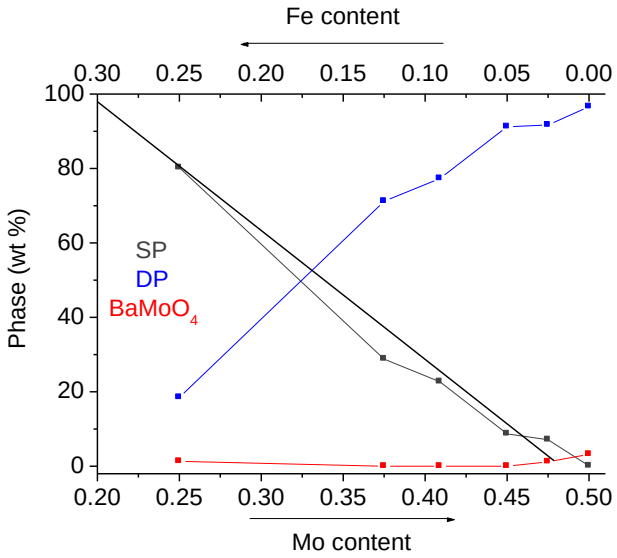

Figure 4.18: Evolution of % phase by weight with increasing the Mo content and decreasing the Fe content, based on Rietveld refinements against XRD data for the series of BSCFM compositions for which the B-site is half-filled with Co.

Another interesting observation from *Figure 4.19*, is the evolution in the weight % of the $BaMoO_4$ phase. The formation of the impurity phase is suppressed with increasing the Mo

content, and subsequently decreasing the Fe content, from BSCFMo0.25-(Co/Fe=2) (1.3(1)% $BaMoO_4$) to BSCFMo0.45-(Co/Fe=10), as discussed in *Section 4.3.4.3*. However, for the higher Mo contents in BSCFMo0.475-(Co/Fe=20) and BSCFMo0.5-(Co/Fe=∞), it increases slightly to 1.2(1)% and 3.2(1)% respectively.

As discussed previously (*Section 4.1.3*), the driving force for the formation of the DP phase is the B-site ordering induced by the adequate differences in charge and size of the B-site cations. Upon substitution with Mo^{6+}, B-site ordering occurs between the larger and lower charged Co^{2+} (0.745 Å) ions and the smaller and higher charged Mo^{6+} (0.59 Å), resulting in a Co-rich and a Mo-rich octahedral site. Complete B-site order would be therefore expected for Mo=0.5, however addition of Mo≥ 0.475 results in the formation of $BaMoO_4$ impurity phase. The BSCMo0.5-(Co/Fe=∞) specimen with nominal composition $Ba_{0.5}Sr_{0.5}Co_{0.5}Fe_0Mo_{0.5}O_{3-\delta}$ (or $BaSrCoMoO_6$) is an SP-free compound within error, but contains some small amount of $BaMoO_4$. This demonstrates that the formation of a pure DP compound is not favoured under the synthesis conditions. According to the literature, the synthesis of the isostructural DP compounds $BaCoMoO_6$ and Ba_2CoWO_6, also crystallising in Fm3m, is accompanied with the formation of the $Ba(Mo,W)O_4$ impurity phase [119] and to the best knowledge of the author, there is no report for impurity-free cubic perovskite report[249-251], whilst the Sr-analogue, Sr_2CoMoO_6 crystallises in tetragonal space group[252-254]. This demonstrates that the formation of $BaMoO_4$ is favoured under the synthesis conditions in this study. This is likely due to the fact that the synthesis is conducted in air and hence some oxidation of Co^{2+} to Co^{3+} might occur and hence resulting in the expulsion of the excess Mo^{6+} as $BaMoO_4$. It is worth noting the synthesis of pure $BaMoO_4$ is reported to be made also at 1000°C in air[255], similarly with the conditions used for the synthesis of BSCFM compounds. Inert or slightly reducing synthesis conditions might prevent the formation of $BaMoO_4$ phases and result in impurity-free $BaSrCoMoO_6$.

Table 4.18: Summary of structural parameters extracted from Rietveld refinements against XRD data for BSCFM for which the B-site is half-filled woth Co, showing phase fractions (Phase %), lattice parameters (Lat.par.), crystallite sizes (Cr.sz), nominal and refined compositions.

	Phase(%) SP DP $BaMoO_4$	**Lat.par. (Å)** a (SP) a (DP) a, c ($BaMoO_4$)	**Cr.sz.(nm)** SP DP *DP-odd*	**Nominal composition** Refined composition
BSCFMo0.25-(Co/Fe=2)**	80.2(6) 18.5(6) 1.3(1)	3.97726(8) 7.97945(60) 5.549(1), 12.824(5)	>800[(i)] 79(5) *46(11)*	**$Ba_{0.5}Sr_{0.5}Co_{0.500}Fe_{0.250}Mo_{0.250}O_{3-\delta}$** 98.7%$Ba_{0.5}Sr_{0.5}Co_{0.535(1)}Fe_{0.220(4)}Mo_{0.244(6)}O_{2.84(1)}$ +1.3% $BaMoO_4$
BSCFMo0.375-(Co/Fe=4)(#1)*	28.8(7) 71.2(7) 0	3.98476(14) 7.98108(8) ----------	98(3) 403(41) *70(4)*	**$Ba_{0.5}Sr_{0.5}Co_{0.500}Fe_{0.125}Mo_{0.375}O_{3-\delta}$** $Ba_{0.5}Sr_{0.5}Co_{0.500(4)}Fe_{0.125(5)}Mo_{0.376(2)}O_{2.93(5)}$
BSCFMo0.409-(Co/Fe=6)	22.7(12) 77.3(12) 0	3.98778(24) 7.98275(9) ----------	38(3) 133(4) *49(3)*	**$Ba_{0.5}Sr_{0.5}Co_{0.500}Fe_{0.091}Mo_{0.409}O_{3-\delta}$** $Ba_{0.5}Sr_{0.5}Co_{0.496(2)}Fe_{0.114(1)}Mo_{0.389(7)}O_{2.93(5)}$
BSCFMo0.45-(Co/Fe=10)***	8.7(3) 91.2(3) 0	3.98671(13) 7.98940(4) ----------	317(79) >800[(i)] *>800*[(i)]	**$Ba_{0.5}Sr_{0.5}Co_{0.50}Fe_{0.05}Mo_{0.45}O_{3-\delta}$** $Ba_{0.5}Sr_{0.5}Co_{0486(6)}Fe_{0.087(8)}Mo_{0.425(5)}O_{2.95(8)}$
BSCFMo0.475-(Co/Fe=20)	7.1(3) 91.7(3) 1.2(1)	3.98485(15) 7.99056(4) 5.528(3), 12.67(1)	--- >800[(i)] *>800*[(i)]	**$Ba_{0.5}Sr_{0.5}Co_{0.500}Fe_{0.025}Mo_{0.475}O_{3-\delta}$** 98.8%$Ba_{0.5}Sr_{0.5}Co_{0485(5)}Fe_{0.084(7)}Mo_{0.429(7)}O_{2.96(1)}$ +1.2% $BaMoO_4$
BSCMo0.5-(Co/Fe=∞)	0.1(1) 96.6(2) 3.2(1)	4.16(2) 7.99429(7) 5.557(1), 12.760(4)	---- 97(6) *103(1)*	**$Ba_{0.5}Sr_{0.5}Co_{0.500}Fe_{0.000}Mo_{0.500}O_{3-\delta}$** 96.7%$Ba_{0.5}Sr_{0.5}Co_{0.552(8)}Mo_{0.448(2)}O_{2.97(2)}$ +3.2% $BaMoO_4$

(i) No broadening of the diffraction peaks was observed. The limit of the measureable domain size is in the region of 800 nm.

**As from Section 4.3.3, **As from Section 4.3.4.1, ***As from Section 4.3.4.2*

The lattice parameters of the major DP phase (*Figure 4.19*, plotted as $a_P = a_{DP}/2$) are just slightly increased for the compositional range between BSCFMo0.25-(Co/Fe=2) and BSCFMo0.375-(Co/Fe=4) from 7.97945(60) Å to 7.98108(8) Å respectively, accompanied by an approximately 4 times increase in the DP content from 18.5(6)% to 71.2(7)% accordingly. Moving to higher Mo content and Co/Fe ratio towards BSCMo0.5-(Co/Fe=∞), results in more significantly increase of the DP lattice parameter to 7.99429(7) Å, whilst the refined DP content of 96.6(2)% indicates an increase of about 1.5 times. This demonstrates that the main effect of introducing Mo in the iso-Co compositions, with subsequent decrease in the Fe content, is the increase of the DP volume, which is likely to have very similar composition. When reaching a maximum of approximately 70% for BSCFMo0.375-(Co/Fe=4), the DP composition is likely affected, which however was not refined according to the refinement protocol used.

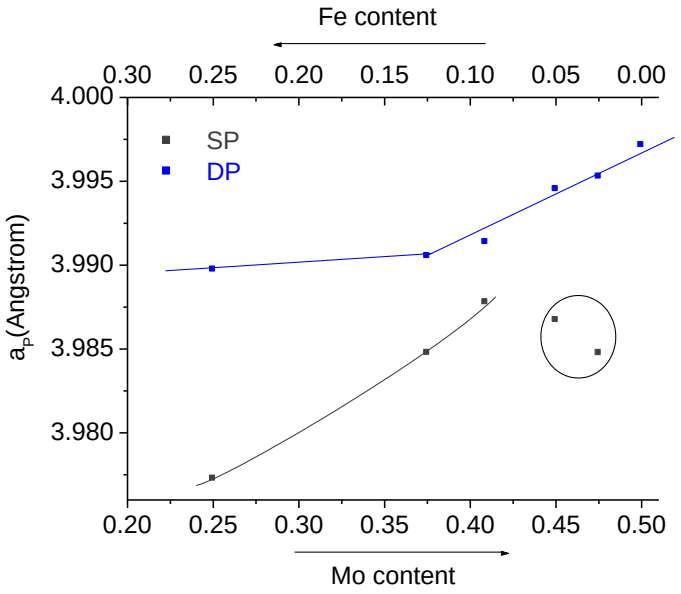

Figure 4.19: Evolution of perovskite lattice parameters for SP ($a_P = a_{SP}$) and DP ($a_P = a_{DP}/2$) with increasing Mo content and decreasing Fe content, in compositions for which their B-site is half-filled with Co.

Considering the global composition, the variable charged transition metals ($Co^{2+/3+/4+}$, $Fe^{3+/4+}$) are reduced upon substitution by d0 Mo^{6+}. In general, cations with lower oxidation state are larger in size than for the same cations higher charged. The ionic radii for Co^{2+} (0.745 Å), in 6-fold coordination environment as in the perovskite structure and high-spin state, is bigger than the corresponding values for Co^{3+} (0.61 Å) and Co^{4+} (0.53 Å). Similarly, Fe^{3+} cations (0.645 Å) are

larger than the Fe^{4+} (0.585 Å) counterparts. Since increasing amount of Mo^{6+} induces the reduction of the transition metals to the lowest oxidation state possible under the synthesis conditions (i.e. Co^{2+} and Fe^{3+}), the perovskite unit cell is expected to expand.

The unit cell for the minor SP phase also expands from 3.97726(8) Å to 3.98778(24) Å for BSCFMo0.25-(Co/Fe=2) and BSCFMo0.409-(Co/Fe=6) respectively. The slight decrease in the SP lattice constants for the BSCFMo0.45-(Co/Fe=10) and BSCFMo0.475-(Co/Fe=20) is most likely due to experimental errors due to the very small 7-8% refined amount.

4.4. Summary and Conclusions

According to the combined refinement of X-ray (XRD) and Neutron diffraction (ND) data, BSCFMo0.375-(Co/Fe=4), with refined composition $Ba_{0.5}Sr_{0.5}Co_{0.500(3)}Fe_{0.125(1)}Mo_{0.375(3)}O_{2.94(1)}$, is a DP-rich compound, consisting of 70.81(10) % DP and 28.13(9) % SP by weight. There is also a small amount of $BaMoO_4$ (1.06 (8) %), detectable only for the sample for which the joint XRD/ND refinement was performed. Both SP and DP components in BSCFMo0.375-(Co/Fe=4) are A-site disordered whilst B-site ordering occurs only in the DP in contrast to the SP counterpart, as coming out from both the joint Rietveld refinement and confirmed by the HAADF analysis. The SP component was refined to $Ba_{0.5}Sr_{0.5}Co_{0.547(9)}Fe_{0.253(2)}Mo_{0.200(8)}O_{2.81(3)}$, with determined Co and Fe in their trivalent states. The DP phase was refined to $Ba_{0.5}Sr_{0.5}Co_{0.480(1)}Fe_{0.071(1)}Mo_{0.449(2)}O_{2.98(2)}$, with high Mo content and Co in its divalent oxidation state, whilst Fe is still present as Fe^{3+}. This demonstrates that the size and charge differences of Co^{2+} (0.745 Å, in high spin state) and Mo^{6+} (0.59 Å) favor the B-site ordering in the DP component, resulting in a Co-rich (refined composition $Co_{0.480(1)}Fe_{0.020(1))}$) and a Mo-rich (refined composition $Mo_{0.449(2)}Fe_{0.051(2)}$) antisite, similarly to the isostructural $BaCoMoO_6$.

The overall low Co oxidation state (calculated to 2.47+) in BSCFMo0.375-(Co/Fe=4) compared to BSCF (calculated to 3.3+), induced by substitution by Mo^{6+}, and the subsequent low oxygen non-stoichiometry (δ= 0.7) are believed to be the reason for the decrease in the linear thermal expansion coefficient (TEC= 13.87×10^{-6} K^{-1}), compared to BSCF (δ= 0.29, TEC= 19.5-20.86 K^{-1}) and hence showing very good matching with conventional used IT-SOFCs electrolytes.

Hence, the introduction of the d0 Mo^{6+} causes the reduction of the d^n Co, Fe cations to lower oxidation states and concomitant decrease of the charge carriers, resulting in low electrical conductivity (Chapter 3, *Section 3.3.1*). The good performance of BSCF has been attributed to its high oxygen non-stoichiometry and high oxygen ionic mobility in the bulk[69]. Hence, against expectation, BSCFMo0.375-(Co/Fe=4) is not a poor cathode even if it has lower electrical conductivity and significantly higher oxygen content than BSCF, suggesting that the cathode material behaves in a different way. The good electrochemical performance of BSCFMo0.3.75-(Co/Fe=4) among the rest BSCFM compositions studied must be due to the interplay of the SP and DP component phases.

As coming out from the evolution of the biphasic assemblage with temperature, there are two competing processes that dominate the BSCFMo0.375-(Co/Fe=4) system, favoring the increase of either the SP or the DP content. As coming out from the variable temperature in-situ experiment in combination with the quenching analysis from the last step of the synthesis procedure (annealing at 1000^{o}C for10h) clearly show that temperature favors the enrichment in the entropically favored disordered SP, as indicated by the increase in both weight% and volume weight SP crystallite size. This was attributed to the breaking of the antiphase boundaries in the DP crystallites upon heating. As coming out from the microstructural analysis, the DP crystallites free of antiphase boundaries and corresponding to the DP-odd reflections, represent 71% of the total volume of the DP crystallites for the quenched sample from the synthesis temperature, whilst they represent the 30% and 37% of the total DP volume for the specimen at room temperature and 900^{o}C respectively, as coming out from the in-situ diffraction experiment at the temperature range 25-900^{o}C. However, when the sample was annealed at higher temperature of 1200^{o}C for 10h, followed by either quenching or slow cooling, the SP content in the biphase assemblage is decreased, indicating that the B-site ordering becomes more favourable resulting in higher DP content (86%). Pure DP was not achieved, implying that the reaction occurs via a mechanism based on nucleation and growth, rather than spinodal decomposition for which metastable structures result in a single phase at high temperature.

The two competing processes of favoring the SP or DP formation are evident throughout the whole BSCFM compositional range. The B-site ordering is favored for high Mo content

resulting in gradually increasing DP% content for the example of $BSCFMo_{Mo}$-(Co/Fe=4) series of compositions. For low Mo content (Mo≤0.25), high overall Co/Fe ratio favors the B-site ordering between Co^{2+}-Mo^{6+} due to the high Co content, as in the case of BSCFMo0.125-(Co/Fe=10) which is a biphasic compound, containing 12.7% DP, whilst BSCFMo0.125-(Co/Fe=4) and BSCFMo0.125-(Co/Fe=2) are pure SP compounds from the diffraction data. In the case of the BSCFMo0.25 compositional pair, the major phase in BSCFMo0.25-(Co/Fe=4) is DP with refined content of 61.6(4)%, whilst BSCFMo0.25-(Co/Fe=2) is an SP-rich compound with just 18.5% DP. Moreover, the combination of high Mo and low Fe content, favors the B-site ordering and gradual increase in DP% content in compositions which are half-filled with Co, leading to the SP-free within error BSCFMo0.5-(Co/Fe=∞).

The competing process of SP enrichment in the biphasic compounds, becomes evident for high Mo- containing specimens. In the compositional pairs of BSCFMo0.375 and BSCFMo0.409, the SP phase fraction increases with the increase of the Co/Fe ratio. For instance, the SP% weight fraction in BSCFMo0.375-(Co/Fe=10) is 44.1(4)% SP that is about 1.5 times more than BSCFMo0.375-(Co/Fe=4), indicating that the B-site ordering is less favored and that Mo^{6+} is preferentially accommodated in the SP structure. The study of the $BSCFMo_{Mo}$-(Co/Fe=4) series reveal that even if there is a clear tendency to increasing DP% with increasing Mo content, the fluctuation in lattice parameters of the minor SP phase for Mo≥0.25 in contrast with the DP counterpart, suggest tentatively some non-controlled Mo incorporation into the SP structure.

The formation of the $BaMoO_4$ impurity phase was often encountered in the BSCFM biphasic compounds, with no more than 10% weight fraction in all cases. As coming out from the in-situ diffraction experiment for BSCFMo0.375-(Co/Fe=4), $BaMoO_4$ starts forming at 900^{o}C with refined content of 1.04(8)% and increases with temperature reaching approximately 4% for both samples quenched after 10h annealing at the synthesis temperature (1000^{o}C) and 1200^{o}C. However, the slow cooling from the synthesis temperature seems to favor the incorporation of $BaMoO_4$ in the biphasic assemblage in BSCFMo0.375-(Co/Fe=4).

The expulsion of $BaMoO_4$ from the BSCFM compounds was found to be greatly dependent on the Co/Fe ratio, indicating the maximum Mo that can be introduced into the perovskite biphasic

structure. The formation of 1.3(1)% $BaMoO_4$ in BSCFMo0.25-(Co/Fe=2) highlights that the high charge of Mo^{6+} cannot be compensated by charge balance and reduction of the transition metals. This is due to its relative high overall Fe content that can only be reduced to Fe^{3+} at the synthesis conditions, whilst further reduction to its divalent state needs temperatures above 1560^{o}C in air or more extreme reducing conditions. On the contrary, Co can be reduced to its divalent state upon Mo^{6+} incorporation into the BSCFM system, since Co^{2+} is one of the common oxidation states of cobalt in air. For the $BSCFMo_{Mo}$-(Co/Fe=4) series, $BaMoO_4$ starts forming for Mo≥ 0.409, with increasing content from 1.6(1)% to 7.5(1)% for BSCFMo0.409-(Co/Fe=4) and BSCFMo0.45-(Co/Fe=4) respectively, implying that the system cannot counterbalance the high charge induced by the Mo^{6+} incorporation. The formation of $BaMoO_4$ is further suppressed for as high Mo content as 0.45 in the Co-rich BSCFMo0.45-(Co/Fe=10), with only 0.05Fe in its B-site. Finally, the expulsion of 3.2(1)% $BaMoO_4$ from the end member BSCFMo0.5-(Co/Fe=∞), which does not contain Fe and is an SP-free compound, suggest that the formation of a pure DP compound is not favoured under the synthesis conditions in air, that is likely to favor the oxidation of a small amount of Co^{2+} to Co^{3+}.

5. CHAPTER 5-ELECTROCHEMICAL STUDIES OF BSCFM OXIDES

Electrochemical studies of BSCFM oxides

This chapter aims to provide some more insight in the electrochemical properties of BSCFM oxide materials, for which some results were already shown in Chapter 3 (*Section 3.3.3*). The electrochemical measurements, performed by AC impedance spectroscopy, were initially focused on BSCFMo0.375-(Co/Fe=4) (*Section 5.1*) which was found to successfully suppress the phase transition observed for the parent undoped BSCF compound. This composition contains the highest Mo content at the optimal Co/Fe ratio that makes the parent undoped BSCF a good cathode candidate, without favoring the formation of $BaMoO_4$ impurity phase observed with increasing further the Mo content. All these factors contributed to the selection of BSCFMo0.375-(Co/Fe=4) as the starting composition for electrochemical measurements. The starting point was to establish a protocol for the preparation of materials for measurements. The preparation procedure involves a number of different steps which can affect significantly the activity of cathode materials over oxygen reduction; a number of processing variables are discussed in *Section 5.1.1*. The established optimised preparation protocol was then used for the measurement of other compositions in order to evaluate the compositional features controlling the electrochemical performance in the BSCFM family of oxides (*Section 5.2*).

In *Section 5.1.2*, the mechanism of oxygen reduction reaction under variable oxygen partial pressure (pO_2) and temperature for the BSCFM oxides family is investigated for the case of BSCFMo0.375-(Co/Fe=4).

5.1. Electrochemical analysis of BSCFMo0.375-(Co/Fe=4)

5.1.1. Optimisation of symmetrical cells fabrication- key parameters

The electrochemical performance of the BSCFM materials was tested in the 'symmetrical cells' configuration. For this, fine powders are mixed with an organic pore former and the resulting ink is deposited on both sides of a dense electrolyte substrate; in this study screen printing was used for the deposition of the BSCFM inks. The fabrication of symmetrical cells is a complicated procedure including many key steps and hence optimisation of the processing is crucial in order to minimize any ohmic losses[256]. Most importantly is the cathode morphology which is believed to strongly affect the performance[21]. The cathode porosity can be influenced by the ratio of powder: pore former and the temperature needed for the adhesion of the cathode ink onto the electrolyte; at this high temperature step (usually 900-1100 ^{o}C) the organic pore former burns off providing the required porosity to the cathode layer[69]. Both parameters were investigated in the case of BSCFMo0.375-(Co/Fe=4) in order to achieve an optimised behavior.

In addition, the thickness of the deposited cathode ink can also be another key parameter in the preparation of symmetrical cells. It has been recently demonstrated[158] that in the case of the parent BSCF deposited on GDC ($Gd_{0.2}Ce_{0.8}O_{1.9}$) electrolyte by electrostatic slurry spray deposition, the polarisation resistance at 500 °C and the associated activation energy at the temperature range 500-950^{o}C were about 61% and 22% lower when two layers of BSCF cathode coating (thickness about 25 μm) were applied to the electrolyte substrate, compared to one layer. The enhanced performance of the thicker cathode was attributed to the enlargement of the active area for oxygen reduction. This was also the reasoning for fuel cell enhanced performance when double layer LSCF ($La_{0.6}Sr_{0.4}Co_{0.2}Fe_{0.8}O_3$) cathode was used in cells fabricated by Ni-O-SDC anode and SDC electrolyte[257].

The electrolyte chosen for this study was $Ce_{0.8}Sm_{0.2}O_{2-\delta}$ (SDC), which has shown the best chemical compatibility compared to other electrolytes[258-263], and it was used in the original report for BSCF[264]. The electrolyte substrates were obtained from commercial powder (*NexTech Materials Ltd, BET: 40 m^2/g*) by uniaxial pressing (3 tonnes) into disks of 10 mm diameter and sintered at 1400°C for 8 hours to obtain the desirable relative density, this was

measured to 90-95% as described in Chapter 2, *Section 2.7.2.4*. The surface of the electrolyte substrate is another critical parameter that can influence the cathode performance, since it is part of the active sites located at the triple phase boundary (TPB) where the electrolyte-cathode and oxygen meet[265].

In order to identify the best procedure for the fabrication of the symmetrical cells, a range of different BSCFMo0.375-(Co/Fe=4)/SDC/BSCFMo0.375-(Co/Fe=4) cells were measured, varying the key parameters considered to affect the electrode performance. The SOFC cathode performance was evaluated by the measured area-specific resistance (ASR, *Section 2.7.2.4, Equation 2.48*), which is the measured resistance normalised and divided by two to take into account the symmetry of the cell.

5.1.1.1. Particle size of starting materials

The BSCFM materials were prepared via a solid state synthesis (*Sections 2.1* and *3.1.1.2*) which is based on prolonged firing at high temperatures to ensure reaction to products; under these conditions particle agglomeration is favorable. In the case of cathode materials which serve as catalysts for the oxygen reduction, small particle size is required. This is the reason that sol-gel is often employed for cathode materials synthesis resulting in nano-scale particles[266]. In this study, mechanical planetary ball-milling was introduced in order to provide fine powders prior to the fabrication of the cells. Ball-milling is a high energy method of mixing, effective in reducing the particle size and in many cases can result in reaction without any further treatment[267, 268].

The as-made BSCFMo0.375-(Co/Fe=4) powder was ball-milled in isopropanol for 8h in ZrO_2 pots with 10mm ZrO_2 balls. The particle size before and after milling procedure was estimated from the surface area measured by the BET method, according to *Equation 5.1* and are summarised in *Table 5.1*.

$$\text{Average particle size (nm)} = \frac{6}{\text{BET}\left(\text{m}^2/\text{g}\right) \text{x d}\left(\text{g}/\text{cm}^3\right)} \text{ x } 1000 \qquad \textit{Equation 5.1}$$

where BET (m^2/g) is the specific surface area per unit mass and d (g/cm^3) the true density; the density value of $5.71 \text{x} 10^6$ g/cm^3 used for the calculations herein was determined by pycnometry.

Table 5.1: Particle size of BSCFMo0.375-(Co/Fe=4) before and after milling

BSCFMo0.375-(Co/Fe=4)	**As made powder**	**Milled powder**
BET (m^2/g)	0.52	5.16
Particle size (nm)	2018.2	203.4

As can be seen from *Table 5.1,* the particle size is reduced by approximately an order of magnitude when ball-milling is used and therefore this step was considered crucial for the preparation procedure of the powders for electrochemical measurements.

5.1.1.2. Effect of cathode thickness and electrolyte surface

In order to evaluate the best performance for BSCFMo0.375-(Co/Fe=4), two parallel experiments were performed using two different pore-formers, shown in *Figure 5.1A* (Transport paste, item#311006 from fuelcell materials) and *Figure 5.1B* (V006 from Heraeus) respectively.

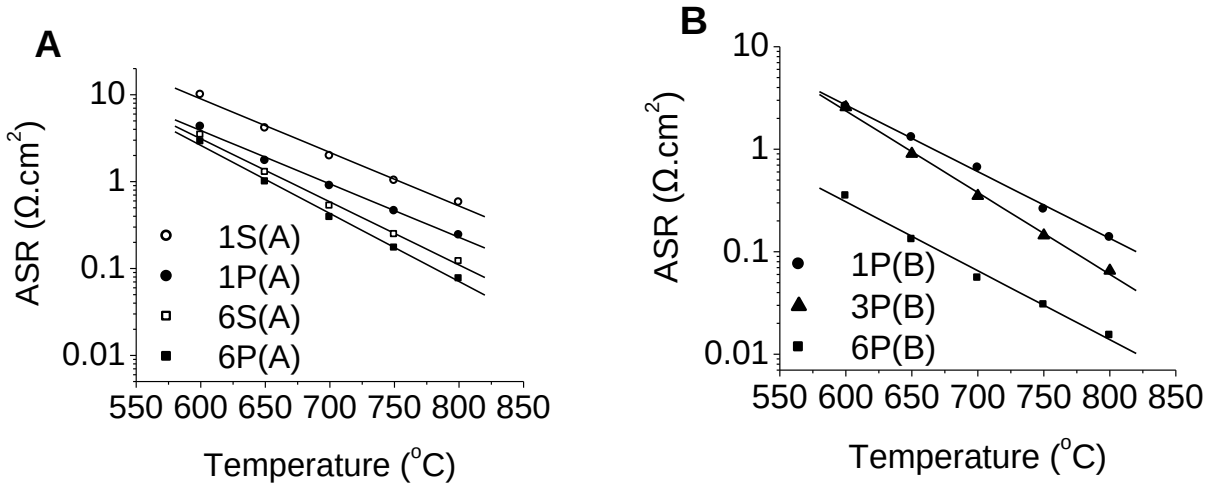

Figure 5.1: Measured area specific resistance (ASR) over the temperature range 600-800°C for symmetrical cells of BSCFMo0.375-(Co/Fe=4), prepared by mixing 60:40 ratio by weight powder of BSCFMo0.375-(Co/Fe=4) with an organic pore-former (A) Transport paste (item# 311006 from fuel cell materials) and (B) V-006 from Heraeus. The cells varied in the thickness of the cathode coating and the preparation of the SDC electrolyte substrate, as listed in Table 5.2. All the symmetric cells were heated at the same conditions for the adhesion of the cathode coating onto the electrolyte substrate.

All the inks consisted of 60:40 by weight ratio of powder: pore former for both experiments and after the printing all cells were heated at the same conditions (950°C for 3h). The variables in the

fabrication of the cells were the thickness of the deposited cathode layer (1, 3 or 6 layers, about 4μm each as established from SEM, *Section 5.1.1.4*). The preparative treatment of the surface of the SDC electrolyte was also a variable, used either just after the sintering (sintered) or polished with SiC sandpapers (first with No.240, then with No.320 and finally No.600) to ensure similar thickness (ca. 1.5-2.0mm measured by caliper) and removal of impurities. *Table 5.2* summarises the variables for the BSCFMo0.375-(Co/Fe=4) cells, the measured area specific resistance (ASR) and the associated activation energy over the whole temperature range measured (600-800^{o}C).

Table 5.2: List of symmetrical cells of BSCFMo0.375-(Co/Fe=4) on SDC, fabricated under different conditions, varying in the pore-former, the layers of the cathode coating and the surface of the electrolyte surface, and their electrochemical performance as evaluated by the measured area specific resistance (ASR) and the associated activation energy.

Cell code	**Pore-former**	**Cathode layers**	**SDC substrate**	**ASR (Ω.cm^2) 650^{o}C**	**ASR (Ω .cm^2) 700^{o}C**	**ASR (Ω.cm^2) 750^{o}C**	**Ea (eV)**
1S(A)	A	1	Sintered	4.115	1.973	1.0265	1.15
1P(A)	A	1	Polished	1.739	0.893	0.439	1.14
6S(A)	A	6	Sintered	1.281	0.524	0.246	1.35
6P(A)	A	6	Polished	0.997	0.381	0.172	1.46
1P(B)	B	1	Polished	1.301	0.660	0.260	1.20
3P(B)	B	3	Polished	0.903	0.350	0.144	1.48
6P(B)	B	6	Polished	0.132	0.055	0.0303	1.25

The thickness of the cathode layer seems to be an important factor for the performance of the cells measured using the organic pore-former A (*Figure 5.1A* and *Table 5.2*). The measured ASR in experiment A was found to be lower when applying 6 layers of the cathode ink (cells 6S(A), ASR(650^{o}C)= 1.281 Ω.cm^2 and 6P(A), ASR(650^{o}C)= 0.997 Ω.cm^2) compared to the mono-layered cathode cells (cells 1S(A), ASR(650^{o}C)= 4.115 Ω.cm^2 and 1P(A), ASR(650^{o}C)= 1.739 Ω.cm^2 respectively), regardless the nature of the SDC electrolyte substrate. This is confirmed by the second set of cells, made by the binder B (*Figure 5.1B* and *Table 5.2*), showing that the lowest cathode polarisation resistance was achieved for the 6-layered cathode ink (cell 6S(B),

ASR(650^{o}C)= 0.132 Ω.cm^2) compared to 1 (cell 1P(B)) or 3-layered (cell 3P(B)) inks deposited on the polished SDC substrate with obtained ASRs of 1.301 and 0.903 Ω.cm^2 respectively . Moreover, the preparative treatment of the electrolyte substrate seems to affect the performance of the measured cells. In experiment A, the polished cells show lower ASR compared to the non-polished specimens. The measured ASR of the mono-layer deposited cathode coating on the sintered SDC substrate (1S(A), 4.115 Ω.cm^2 at 650^{o}C) is about two times lower than the corresponding polished cell (1P(A), 1.739 Ω.cm^2 at 650^{o}C). Similarly, the electrochemical performance of the 6-layered cell on the sintered SDC substrate (6S(A) and 6P(A)) is improved when the electrolyte surface is slightly polished, with obtained ASR values of 1.281 and 0.997 Ω.cm^2 respectively. The activation energy of all cells vary between 1.15-1.48 eV, with minimum cell 1P(A) and maximum for cell 3P(B), hence no trend was observed. The average activation energy for all BSCFMo0.375-(Co/Fe=4) cells measured was 1.3(1) eV. Overall, the lowest resistance was obtained for the 6-layered deposited cathode, made by binder B, on the polished SDC surface (cell 6P(B)).

The dependence of the electrochemical activity towards the oxygen reduction reaction (ORR) on the thickness of the deposited cathode coating has been also reported for the parent BSCF [158, 264] and associated with the extent of the bulk cathode oxygen path in the case of mixed electronic-ionic conductors compared to pure electronic conductors [68]. This suggests that the oxygen ionic conductivity of BSCFMo0.375-(Co/Fe=4) is not negligible. As coming out from the extensive structural analysis in Chapter 4, BSCFMo0.375-(Co/Fe=4) consists mainly (70% by weight) by the double perovskite phase (DP), which is oxygen stoichiometric (*Section 4.1.3*), and 30% by weight of single perovskite (SP), which has a significant number of oxygen vacancies. Hence the number of oxygen vacancies in the total is likely attributed to be the minor SP component.

The importance of polishing the SDC electrolyte substrate can be related to the removal of surface contamination but also to the increase of the surface roughness, which can result in increasing the cathode/electrolyte interface providing more active sites for (ORR). As aforementioned, in the case of $La_{0.8}Sr_{0.2}CoO_{3-\delta}$ (LSC) symmetrical cells on SDC, the polishing of the SDC electrolyte surface leads to worse performance which was attributed to the increase of the interfacial resistance between the electrode-electrolyte[269]. However, for the BSCFMo0.375-

(Co/Fe=4) there is no significant reaction with SDC (Chapter 3, *Section 3.3.3.3*) and hence it is unlikely to result in deterioration of the electrochemical performance due to the formation of secondary insulating phases.

5.1.1.3. Effect of powder: pore former ratio and adhesion temperature

As established from *Section 5.1.1.2*, the best performance was obtained for the 6-layered deposited cathode resulting in approximately 20μm (*Section 5.1.1.4*), made with binder B, on the polished SDC surface (cell 6P(B)). A third experiment was carried out in order to investigate the effect of the ratio powder: binder and the temperature for the adhesion of the cathode layers to the electrolyte, whilst keeping the rest of the parameters constant. For this, two more symmetrical cells were prepared (shown in *Figure 5.2* and *Table 5.3*, including the information of the optimised cell 6P(B)); one heated at 950^{o}C for 3h as cell 6P(B) but with 50:50 by weight powder: pore former ratio(cell code: 6P(B)-ratio=50:50), and one which was heated at 1000^{o}C for 3h (cell code 6P(B)-T=1000) whilst keeping the ratio to 60:40 as in *Section 5.1.1.2*.

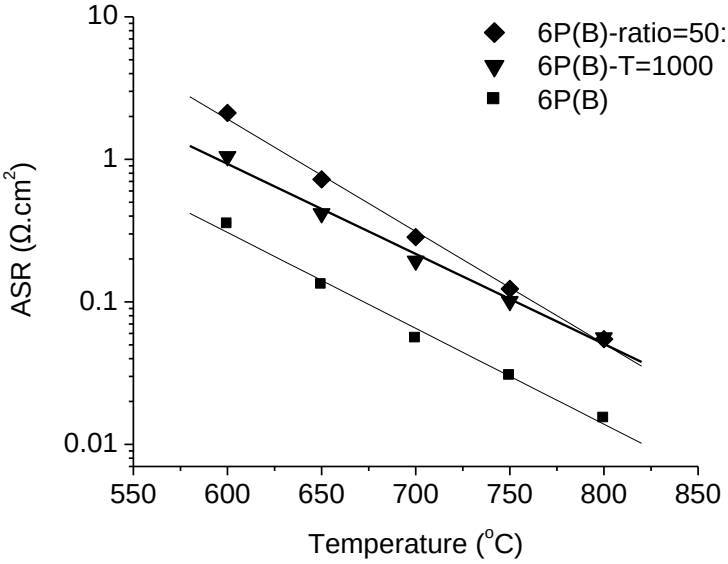

Figure 5.2: Measured area specific resistance (ASR) at the temperature range 600-800oC for symmetrical cells of BSCFMo0.375-(Co/Fe=4), prepared by depositing 6-layers on polished SDC electrolyte surface. The cells varied in the powder: pore former ratio and the adhesion temperature, as listed in Table 5.3.

As can be deduced from *Figure 5.2* and *Table 5.3*, the electrochemical performance of BSCFMo0.375-(Co/Fe=4), is deteriorated for both cells for which the fabrication procedure deviated from the ideal as established in *Section 5.1.1.2* and represented by cell 6P(B), resulting in higher ASR values. The most significant effect is observed for the cell which was made by mixing 50:50 by weight powder: pore-former (cell '6P(B)-ratio=50:50'), with obtained ASR value of 0.724 $\Omega.cm^2$ at 650^oC, that is about five times higher than the best obtained ASR for cell 6P(B) (ASR= 0.132 $\Omega.cm^2$ at 650^oC). This is most likely related to the decrease of the cathode material available for ORR. It should be also noted that when the powder: pore former ratio was kept to 70:30, the viscosity of the produced ink was too high and did not allow the deposition of the cathode ink to the electrolyte substrate by screen-printing. This indicates that 60:40 is the 'golden' ratio for optimised morphology, providing the required porosity but also sufficient cathode mass. The procedure established for the cell 6P(B), seems to be also optimised regarding the adhesion temperature. Whilst temperatures $\leq 900^oC$ resulted in delamination of the cathode coating from the electrolyte substrate, higher temperatures for cell '6P(B)-T=1000' (ASR of 0.417 $\Omega.cm^2$ at 650^oC) deteriorate the electrochemical performance of 6P(B), due to the agglomeration favored as temperature increases. This demonstrates that smaller particles result in higher active area for ORR resulting in enhanced cathode performance.

Table 5.3: List of symmetrical cells of BSCFMo0.375-(Co/Fe=4) on SDC and their electrochemical performance as evaluated by the measured area specific resistance (ASR) and the associated activation energy over the whole temperature range measured. All cells were prepared by depositing 6-layers on polished SDC electrolyte surface and varying in the powder: pore former ratio and the adhesion temperature.

Cell code	**Adhesion temperature (^oC)**	**Powder: pore former Ratio**	**ASR ($\Omega.cm^2$) 650^oC**	**ASR ($\Omega .cm^2$) 700^oC**	**ASR ($\Omega.cm^2$) 750^oC**	**Ea (eV)**
6P(B)	950	60:40	0.132	0.055	0.030	1.25
6P(B)-ratio=50:50	950	50:50	0.724	0.284	0.123	1.47
6P(B)-T=1000	1000	60:40	0.417	0.194	0.101	1.18

5.1.1.4. Charactersisation of cells before measurement

The morphology of a symmetrical cell for BSCFMo0.375-(Co/Fe=4) prepared under the optimised protocol described in *Section 5.1.1* was evaluated by SEM*. The cross-sectional image (*Figure 5.3*) of the fractured electrolyte/cathode bi-layer reveals a well-defined interface between the two components. The cathode coating presents a required highly porous morphology; with a homogeneous thickness of approximately 20 μm. It also indicates the SDC electrolyte with a fully dense structure, and good adhesion to electrode. Representative surface images are shown in Chapter 3 (*Section 3.3.3.2*).

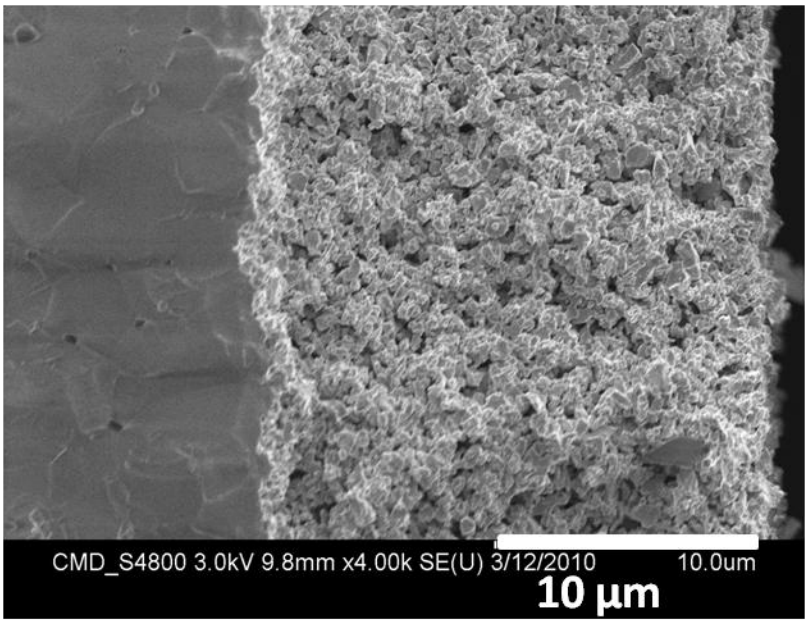

Figure 5.3: Cross- sectional image of symmetrical cell, consisting of a porous BSCFMo0.375-(Co/Fe=4) coating onto the SDC electrolyte substrate, fabricated under the optimised procedure described in Section 5.1.1

∗ The SEM image of the cell was taken by Dr.C.P. Ireland.

Moreover, XRD data of the BSCFMo0.375-(Co/Fe=4) powder scrapped-off the symmetrical cell just before measurement (orange line in *Figure 5.4*) showed no additional phases present compared to the as-made material (blue line in *Figure 5.4*). Small $BaMoO_4$ impurity phase was identified after the milling step (light blue line in *Figure 5.4*), which was however incorporated in the structure during the heating at 950^{o}C required for the adhesion of the cathode to the electrolyte.

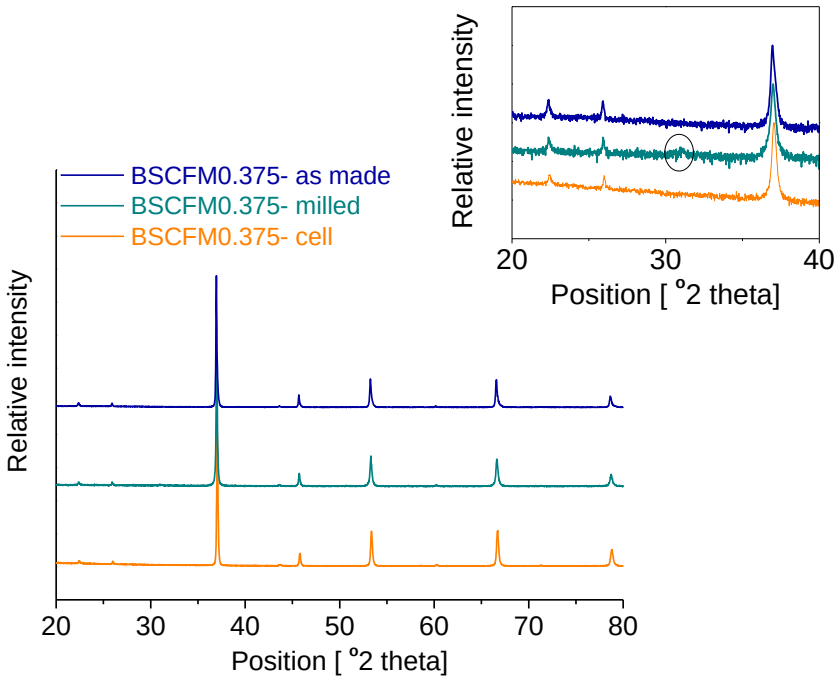

Figure 5.4: XRD patterns for BSCFMo0.375-(Co/Fe=4) powder:as made (blue), after the milling step (light blue) and scrapped off the SDC electrolyte after completion of the fabrication procedure.

5.1.2. Study of the cathode reaction mechanism under variable oxygen content and temperature

The mechanism of oxygen reduction for BSCFMo0.375-(Co/Fe=4) was studied as a function of oxygen partial pressure (pO_2) range 0.0028-0.21 (air), at the temperature range 600-850^{o}C in 50^{o}C steps. This oxygen partial pressure range was chosen in order to ensure that no decomposition of the compound occurs at these reducing conditions. The parent BSCF manifests excellent stability up to 10^{-5} atm[270] and hence BSCFMo0.375-(Co/Fe=4), which shows enhanced stability and reactivity compared to the undoped material (Chapter 3, *Section 3.2.2* and *Section 3.3.3.3* respectively), is not expected to have stability issues at $pO_2 \geq 0.0028$ atm.

As discussed in *Section 2.7.2.4*, the gas pressure was measured by an electrometer and the measured readings in voltage were converted to pO_2 (atm). The specimen, in the symmetrical cell configuration, was heated to the highest temperature (850^{o}C) and left to equilibrate with the gas atmosphere (*Table 5.4*) for about 12 hours (overnight). Measurements were collected during the cooling, allowing 90 min for thermal equilibration at each target temperature.

Table 5.4: List of gas mixtures used to achieve the oxygen partial pressure (pO_2) used in this study

pO_2 (atm)	**Gas 1**	**Gas 2**
0.21	Air 20 ml/min	-
0.1	100% Ar 24 ml/min	100% O_2 0.3 ml/min
0.01	1% O_2/Ar 22.3 ml/min	-
0.005	100% Ar 16.1 ml/min	1% O_2/Ar 10.1 ml/min
0.0028	100% Ar 17.6 ml/min	1% O_2/Ar 1.5 ml/min

5.2.2.1. Dependence on temperature

The temperature dependence of the cathode resistance is shown below at pO_2=0.01 atm (*Figure 5.5A*) for four different temperatures (650, 700, 750 and 800°C). The area specific resistance decreases with increasing the temperature from 1.218 Ω.cm^2 at 650°C to 0.222 Ω.cm^2 at 800°C. At 650°C, the impedance arc can be described as a single depressed semi-circular arc (*Figure 5.5B*), due to the small arc component at the relaxation frequency range f_r= 10^2-10^3 Hz and the dominating large arc at f_r= 10^{-1}-10^2 Hz. At higher temperatures (*Figure 5.5C*), a third impedance arc evolved beginning at about 10^0 Hz, with slight but gradual shift of f_r to larger values with increasing the temperature from 700°C (f_r= 1 Hz) to 750°C (f_r= 3 Hz) and 800°C (f_r=5 Hz).

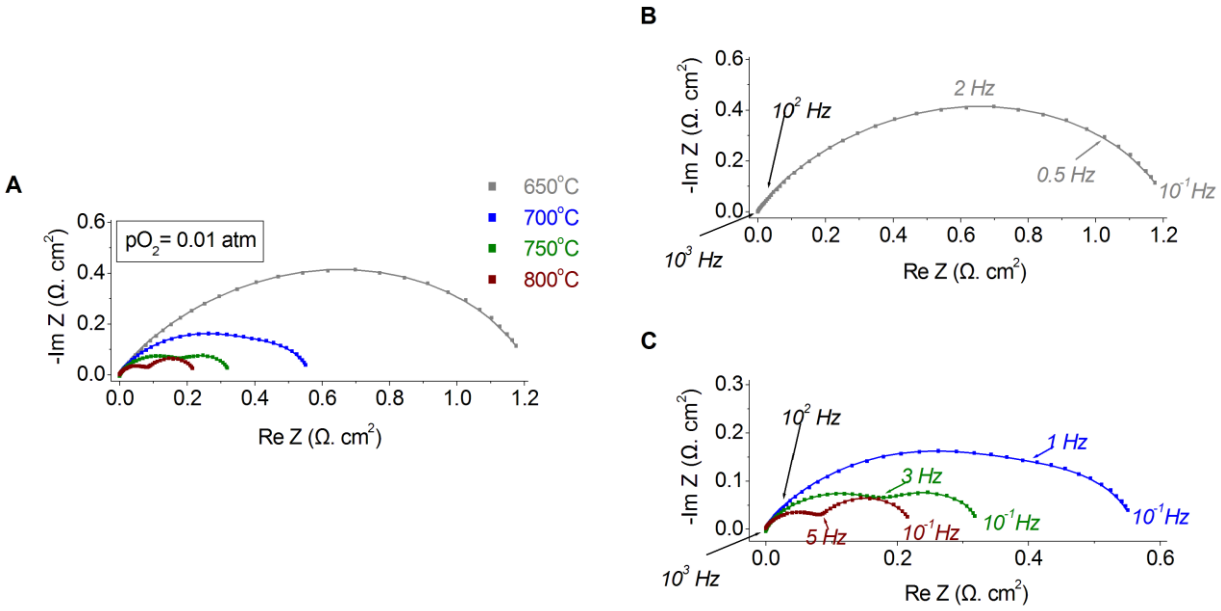

Figure 5.5: (A) Superimposed Nyquist plots and fittings to equivalent circuit models (ECM) at different temperatures, in the range 650- 800°C, for BSCFMo0.375-(Co/Fe=4) at pO_2= 0.01 atm, which are shown in greater detail in: (B) separate Nyquist plot at 650°C and (C) superimposed Nyquist plots at 650, 700 and 750°C, in higher magnification, where arrows indicate the frequency range of the consisting arcs. The symbols are the measured data and lines are from the fitting to equivalent circuit models (ECM). The arcs have been normalised to zero on the x-axis and y-axis to remove the electrolyte and wiring contribution respectively.

The three impedance arcs, associated with the cathode response, were named according to the frequency range appearing as high (HF, f_r=10^3-10^2 Hz), medium (MF, f_r= 10^2-10^0 Hz) and low

frequency (LF, f_r= 10^0-10^{-1} Hz) and complex planes were fitted to an equivalent circuit model (ECM) consisting of three R-CPE elements connected in series (*Figure 5.6*), where R-CPE stands for a resistor (R) and constant-phase element (CPE) connected in parallel. For temperatures above 800oC, the HF arc was negligibly small and no R-CPE element was used to model its response; this did not cause any change in the overall fit. As introduced in *Section 2.7.2.2*, a CPE element is often used to fit real experimental data from systems which show deviation from a true capacitor behavior; in the case of the electrode response, it is a result of various reasons such as the electrode porosity, surface effects (roughness, inhomogeneity, reactivity), distribution of reaction rates and non-uniform current distribution[271, 272]. An inductor element and another resistor component were added, in series to the three R-CPE elements, in order to fit the contribution of the wires and the electrolyte respectively.

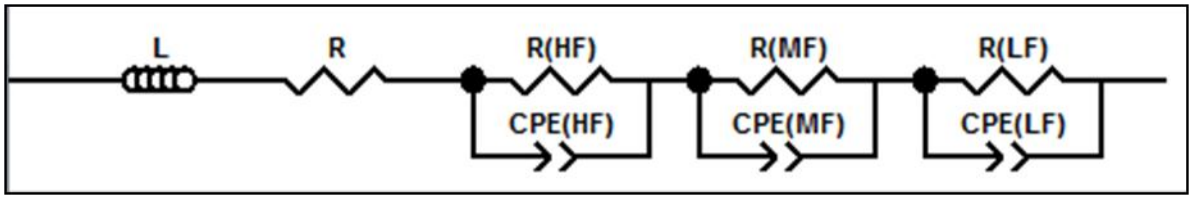

Figure 5.6: Equivalent circuit model used for the fitting of the impedance arcs, where R represents a resistor term and CPE a constant-phase element.

The arcs in *Figure 5.5* have been normalised to zero on the x-axis and y-axis to remove the electrolyte and wiring contribution respectively; the fitting to the ECM is represented by lines, whilst the symbols are the measured data. The pseudo-capacitance values of the CPE elements were calculated according to:

$$C = (R^{1-n} Q)^{1/n} \qquad \textit{Equation 5.2}$$

where R is the element resistance, Q is the pseudo-capacitance and n is the parameter related to the arc depression angle (this is discussed in greater detail in *Section 2.7.2.2*) and divided by A/2 (where A is the area of the surface) to take into consideration the geometry of the cell.

The resulted fitting parameters for the resistance (R) and pseudo-capacitance (C) values for each arc are summarised in *Table 5.5*, including the total electrode area specific resistance (ASR= R(HF)+ R(MF)+ R(LF)).

Table 5.5: Summary of resistance (R) and pseudo-capacitance (C) values derived from the fitting of the impedance arcs, at the temperature range 600-850^oC and at constant oxygen partial pressure 0.01 atm, to the equivalent circuit model consisting of 3 R-CPE elements, each one describing the response of each of the arcs present at high (HF, f_r= 10^3-10^2Hz), medium (MF, f_r=10^2-10^0 Hz) and low (LF, f_r=10^0-10^{-1} Hz) frequency. The total area specific resistant is also included.

T (^oC)	**Total** ASR ($\Omega.cm^2$)	**HF** R ($\Omega.cm^2$)	C ($F.cm^{-2}$)	**MF** R ($\Omega.cm^2$)	C ($F.cm^{-2}$)	**LF** R ($\Omega.cm^2$)	C ($F.cm^{-2}$)
600	3.249	0.030	7.31 x10^{-2}	2.762	12.6 x10^{-2}	0.457	0.12 x10^{0}
650	1.218	0.026	6.23 x10^{-2}	0.785	18.8 x10^{-2}	0.407	0.10 x10^{0}
700	0.641	0.018	11.4 x10^{-2}	0.423	7.38 x10^{-2}	0.200	2.33 x10^{0}
750	0.324	0.013	10.1 x10^{-2}	0.172	6.86 x10^{-2}	0.139	2.02 x10^{0}
800	0.222	-	-	0.088	5.31 x10^{-2}	0.134	2.21 x10^{0}
850	0.186	-	-	0.046	5.59 x10^{-2}	0.140	2.22 x10^{0}

As it can be seen in *Table 5.5*, the derived pseudo-capacitance values are in the order of 10^{-2} $F.cm^{-2}$ for the HF and MF arcs and in the order of 100 $F.cm^{-2}$ for the LF arc. These are in the range of typical chemical pseudo-capacitances 10^{-4}-10^{1} $F.cm^{-2}$ associated with the electrochemical processes in a porous mixed electronic-ionic conductor, with the exact values depending on the nature and the geometry of the electrode cell, and hence much larger than the typical 'double layer' electrode-electrolyte interfacial capacitances (typically 10^{-7}-$10^{-4}F.cm^{-2}$)[135, 273].

The total electrode resistance ASR (*Table 5.5)* decreases significantly with increasing the temperature from 3.249 $\Omega.cm^2$ at 600^{o}C to 0.186 $\Omega.cm^2$ at 850^{o}C. The resistance associated with the MF and LF arcs is one to two orders of magnitude larger than the fitted resistance terms for the HF arc at the temperatures 600-750^{o}C, and no fitting was possible for the HF arc at 800 and 850^{o}C. The resistance of the MF arc is larger than the LF arc at the 600-750^{o}C range, but the overall resistance is dominated by the LF arc at 800 and 850^{o}C. The effect of temperature is more significant on the resistance of the MF arc, which decreases from 2.762 $\Omega.cm^2$ at 600^{o}C to 0.046 $\Omega.cm^2$ at 850^{o}C. The resistance terms of the HF and LF arcs also decrease slightly with

increasing the temperature, from 0.030 Ω.cm^2 and 0.457 Ω.cm^{2}at 600^{o}C to 0.013 Ω.cm^2 and 0.140 Ω.cm^2 at 850^{o}C respectively.

The temperature dependence of the resistance associated to each arc, at pO_2= 0.01 atm, is demonstrated graphically in *Figure 5.7*, allowing the calculation of the associated activation energy (*Ea*) from the Arrhenius equation at the whole temperature range used in this experiment.

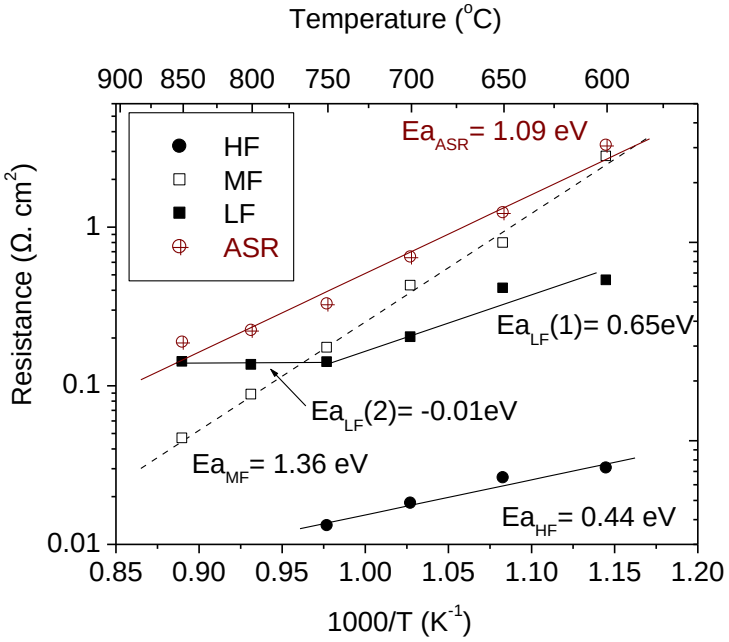

Figure 5.7: Arrhenius plots of the resistance against temperature for the high (HF, f_r= 10^3-10^2Hz), medium (MF, f_r=10^2-10^0 Hz) and low (LF, f_r=10^0-10^{-1} Hz) frequency arcs at pO_2= 0.01atm, shown in closed circles, open squares and closed squares respectively and calculated activation energies. The total area specific resistance (ASR) is shown in red crossed circles.

The Ea corresponding to the MF (Ea= 1.36eV) arc was found about two to three times larger compared to both the Ea of the HF (Ea= 0.44 eV) and the LF (Ea= 0.65 eV at 600-750^{o}C) arcs. The thermal dependence of the LF arc at 750-850^{o}C is negligible as indicated by the negative value of the associated activation energy (Ea_{LF}(2)= -0.01eV). The activation energy of the total area specific resistance (Ea= 1.09 eV) is close in value to the dominating MF. The derived activation energies for the total and individual resistant terms at the whole pO_2 range measured are summarised in *Table 5.6*, whilst the Arrhenius plots are shown in Appendix D.

Table 5.6: Calculated activation energy (Ea) in eV for the total resistance and the individual arcs, present at high (HF, f_r= 10^3-10^2Hz), medium (MF, f_r=10^2-10^0 Hz) and low (LF, f_r=10^0-10^{-1} Hz) frequency, at the whole oxygen partial pressure range measured (pO_2= 0.21-0.0028 atm). The total resistance (ASR) is also included, where ASR= R(HF)+ R(MF)+ R(LF))

pO_2 (atm)	Ea (total)	Ea (HF)	Ea (MF)	Ea (LF)
0.210	1.23	0.28	1.73	0.69
0.100	1.35	0.64	1.75	1.13
0.010	1.09	0.44	1.36	0.65 (600-750^{o}C) -0.01 (750-850^{o}C)
0.005	1.09	1.61	1.27	0.78 (600-750^{o}C) -0.02 (750-850^{o}C)
0.0028	0.91	2.27	1.20	0.70 (600-750^{o}C) -0.02 (750-850^{o}C)
Mean Ea	1.12	1.05	1.46	0.71 (600-750^{o}C) for $pO_2\leq$ 0.01 atm -0.02 (750-850^{o}C) for $pO_2\leq$ 0.01 atm 0.91 (600-850^{o}C) for pO_2>0.01 atm

The total activation energy decreases with the decrease in pO_2 from 1.23eV in air (pO_2=0.21 atm) to 0.91 eV at pO_2= 0.0028 atm. On the contrary, the activation energy corresponding to the HF arc increases with decreasing the oxygen concentration in the input gas. The Ea (HF) is likely influenced by experimental errors associated with the small observed arcs and the limited number of temperature points, since no HF arc was fitted for T$\geq$ 800^{o}C. This suggests tentatively that a mean activation energy of Ea(HF)= 1.0±0.04 eV can be calculated, in order to approximate the temperature dependence of the HF arc over the whole pO_2 range measured. The MF arc shows a pronounced thermal activation behavior, which decreases slightly with the decrease of the pO_2 from 1.73 eV in air to 1.20 eV at pO_2= 0.0028 atm, similarly with the tendency observed for the total activation energy. The Ea(LF) shows three distinct behaviors depending on the gas concentration and temperature: at high oxygen partial pressure (pO_2= 0.21 and 0.1 atm) an overall average activation energy of 0.91 eV, whilst at lower oxygen partial pressure ($pO_2\leq$ 0.01 atm) the thermal behavior is different at 600-750^{o}C (average Ea= 0.71eV) and 750-850^{o}C (average Ea= -0.02eV). Hence, the processes associated with the LF arc $pO_2\leq$ 0.01 atm are influenced by the temperature demonstrating that the small thermal dependence at 600-750^{o}C

becomes negligible at temperatures above 750°C. Overall, the Ea(LF) is smaller than the Ea(MF) at all gas compositions and this suggests that the energy barrier for the ORR is predominantly influenced by the process associated with the MF arc and tentatively by the HF arc. The study of the dependence of each arc's impedance characteristics on the oxygen partial pressure (*Section 5.2.2.2*) will give more insight about the associated physical origin.

5.2.2.2. Dependence on oxygen partial pressure

The dependence of the cathode resistance on the oxygen partial pressure (pO_2) is shown in *Figure 5.8A* for five different oxygen contents (pO_2= 0.21, 0.10, 0.01, 0.005 and 0.0028 atm) at constant temperature 750°C. The total electrode resistance increases on decreasing the pO_2 from 0.038 Ω.cm^2 in air (pO_2= 0.21atm) to 0.324 Ω.cm^2 and 0.894 Ω.cm^2 at pO_2= 0.01atm and pO_2= 0.0028atm respectively.

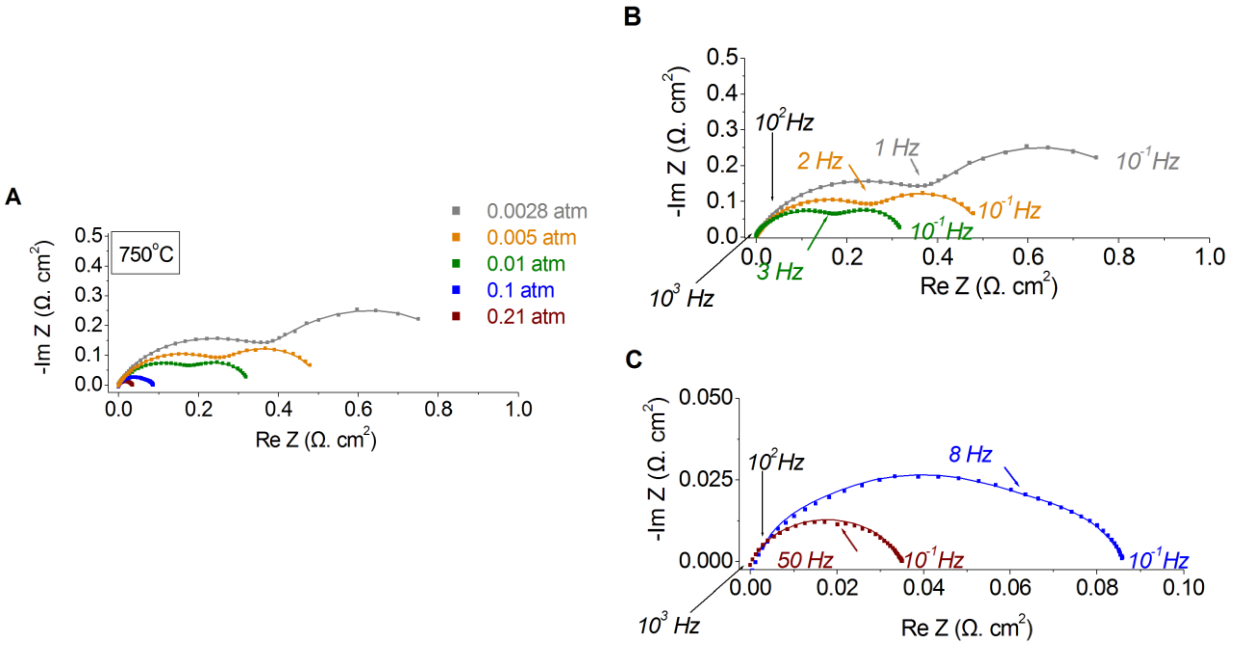

Figure 5.8: (A) Superimposed Nyquist plots and fittings to equivalent circuit models (ECM) at different oxygen partial pressures, in the range pO_2=0.0028-0.21 atm, for BSCFMo0.375-(Co/Fe=4) at 750°C, which are shown in greater detail in (B) for pO_2=0.0028, 0.005 and 0.01 atm and in (C) for pO_2= 0.1 and 0.21 atm, where arrows indicate the frequency range of the consisting arcs. The symbols are the measured data and lines are from the fitting to ECM. The arcs have been normalized to zero on the x-axis and y-axis to remove the electrolyte and wiring contribution respectively.

Taking as a starting point the impedance arc at pO_2= 0.01 atm (*Figure 5.8B)*, which was discussed in *Section 5.2.2.1*, three semicircular arcs can be distinguished by the frequency range appearing; a high frequency (HF f_r=10^3-10^2 Hz), a medium (MF, f_r = 10^3-10^1 Hz) and a low frequency (LF, f_r =10^0-10^{-1} Hz) arc. With the decrease in oxygen content to $pO_{2=}$ 0.005atm and 0.0028 atm the diameter of both MF and LF arcs increase, accompanied by a slight but gradual shift in the frequency that they deconvolute, to smaller values in the range of f_r =1-3 Hz.

On the contrary, when the oxygen partial pressure increases to pO_2= 0.1 (*C)*, both MF and LF arcs decrease and gradually merge into one resulting in a single depressed arc in air (pO_2=0.21 atm.), for which the deconvolution frequency has increased significantly to f_r =50 Hz. Close examination of the impedance responses reveals that the HF arc is existent at all pO_2 environments at 750^{o}C, as the reason of the asymmetry observed for the MF arc, and hence it was also included in the fitting of the impedance responses, using the equivalent circuit model of 3 R-CPE elements in series as described in *Figure 5.6*. The resulting resistance and pseudo-capacitance values from the fitting of the arcs are given in *Table 5.7*, including the total resistance (ASR), whilst the actual graphs can be found in Appendix D.

Table 5.7: Summary of resistance (R) and pseudo-capacitance (C) values derived from the fitting of the impedance arcs, at pO_2= 0.0028-0.21 atm at 750^{o}C, to the equivalent circuit model consisting of 3 R-CPE elements, each one describing the response of each of the arcs present at high (HF, f_r= 10^3-10^2Hz), medium (MF, f_r=10^2-10^0 Hz) and low (LF, f_r=10^0-10^{-1} Hz) frequency. The total resistance (ASR) is also included, where ASR= R(HF)+ R(MF)+ R(LF)).

pO_2 (atm)	**Total**	**HF**		**MF**		**LF**	
	ASR ($\Omega.cm^2$)	R ($\Omega.cm^2$)	C ($F.cm^{-2}$)	R ($\Omega.cm^2$)	C ($F.cm^{-2}$)	R ($\Omega.cm^2$)	C ($F.cm^{-2}$)
0.21	0.038	0.006	$6.64x10^{-2}$	0.020	$25.2x10^{-2}$	0.012	$0.94x10^{0}$
0.10	0.082	0.010	$7.42x10^{-2}$	0.043	$8.81x10^{-2}$	0.029	$0.96x10^{0}$
0.01	0.324	0.013	$10.1x10^{-2}$	0.172	$6.86x10^{-2}$	0.139	$2.02x10^{0}$
0.05	0.500	0.012	$10.1x10^{-2}$	0.261	$5.72x10^{-2}$	0.228	$2.03x10^{0}$
0.0028	0.894	0.008	$16.1x10^{-2}$	0.399	$5.72x10^{-2}$	0.487	$2.02x10^{0}$

As it can be seen *Table 5.7*, the calculated pseudo-capacitance values corresponding to the LF arc (C= 10^0 F.cm^{-2}) are about two orders of magnitude larger than for the HF and LF (C= 10^{-2} F.cm^{-2}), which is in agreement with the outcome of the temperature dependence (*Section 5.2.2.1*), indicating that this is a global observation at the whole temperature and pO_2 range of the experiment. The pseudo-capacitance of the MF arc decrease with the decrease in oxygen content from 25.2x 10^{-2} F.cm^{-2} in air to 5.7210^{-2} x 10^{-2} F.cm^{-2}, whilst the opposite trend was observed for the HF arc with increasing from C= 6.64 x 10^{-2} F.cm^{-2} in air to C= 16.1 x 10^{-2} F.cm^{-2} at pO_2= 0.0028 atm.

The total resistance increases significantly with decreasing the oxygen partial pressure (*Table 5.7*) at 750^{o}C. This demonstrates the importance of the concentration of the input gas in oxygen on the electrochemical performance of BSCFMo0.375-(Co/Fe=4) on catalysing the oxygen reduction reaction, indicating that oxygen is involved in the rate determining step. Similarly, the resistance associated to the MF and LF component arcs increase with decreasing the pO_2. This is more significant for the LF arc, with fitted resistance of 0.012 Ω.cm^2 in air, which is about 40 times smaller than the obtained resistance of 0.487 Ω.cm^2 at pO_2= 0.028 atm. The LF arc dominates the total impedance response at pO_2= 0.028 atm, whilst the resistance of the MF component is larger for the lower pO_2 environments and the resistance of the HF arc is the minor impedance component in the whole pO_2 range measured, with varying slightly between 0.006-0.0013 Ω. cm^2.

The effect of pO_2 on the fitted resistance terms corresponding to each arc is graphically illustrated in *Figure 5.9*, according to *Equation 5.3* demonstrating a power (-m) dependence on pO_2.

$$R = k\, p_{O_2}^{-m} \qquad \textit{Equation 5.3}$$

The resistance associated with the LF arc decreases significantly with the increase of the pO_2, showing almost linear dependence with the pO_2 (m= 0.80), whilst the effect on the resistance of the HF arc is very low (m= 0.08). The resistance of the MF arc also decreases with the increase of the pO_2 and was found to follow a power law dependence of m= 0.66.

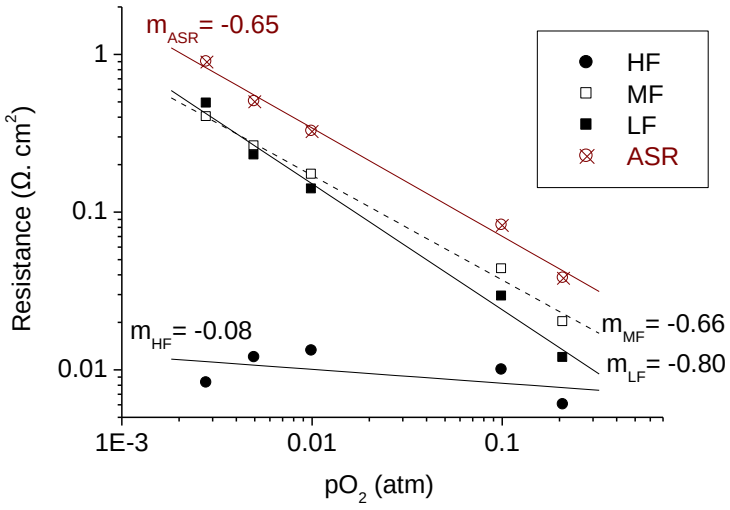

Figure 5.9: Effect of oxygen partial pressure (pO_2) on the resistance (R) of the high (HF, f_r= 10^3-10^2Hz), medium (MF, f_r=10^2-10^0 Hz) and low (LF, f_r=10^0-10^{-1} Hz) frequency arcs, shown in closed circles, open squares and closed squares respectively and the exponent m. The total area specific resistance (ASR) is represented in red crossed circles.

The process of fitting of the impedance response to the ECM in *Figure 5.6* and plotting the resistance terms associated to each arc against the pO_2 was repeated for the whole temperature range measured (600-850^{o}C) and the outcomes are tabulated in *Table 5.8*, whilst the graphs are shown in Appendix D.

Table 5.8: Power (m) dependence on the pO_2 for the total resistance and the individual arcs, present at high (HF, f_r= 10^3-10^2Hz), medium (MF, f_r=10^2-10^0 Hz) and low (LF, f_r=10^0-10^{-1} Hz) frequency, at the whole oxygen partial pressure temperature measured (600-850^{o}C).

T (^{o}C)	m (ASR)	m (HF)	m (MF)	m (LF)
600	0.51	0.17	0.52	0.78
650	0.55	0.40	0.43	0.98
700	0.56	-0.09	0.59	1.28
750	0.65	0.08	0.66	0.80
800	0.75	-	0.68	0.89
850	0.84	-	0.76	0.98
Mean m	0.67	0.29 (T≤650^{o}C) -0.005(T>650^{o}C)	0.61	0.95

As discussed in detail in *Section 2.7.2.3*, the value of the exponent m can be used in order to determine the species involved in the rate determining step associated to the resistant arcs in the impedance response and hence assign them to physical processes.

From *Table 5.8*, the value of the exponent m varies between 0.52-0.76 for the MF arc, with an average value of 0.61 over the temperature range measured. Hence, the MF arc shows an approximately $pO_2^{1/2}$ dependence, which is associated with the dissociative adsorption, assuming that Langmuir's isotherm can be used [19, 161, 274]. This has also been shown for the parent undoped BSCF on $Gd_{0.2}Ce_{0.8}O_{1.9}$ (GDC) electrolyte related with the low frequency part of the impedance spectra obtained at 600°C at pO_2= 0.21-0.8 atm [158], but also other Co-containing cathodes such as $La_{0.7}Sr_{0.3}CoO_{3-\delta}$ on YSZ at pO_2= 10-6-0.21 at 373°C [160]and $Sm_{0.5}Sr_{0.5}CoO_3$ on SDC at pO2= 10^{-2}-1 atm at 800°C [161].

The LF arc shows strong dependence on the pO_2, since the m value is between 0.78-1.28, with an average of 0.95 over the whole temperature measured. This is close to a simple inverse proportionality (m=1), indicating that the gas phase molecular oxygen diffusion inside the electrode pores and/or at the surface is the RDS, since the cathodic gas diffusion resistance (R_D) has been found to be inversely proportional to the pO_2 (i.e. m=1) [157, 275, 276], for pO_2<1 atm. This is in agreement with the findings for BSCF on $La_{0.9}Sr_{0.1}Ga_{0.8}Mg_{0.2}O_{3-\delta}$ (LSGM) at 550-700°C [159] with m= 0.77-0.98 for the low-frequency part of impedance spectra obtained at 550-700°C, over the pressure range pO_2= 0.16-1 atm. Moreover, LSCF ($La_{0.8}Sr_{0.2}Co_{0.2}Fe_{0.8}O_{3-\delta}$) on a $Ce_{0.8}Gd_{0.2}O_{2-\delta}$ electrolyte shows a $pO_2^{1.42}$ dependence for the low frequency part above 700°C [81].

The m value for the HF arc shows clearly two different pO_2 dependencies at temperatures below 800°C, likely influenced by the big errors associated due to the small resistance values, whilst at temperatures above 800°C was too small and hence was not fitted in the ECM model. The HF arc at 700°C (m= -0.09) and 750°C (m= 0.08) can be related to ionic diffusion in the cathode on the basis of the weak dependence of R^{-1} on pO_2[156, 273], assuming that the oxygen deficiency and thus the concentration of oxygen vacancies carrying the oxide ionic current does not increase

significantly by decreasing the pO_2 from 0.21 to 0.0028atm. The pO_2 dependence of the HF arc becomes slightly more significant, at temperatures below 700°C, with m= 0.17 (600°C) and m= 0.40 (650°C), with a mean value of 0.29. This suggests that the resistance of the HF arc can be possibly linked to the $pO_2^{1/4}$ dependence reported for charge transfer limiting processes in a mixed electronic-ionic conductor[155, 274] as for instance m= 0.22 for BSCF on $Gd_{0.2}Ce_{0.8}O_{1.9}$ (GDC) electrolyte related with the small arc at the high frequency part of the impedance spectra obtained at 600°C at pO_2= 0.21-0.8 atm [158]. Moreover, LSCF ($La_{0.8}Sr_{0.2}Co_{0.2}Fe_{0.8}O_{3-\delta}$) on a $Ce_{0.8}Gd_{0.2}O_{2-\delta}$ electrolyte shows a $pO_2^{0.23}$ dependence for the major resistance at the high frequency range above 700°C [81].

The total resistance (ASR) shows almost parallel evolution of the m value from 0.51 to 0.65, as increasing the temperature from 600°C to 750°C, with the MF arc (m= 0.52 to 0.66 respectively), indicating that at these conditions the impedance of BSCFMo0.375-(Co/Fe=4) is dominated by the dissociative adsorption as described by the MF arc. However, this is not the case at the higher temperatures of 800°C and 850°C, with m= 0.75 and 0.84, approaching the m values for the LF arc, suggesting that at T ≥ 800°C the gas phase diffusion at the pO_2 range measured.

5.2.2.3. Mechanism

To summarise (*Table 5.9*), the impedance response of BSCFMo0.375-(Co/Fe=4), at the temperature range 600-850°C and pO_2 range 0.0028-0.21 atm, consisted of three resistance terms named according to the characteristic relaxation frequency appearing as high (HF, f_r= 10^3-10^2 Hz), medium (MF, f_r= 10^2-10^0 Hz) and low frequency (LF, f_r= 10^0-10^{-1} Hz). The shift to bigger values of the f_r that the MF and LF deconvolute, with the increase of the pO_2 and T, is in agreement with the cathode related processes and it can be even used in assigning the resistance arcs in different processes [277, 278].

The MF arc was associated to oxygen dissociative adsorption, based on the approximately $pO_2^{1/2}$ dependence, and was found to have the largest activation energy over the whole temperature range measured (mean Ea= 1.45 eV, over the whole pO_2 range studied). The fact that atomic oxygen is involved in the process described by the MF arc, is also supported by the increased pseudo-capacitance values as the temperature decreases (*Table 5.5*) or the pO_2 increases (*Table*

5.7), due to the accumulation of charge when the concentration of oxygen ionic species increases resulting in lower mobility[274].

Table 5.9: List of impedance characteristics for the high (HF, f_r= 10^3-10^2 Hz), medium (MF, f_r= 10^2-10^0 Hz) and low (LF, f_r= 10^0-10^{-1} Hz) frequency arcs, together with their dependencies on temperature and oxygen partial pressure and identified process.

	HF	MF	LF
Relaxation frequency (f_r, Hz)	10^3-10^2	10^2-10^0	10^0-10^{-1}
Contribution in total ASR	Not fitted at T≥ 800°C	Dominating in air and $pO_2 \geq 0.005$ atm*	Dominating at $pO_2 \leq 0.005$ atm*
Pseudocapacitance (F. cm^{-2})	10^{-2}	10^{-2}	10^0
Dependence on temperature	<Ea>= 1.02 eV	Significant <Ea>= 1.45 eV	Low <Ea>= -0.02-0.91 eV, depending on pO_2 and T range
Dependence on oxygen partial pressure (pO_2)	weak 0.29 (T≤650°C) -0.005(T>650°C)	<m>= 0.61	significant <m>= 0.95
Identified Process	Charge transfer (T≤650°C) Oxygen ionic diffusion (T>650°C)	Dissociative adsorption	Gas phase diffusion

**At pO_2= 0.005 atm, the LF arc dominates at T≥ 800°C*

The resistance of the MF dominates the impedance response at $pO_2 \geq 0.001$ atm, over the whole temperature range measured, and at pO_2= 0.005 atm for temperatures below 800°C. This indicates that the oxygen dissociative adsorption (or oxygen chemical exchange) is the process that affects the cathode performance of BSCFMo0.375-(Co/Fe=4) in air and can explain the observation that increasing the thickness of the deposited cathode results in lowering of the total resistance (*Section 5.1.1.2*) due to the extension of the active area in larger volume and hence increase of the reactive sites for ORR. The oxygen exchange has also been reported to be the slow step for the parent undoped BSCF [158, 159]. Hence, the mechanism for oxygen reduction of

BSCFMo0.375-(Co/Fe=4), containing approximately 70% double perovskite and 30% single perovskite, as established from the structural analysis (Chapter 4, *Section 4.1.3*), resembles the behavior of the parent undoped single perovskite BSCF. This is in agreement with the findings for the double perovskite system $GdBaCo_2O_{5+\delta}$ [279], the commonly used cathode material $La_{0.8}Sr_{0.2}Co_{0.2}Fe_{0.8}O_{3-\delta}$ (LSCF) [81, 156] and the generally accepted view that the ORR in cathode materials is limited by surface oxygen exchange and solid-state diffusion[273, 280].

The resistance of the LF arc was attributed to gas phase oxygen diffusion inside the electrode pores and/or at the surface, due to the significant dependence on the oxygen partial pressure (mean m= 0.95) and low activation energy (Ea= -0.02-0.91 eV depending on pO_2 and T range), suggesting a nearly non-activated process. This is corroborated by the corresponding high pseudo-capacitance values of 10^0 $F.cm^{-2}$, which are two orders of magnitude larger than for the MF and HF arc, indicating larger oxygen chemical storage [156]. The LF arc dominates the impedance response at pO_2= 0.0028 atm, at the whole temperature range measured, and at temperatures above 800^{o}C for pO_2= 0.05 atm. Hence the oxygen diffusion limits the cathode performance at low oxygen pressure and high temperatures. This has been related to gas phase/ Knudsen diffusion in the pores of the electrode at low O_2 concentrations[280]. In general, Knudsen flow occurs when a gas with low density enters a porous system for which the pore diameter is smaller than the mean free path of the diffusing gas molecules; in these cases the gas molecules collide with the pore walls more frequently than contributing to the flow. The minimum pO_2 limit for diffusion dominance depends mainly on the cathode morphology and the fabrication procedure; in most examples in the literature Knudsen diffusion limits significantly the ORR for pO_2 below approximately 0.01 atm for the $La_{1-x}Sr_xCoO_{3-\delta}$ (LSC) [280], (La,Sr)MnO_3 (LSM) [281], BSCF[159], $La_{0.8}Sr_{0.2}Co_{0.2}Fe_{0.8}O_{3-\delta}$ (LSCF) [81, 156] and LSCF composites with GDC[282] systems.

The resistance of the HF arc is about one order of magnitude smaller than the rest resistance contributions and becomes negligible at temperatures above 800^{o}C. At temperatures 700-750^{o}C, the impedance response of the HF arc shows a very weak dependence on the oxygen gas concentration changes (m= -0.005), implicating an oxygen ionic diffusion limiting step. However, the ionic contribution becomes smaller at 600-650^{o}C, and the R^{-1}(HF) demonstrates a nearly $pO_2^{1/4}$ dependence (m= 0.29), which was related to charge transfer processes. It would be

interesting to correlate this information, with the total conductivity of BSCFMo0.375-(Co/Fe=4) measured by dc (Chapter 3, *Section 3.3.1*), which was attributed to the charge transfer process based on the polaron hopping between the M^{3+} and M^{4+} cations, but direct comparison of the obtained conductivity values would be imprudent due to the differences in porosity and geometry between the two methods. However, the obtained activation energy of 0.246 eV in air by the d.c. method, is in close agreement with the obtained Ea= 0.28 eV from this experiment in air and hence it is a good indication that the resistance of the HF arc is associated with charge transfer at 600-650^{o}C. The activation energy increases with the decrease of oxygen content (*Table 5.6*), possibly influenced by the errors associated with the small resistance values, with a mean calculated value of 1.02 eV over the whole pO_2 range measured, suggesting that the charge transfer and oxygen ionic conductivity associated to the HF arc have a considerable contribution to the total activation energy (<Ea>= 0.95).

5.2. Other compositions

5.2.1. Effect of Mo content

The cathodic performance was measured for the parent undoped BSCF and a range of Mo-doped BSCF compositions with Co/Fe ratio=4 with varying the Mo content in the B-site (abbreviated as $BSCFMo_{x+y}$-(Co/Fe=4), $0 \leq x+y \leq 0.45$), in air at the temperature range 600-850^{o}C. All the symmetrical cells were fabricated according to the optimised protocol established in (*Section 5.1.1*) and their impedance response is shown in *Figure 5.10* at 650^{o}C. The measurements were repeated (*Table 5.10*) for most of the compositions, showing good reproducibility, and the one giving the lowest resistance is plotted. The high Mo-containing compositions BSCFMo0.409-(Co/Fe=4) and BSCFMo0.45-(Co/Fe=4) show worse electrochemical performance among this series of compounds, with obtained ASR values at 650^{o}C of 0.593 and 1.06 Ω.cm^2 respectively, suggesting that the high amount of Mo is not beneficial for the ORR.

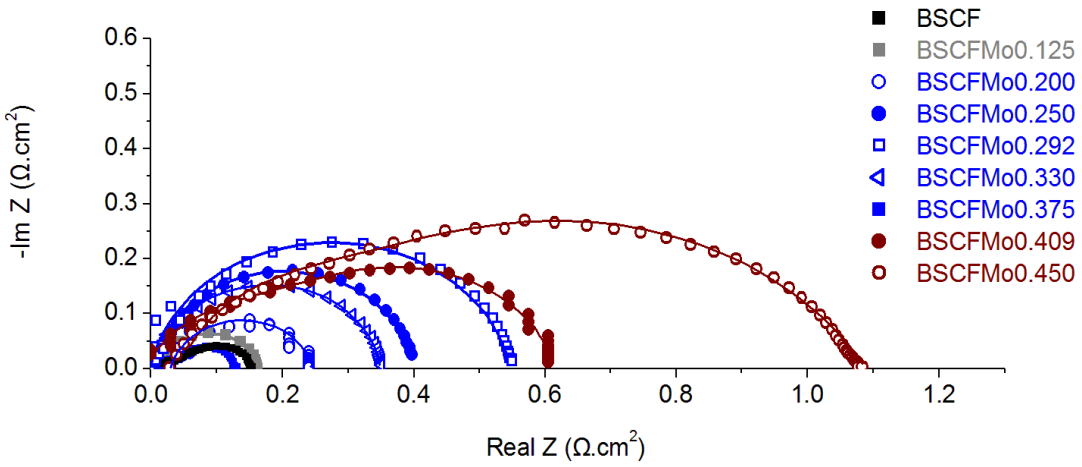

Figure 5.10: Electrochemical impedance arcs at 650^{o}C for a range of $BSCFM_{Mo}$-(Co/Fe=4) compositions, with 0 ≤Mo≤0.45, normalised to zero on the x-axis to remove the electrolyte contribution.

However, BSCFMo0.375-(Co/Fe=4), shows the best cathode performance with ASR (650^{o}C) of 0.132 Ω.cm^2, which is comparable with the values obtained for the parent un-doped BSCF (ASR= 0.157 Ω.cm^2) and the low Mo containing BSCFMo0.125-(Co/Fe=4) (ASR= 0.161 Ω.cm^2)

at 650°C under the conditions measured. The measured resistance for the rest of the $BSCFMo_{x+y}$-(Co/Fe=4) compositions, with $0.2 \leq (x+y) \leq 0.33$, varies between 0.222 $\Omega.cm^2$ to 0.552 $\Omega.cm^2$ with a minimum observed for BSCFMo0.20-(Co/Fe=4) and the maximum for BSCFMo0.292-(Co/Fe=4).

Table 5.10: *Calculated ASR ($\Omega.cm^2$) at 650°C and associated activation energy (Ea) over the whole temperature range measured (600-800°C) for a range of $BSCFM_{x+y}$-(Co/Fe=4) compositions with $0 \leq (x+y) \leq 0.45$, including the nominal composition and the phase region where they were classified* in Chapter 4, *Section 4.3.3*.

Abbreviation	**Phase region**	**B-site composition**		**ASR (650°C)**	**Ea (eV)**
BSCF	SP	$Co_{0.800}Fe_{0.200}$	1st	0.157	0.77
			2nd	0.174	1.31
BSCFMo0.125-(Co/Fe=4)	SP	$Co_{0.700}Fe_{0.175}Mo_{0.125}$	1st	0.161	1.19
			2nd	0.196	1.13
BSCFMo0.200-(Co/Fe=4)	SP/DP	$Co_{0.640}Fe_{0.160}Mo_{0.200}$	1st	0.222	1.15
BSCFMo0.250-(Co/Fe=4)	SP/DP	$Co_{0.600}Fe_{0.150}Mo_{0.250}$	1st	0.402	1.29
			2nd	0.415	1.17
BSCFMo0.292-(Co/Fe=4)	SP/DP	$Co_{0.566}Fe_{0.142}Mo_{0.292}$	1st	0.552	1.30
			2nd	0.609	1.23
BSCFMo0.330-(Co/Fe=4)	SP/DP	$Co_{0.536}Fe_{0.134}Mo_{0.330}$	1st	0.341	1.33
			2nd	0.347	1.33
BSCFMo0.375-(Co/Fe=4)	SP/DP	$Co_{0.500}Fe_{0.125}Mo_{0.375}$	1st	0.208	1.18
			2nd	0.132	1.25
BSCFMo0.409-(Co/Fe=4)	SP/DP+ $BaMoO_4$	$Co_{0.473}Fe_{0.118}Mo_{0.409}$	1st	0.593	1.52
BSCFMo0.450-(Co/Fe=4)	SP/DP+ $BaMoO_4$	$Co_{0.440}Fe_{0.110}Mo_{0.450}$	1st	1.06	1.57

This demonstrates that the electrochemical performance of this series of Mo-doped BSCF compositions is not a simple relation with the Mo content (*Figure 5.11*) and implicates the

structural differences (*Table 5.10*). As discussed in (Chapter 4, *Section 4.3.3*), small amount of Mo (Mo ≤ 0.125) favors the formation of single perovskite (SP) phases by XRD, whilst higher Mo content (0.125 < Mo < 0.409) results in the formation of double perovskite (DP) crystallites coexisting with the SP with a clear evolution of the volume of the DP crystallites with the amount of Mo, and higher amount of Mo (Mo ≥ 0.409) favors the formation of increasing amount of $BaMoO_4$ impurity phase in the biphasic SP/DP specimens.

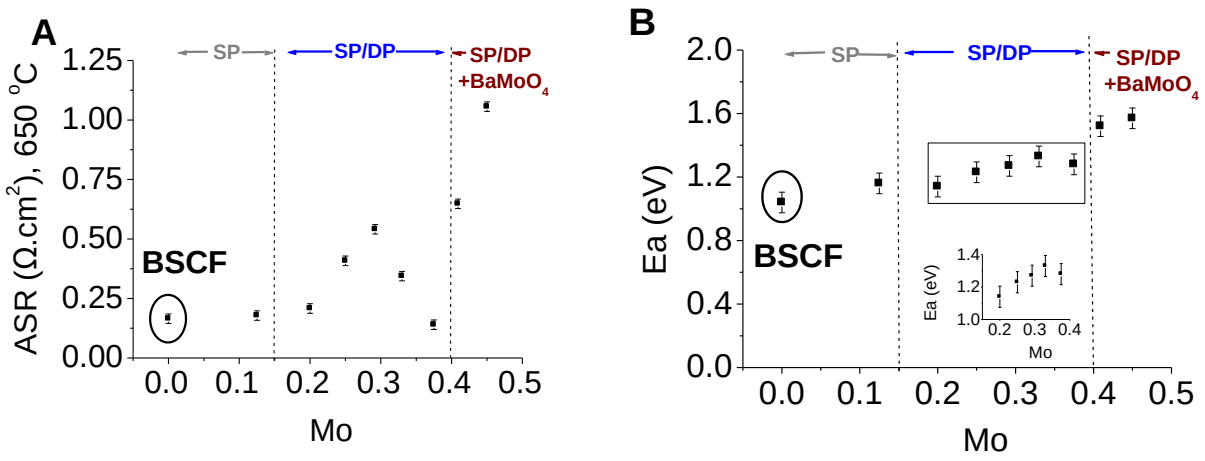

Figure 5.11: Evolution with Mo content of (A) measured area specific resistance (ASR) at 650°C and (B) associated activation energy over the whole temperature range measured, for a range of $BSCFM_{Mo}$-(Co/Fe=4) compositions (0≤Mo≤0.45), classified as single perovskites 'SP' for low Mo content, as biphasic single and double perovskite ('SP/DP') compounds with increasing the Mo content and biphasic SP/DP structures with formation of $BaMoO_4$ impurity phase ('SP/DP+$BaMoO_4$') for Mo> 0.4.

As can be seen in *Figure 5.11A*, the introduction of Mo in the B-site of BSCF up to 0.292, results in the increase of the cathode polarisation resistance with increasing the Mo amount and subsequently DP% content. This can be explained as the combined effect of reducing the electronic and ionic charge carriers, due to the reduction of the transition metals upon substitution with Mo^{6+} (Chapter 3, *Section 3.3.1*) and the decrease in the number of oxygen vacancies induced by the B-site ordering and formation of DP crystallites. However, this is not the case for the SP/DP biphasic compounds with higher Mo content than 0.292 in the B-site. BSCFMo0.33-(Co/Fe=4) shows lower ASR values compared to the lower Mo containing BSCFMo0.292-(Co/Fe=4) and there is an abrupt jump in the ASR values from BSCFMo0.292-

(Co/Fe=4) to BSCFMo0.375-(Co/Fe=4), showing as good properties as BSCFMo0.125-(Co/Fe=4) and the undoped BSCF. The highest polarisation resistance observed for the BSCFMo0.409-(Co/Fe=4) and BSCFMo0.45-(Co/Fe=4) compositions belonging to the SP/DP+ $BaMoO_4$ phase area is likely linked with the formation of $BaMoO_4$, as it is generally accepted that impurities and secondary phases are likely to retard the ORR and in particular the electrochemical kinetic processes occurring at the interface, resulting in ohmic losses[21]. $BaMoO_4$ is a worse electronic and ionic conductor [283]compared to BSCF, hence increasing amount is expected to result in deterioration of the electrochemical properties of the BSCFM materials.

Moreover, it is interesting to note that the derived activation energy over the whole temperature range measured for the impurity-free Mo-containing BSCF compositions ($0.125 \leq Mo \leq 0.375$) is 1.1-1.3eV (*Figure 5.11*B), i.e. equal within error estimated as 0.1eV in Section 5.2.2. This suggests similarities in the oxygen reduction mechanism. However, the associated activation of 1.52 eV and 1.57 eV, for the BSCFMo0.409-(Co/Fe=4) and BSCFMo0.45-(Co/Fe=4) compositions containing $BaMoO_4$, is clearly higher than for the impurity-free compositions. This demonstrates that the presence of the insulating $BaMoO_4$ phase increases the energy barrier for ORR, possibly related with the activation energy for the charge transfer mechanism, which was found to contribute to the overall activation energy in the case of BSCFMo0.375-(Co/Fe=4) (*Section 5.1.2*).

Overall, the enhanced performance of BSCFMo0.375-(Co/Fe=4) among the $BSCFMo_{Mo}$-(Co/Fe=4) compositions studied herein, suggests that the SP/DP microstructure of the BSCFM materials becomes optimal at the highest DP fraction, near the limit where the undesirable $BaMoO_4$ impurity phase starts to form and affect the cathode performance. It is likely that the channels for fast oxygen mobility are best designed in the 'golden' SP/DP ratio of approximately 30:70 for BSCFMo0.375-(Co/Fe=4) with specific compositions (Chapter 4, *Section 4.1.3*), in the highly Mo containing environment that provides the active sites for the ORR.

5.2.2. Analysis of errors associated with the electrochemical measurements

Although identical procedure for the synthesis of the compounds (*Section 2.1*), fabrication and measurement of symmetrical cells was followed (*Section 5.1.1*), random errors are inevitable and always expected in a multi-step process. Errors can be associated to small variations in porosity and/or dimensions between the measured repeated specimens. As aforementioned, most of the electrochemical measurements of each composition were repeated to ensure reproducibility. This allowed to roughly estimating the errors associated with this type of measurements. The measured ASR and the associated calculated activation at the temperature range measured (600-800^{o}C) corresponding to the seven compositions for which duplicate measurements were available, are summarized in *Table 5.11, i*ncluding the mean values in the form of (mean value) ± (standard error).

The mean value is given by the average of the two independent measurements, according to the formula:

$$\text{Mean } (\mu) = \frac{\Sigma(X_i)}{N} \qquad \textit{Equation 5.4}$$

where $\Sigma(X_i)$ is the sum of the values corresponding to each measurement (X_i) and N is the population of values or number of individual measurements and in this case N=2.

The standard error of the mean is given by the formula:

$$SE = \frac{\sigma}{\sqrt{N}} \qquad \textit{Equation 5.5}$$

where σ is the standard deviation of the population, calculated by:

$$\sigma = \sqrt{\frac{\Sigma\ (xi - \mu)^2}{N}} \qquad \textit{Equation 5.6}$$

For a statistically reliable dataset, N should be as large as possible to allow the plot of normal (Gaussian) distribution, also known as 'bell curve'. This means that in order to provide a reliable value for the standard deviation and standard error, each measurement should have been ideally repeated more than two times.

Table 5.11: List of information (area specific resistance (ASR at 650^{o}C) in Ω.cm^2 and activation energy (Ea, in eV)) obtained from duplicate electrochemical measurements for the BSCFM compositions and mean values in the form of <mean value> ± (standard error) for each composition. An average error in ASR (650^{o}C) and Ea was calculated for all the compositions studied.

Abbreviation		**ASR (650^{o}C)**	**<ASR> (650^{o}C)**	**Ea (eV)**	**<Ea > (eV)**
BSCF	1st	0.157	0.166± 0.009	0.77	1.05± 0.27
	2nd	0.174		1.31	
BSCFMo0.125-(Co/Fe=4)	1st	0.161	0.179± 0.018	1.19	1.16± 0.03
	2nd	0.196		1.13	
BSCFMo0.250-(Co/Fe=4)	1st	0.402	0.409± 0.007	1.29	1.23± 0.06
	2nd	0.415		1.17	
BSCFMo0.292-(Co/Fe=4)	1st	0.552	0.581± 0.029	1.30	1.27± 0.04
	2nd	0.609		1.23	
BSCFMo0.330-(Co/Fe=4)	1st	0.341	0.344± 0.003	1.33	1.33± 0.00
	2nd	0.347		1.33	
BSCFM0.375-(Co/Fe=4)	1st	0.208	0.170± 0.038	1.18	1.22± 0.04
	2nd	0.132		1.25	
BSCFMo0.45-(Co/Fe=10)	1st	0.505	0.570± 0.024	1.38	1.45± 0.07
	2nd	0.634		1.51	
Average error			**0.024**		**0.07**

An average error was then estimated for the ASR values at each temperature and the activation energy (Ea), from the population/number of standard errors derived from the analysis of each composition.

$$\text{Average error} = \frac{\sum_1^{SE=7}(SE)}{N'} \qquad \textit{Equation 5.7}$$

where $\sum_1^{SE=7}(SE)$ is the sum of the standard errors for the population of N' = 7 corresponding to the 7 individual standard errors (SE) derived from the duplicates of each of the 7 BSCFM compositions.

The average error for the ASR (650^{o}C) was estimated at 0.024 Ω.cm^{2} and the average error for the associated activation energy (Ea) at 0.07 eV. This provides a rather empirical way of approximating the errors associated for measurements that duplicate cells were not measured. It also provides a normalized way for comparing the very close, in actual numbers, values for ASR and Ea for all the BSCFM compositions. By this way, the deduction whether the differences in their electrochemical performance are controlled by the errors associated with this type of measurements is facilitated.

5.2.3. Effect of Co/Fe ratio

The Co/Fe ratio has been briefly discussed previously (Chapter 3, *Section 3.3.3*), suggesting that the electrochemical performance is optimised when it is kept to 4 as the parent undoped BSCF material. Herein, it is discussed further in terms of lower and higher Co/Fe than 4.

5.2.3.1. Low Co/Fe

The compositional pair of BSCFMo0.2-(Co/Fe=3) and BSCFMo0.2-(Co/Fe=4), equally containing 20% Mo in their B-site but differing in the Co/Fe ratio, was investigated in terms of their electrochemical performance. Both compositions were classified in the SP/DP phase region (Chapter 4, *Section 4.3.4.1*). The polarization resistance of BSCFMo0.2-(Co/Fe=3) is higher than for BSCFMo0.2-(Co/Fe=3) at the whole temperature range measured, suggesting important influence of the Co/Fe ratio on the cathode electrocatalytic properties. For instance, at 650^{o}C (*Figure 5.12A*), the obtained ASR values are 0.305 and 0.222 Ω.cm^2 for Co/Fe equal to 3 and 4 respectively. The higher ASR for BSCFMo0.2-(Co/Fe=3) is associated with a slightly higher activation energy over the whole temperature range of 1.20 eV (*Figure 5.12B*), compared to 1.15 eV for BSCFMo0.2-(Co/Fe=4).

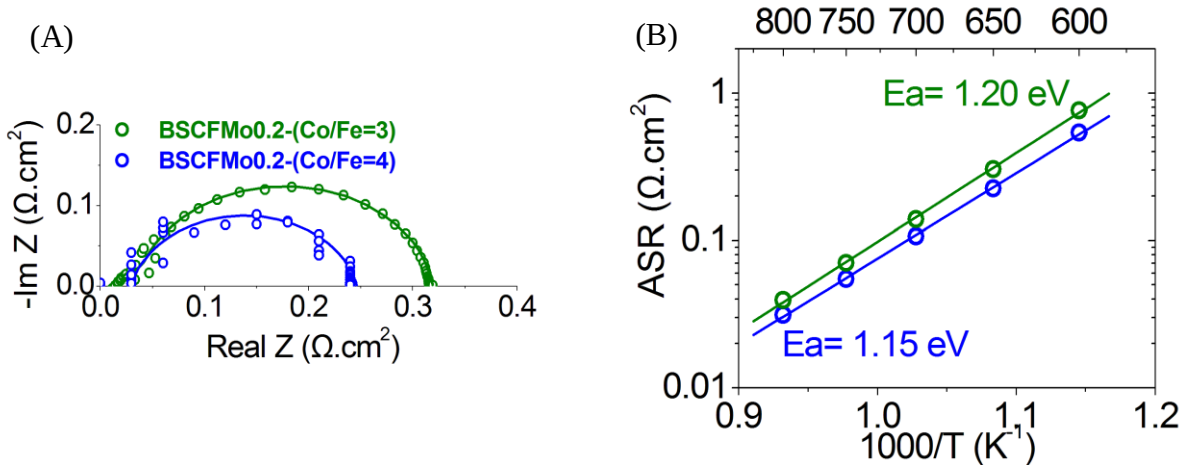

Figure 5.12: (A) Electrochemical impedance arcs at 650^{o}C for BSCFMo0.2-(Co/Fe=4) and BSCFMo0.2-(Co/Fe=3), normalised to zero on the x-axis to remove the electrolyte contribution and (B) calculated ASR over the temperature range measured and associated activation energy.

The difference in absolute values, Δ (ASR)= 0.083 Ω.cm^2, is about 3.5 times larger than the average error associated with the measurements (0.024 Ω.cm^2 at 650^{o}C, Section 5.2.2). However, the difference in activation energy, Δ (Ea)= 0.05 eV, is in the range/order of the estimated average error (0.07 eV, Section 5.2.2) and hence equal within error. This suggests that the observed differences in ASR of the two iso-Mo containing compositions are related to their structural differences. As coming out from the structural analysis (Chapter 4, *Section 4.3.4.1*), BSCFMo0.2-(Co/Fe=4) is DP-richer (79.1(7)%) and favors the formation of bigger perovskite unit cells (a_{SP}=3. 98187(9) Å, a_{DP}= 7.9868(6)Å) than BSCFMo0.2-(Co/Fe=3), with refined DP% content of 68.4(4)% and refined lattice parameters a_{SP}=3.97790(8) Å, a_{DP}= 7.9804(3) Å) (*Table 5.12*). This was attributed to the higher overall Co content in BCFMo0.2-(Co/Fe=4) than BCFMo0.2-(Co/Fe=3), favoring the B-site ordering upon introduction of Mo^{6+}. As established in *Section 5.2.1*, the increase of the DP% content is not beneficial for the ASR in most cases, due to the decrease in both electronic and oxygen ionic charge carriers. Hence, the improved performance of BSCFMo0.2-(Co/Fe=4) compared to BSCFMo0.2-(Co/Fe=3) must be related to the differences in overall and individual SP, DP compositions.

Table 5.12: Calculated ASR (Ω.cm^2) *at 600^{o}C and 650^{o}C and associated activation energy over the whole temperature range measured (600-800^{o}C) for the iso-Mo compositional pair BSCFMo0.2-(Co/Fe=3) and BSCFMo0.2-(Co/Fe=4), including structural information Chapter 4, Section 4.3.4.1.*

Abbreviation	**B-site composition**	**SP% DP%**	**a(SP), Å a(DP), Å**	**ASR (600^{o}C)**	**ASR (650^{o}C)**	**Ea (eV)**
BSCFMo0.2-(Co/Fe=3)	$Co_{0.60}Fe_{0.20}Mo_{0.20}$	68.4(4) 31.6(4)	3.97730(8) 7.9804(3)	0.760	0.305	1.20
BSCFMo0.2-(Co/Fe=4)*	$Co_{0.64}Fe_{0.16}Mo_{0.20}$	79.1(7) 20.9(7)	3.98187(9) 7.9868(6)	0.538	0.222	1.15

**As from Section 5.2.1.*

In an effort to explain the observed behavior of the iso-Mo-containing compositions, the undoped parent materials were considered. As reported in the literature, $Ba_{0.5}Sr_{0.5}Co_{0.8}Fe_{0.2}O_{3-\delta}$ shows the best electrochemical performance and the highest oxygen permeation flux among the compositions in the $Ba_{0.5}Sr_{0.5}Co_{1-x}Fe_xO_{3-\delta}$ family[95, 284]. The polarisation resistance of $Ba_{0.5}Sr_{0.5}Co_{0.6}Fe_{0.4}O_{3-\delta}$ and $Ba_{0.5}Sr_{0.5}Co_{0.8}Fe_{0.2}O_{3-\delta}$ is reported to be 0.13 and 0.085 $\Omega.cm^2$ respectively, at 600^oC[95]. Although the actual numbers are not directly comparable with this study, due to differences in the preparation of the cells, it can be deduced that the ASR values are increased by a factor of 1.5 when decreasing the actual Co content from 0.8 to 0.6 and the Co/Fe ratio from 4 to 1.5. Assuming proportional relationship of the ASR values with the Co/Fe ratio, one would expect increase by a factor 0.75 from BSCFMo0.2-(Co/Fe=4) to BSCFMo0.2-(Co/Fe=3) at 600^oC. The observed ASR values for BSCFMo0.2-(Co/Fe=4) and BSCFMo0.2-(Co/Fe=3) at 600^oC are 0.538 and 0.760 $\Omega.cm^2$ respectively with a calculated increment factor of 0.76/0.538= 1.4, which is the same as in the case of $Ba_{0.5}Sr_{0.5}Co_{0.8}Fe_{0.2}O_{3-\delta}$ and $Ba_{0.5}Sr_{0.5}Co_{0.6}Fe_{0.4}O_{3-\delta}$. The fact that the actual content of BSCFMo0.2-(Co/Fe=3) is 0.6 as in $Ba_{0.5}Sr_{0.5}Co_{0.6}Fe_{0.4}O_{3-\delta}$, suggests that it is the actual amount of Co that influences the electrochemical properties, rather than the Co/Fe ratio, for both BSCF and BSCFM materials, at low Mo content. It should be noted though that this is just an observation based on limited number of data and hence more work needs to be done to understand this behavior.

5.2.3.2. High Co/Fe

In order to investigate the compositional features leading to the enhanced performance of BSCFMo0.375-(Co/Fe=4) (Chapter 3 and *Section 5.2.1*), the electrochemical properties of the iso-Mo containing BSCFMo0.375-(Co/Fe=10) was also measured following the same protocol for fabrication of the cells and measurement, as established in *Section 5.1.1*. The impedance data for BSCFMo0.45-(Co/Fe=10) (Chapter 3, *Section 3.3.3*), which has the same Co/Fe ratio as BSCFMo0.375-(Co/Fe=10) but higher Mo content are also included in this study for comparison reasons. The polarization resistance of BSCFMo0.375-(Co/Fe=10) is about five times larger than BSCFMo0.375-(Co/Fe=4) at 650°C (*Figure 5.13*A) with obtained ASR values of 0.641 and 0.132 Ω.cm^2. This is also higher than the observed ASR for BSCFMo0.45-(Co/Fe=10) of 0.505 Ω.cm^2 at 650°C. Moreover, the obtained activation energy over the whole temperature range measured (*Figure 5.13B*) is higher in the case of the compositions with higher Co/Fe ratio, with calculated values of 1.70 eV for BSCFMo0.375-(Co/Fe=10) and 1.51 eV for BSCFMo0.45-(Co/Fe=10), compared to 1.25 eV for BSCFMo0.375-(Co/Fe=4).

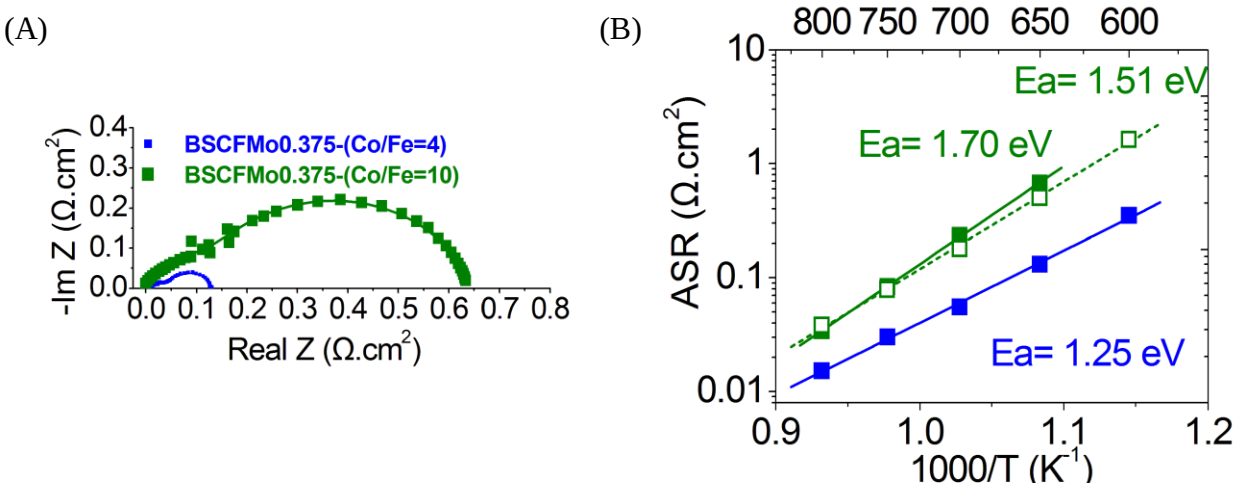

Figure 5.13: (A) Electrochemical impedance arcs at 650°C for BSCFMo0.375-(Co/Fe=4), BSCFMo0.375-(Co/Fe=10) and BSCFMo0.45-(Co/Fe=10), normalised to zero on the x-axis to remove the electrolyte contribution and (B) calculated ASR over the temperature range measured and associated activation energy (Ea).

The differences in ASR values and calculated activation energy for this set of BSCFM compositions are bigger than the average errors associated with this type of measurements

(Δ(ASR)= 0.024 $\Omega.cm^2$ at 650^oC and Δ(Ea)= 0.07 eV, from *Section 5.2.2*), implying that the differences in their electrochemical properties are due to the compositional differences. The nominal B-site compositions for these compounds are given in *Table 5.13*. The five times larger ASR obtained for BSCFMo0.375-(Co/Fe=10) compared to BSCFMo0.375-(Co/Fe=4), demonstrates that it is not solely the high amount of Mo that influence the catalytic properties over ORR and implicates their structural differences. Moreover, it is not a simple relation with the Co content, as suggested in *Section 5.2.3.1* for the Mo content of 0.2, since BSCFMo0.375-(Co/Fe-10) has higher overall Co content (Co0.582) than BSCFMo0.375-(Co/Fe=4) and BSCFMo0.45-(Co/Fe=10) (both Co0.500).

Table 5.13: Calculated ASR ($\Omega.cm^2$) at 600^oC and 650^oC and associated activation energy over the whole temperature range measured (600-800^oC) for the iso-Mo compositional pair BSCFMo0.375-(Co/Fe=4) and BSCFMo0.375-(Co/Fe=10), including the impedance results for BSCFMo0.45-(Co/Fe=10) and structural information for all from Chapter 4, Section 4.3.4.2.

Abbreviation	**B-site composition**	**SP%** **DP%**	**a(SP), Å** **a(DP), Å**	**ASR** **(650^oC)**	**Ea** **(eV)**
BSCFMo0.375-(Co/Fe=4)*	$Co_{0.500}Fe_{0.050}Mo_{0.375}$	28.8(7) 71.2(7)	3.98476(14) 7.98108(8)	0.132	1.25
BSCFMo0.375-(Co/Fe=10)	$Co_{0.582}Fe_{0.043}Mo_{0.375}$	44.1(4) 55.9(4)	3.98504(8) 7.99625(14)	0.641	1.70
BSCFMo0.45-(Co/Fe=10)**	$Co_{0.500}Fe_{0.050}Mo_{0.450}$	8.7(3) 91.2(3)	3.98671(13) 7.98940(4)	0.505	1.51

**As from Section 5.2.1.*

***As from Chapter 3, Section 3.3.3*

This implicates the structural differences of these SP/DP classified compositions (Chapter 4, *Section 4.3.4.2*). BSCFMo0.375-(Co/Fe=10) is DP-poorer, with refined DP% content of 55.9% compared to 71.2(7)% for BSCFMo0.375-(Co/Fe=4) (*Table 5.13*). Moreover, the bigger perovskite lattice parameters for BSCFMo0.375-(Co/Fe=10), especially for the major DP component (a_{DP}= 7.99625Å) compared to BSCFMo0.375-(Co/Fe=4) (a_{DP}= 7.98108Å), demonstrate the compositional changes in the individual SP and DP phases. The increase of the perovskite cells with the increase of Co/Fe was observed for the whole compositional range.

This was attributed to the higher amount of the bigger Co compared to Fe overall, but also in the individual SP and DP phases, for the composition with higher Co/Fe ratio in iso-Mo containing compositional pairs (Chapter 4, *Section 4.3.4*). According to this segregation scenario, the DP component in BSCFMo0.375-(Co/Fe=10) can incorporate higher amount of Mo^{6+} than BSCFMo0.375-(Co/Fe=4) since it can afford the induced reduction of its transition metals (Co and Fe) due to its higher Co content; Co can be reduced to Co^{2+} whilst Fe to Fe^{3+} at the conditions of the experiment (Chapter 4, *Section 4.3.4.3*). Since the overall Mo content for these compositions is the same, the SP component of BSCFMo0.375-(Co/Fe=10) will be poorer in Mo than BSCFMo0.375-(Co/Fe=4). It is hard to conclude which factor controls the activity over ORR in the iso-Mo containing compositions. However, it can be tentatively suggested that the structural differences are affecting primarily the oxygen dissociative adsorption, determined as the rate determining step for BSCFMo0.375-(Co/Fe=4) in air *(Section 5.2.2.3*), resulting also in the observed increase of the associated activation energy for BSCFMo0.375-(Co/Fe=10).

The improved performance of BSCFMo0.45-(Co/Fe=10) compared to the lower Mo containing BSCFMo0.375-(Co/Fe=10), in terms both of measured ASR and activation energy, is in agreement with the findings for the compositions with Co/Fe=4 discussed in *Section 5.2.1*. The high Mo content, close to the maximum limit where $BaMoO_4$ resistant impurity phase starts forming, is considered beneficial for the electrochemical properties, possibly related with redistribution of the cations in the perovskite phases.

5.3. Summary and discussion

The electrochemical performance of the BSCFM materials is a function of three main processes as established from the experiment in variable gas atmosphere and temperature for BSCFMo0.375-(Co/Fe=4). The oxygen dissociative adsorption was found to primarily control the impedance response in air and at $pO_2 \geq 0.01$ atm for the whole temperature range measured. This explains that the performance of BSCFMo0.375-(Co/Fe=4) is greatly improved when the thickness of the deposited cathode on the SDC electrolyte is increased, due to the extension of the bulk active area for oxygen reduction reaction (ORR). Moreover, the surface roughness of the SDC electrolyte substrate was found beneficial for the electrochemical performance, as it increases the cathode-electrolyte interfaces resulting in extent of the triple-phase boundary where the ORR takes place. At low pO_2, the oxygen dissociative adsorption becomes less significant and the gas phase diffusion dominates the impedance response at $pO_2 = 0.0028$ atm for the whole temperature range and at $pO_2 = 0.05$ atm for temperatures above 800^{o}C. The resistance associated with the electronic and ionic charge transfer remains relatively low for BSCFMo0.375-(Co/Fe=4) compared to the main processes identified, at the whole temperature and pO_2 range measured.

As coming out from the analysis of more Mo-doped BSCF compositions, the ones having Co/Fe ratio= 4 show enhanced electrochemical performance compared to iso-Mo containing specimens differing in the Co/Fe ratio. This was attributed to the structural differences of the consisting single (SP) and double (DP) perovskite phases in the BSCFM materials, likely differing in composition depending on the Co/Fe ratio. It is interesting to note though that the best electrochemical performance in the $Ba_{0.5}Sr_{0.5}Co_{1-x}Fe_xO_{3-\delta}$ series of oxides was also obtained for for the parent undoped $Ba_{0.5}Sr_{0.5}Co_{0.8}Fe_{0.2}O_{3-\delta}$, also with Co/Fe ratio equal to 4. This suggests similarities in the mechanism of cations distribution into the distinct SP and DP phases for the Mo-doped compositions.

In the series of $BSCFMo_{Mo}$-(Co/Fe=4) compositions studied, $0 \leq Mo \leq 0.45$, the measured ASR increases linearly with the Mo content up to 0.292, demonstrating the effect of reduced number of charge and oxygen ionic carriers due to the increase in the DP% content. However, this is not the case for higher Mo containing specimens, since the resistance values gradually decrease with

the increase of Mo content for BSCFMo0.33-(Co/Fe=4) and BSCFMo0.375-(Co/Fe=4). Increasing amount of Mo favors the formation of $BaMoO_4$ impurity phase, which is believed to be a poor electronic and ionic conductor, resulting in gradually higher ASR and associated activation energy for BSCFMo0.409-(Co/Fe=4) and BSCFMo0.45-(Co/Fe=4).

In conclusion, the lowest ASR among the compositions studied was obtained for BSCFMo0.375-(Co/Fe=4). This could be possibly related to the fact that the protocol for fabrication of the symmetrical cells was established for this composition and adopted for the rest. Further optimisation of the preparation procedure to specific compositions could possibly result to improved morphology and hence enhanced performance for other BSCFM compositions. As a starting point, it would be useful to develop a method of selecting the adhesion temperature of the cell according to the melting point of each composition in order to carefully control the morphology of the cathode layer. It should be noted though that the resulting morphology of the cathode layer does not show important dependence on the BSCFM composition, as determined by measuring the porosity of selected compositions (Chapter 3, *Section 3.3.3.2*), all made by the established protocol. In addition to this, the random errors associated with this type of measurements are smaller than the observed differences in the obtained resistance of each composition. Hence the performance of the BSCFM specimens seems to be more prone to variations in composition, which controls the resulting structure, rather than anything else.

6. CONCLUSIONS AND FUTURE WORK

Conclusions and future work

A range of $Ba_{0.5}Sr_{0.5}Co_{0.8-x}Fe_{0.2-y}Mo_{x+y}O_{3-\delta}$ ($BSCFM_{x+y}$-(Co/Fe=x/y)) compositions, with variants the Mo (x+y) content and Co/Fe (x/y) ratio was synthesised, followed by structural characterisation and evaluation as cathode materials for intermediate temperature (600-800^{o}C) solid oxide fuel cells (IT-SOFCs).

The compounds were initially prepared by solid-state synthesis based on the combination of high temperature heating steps with thorough mixing by hand-grinding. The inhomogeneity problems identified by energy dispersive spectroscopy (EDS) led to the replacement of initial hand-grinding steps by mechanical ball-milling.

The BSCFM compounds were characterised by a combination of X-ray diffraction and microscopy techniques. Introducing Mo^{6+} into the cubic perovskite structure of the parent $Ba_{0.5}Sr_{0.5}Co_{0.8}Fe_{0.2}O_{3-\delta}$ (BSCF) was found to favor the formation of biphasic compounds, consisting of 'single' (SP, lattice parameter a_p~3.9 Å isostructural to the parent undoped compound, crystallizing in space group $Pm\bar{3}m$) and 'double' perovskite phases (DP, double unit cell, lattice parameter $2a_p$~7.8 Å, crystallizing in space group $Fm\bar{3}m$). The doubling of the unit cell was attributed to the B-site ordering between Co^{2+} (0.745 Å) and Mo^{6+} (0.59Å) induced by the considerable difference in cations charge and size; the presence of Co^{2+} is due to the reduction of Co^{3+} and Co^{4+} in BSCF upon introducing Mo^{6+}. The SP and DP phases coexisted in all BSCFM compositions studied, with increasing DP volume as the Mo^{6+} content was increased, as evidenced by dark field (DF) TEM imaging.

The SP:DP phase ratio varied depending on the Mo content and the Co/Fe ratio, as coming out from the structural characterisation by Rietveld refinement of X-ray diffraction (XRD) data collected at room temperature. For the series of $BSCFM_{x+y}$-(Co/Fe=4) compositions, the Mo0.125 content in BSCFMo0.125-(Co/Fe=4) favors the formation of pure SP compound by XRD but small DP domains were visible from the DF-TEM images, whilst 20.9(7)% DP was refined for BSCFM0.20-(Co/Fe=4). Further increase of the of the DP character was observed for greater Mo amount in the same series of $BSCFM_{x+y}$-(Co/Fe=4) compositions, with refined 71.2(7)% DP in BSCFMo0.375-(Co/Fe=4). Higher Mo content of the Mo content led to approximately 85% DP in BSCFMo0.409-(Co/Fe=4) and BSCFMo0.45-(Co/Fe=4) and the expulsion of 1.6(1)% and 7.5(1)% $BaMoO_4$ impurity phase respectively. The exact compositional limits for the formation of DP and $BaMoO_4$ phases were found to be dependent on the Co/Fe ratio, with higher Co/Fe ratio favoring the formation of refineable DP content for as low as Mo0.125 in BSCFMo0.125-(Co/Fe=10) and BSCFMo0.45-(Co/Fe=10) being an impurity-free biphasic compound. On the contrary, 1.3(1)% $BaMoO_4$ impurity phase was refined for as low as Mo0.25 in BSCFMo0.25-(Co/Fe=2).

The long term phase stability of the BSCFM compounds at the operational temperature was evaluated by extended annealing at 750^{o}C for 120h (5 days). It was found out that the introduction of Mo^{6+} into the BSCF structure suppresses the phase transition to competing hexagonal polymorph phases encountered for the parent compound, which limits its application for long-term operation. According to the literature, the reason for the instability is the high Co content in BSCF and the preference of the transition of Co^{3+} (HS) to Co^{3+} (LS) with the latter preferring to be accommodated in hexagonal phases. As coming out from the stability experiments on the BSCFM compositions, the spin transition is not observed when the overall Co content is less than Co0.58. Moreover, the formation of the stable DP structure is believed to be an additional stabilisation factor for the SP/DP biphasic compounds, similarly to the isostructural $Ba_2CoMo_{0.5}Nb_{0.5}O_{6-\delta}$ and Ba_2CoMoO_6.

The electrical properties of the BSCFM compositions, measured by the four-probe d.c. method, were found to be dependent on the Mo content, with decreased electrical conductivity values as the Mo content increases. This was attributed to decrease of the concentration of M^{4+}-M^{3+} pairs

(where M: Co,Fe) which are considered as the electronic charge carriers of the transition metals due to the reduction upon introduction of Mo^{6+}. The concomitant decrease in the number of oxygen vacancies, as coming out from the thermogravimetric analysis (TGA) of selected key compositions, is expected to have a considerable effect on the ionic conductivity properties.

The electrochemical properties of the BSCFM compounds were found to be dependent on the overall composition. As coming out from the a.c. impedance measurements, the compositions having Co/Fe ratio= 4 show enhanced electrochemical performance compared to iso-Mo containing specimens differing in the Co/Fe ratio. This was attributed to the structural differences of the individual SP and DP, likely differing in composition depending on the Co/Fe ratio. According to the proposed segregation scenario, the compositions having lower overall Co/Fe form SP or SP/DP biphasic compounds which have analogically lower Co/Fe ratio in each of the perovskite phases compared to BSCFM compounds with higher overall Co/Fe ratio. Consequently, this implies that the amount of Mo incorporated in each phase is controlled by the Co/Fe ratio.

In the series of $BSCFM_{x+y}$-(Co/Fe=4) compositions studied, the measured area specific resistance (ASR) increases with the Mo content for up to Mo0.292 accompanying the reduced number of charge and oxygen ionic carriers. However, this is not the case for higher Mo containing specimens, since the resistance values gradually decrease with the increase of Mo content reaching the minimum for BSCFMo0.375-(Co/Fe=4), which is the highest Mo containing $BaMoO_4$-free composition for the $BSCFM_{x+y}$-(Co/Fe=4) series of compounds. The formation of $BaMoO_4$ results in larger ASR values most likely related to poor electronic and ionic conductivity properties of the impurity phase.

The best electrochemical performance among all the compositions studied was found for BSCFMo0.375-(Co/Fe=4) with obtained ASR values of 0.351 $\Omega.cm^2$ and 0.13 $\Omega.cm^2$ at 600^{o}C and 650^{o}C respectively; these are comparable with the 0.13-2.1 $\Omega.cm^2$ range of reported ASR values at 600^{o}C for the parent undoped BSCF, depending on processing conditions and the electrolyte used. As coming out from the experiment in variable gas atmosphere and temperature, the electrochemical performance of BSCFMo0.375-(Co/Fe=4) is limited primarily by the oxygen dissociative adsorption in air and at $pO_2 \geq 0.01$ atm over the whole temperature range measured. The impedance response is dominated by gas phase diffusion at $pO_2 = 0.0028$ atm for the whole temperature range and at $pO_2 = 0.05$ atm for temperatures above 800^{o}C.

The structure of BSCFMo0.375-(Co/Fe=4) was extensively characterised in order to identify the structural features that lead to optimal electrochemical activity of the BSCFM system. The joint Rietveld refinement of Neutron (ND) and X-ray diffraction data (XRD) revealed that it consists of approximately 70.81(10)% DP and 28.13(9)% with compositions $BaSrCo_{0.961(2)}Fe_{0.142(2)}Mo_{0.897(3)}O_{5.95(3)}$ and $Ba_{0.5}Sr_{0.5}Co_{0.547(9)}Fe_{0.253(2)}Mo_{0.200(8)}O_{2.81(3)}$ respectively. The SP is Mo-poor and has a considerable amount of oxygen vacancies, whilst the DP is Mo-rich and oxygen stoichiometric. There are two B- antisites in the DP component; a Mo-rich and a Co-rich site which alternate in three dimensions as confirmed by High Angle Annular Dark Field (HAADF) imaging. The refined overall oxygen content of 2.94(1) in BSCFMo0.375-(Co/Fe=4) is in close agreement with the outcome of the iodometric titration (2.96(9)) and the reduction experiment monitored by thermogravimetric analysis (TGA) (2.91). The Mössbauer analysis revealed that Fe adopts its trivalent state in both constituent phases; this allows the calculation of a Co oxidation state of +3.04 in the SP and +2.18 in the DP, taking into consideration the stability of Mo^{6+} and the refined oxygen content.

In conclusion, BSCFMo0.375-(Co/Fe=4) shows the best electrochemical performance among the compositions studied and does not suffer from the long-term structural stability encountered in the BSCF parent material. Moreover, the improved chemical and thermal (TEC= 13.87×10^{6} K^{-1} at 500-800^{o}C) compatibility with commonly used electrolytes, such as $Sm_{0.2}Ce_{0.8}O_{1.9}$ (SDC20), compared to the undoped compound. These indicate that BSCFMo0.375-(Co/Fe=4) has much potential as an SOFC cathode. It would be interesting to measure the electrochemical properties of the individual SP and DP components and mixtures of them in various ratios in order to understand better the role of each phase to the overall performance and possibly improve further the cathode properties. Future work targeting at lowering the associated resistance could also involve preparation of composites in appropriate ratios with electrolytes or porous electrolyte layers at the cathode-electrolyte interface; both cases can provide more active sites for oxygen reduction due to the introduction of additional oxygen ion carriers.

7. PUBLICATIONS FROM THIS THESIS

M.A. Tsiamtsouri[1], A.Demont[1], R. Sayers[1], S. Romani, P. Chater, H. Niu, C. Martí-Gastaldo, Z. Xu, Z.Q. Deng, Y. Bréard, M.F. Thomas, J.B. Claridge, M.J.Rosseinsky '*Single sublattice epitaxial phase separation driven by charge frustration in a complex oxide'*, Manuscript being reviewed in Nature Chemistry (2012).

REFERENCES

1. Kordesch, K.V., Simader, G.R. , *Environmental Impact of Fuel Cell Technology*. Chemical Reviews, 1995. **95**: p. 191-207.
2. Dresselhaus, M.S., Thomas, I. L. , *Alternative energy technologies.* Nature, 2001. **414**: p. 332-337.
3. Huang, K., Goodenough, J.B., *Solid oxide fuel cell technology- principles, performance and operation*. 2009: Woodhead Publishing Limited.
4. *Alternative Fuels and the Environment*, ed. F.S. Sterrett. 1994: Lewis Publishers, CRC Press.
5. Momirlan, M., Veziroglu, T.N. , *The properties of hydrogen as fuel tomorrow in sustainable energy system for a cleaner planet.* International Journal of Hydrogen Energy, 2005. **30**(7): p. 795–802.
6. Schœnbeinf, C.F., *On the Voltaic Polarization of certain Solid and Fluid Substances.* Philosophical Magazine, 1838. **14**: p. 43-45.
7. Grove, W.R., *On voltaic series and the combination of gases by platinum.* Philosophical Magazine, 1839. **14**: p. 127-130.
8. Mond, L., Langer, C. , *A New Form of Gas Battery* Proceedings of the Royal Society of London, 1889. **46**: p. 296-304.
9. Weissbart, J., Ruka, R., *A Solid Electrolyte Fuel Cell* Journal of the Electrochemical Society, 1962. **109**(8): p. 723-726.
10. Brett, D.J.L., Atkinson, A., Brandon, N.P., Skinner, S.J., *Intermediate temperature solid oxide fuel cells.* Chemical Society Reviews, 2008. **37**: p. 1568–1578.
11. Larminie, J. and A. Dicks, *Fuel Cell Systems Explained*. 2003: John Wiley & Sons.
12. Minh, N.Q., *Ceramic Fuel Cells.* Journal of the American Ceramic Society 1993. **76** p. 563-588.
13. Minh, N.Q., Takahashi, T., *Science and technology of ceramic fuel cells*. 1995: Elsevier Science B.V.
14. *Fuel Cell Education.* Fuel Cell Store, 2012: p. http://fuelcellstore.com/education.asp.
15. Larmine J, A.D., *Fuel cell systems explained*. 2000: John Wiley & Sons.
16. . Handbook of Fuel Cells: Fundamentals, Technology, Applications, ed. W. Vielstich, Lamm, A., Gasteiger, Hubert A. . 2003: John Wiley & Sons.
17. Haile, S.M., *Fuel cell materials and components.* Acta Materialia, 2003. **51** (19): p. 5981-6000.
18. Singhal, S.C., *Solid oxide fuel cells for stationary, mobile, and military applications.* Solid State Ionics, 2002. **152-153**: p. 405-410.
19. Takeda, Y., Kanno, R., Noda, M., Tomida, Y., Yamamoto, O. , *Cathodic polarisation phenomena of perovskite oxide electrodes with stabilised zirconia.* Journal of the Electrochemical Society, 1987. **134**(11): p. 2656-2661.
20. Jacobson, A.J., *Materials for Solid Oxide Fuel Cells.* Chemistry of Materials, 2010. **22**: p. 660-674.

21. Adler, S.B., *Factors Governing Oxygen Reductiom in Solid Oxide Fuel Cell Cathodes.* Chemical Reviews, 2004. **104**: p. 4971-4843.
22. Tsipis, E.V., Kharton, V.V. , *Electrode materials and reaction mechanisms in solid oxide fuel cells: a brief review, I. Performance-determining factors.* Journal of Solid State Electrochemistry 2008. **12**: p. 1039–1060.
23. Boivin, J.C., Mairesse, G. , *Recent Material Developments in Fast Oxide Ion Conductors* Chemistry of Materials, 1998. **10**(10): p. 2870-2888.
24. Steele, B.C.H., *Survey of materials selection for ceramic fuel cells II. Cathodes and anodes.* Solid State Ionics, 1996. **86-88**(2): p. 1223–1234.
25. Chiang, Y.M., Birnie III, D., Kingery, W.D. , *Physical Ceramics: Principles for Ceramic Science and Engineering*. 1997: John Wiley & Sons.
26. Chroneos, A., Yildiz, B., Tarancon, A., Parfitta, D., Kilner, J.A. , *Oxygen diffusion in solid oxide fuel cell cathode and electrolyte materials: mechanistic insights from atomistic simulations.* Energy & Environmental Science, 2011. **4**: p. 2774–2789.
27. West, A.R., *Basic Solid State Chemistry, 2nd edition*. 1996: John Wiley & Sons.
28. Voorhoeve, R.J.H., Remeika, J.P.,Trimble, L.E. , *Defect chemistry and catalysis in oxidation and reduction over perovskite-type oxides.* Annals of the New York Academy of Sciences, 1976. **3**: p. 3-20.
29. Fierro, J.L.G., *Metal Oxides, Chemistry and Applications*. 2006: Taylor & Francis Group, LLC.
30. Miessler, G.L., Tarr, D.A. , *Inorganic Chemistry, 3rd Edition*. 1991: Pearson Education International.
31. Elliott, S., *The Physics and Chemistry of Solids*. 1998: John Wiley & Sons.
32. Nave, C.R., *Band Theory of Solids.* HyperPhysics, Department of Physics and Astronomy Georgia State University, 2010: p. http://hyperphysics.phy-astr.gsu.edu/hbase/solids/band.html#c1.
33. Rao, C.N.R., Raveaus, B., *Transition Metal Oxides: Structure, Properties and Synthesis of Ceramics Oxides, 2nd edition*. 1998: John Wiley & Sons.
34. Mehrer, H., *Diffusion in Solids: Fundamentals, Methods, Materials,Diffusion-Controlled Processes.* Springer Series in Solid-State Sciences, 2007. **155**(Part I): p. 95-104.
35. Martínez, J.P., *Síntesis y caracterización de materiales con estructura tipo perovskita para pilas de combustible de óxido sólido de temperatura intermedia*. 2006, Universidad de Laguna.
36. Kilner, J.A., Brook, R.J. , *A study of oxygen ion conductivity in doped non-stoichiometric oxides.* Solid State Ionics 1982. **6**: p. 237-252.
37. Mitchell, R.H., *Perovskites: Modern and Ancient*. 2002: Almaz Press Inc.
38. Goldschmidt, V.M., *Die Gesetze der Krystallochemie.* Die Naturwissenschaften, 1927. **21**: p. 477-485.
39. Anderson, M.T., Greenwood, K.B., Taylor, G.A., Poeppelmeier, K.R., *B-cation arrangements Iin double perovskites.* Progress in Solid State Chemistry 1993. **22**: p. 197-233.
40. Knapp, M.C., Woodward, P.M. , *A-site cation ordering in $AA'BB'O_6$ perovskites.* Journal of Solid State Chemistry 2006. **179**: p. 1076-1085.
41. Brandon, N.P., Skinner,S., Steele, B.C.H. , *Recent advances in materials for fuel cells* Annual Review of Materials Research, 2003. **33**: p. 183-213.

42. Skinner, S.J., Laguna-Bercero, M.A., *Advanced Inorganic Materials for Solid Oxide Fuel Cells*. Energy Materials, ed. D.W. Bruce, Walton, R. I., O'Hare, D. 2011: John Wiley & Sons.
43. Steele, B.C.H., *Materials for IT-SOFC stacks,35 years R&D: the inevitability of gradualness?* Solid State Ionics 2000. **134**: p. 3-20.
44. Huang, K., Lee, H.Y., Goodenough, J.B. , *Sr- and Ni-Doped $LaCoO_3$ and $LaFeO_3$ Perovskites: New Cathode Materials for Solid -Oxide Fuel Cells.* Journal of Electrochemical Society, 1998. **145**(9): p. 3220-3227.
45. Casselton, R.E.W., *Blackening in yttria stabilized zirconia due to cathodic processes at solid platinum electrodes.* Journal of Applied Electrochemistry, 1974. **4**(1): p. 25-48.
46. Yamamoto, O., Takeda,Y., Kanno, R., Noda,M. , *Perovskite-type oxides as oxygen electrodes for high temperature oxide fuel cells.* Solid State Ionics 1987. **22**(2): p. 241-246.
47. Simner, S.P., Shelton, J.P., Anderson, M.D., Stevenson, J.W., *Interaction between $La(Sr)FeO_3$ SOFC cathode and YSZ electrolyte.* Solid State Ionics 2003. **161**(1-2).
48. Arachi, Y., Sakai, H., Yamamoto, O., Takeda, Y., Imanishai, N. , *Electrical conductivity of the ZrO_2-Ln_2O_3 (Ln=lanthanides) system.* Solid State Ionics, 1999. **121**(1-4): p. 133–139.
49. Politova, T.I., Irvine, J.T.S. , *Investigation of scandia–yttria–zirconia system as an electrolyte material for intermediate temperature fuel cells—influence of yttria content in system $(Y_2O_3)_x(Sc_2O_3)_{(11-x)}(ZrO_2)_{89}$.* Solid State Ionics, 2004. **168**(1-2): p. 153–165.
50. Hui, S.R., Roller, J., Yick, Sing, Zhang, Xinge, Decès-Petit, C., Xie, Y., Maric, R., Ghosh, D. , *A brief review of the ionic conductivity enhancement for selected oxide electrolytes.* Journal of Power Sources, 2007. **172**(2): p. 493–502.
51. Kawada, T., Yokokawa, H., Dokiya, M., Sakai, N., Horita, T., Van Herle, J., Sasaki, Kazutaka *Ceria-Zirconia Composite Electrolyte for Solid Oxide Fuel Cells.* Journal of Electroceramics, 1997. **1**(2): p. 155-164.
52. Ishihara, T., Matsuda, H., Takita, Y., *Doped $LaGaO_3$ Perovskite Type Oxide as a New Oxide Ionic Conductor.* Journal of the American Chemical Society, 1994. **116** p. 3801-3803.
53. Huang, K., Feng, M., Goodenough, J.B. , *Sol-Gel Synthesis of a New Oxide-Ion Conductor Sr- and Mg-Doped $LaGaO_3$ Perovskite* Journal of the American Ceramic Society, 1996. **79**(4): p. 1100–1104.
54. Huang, K., Tichy, R.S., Goodenough, J.B. , *Superior Perovskite Oxide-Ion Conductor; Strontium- and Magnesium-Doped $LaGaO_3$: I, Phase Relationships and Electrical Properties.* Journal of the American Ceramic Society, 1998. **81**(10): p. 2565–2575.
55. Huang, K., Feng, M., Goodenough, J.B., Schmerling, M., *Characterization of Sr-Doped $LaMnO_3$ and $LaCoO_3$ as Cathode Materials for a Doped $LaGaO_3$ Ceramic Fuel Cell* Journal of Electrochemical Society, 1996. **143**(11): p. 3630-3636.
56. Yamaji, K., Horita, T., Ishikawa, M., Sakai, N., Yokokawa, H., *Chemical stability of the $La_{0.9}Sr_{0.1}Ga_{0.8}Mg_{0.2}O_{2.85}$ electrolyte in a reducing atmosphere.* Solid State Ionics, 1999. **121**(1-4): p. 217–224.
57. Tsipis, E.V., Kharton, V.V. , *Electrode materials and reaction mechanisms in solid oxide fuel cells: a brief review, II. Electrochemical behavior vs. materials science aspects.* Journal of Solid State Electrochemistry 2008. **12**: p. 1367-1391.

58. Keep, C.W., Baker, R.T.K., France, J.A., *Origin of filamentous carbon formation from the reaction of propane over nickel.* Journal of Catalysis, 1977. **47**(2): p. 232-238.
59. Alzate-Restrepo, V., Hill, J.M., *Effect of anodic polarization on carbon deposition on Ni/YSZ anodes exposed to methane.* Applied Catalysis A: General, 2008. **342**(1): p. 49-55.
60. Tao, S., Irvine, J.T.S. , *Discovery and Characterization of Novel Oxide Anodes for Solid Oxide Fuel Cells.* The Chemical Record, 2004. **4**(2): p. 83-95.
61. Fergus, J.W., *Oxide anode materials for solid oxide fuel cells.* Solid State Ionics, 2006. **177**(17-18): p. 1529–1541.
62. Boukamp, B.A., *Fuel cells: The amazing perovskite anode.* Nature Materials, 2003. **2**(5): p. 294-296.
63. A. Petric, S.H., *Evaluation of yttrium-doped $SrTiO_3$ as an anode for solid oxide fuel cells.* Journal of the European Ceramic Society, 2002. **22**(9-10): p. 1673-1681.
64. Mukundan, R., Brosha, E.L.,Garzon, F.H. , *Sulfur Tolerant Anodes for SOFCs* Electrochemical and Solid-State Letters 2004. **7**(1): p. A5-A7.
65. Skinner, S.J., *Recent advances in perovskite-type materials for SOFC cathodes.* Fuel Cells Bulletin, 2001. **4**(33): p. 6-12.
66. Kilner, J.A., *Ceramic Electrodes for SOFC's.* Boletín de la Sociedad Española de Cerámica y Vidrio 1998. **37**(2-3): p. 247-255.
67. Sun, C., Hui, R., Roller, J. , *Cathode materials for solid oxide fuel cells: a review.* Journal of Solid State Electrochemistry 2010. **14**: p. 1125-1144.
68. Aguadero, A., Fawcett, L., Taub, S., Woolley, R., Wu, K.T., Xu, N., Kilner, J.A., Skinner, S.J. , *Materials development for intermediate-temperature solid oxide electrochemical devices.* Journal of Materials Science, 2012. **47**(9).
69. Zhou, W., Ran, R., Shao, Z., *Progress in understanding and development of $Ba_{0.5}Sr_{0.5}Co_{0.8}Fe_{0.2}O_{3-\delta}$-based cathodes for intermediate temperature solid-oxide fuel cells: A review.* Journal of Power Sources 2009. **192**: p. 231–246.
70. Badwal, S.P.S., Foger, K. , *Solid Oxide Electrolyte Fuel Cell Review.* Ceramics International 1996. **22**: p. 257-265.
71. Ralph, J.M., Schoeler, A. C., Krumpelt, M. , *Materials for lower temperature solid oxide fuel cells.* Journal of Materials Science, 2001. **36**: p. 1161-1172.
72. Jiang, S.P., *A comparison of O_2 reduction reactions on porous (La,Sr)MnO_3 and (La,Sr)(Co,Fe)O_3 electrodes.* Solid State Ionics, 2002. **146**(1-2): p. 1–22.
73. Bak, T., Nowotny, J., Rekas, M., Ringer, S., Sorrell, C.C. , *Defect Chemistry and Electrical Properties of $La_{1-x}Sr_xCoO_{3-\delta}$, IV. Electrical Properties.* Ionics 2001. **7**.
74. Figueiredo, F.M., Marques, F.M.B., Frade,J.R. , *Electrochemical permeability of $La_{1-x}Sr_xCoO_{3-\delta}$ materials.* Solid State Ionics, 1998. **111**(3-4): p. 273–281.
75. Mizusaki, J., Tabuchi, J.,Matsuura, T., Yamauchi, S., Fueki, K., *Electrical Conductivity and Seebeck Coefficient of Nonstoichiometric $La_{1-x}Sr_xCoO_{3-\delta}$* Journal of Electrochemical Society, 1989. **136**(7): p. 2082-2088.
76. Tai, L.-W., Nasrallah, M.M., Anderson, H.U., Sparlin, D.M., Sehlin, S.R. , *Structure and electrical properties of $La_{1-x}Sr_xCo_{1-y}Fe_yO_3$. Part 1. The system $La_{0.8}Sr_{0.2}Co_{1-y}Fe_yO_3$.* Solid State Ionics, 1995. **76**(3-4): p. 259-271.
77. Tietz, F., *Thermal Expansion of SOFC Materials.* Ionics, 1999. **5**.

78. L.-W. Tai, M.M.N., H.U. Anderson, D.M. Sparlin, S.R. Sehlin, *Structure and electrical properties of $La_{1-x}Sr_xCo_{1-y}Fe_yO_3$. Part 2. The system $La_{1-x}Sr_xCo_{0.2}Fe_{0.8}O_3$.* Solid State Ionics, 1995. **76**(3-4): p. 273-283.
79. L-W. Tai, M.M.N., H.U. Anderson, *Thermochemical Stability, Electrical Conductivity, and Seebeck Coefficient of Sr-Doped $LaCo_{0.2}Fe_{0.8}O_{3-\delta}$.* Journal Of Solid State Chemistry 1995. **118**(1): p. 117–124.
80. Tai, L.-W., Nasrallah, M.M., Anderson, H.U., Sparlin, D.M., Sehlin, S.R. , *Structure and electrical properties of $La_{1-x}SrxCo_{1-y}Fe_yO_3$. Part 2. The system $La_{1-x}Sr_xCo_{0.2}Fe_{0.8}O_3$.* Solid State Ionics, 1995. **76**(3-4): p. 273-283.
81. Esquirol, A., Brandon, N. P., Kilner, J. A., Mogensen, M. , *Electrochemical Characterization of $La_{0.6}Sr_{0.4}Co_{0.2}Fe_{0.8}O_3$ Cathodes for Intermediate-Temperature SOFCs* Journal of Electrochemical Society 2004. **151**(11): p. A1847-A1855.
82. Chen, C.C., Nasrallah, M. M., Anderson, H. U., Alim, M. A. , *Immittance Response of $La_{0.6}Sr_{0.4}Co_{0.2}Fe_{0.8}O_{3-\delta}$ Based Electrochemical Cells.* Journal of Electrochemical Society, 1995. **142**(2): p. 491-496.
83. Teraoka, Y., Zhang, H.M., Okamoto, K., Yamazoe, N. , *Mixed ionic-electronic conductivity of $La_{1-x}SrxCo_{1-y}FeyO_{3-\delta}$ perovskite-type oxides.* Materials Research Bulletin, 1988. **23**(1): p. 51–58.
84. Esquirol, A., Kilner, J., Brandon, N., *Oxygen transport in $La_{0.6}Sr_{0.4}Co_{0.2}Fe_{0.8}O_{3-\delta}/Ce_{0.8}Ge_{0.2}O_{2-x}$ composite cathode for IT-SOFCs* Solid State Ionics 2004. **175**(1-4): p. 63-67.
85. Wang S., K.T., Nagata S., Honda T., Kaneko T., Iwashita N., Dokiya M., *Performance of a $La_{0.6}Sr_{0.4}Co_{0.8}Fe_{0.2}O_3$-$Ce_{0.8}Gd_{0.2}O_{1.9}$-Ag cathode for ceria electrolyte SOFCs.* Solid State Ionics 2002. **146**(3-4): p. 203-210.
86. Frank Tietz, Q.F., Vincent A. C. Haanappel, Andreas Mai, Norbert H. Menzler, Sven Uhlenbruck, *Materials Development for Advanced Planar Solid Oxide Fuel Cells.* International Journal of Applied Ceramic Technology, 2007. **4**(5): p. 436–445.
87. Tietz, F., Mai, A., Stöver, D., *From powder properties to fuel cell performance – A holistic approach for SOFC cathode development.* Solid State Ionics, 2008. **179**(27-32): p. 1509-1515.
88. Shao, Z., Haile, S.M. , *A high-performance cathode for the next generation of solid-oxide fuel cells.* Nature 2004. **431**: p. 170-173.
89. McIntosh, S., Vente, J.F. W., Haije,G., Blank, D. H. A.and Bouwmeester, H. J. M., *Oxygen Stoichiometry and Chemical Expansion of $Ba_{0.5}Sr_{0.5}Co_{0.8}Fe_{0.2}O_{3-\delta}$ Measured by in Situ Neutron Diffraction.* Chemistry of Materials, 2006. **18**: p. 2187-2193.
90. Wei, B., Lü, Z., Li, S., Liu, Y., Liu, K., Sua,W., *Thermal and Electrical Properties of New Cathode Material $Ba_{0.5}Sr_{0.5}Co_{0.8}Fe_{0.2}O_3-\delta$ for Solid Oxide Fuel Cells.* Electrochemical and Solid-State Letters, 2005. **8**(8): p. A428-A43.
91. Švarcová, S., Wiik, K., Tolchard, J., Bouwmeester, H.J.M., Grande, T., *Structural instability of cubic perovskite $BaxSr_{1-x}Co_{1-y}Fe_yO_{3-\delta}$.* Solid State Ionics 2008. **178**: p. 1787-1791.
92. Mueller, D.N., De Souza, R.A., Weirich, T.E., Roehrens, D., Mayer, J., Martin, M., *A kinetic study of the decomposition of the cubic perovskite-type oxide $Ba_xSr_{1-x}Co_{0.8}Fe_{0.2}O_{3-\delta}$ (BSCF) (x = 0.1 and 0.5).* Physical Chemistry Chemical Physics, 2010. **12**: p. 10320-10328.

93. Niedrig , C., Taufall, S., Burriel, M., Menesklou, W., Wagner, S.F., Baumann, S., Ivers-Tiffée, E., *Thermal stability of the cubic phase in $Ba_{0.5}Sr_{0.5}Co_{0.8}Fe_{0.2}O_{3-\delta}$ (BSCF)1.* Solid State Ionics, 2011. **197** p. 25-31.
94. Arnold, M., Gesing,T.M., Martynczuk, J., Feldhoff, A., *Correlation of the Formation and the Decomposition Process of the BSCF Perovskite at Intermediate Temperatures.* Chemistry of Materials, 2008. **20**: p. 5851-5858.
95. Chen, Z., Ran, R., Zhou, W., Shao, Z., Liu, S., *Assessment of $Ba_{0.5}Sr_{0.5}Co_{1-y}Fe_yO_{3-\delta}$ (y = 0.0–1.0) for prospective application as cathode for IT-SOFCs or oxygen permeating membrane.* Electrochimica Acta 2007. **52**: p. 7343-7351.
96. Kim, J.H., Manthiram, A., *Low Thermal Expansion $RBa(Co,M)_4O_7$ Cathode Materials Based on Tetrahedral-Site Cobalt Ions for Solid Oxide Fuel Cells.* Chemistry of Materials, 2010. **22**: p. 822-831.
97. Kim, J.H., Kim, Y.N., Bi, Z., Manthiram, A., Paranthaman, M. P., Huq, A., *High temperature phase stabilities and electrochemical properties of $InBaCo_{4-x}Zn_xO_7$cathodes for intermediate temperature solid oxide fuel cells.* Electrochimica Acta, 2011. **56**(16): p. 5740–5745.
98. Vert, V.B., Serra, J.M., Jordá, J.L. , *Electrochemical characterisation of $MBaCo_3ZnO_{7+\delta}$(M=Y, Er, Tb) as SOFC cathode material with low thermal expansion coefficient.* Electrochemistry Communications, 2010. **12**(2): p. 278–281.
99. Kim, Y.N., Kim, J.H., Manthiram, A., *Characterization of $(Y_{1-x}Ca_x)BaCo_{4-y}Zn_yO_7$ as cathodes for intermediate temperature solid oxide fuel cells.* International Journal of Hydrogen Energy, 2011. **36**(23): p. 15295–15303.
100. Chroneos, A., Parfitt, D., Kilner, J.A., Grimes, R.W. , *Anisotropic oxygen diffusion in tetragonal $La_2NiO_{4+\delta}$: molecular dynamics calculations.* Journal of Materials Chemistry, 2010. **20**: p. 266-270.
101. Skinner, S.J., Kilner, J.A., *Oxygen diffusion and surface exchange in $La_{2-x}Sr_xNiO_{4+\delta}$.* Solid State Ionics, 2000. **135**(1-4): p. 709–712.
102. Pérez-Coll, D., Aguadero, A., Escudero, M.J., Núñez, P., Daza, L. , *Optimization of the interface polarization of the La_2NiO_4-based cathode working with the $Ce_{1-x}Sm_xO_{2-\delta}$ electrolyte system.* Journal of Power Sources, 2008. **178**(1): p. 151–162.
103. Zinkevich, M., Aldinger, F., *Thermodynamic analysis of the ternary La–Ni–O system.* Journal of Alloys and Compounds, 2004. **375**(1-2): p. 147-161.
104. Amow, G., Skinner, S. J. , *Recent developments in Ruddlesden–Popper nickelate systems for solid oxide fuel cell cathodes.* Journal of Solid State Electrochemistry, 2006. **10**(8): p. 538-546.
105. Maignan, A., Martin, C., Pelloquin, D., Nguyen, N., Raveau, B. , *Structural and Magnetic Studies of Ordered Oxygen-Deficient Perovskites $LnBaCo_2O_{5+\delta}$, Closely Related to the "112" Structure.* Journal of Solid State Chemistry, 1999. **142**(2): p. 247–260.
106. Tarancon, A., Skinner, S.J., Chater, R.J., Hernandez-Ramırez, F., Kilner, .A. , *Layered perovskites as promising cathodes for intermediate temperature solid oxide fuel cells.* Journal of Materials Chemistry, 2007. **17**: p. 3175–3181.
107. Chang, A., Skinner, S.J., Kilner, J.A. , *Electrical properties of $GdBaCo_2O_{5+x}$ for ITSOFC applications.* Solid State Ionics, 2006. **177**(19-25): p. 2009–2011.

108. Peña-Martínez, J., Tarancón, A., Marrero-López, D., Ruiz-Morales, J. C., Núñez, P., *Evaluation of $GdBaCo_2O_{5+\delta}$ as Cathode Material for Doped Lanthanum Gallate Electrolyte IT-SOFCs* Fuel Cells, 2008. **8**(5): p. 351–359.
109. Kim, J.H., Cassidy, M., Irvine, J.T.S., Bae, J. , *Advanced Electrochemical Properties of $LnBa_{0.5}Sr_{0.5}Co_2O_{5+\delta}$ (Ln = Pr, Sm, and Gd) as Cathode Materials for IT-SOFC.* Journal of The Electrochemical Society, 2009. **156**(6): p. B682-B689.
110. Kim, J.H., Prado, F., Manthiram, A. , *Characterization of $GdBa_{1-x}Sr_xCo_2O_{5+\delta}$ $(0\leq x\leq 1.0)$ Double Perovskites as Cathodes for Solid Oxide Fuel Cells* Journal of Electrochemical Society, 2008. **155**(10): p. B1023-B1028.
111. Gong, W., Yadav, M., Jacobson, A.J. , *A Comparison of Electrochemical Performance of Double Perovskite $REBaCo_2O_{5+x}$ Cathodes in Symmetrical Solid Oxide Fuel Cells.* Materials Research Society Symposium Proceedings, 2008. **1126**.
112. Bae, J.M., Steele, B.C.H. , *Properties of Pyrochlore Ruthenate Cathodes for Intermediate Temperature Solid Oxide Fuel Cells.* Journal of Electroceramics, 1999. **3**(1): p. 37-46.
113. Zhong, Z., *Bismuth Ruthenate-Based Pyrochlores for IT-SOFC Applications* Electrochemical and Solid-State Letters, 2006. **9**(4): p. A215-A219.
114. Zhao, H., Teng, D.,Zhang, X., Zhang, C., Li, X., *Structural and electrochemical studies of $Ba_{0.6}Sr_{0.4}Co_{1-y}Ti_yO_{3-\delta}$ as a new cathode material for IT-SOFCs.* Journal of Power Sources, 2009. **186** p. 305-310.
115. Meng, X., Meng, B., Tan, X., Yang, N., Ma, Z.F. , *Synthesis and properties of $Ba_{0.5}Sr_{0.5}(Co_{0.6}Zr_{0.2})Fe_{0.2}O_{3-\delta}$ perovskite cathode material for intermediate temperature solid-oxide fuel cells.* Materials Research Bulletin, 2009. **44**: p. 1293-1297.
116. Park, J., Zou, J., Yoon, H., Kim, G., Chung, J.S. , *Electrochemical behavior of $Ba_{0.5}Sr_{0.5}Co_{0.2-x}Zn_xFe_{0.8}O_{3-\delta}$ (x= 0-0.2) perovskite oxides for the cathode of solid oxide fuel cells.* International Journal of Hydrogen Energy, 2011. **36**: p. 6184-6193.
117. Fang, S.M., Yoo, C.Y., Bouwmeester, H.J.M. , *Performance and stability of niobium-substituted $Ba_{0.5}Sr_{0.5}Co_{0.8}Fe_{0.2}O_{3-\delta}$ membranes.* Solid State Ionics 2011. **195**: p. 1-6.
118. Haworth, P., Smart, S., Glasscock, J., Diniz da Costa, J.C. , *Yttrium doped BSCF membranes for oxygen separation.* Separation and Purification Technology, 2011. **81**: p. 88-93.
119. Martínez-Lope, M.J., Alonso, J. A., Casais, M.T., Fernández-Díaz, M. T., *Preparation, Crystal and Magnetic Structure of the Double Perovskites Ba_2CoBO_6 (B = Mo, W).* European Journal of Inorganic Chemistry, 2002. **2002**(9): p. 2463–2469.
120. Deng, Z.Q., Smit, J.P., Niu, H.J., Evans, G., Li, M.R., Xu, Z.L., Claridge, J.B., Rosseinsky, M.J. , *B Cation Ordered Double Perovskite $Ba_2CoMo_{0.5}Nb_{0.5}O_{6-\delta}$ As a Potential SOFC Cathode.* Chemistry of Materials, 2009. **21**: p. 5154-5162.
121. *Molybdenum Chemistry & Uses.* International Molybdenum Association (IMOA), 2012: p. http://www.imoa.info/index.php.
122. *Powder diffraction & Rietveld School.* Durham University, 2010.
123. Krumeich, F., *Properties of Electrons, their Interactions with Matter and Applications in Electron Microscopy.* The Electron Microscopy Site, 2012: p. http://www.microscopy.ethz.ch/.
124. Goodhew, P., Fretwell, A.,Tanovic, B., Jones, I.,Green, A., Brook, D. , *Electron Diffraction.* Matter website, 2000(University of Liverpool): p. http://www.matter.org.uk/diffraction/electron/electron_diffraction.htm.

125. Pynn, R., *Neutron Scattering-A Primer*. Los Alamos Science 1990. **19**: p. http://www.fas.org/sgp/othergov/doe/lanl/pubs/00326651.pdf.
126. Bacon, G.E., *Neutron diffraction*. 1979: Clarendon Press, Oxford.
127. *Neutron scattering lengths and cross sections.* National Institute of Standards and Technology (NIST), 2012: p. http://www.ncnr.nist.gov/resources/n-lengths/.
128. *Precession diffraction..right solution for nanostructure determination.* NanoMEGAS Website, 2012: p. http://www.nanomegas.com/PrecessionNew.php.
129. Birkbeck College, U.o.L., *Generation of X-rays.* Advanced Certificate in Powder Diffraction on the Web, 1997-2006: p. http://pd.chem.ucl.ac.uk/pdnn/inst1/xrays.htm.
130. Birkbeck College, U.o.L., *Instrumentation II: Synchrotron Sources and Methods.* Advanced Certificate in Powder Diffraction on the Web, 1997-2006: p. http://pd.chem.ucl.ac.uk/pdnn/inst2/synindex.htm.
131. Birkbeck College, U.o.L., *Neutron Sources and Methods.* Advanced Certificate in Powder Diffraction on the Web, 1997-2006: p. http://pd.chem.ucl.ac.uk/pdnn/inst3/neutronx.htm.
132. *How ISIS works.* ISIS website, 2012: p. http://www.isis.stfc.ac.uk/about-isis/how-isis-works6313.html.
133. Smith, R.I., Hull, S., *User Guide for the Polaris Powder Diffractometer at ISIS.*
134. Thompson, S.P., Parker, J. E., Potter, J., Hill, T. P.,Birt, A., Cobb, T. M., Yuan, F., Tang, C. C. , *Beamline I11 at Diamond: A new instrument for high resolution powder diffraction.* Review of Scientific Instruments, 2009. **80**(7): p. 075107 (9pages).
135. Irvine, J.T.S., Sinclair, D.C., West, A.R., *Electroceramics: Characterization by Impedance Spectroscopy*. Advanced Materials, 1990. **2**(3): p. 132-138.
136. *HRPD instrument.* ISIS website, 2012: p. http://www.isis.stfc.ac.uk/instruments/hrpd/.
137. Rietveld, H.M., *A profile refinement method for nuclear and magnetic structures.* Journal of Applied Crystallography, 1969. **2**: p. 65-71.
138. Coelho, A.A., *TOPAS Academic: General Profile and Structure Analysis Software for Powder Diffraction Data* Bruker AXS, Karlsruhe - Germany, 2010.
139. Schwartzenbach, D., Abrahams, S.C., Flack, H D., Prince, E., and Wilson, A.J.C., *Statistical descriptors in crystallography.* Acta Crystallographica Section A: Foundations of Crystallography, 1995. **51**: p. 565-569.
140. Schwartzenbach, D., Abrahams, S.C., Flack, H D., Prince, E., Wilson, A.J.C., *Statistical descriptors in crystallography, Uncertainty of measurement.* 1996: p. http://ww1.iucr.org/comm/cnom/statdes/uncert.html.
141. Young, R.A., *Introduction to the Rietveld method*. The Rietveld Method, ed. R.A. Young. 1995: Oxford University Press.
142. Pitcher, M.J., *The Structures and Properties of Layered Pnictides and Oxychalcogenides*, in *Balliol College*. 2011, University of Oxford.
143. Le Bail, A., Duroy, H., and Fourquet, J. L., *Ab Initio structure determination of $LiSbWO_6$ by X-ray powder diffraction.* Materials Research Bulletin, 1988. **23**: p. 447–452.
144. Pawley, G.S., *Unit-cell refinement from powder diffraction scans* Journal of Applied Crystallography, 1981. **14**: p. 357-361.
145. Toby, B.H., *R factors in Rietveld analysis: How good is good enough?* Powder Diffraction 2006. **21**(1): p. 67-70.
146. Krumeich, F., *Transmission Electron Microscopy (TEM).* The Electron Microscopy Site, 2012: p. http://www.microscopy.ethz.ch/.

147. Krumeich, F., *Scanning Electron Microscopy (SEM)*. The Electron Microscopy Site, 2012: p. http://www.microscopy.ethz.ch/.
148. West, A.R., *Basic Solid State Chemistry*. 2003: John Wiley & Sons.
149. Krumeich, F., *Scanning Transmission Electron Microscopy (STEM).* The Electron Microscopy Site, 2012: p. http://www.microscopy.ethz.ch/.
150. *Introduction to Mössbauer Spectroscopy.* Mössbauer Spectroscopy, Group, 2012(Royal Society of Chemistry): p. http://www.rsc.org/Membership/Networking/InterestGroups/MossbauerSpect/intro.asp.
151. Francis, M., *Systematic trends of the 57Fe Mössbauer isomer shifts in (FeOn) and (FeFn) polyhedra. Evidence of a new correlation between the isomer shift and the inductive effect of the competing bond T-X (→ Fe) (where X is O or F and T any element with a formal positive charge).* Journal Of Physics And Chemistry Of Solids, 1985. **46**(7): p. 763-769.
152. Groover, M.P., *Fundamentals of Modern Manufacturing: Materials, Processes, and Systems*. 2010: John Wiley &Sons.
153. *Impedance Spectroscopy: Emphasising solid materials and systems*, ed. J.R. MacDonald. 1987: John Wiley & Sons.
154. Irvine, J.T.S., Sinclair, D.C., West, A.R. , *Electroceramics: Characterization by Impedance Spectroscopy* Advanced Materials Volume, 1990. **2**(3): p. 132–138.
155. Wang, D.Y., Nowick, A. S. , *Cathodic and Anodic Polarization Phenomena at PlatinumElectrodes with Doped CeO_2 as Electrolyte : I . Steady-State Overpotential.* Journal of the Electrochemical Society, 1979. **126**(7): p. 1155-1165.
156. Kournoutis, V.C., Tietz,F., Bebelis, S. , *AC Impedance Characterisation of a $La_{0.8}Sr_{0.2}Co_{0.2}Fe_{0.8}O_{3-\delta}$ Electrode.* Fuel Cells, 2009. **9**(6): p. 852-860.
157. Leonide, A., Sonn, V., Weber, A., Ivers-Tifee, E., *Evaluation and Modeling of the Cell Resistance in Anode-Supported Solid Oxide Fuel Cells* Journal of the Electrochemical Society, 2008. **155**(1): p. B36-B41.
158. Choi, J., Park, I., Lee, H., Shin, D., *Effect of enhanced reaction area in double layered $Ba_{0.5}Sr_{0.5}Co_{0.8}Fe_{0.2}O_{3-\delta}$ cathode for intermediate temperature solid oxide fuel cells.* Solid State Ionics 2012. **216**: p. 54-57.
159. Liu, B., Zhang, Y., Zhang, L., *Oxygen reduction mechanism at $Ba_{0.5}Sr_{0.5}Co_{0.8}Fe_{0.2}O_{3-\delta}$ cathode for solid oxide fuel cell.* International journal of hydrogen energy 2009. **34**: p. 1008-1014.
160. Ringuede, A., Fouletier, J., *Oxygen reaction on strontium-doped lanthanum cobaltite dense electrodes at intermediate temperatures.* Solid State Ionics, 2001. **139**: p. 167-177.
161. Fukunaga, H., Koyama, M., Takahashi, N., Wen, C., Yamada, K., *Reaction model of dense $Sm_{0.5}Sr_{0.5}CoO_3$ as SOFC cathode.* Solid State Ionics, 2000. **132**: p. 279-285.
162. Brunauer, S., Emmett , P. H., Teller, E., *Adsorption of Gases in Multimolecular Layers.* Journal of the American Chemical Society, 1938. **60**(2): p. 309-319.
163. Keller, J.U., Staudt, R. , *Gas Adsorption Equilibria: Experimental Methods and Adsorptive Isotherms*. 2005: Springer.
164. Mitchell, R.H., *Perovskites: Modern and Ancient*. 2002: Mineralogical Society of America
165. Rao, C.N.R., Raveau, B., *Transition Metal Oxides*. 1998: John Wiley & Sons.
166. Fierro, J.L.G., *Metal Oxides- Chemistry and Applications*. 2006: Taylor & Francis Group, LLC.

167. Wilke, M., Farges, F., Petit, P.E., Brown, G.E. Jr., Martin, F., *Oxidation state and coordination of Fe in minerals: An Fe K-XANES spectroscopic study*. American Mineralogist 2001. **86**(5-6): p. 714-730.
168. Koster, H.M., F.H.B., *Powder diffraction of the cubic perovskite $Ba_{0.5}Sr_{0.5}Co_{0.8}Fe_{0.2}O_{3-\delta}$.* Powder Diffraction 2003. **18**: p. 56-59
169. Knapp, M.C., Woodward, P.M, *A-site cation ordering in $AA'BB'O_6$ perovskites.* Journal of Solid State Chemistry 2006. **179**(4): p. 1076-1085.
170. Bruce, D.W., Walton, R., O'Hare, D., *Functional Oxides*. 2012: John Wiley & Sons.
171. Glazer, A.M., *The Classification of Tilted Octahedra in Perovskites.* Acta Crystallographica, 1972. **B28**: p. 3384-3392.
172. Fu, W.T., Au, Y.S., Akerboom, S., IJdo, D.J.W, *Crystal structures and chemistry of double perovskites $Ba_2M(II)M'(VI)O_6$ (M = Ca, Sr, M'= Te, W, U).* Journal of Solid State Chemistry 2008. **181**: p. 2523- 2529.
173. Cavalcante, L.S., Sczancoski, J.C., Tranquilin, R.L., Joya, M.R., Pizani, P.S., Varela, J.A., Longo, E., *$BaMoO_4$ powders processed in domestic microwave-hydrothermal: synthesis, characterization and photoluminescence at room temperature.* Journal of Physics and Chemistry of Solids 2008. **69**: p. 2674-2680
174. Perier-Camby, L., Thomas, G. , *Solid way synthesis of barium aluminate. Kinetic study of the formation of intermediate compounds.* Solid State Ionics, 1993. **63-65**: p. 128-135.
175. Bolt, P.H., Habraken, F. H. P. M., Geus, J. W., *The influence of an intermediate MoO_3 layer on the solid state reaction of cobalt oxide with γ-Al_2O_3.* Catalysis Letters, 1996. **36**(3-4): p. 183-185.
176. Efimov, K., Xu, Q., Feldhoff, A., *Transmission Electron Microscopy Study of $Ba_{0.5}Sr_{0.5}Co_{0.8}Fe_{0.2}O_{3-\delta}$ Perovskite Decomposition at Intermediate Temperatures.* Chemistry of Materials, 2010. **22**: p. 5866-5875.
177. Švarcová, S., Wiik, K., Tolchard, J., Bouwmeester, H.J.M., Grande, T., *Structural instability of cubic perovskite $Ba_xSr_{1-x}Co_{1-y}Fe_yO_{3-\delta}$.* Solid State Ionics 2008. **178**: p. 1787-1791.
178. Mueller, D.N., De Souza,R.A., Weirich,T. E., Roehrens,D., Mayerb, J., Martina,M., *A kinetic study of the decomposition of the cubic perovskite-type oxide $Ba_xSr_{1-x}Co_{0.8}Fe_{0.2}O_{3-\delta}$ (BSCF) (x = 0.1 and 0.5).* Physical Chemistry Chemical Physics, 2010. **12**: p. 10320-10328.
179. Wang, L., *$Ba_{1-x}Sr_xCo_yFe_{1-y}O_{3-\delta}$ SOFC cathode materials: Bulk properties, kinetics and mechanism of oxygen reduction*, in *Max-Planck-Institut fur FestkÄorperforschung*. 2009: Stuttgart.
180. Lim, Y.H., Lee, J., Yoon, J.S.,Chul, E.K., Hwang, H.J., *Electrochemical performance of $Ba_{0.5}Sr_{0.5}Co_xFe_{1-x}O_{3-\delta}$ (x = 0.2–0.8) cathode on a ScSZ electrolyte for intermediate temperature SOFCs.* Journal of Power Sources, 2007. **171**(1): p. 79–85.
181. Fang, S.M., Yoo, C.-Y., Bouwmeester, H.J.M., *Performance and stability of niobium-substituted $Ba_{0.5}Sr_{0.5}Co_{0.8}Fe_{0.2}O_{3-\delta}$ membranes.* Solid State Ionics 2011. **195**: p. 1-6.
182. Deng, Z.Q., Smit, J.P., Niu, H.J., Evans, G., Li, M.R., Xu, Z.L., J.B. Claridge, Rosseinsky, M.J. , *B Cation Ordered Double Perovskite $Ba_2CoMo_{0.5}Nb_{0.5}O_{6-\delta}$ as a Potential SOFC Cathode.* Chemistry of Materials 2009. **21**: p. 5154-5162.
183. Liu, Q., Dong, X., Xiao, G., Zhao, F., Chen, F. , *A Novel Electrode Material for Symmetrical SOFCs.* Advanced Materials, 2010. **22**(48): p. 5478–5482.

184. Xiao, G., Liu, Q.,Zhao, F., Zhang, L., Xia, C., Chen, F. , *$Sr_2Fe_{1.5}Mo_{0.5}O_6$ as Cathodes for Intermediate-Temperature Solid Oxide Fuel Cells with $La_{0.8}Sr_{0.2}Ga_{0.87}Mg_{0.13}O_3$ Electrolyte.* J. Electrochem. Soc. , 2011. **158**: p. B455-B460.
185. Jung, J., Misture, S.T., Edwards, D. D. , *The electronic conductivity of $Ba_{0.5}Sr_{0.5}Co_xFe_{1-x}O_{3-\delta}$ (BSCF: x=0-1.0) under different oxygen partial pressures.* Journal of Electroceramics 2010. **24**: p. 261-269.
186. Carter, S., Selcuk, A., Chater, R.J., Kajda, J., Kilner, J.A., Steele, B.C.H. , *Oxygen transport in selected nonstoichiometric perovskite-structure oxides.* Solid State Ionics, 1992. **53-56, Part 1**: p. 597–605.
187. Yáng, Z., Harvey, A.S., Infortuna, A., Schoonman, J., Gauckler, L.J. , *Electrical conductivity and defect chemistry of $Ba_xSr_{1-x}Co_yFe_{1-y}O_{3-\delta}$ perovskites.* Journal of Solid State Electrochemistry, 2011. **15**: p. 277-284.
188. Lu, H., Cong, Y., Yang, W.S. , *Oxygen permeability and stability of $Ba_{0.5}Sr_{0.5}Co_{0.8}Fe_{0.2}O_{3-\delta}$ as an oxygen-permeable membrane at high pressures.* Solid State Ionics, 2006. **177**(5-6): p. 595-600.
189. Zhao, H., Shen, W., Zhub, Z., Li, X.,Wang, Z., *Preparation and properties of $BaxSr_{1-x}Co_yFe_{1-y}O_{3-\delta}$ cathode material for intermediate temperature solid oxide fuel cells.* Journal of Power Sources 2008. **182**: p. 503-509.
190. McIntosh, S., Vente, J.F., Haije, W.G., Blank, D.H.A.,Bouwmeester, H.J.M. , *Structure and oxygen stoichiometry of $SrCo_{0.8}Fe_{0.2}O_{3-\delta}$ and $Ba_{0.5}Sr_{0.5}Co_{0.8}Fe_{0.2}O_{3-\delta}$.* Solid State Ionics, 2006. **177**(19-25): p. 1737–1742.
191. McIntosh, S., Vente, J.F., Haije, W.G., Blank, D.H.A.,Bouwmeester, H.J.M. , *Oxygen Stoichiometry and Chemical Expansion of $Ba_{0.5}Sr_{0.5}Co_{0.8}Fe_{0.2}O_{3-\delta}$ Measured by in Situ Neutron Diffraction.* Chemistry of Materials, 2006. **18**(8): p. 2187-2193.
192. Harvey, A.S., Litterst, F.J., Yang, Z., Rupp, J.L.M., Infortuna, A., Gauckler, L.J., *Oxidation states of Co and Fe in $Ba_{1-x}Sr_xCo_{1-y}Fe_yO_{3-\delta}$ (x, y = 0.2–0.8) and oxygen desorption in the temperature range 300–1273 K.* Physical Chemistry Chemical Physics 2009. **11**(17): p. 3090-3098.
193. Meng, X., Meng, B., Tan, X., Yang, N., Ma, Z.F., *Synthesis and properties of $Ba_{0.5}Sr_{0.5}(Co_{0.6}Zr_{0.2})Fe_{0.2}O_{3-\delta}$ perovskite cathode material for intermediate temperature solid-oxide fuel cells.* Materials Research Bulletin 2009. **44** p. 1293-1297.
194. Zhao, H., Teng, D., Zhang, X., Zhang, C., Li, X., *Structural and electrochemical studies of $Ba_{0.6}Sr_{0.4}Co_{1-y}Ti_yO_{3-\delta}$ as a new cathode material for IT-SOFCs.* Journal of Power Sources 2009. **186**: p. 305-310.
195. Xiao, G., Liu, Q., Wang, S., Komvokis, V. G., Amiridis, M.D., Heyden, A., Mac, S., Chen, F., *Synthesis and characterization of Mo-doped $SrFeO_{3-\delta}$ as cathode materials for solid oxide fuel cells.* Journal of Power Sources 2012. **202**: p. 63- 69.
196. Petric, A., Huang, P., Tietz, F. , *Evaluation of La-Sr-Co-Fe-O perovskites for solid oxide fuel cells and gas separation membranes.* Solid State Ionics, 2000. **135**: p. 719-725.
197. Vente, J., McIntosh, S., Haije, W., Bouwmeester, H. , *Properties and performance of $Ba_xSr_{1-x}Co_{0.8}Fe_{0.2}O_{3-\delta}$ materials for oxygen transport membranes.* Journal of Solid State Electrochemistry 2006. **10**: p. 581-588.
198. Li, S., Lu, Z., Wei, B.,Huang, X., Miao, J., Cao, G., Zhu, R., Su, W., *A study of $(Ba_{0.5}Sr_{0.5})_{1-x}Sm_xCo_{0.8}Fe_{0.2}O_{3-\delta}$ as a cathode material for IT-SOFCs.* Journal of Alloys and Compounds, 2006. **426**: p. 408-414.

199. Li, S., Lu, Z., Aia, N., Chen, K., Su, W., *Electrochemical performance of $(Ba_{0.5}Sr_{0.5})_{0.9}Sm_{0.1}Co_{0.8}Fe_{0.2}O_{3-\delta}$ as an intermediate temperature solid oxide fuel cell cathode.* Journal of Power Sources 2007. **165**: p. 97-101.
200. Zhou, W., Ran, R., Shao, Z., Jin, W., Xu, N., *Evaluation of A-site cation-deficient $(Ba_{0.5}Sr_{0.5})_{1-x}Co_{0.8}Fe_{0.2}O_{3-\delta}$ (x>0) perovskite as a solid-oxide fuel cell cathode.* Journal of Power Sources 2008. **182**: p. 24-31.
201. Zhou, W., Ran, R., Shao, Z., Zhuang, W., Jia, J., Gu, H., Jin, W., Xu, N., *Barium- and strontium-enriched $(Ba_{0.5}Sr_{0.5})_{1+x}Co_{0.8}Fe_{0.2}O_{3-\delta}$ oxides as high-performance cathodes for intermediate-temperature solid-oxide fuel cells.* Acta Materialia 2008. **56**: p. 2687-2698.
202. Li, S., Lü, Z., Huang, X., Su, W. , *Thermal, electrical, and electrochemical properties of Nd-doped $Ba_{0.5}Sr_{0.5}Co_{0.8}Fe_{0.2}O_{3-\delta}$ as a cathode material for SOFC.* Solid State Ionics 2008. **178**: p. 1853-1858.
203. Lim, Y.H., Lee, J., Yoon, J.S., Kim, C.E., Hwang, H.J. , *Electrochemical performance of $Ba_{0.5}Sr_{0.5}Co_xFe_{1-x}O_{3-\delta}$ (x = 0.2–0.8) cathode on a ScSZ electrolyte for intermediate temperature SOFCs.* Journal of Power Sources 2007. **171**: p. 79-85.
204. Pena-Martınez, J., Marrero-Lopez, D., Ruiz-Morales, J.C., Nunez, P., Sanchez-Bautista, C., Dos Santos-Garcıa, A.J.,Canales-Vazquez, J. , *On $Ba_{0.5}Sr_{0.5}Co_{1-y}Fe_yO_{3-\delta}$ (y=0.1–0.9) oxides as cathode materials for $La_{0.9}Sr_{0.1}Ga_{0.8}Mg_{0.2}O_{2.85}$ based IT-SOFCs.* International Journal of Hydrogen Energy, 2009. **34**: p. 9486- 9495.
205. Lee, S., Lim, Y., Lee, E.A., Hwang, H.J., Moon, J.W., *$Ba_{0.5}Sr_{0.5}Co_{0.8}Fe_{0.2}O_{3-\delta}$ (BSCF) and $La_{0.6}Ba_{0.4}Co_{0.2}Fe_{0.8}O_{3-\delta}$ (LBCF) cathodes prepared by combined citrate-EDTA method for IT-SOFCs.* Journal of Power Sources 2006. **157**: p. 848-854.
206. Shao, Z., Haile, S.M. , *A high-performance cathode for the next generation of solid-oxide fuel cells.* Nature 2004. **431**: p. 170-173.
207. Wang, K., Ran, R., Zhou, W., Gu, H., Shao, Z., Ahn, J., *Properties and performance of $Ba_{0.5}Sr_{0.5}Co_{0.8}Fe_{0.2}O_{3-\delta}$+$Sm_{0.2}Ce_{0.8}O_{1.9}$ composite cathode.* Journal of Power Sources 2008. **179**: p. 60-68.
208. Zhou, W., Shao, Z., Ran, R., Chen, Z., Zeng, P., Gu, H., Jin, W., Xu, N., *High performance electrode for electrochemical oxygen generator cell based on solid electrolyte ion transport membrane.* Electrochimica Acta 2007. **52** p. 6297-6303.
209. Chengjun, Z., Cuishan, Y., Luomeng, C. , *Preparation and performance of Pr-doped $Ba_{0.5}Sr_{0.5}Co_{0.8}Fe_{0.2}O_{3-\delta}$ cathode for IT-SOFCs.* Journal of Rare Earths, 2011. **29**(11): p. 1070-1074.
210. Steele, B.C.H., Solid State Ionics, 1996. **86-88**: p. 1223.
211. Sahibzada, M., Steele, B.C.H., Zheng, K., Rudkin, R.A., Bae, J.M., Kiratzis, N., Waller, D., I.S. Metcalfe, Proceedings of the Second European Solid Oxide Fuel Cell Forum, 1996. **Oslo**: p. 687.
212. Sahibzada, M., Benson, S.J., Rudkin, R.A., Kilner, J.A. , *Pd-promoted $La_{0.6}Sr_{0.4}Co_{0.2}Fe0.8_{O3}$ cathodes.* Solid State Ionics, 1998. **113-115**: p. 285-290.
213. Steele, B.C.H., Bae, J.-M. , *Properties of $La_{0.6}Sr_{0.4}Co_{0.2}Fe_{0.8}O_{3-x}$ (LSCF) double layer cathodes on gadolinium-doped cerium oxide (CGO) electrolytes: II. Role of oxygen exchange and diffusion.* Solid State Ionics, 1998. **106**(3-4): p. 255-261.
214. Tarancon, A., Skinner,S., Chater,R.J., Hernandez-Ramıreza, F., Kilner, J.A. , *Layered perovskites as promising cathodes for intermediate temperature solid oxide fuel cells.* Journal of Materials Chemistry, 2007 **17**: p. 3175-3181.

215. Lia, N., Lü, Z., Wei, B., Huang, X.,Chen, K., Zhang, Y., Su, Wenhui *Characterization of $GdBaCo_2O_{5+\delta}$ cathode for IT-SOFCs.* Journal of Alloys and Compounds, 2008. **454**(1-2): p. 274-279.
216. Jiang, Q., *Mixed-Conducting Oxygen Permeable Ceramic Membrane and its Application in the Production of Synthesis Gas*, in *Chemical Engineering*. 2010, University of Kansas.
217. Chen, C., Chang, C.L., Hwang, B.H., *Electrochemical and microstructure characteristics of $Ba_{0.5}Sr_{0.5}Co_{0.8}Fe_{0.2}O_{3-\delta}$(BSCF) cathodes prepared by citrate precursor method for SOFCs.* Materials Chemistry and Physics, 2009. **115** p. 478-482.
218. Zhu, Q., Jin, T., Wang, Y., *Thermal expansion behavior and chemical compatibility of $Ba_xSr_{1-x}Co_{1-y}Fe_yO_{3-\delta}$ with 8YSZ and 20GDC.* Solid State Ionics 2006. **177**: p. 1199-1204.
219. Wang, K., Ran, R., Zhou, W., Gu, H.X., Shao, Z.P., Ahn, J. , *Properties and performance of $Ba_{0.5}Sr_{0.5}Co_{0.8}Fe_{0.2}O_{3-\delta}$ + $Sm_{0.2}Ce_{0.8}O_{1.9}$ composite cathode.* Journal of Power Sources 2008. **179**: p. 60-68.
220. *Advanced Certificate in Powder Diffraction on the Web.* School of Crystallography, Birkbeck College, University of London, 2006: p. http://pd.chem.ucl.ac.uk/pdnn/pdindex.htm#diff2.
221. Housecroft, C., Constable, E.C., *Chemistry*. 2006: Pearson Education Limited.
222. *Neutron scattering lengths and cross sections.* National Institute of Standards and Technology (N.I.S.T), 2003: p. http://www.ncnr.nist.gov/resources/n-lengths/.
223. Zhang, Q., Rao, G.H., Feng, X.M., Ouyang, Z.W., Liu, G.Y., Toby, B.H., Liang J.K. , *Selective substitution of vanadium for molybdenum in $Sr_2(Fe_{1-x}V_x)MoO_6$ double perovskites.* Journal of Solid State Chemistry, 2006. **179** p. 2458-2465.
224. Coelho, A.A., *Users Manual for TOPAS Academic: General Profile and Structure Analysis Software for Powder Diffraction Data*. 2010, Bruker AXS: Karlsruhe, Germany.
225. Dinnebier, R.E., Billinge S.J.L., *Powder Diffraction: Theory and Practice*. 2009: Royal Society of Chemistry.
226. Joubert, J.M., Cerný, R., Latroche, M., Percheron-Guégan, A., Yvon, K., *Site Occupancies in the Battery Electrode Material $LaNi_{3.55}Mn_{0.4}Al_{0.3}Co_{0.75}$ as Determined by Multiwavelength Synchrotron Powder Diffraction.* Journal of Applied Crystallography, 1998. **31**: p. 327–332.
227. McIntosh, S., Vente, J.F., Haije, W. G., Blank, D.H.A., Bouwmeester, H.J.M. , *Structure and oxygen stoichiometry of $SrCo_{0.8}Fe_{0.2}O_{3-\delta}$ and $Ba_{0.5}Sr_{0.5}Co_{0.8}Fe_{0.2}O_{3-\delta}$.* Solid State Ionics, 2006. **177**.
228. Karppinen, M., Matvejeff, M., Salomäki K. and Yamauchi H. , *Oxygen content analysis of functional perovskite-derived cobalt oxides* J. Mater. Chem, 2002. **12**: p. 1761-1764.
229. Kamata, K., Nakamura, T., Sata,T., *Valence stability of molybdenum in alkaline earth molybdates.* Materials Research Bulletin, 1975. **10**.
230. Selvaduray, G.S., *Ellingham Diagram Web Tool Tutorial.* San Jose State University, 2012: p. http://www.engr.sjsu.edu/ellingham/tutorial.html.
231. Jung, J., Misture, S. T., Edwards, D. D. , *Oxygen stoichiometry, electrical conductivity, and thermopower measurements of BSCF ($Ba_{0.5}Sr_{0.5}Co_xFe_{1-x}O_{3-\delta}$, $< x < 0.8$) in air.* Solid State Ionics, 2010. **181**: p. 1287-1293.

232. Vente, J., McIntosh, S., Haije, W., Bouwmeester, H. , *Properties and performance of $Ba_xSr_{1-x}Co_{0.8}Fe_{0.2}O_{3-\delta}$ materials for oxygen transport membranes.* Journal of Solid State Electrochemistry, 2006. **10**: p. 581-588.
233. Song, K.W., Lee, K.T. , *Characterization of $Ba_{0.5}Sr_{0.5}M_{1-x}Fe_xO_{3-\delta}$ (M = Co and Cu) perovskite oxide cathode materials for intermediate temperature solid oxide fuel cells.* Ceramics International 2012. **38** p. 5123–5131.
234. Uhlenbruck, S., Tietz, F. , *High-temperature thermal expansion and conductivity of cobaltites: potentials for adaptation of the thermal expansion to the demands for solid oxide fuel cells.* Materials Science and Engineering 2004. **B107**: p. 277-282.
235. Huang, K., Lee, H. Y., Goodenough, J.B. , *Sr- and Ni-Doped $LaCoO_3$ and $LaFeO_3$ Perovskites: New Cathode Materials for Solid-Oxide Fuel Cells.* Journal of the Electrochemical Society 1998. **145**: p. 3220-3227.
236. Bhide, V.G., Rajoria, D.S., Reddy, Y.S., Rao, G. R., Rao, Subba, G.V., Rao, C.N., *Localized-to-itinerant electron transitions in rare-earth cobaltates.* Physical Revoew Letters, 1972. **28**: p. 1133–1136.
237. Raccah, P.M., Goodenough, J.B., *First-order localized-electron to collective-electron transition in $LaCoO_3$.* Physical Review, 1967. **155**: p. 932–943.
238. Mori, M., Sammes, N.M. , *Sintering and thermal expansion characterization of Al-doped and Co-doped lanthanum strontium chromites synthesized by the Pechini method.* Solid State Ionics, 2002. **146**: p. 301–312.
239. Uhlenbruck, S., Tietz, F. , *High-temperature thermal expansion and conductivity of cobaltites: potentials for adaptation of the thermal expansion to the demands for solid oxide fuel cells.* Materials Science and Engineering 2004. **B107**: p. 277-282

240. Ullmann, H., Trofimenko, N., Tietz, F., Stover, D., Ahmad-Khanloub, A. , *Correlation between thermal expansion and oxide ion transport in mixed conducting perovskite-type oxides for SOFC cathodes.* Solid State Ionics 2000. **138**: p. 79–90.
241. Ruffa, A.R., *Thermal expansion in insulating materials.* Journal of Materials Science, 1980. **15**: p. 2258–2267.
242. Kostogloudis, G.C., Ftikos, Ch. , *Properties of A-site-deficient $La_{0.6}Sr_{0.4}Co_{0.2}Fe_{0.8}O_{3-\delta}$-based perovskite oxides.* Solid State Ionics 1999. **126**: p. 143–151.
243. Hansen, K.K., Hansen, K.V., *A-site deficient $(La_{0.6}Sr_{0.4})_{1-s}Fe_{0.8}Co_{0.2}O_{3-\delta}$ perovskites as SOFC cathodes.* Solid State Ionics 2007. **178** p. 1379-1384.
244. Huang, K., Goodenough, J.B., *Solid oxide fuel cell technology*. 2009: Woodhead Publishing Limited.
245. Tietz, F., *Thermal Expansion of SOFC Materials.* Ionics, 1999. **5**: p. 129-139.
246. Moori, M., Hiei, N., Sammes, N., Tompsett, G.A. , *Thermal expansion behaviors and mechanisms for Ca- and Sr- doped lanthanum manganite perovskites under oxidising atmospheres.* Journal of the Electrochemical Society, 2000. **147**: p. 1295-1302.
247. Zhao, H., Teng, D., Zhang, X., Zhang, C., Li, X., *Structural and electrochemical studies of $Ba_{0.6}Sr_{0.4}Co_{1-y}TiyO_{3-\delta}$ as a new cathode material for IT-SOFCs.* Journal of Power Sources 2009. **186** p. 305-310

248. *SOFC powders and pastes.* Fuel Cell Materials market, 2012: p. https://www.fuelcellmaterials.com.

249. Brixner, L.H., *Preparation and structure determination of some new cubic and tetragonally distorted perovskites.* Journal of Physical Chemistry 1960. **64**: p. 165-166.
250. Hirama, T., Tsujii, N. , Kitazawa, H., Kido, G., *La-substitution effects on double perovskite compound Ba_2CoMoO_6.* Physica B 2005. **359-361**: p. 1336–1338.
251. Fresial, E.J., Katz, L., Ard, R., *Cation Substitution in Perovskite-like Phases.* Journal of the American Chemical Society, 1959. **81**(18): p. 4783–4785.
252. Ivanov, S.A., Eriksson, S.-G., Tellgren, R.,Rundlof, H., Tseggai, M., *The magnetoelectric perovskite Sr_2CoMoO_6: An insight from neutron powder diffraction* Materials Research Bulletin, 2005. **40**(5): p. 840-849.
253. Viola, M.C., Martı´nez-Lope,M. J., Alonso, J. A., Velasco,P. , Martı´nez,J. L., Pedregosa,J. C., Carbonio,R. E., Ferna´ndez-Dı´az, M. T. , *Induction of Colossal Magnetoresistance in the Double Perovskite Sr_2CoMoO_6.* Chemistry of Materials, 2002. **14**(2).
254. Aguadero, A., Alonso, J. A., Martínez-Coronado, R., Martínez-Lope, M. J., Fernández-Díaz, M. T. , *Evaluation of $Sr_2CoMoO_{6-\delta}$ as anode material in solid-oxide fuel cells: A neutron diffraction study.* Journal of Applied Physics, 2011. **109**: p. 034907-1- 034907-1-6.
255. Marques, A.P.A., Picon, F. C., Melo, D.M. A., Pizani, P.S., Leite, E.R., Varela, J.A., Longo, E. , *Effect of the Order and Disorder of $BaMoO_4$ Powders in Photoluminescent Properties.* Journal of Fluorescence, 2008. **18**: p. 51–59.
256. Mette, J., Primdahl, S., Manon, C., Mogensen, M. , *Performance/structure correlation for composite SOFC cathodes.* Journal of Power Sources, 1996. **61**(1-2): p. 173-181.
257. Hsu, C.S., Hwang, B.H., Xie, Y., Zhang, X., *Enhancement of Solid Oxide Fuel Cell Performance by $La_{0.6}Sr_{0.4}Co_{0.2}Fe_{0.8}O_{3-\delta}$ Double-Layer Cathode.* Journal of The Electrochemical Society, 2008. **155**(12): p. B1240-B1243.
258. Wang, K., Ran, R., Zhou, W., Gu, H.X., Shao, Z.P., Ahn, J. , *Properties and performance of $Ba_{0.5}Sr_{0.5}Co_{0.8}Fe_{0.2}O_{3-\delta}$ + $Sm_{0.2}Ce_{0.8}O_{1.9}$ composite cathode.* Journal of Power Sources, 2008. **179** p. 60-68.
259. Peña-Martínez, D.M.-L., J., Ruiz-Morales, J.C., Buergler, B.E., Núñez, P., Gauckler, L.J. , *SOFC test using $Ba_{0.5}Sr_{0.5}Co_{0.8}Fe_{0.2}O_{3-\delta}$ as cathode on $La_{0.9}Sr_{0.1}Ga_{0.8}Mg_{0.2}O_{2.85}$ electrolyte.* Solid State Ionics, 2006. **177**: p. 2143-2147.
260. Peña-Martínez, J., Marrero-López, D., Ruiz-Morales, J.C., Núñez, P., Sánchez-Bautista, C., Dos Santos-García, A.J., Canales-Vázquez, J. , *On $Ba_{0.5}Sr_{0.5}Co_{1-y}Fe_yO_{3-\delta}$ ($y = 0.1–0.9$) oxides as cathode materials for $La_{0.9}Sr_{0.1}Ga_{0.8}Mg_{0.2}O_{2.85}$ based IT-SOFCs.* International journal of hydrogen energy, 2009. **34**(23): p. 9486-9495.
261. Zhu, Q., Jina, T., Wang, Y., *Thermal expansion behavior and chemical compatibility of $Ba_xSr_{1-x}Co_{1-y}Fe_yO_{3-\delta}$ with 8YSZ and 20GDC.* Solid State Ionics 2006. **177**: p. 1199-1204.
262. Duan, Z., Yang, M., Yan, A., Hou, Z., Dong, Y., Chong, Y., Cheng, M., Yang, W., *$Ba_{0.5}Sr_{0.5}Co_{0.8}Fe_{0.2}O_{3-\delta}$ as a cathode for IT-SOFCs with a GDC interlayer.* Journal of Power Sources 2006. **160** p. 57-64.
263. Lim, Y.H., Lee, J.,Yoon, J.S.,Kim, C.E.,Hwang, H.J. , *Electrochemical performance of $Ba_{0.5}Sr_{0.5}Co_xFe_{1-x}O_{3-\delta}$ ($x = 0.2–0.8$) cathode on a ScSZ electrolyte for intermediate temperature SOFCs.* J. Power Sources 2007. **171**: p. 79-85.
264. Shao, Z., Haile, S.M. , *A high-performance cathode for the next generation of solid-oxide fuel cells.* Nature, 2004. **431**: p. 170-173.

265. O'Hayre, R., Barnett, D.M., Prinz, F.B., *The Triple Phase Boundary: A mathematical model and Experimental Investigations for Fuel Cells.* Journal of Electrochemical Society, 2005. **152**(2): p. A439-A444.
266. Al-Yousef, Y.M., Ghouse, M., *Synthesis of $Ba_{0.5}Sr_{0.5}Co_{0.2}Fe_{0.8}O_3$ (BSCF) Nanoceramic Cathode Powders by Sol-Gel Process for Solid Oxide Fuel Cell (SOFC) Application.* World Journal of Nano Science and Engineering, 2011. **1**: p. 99-107.
267. Takacs, L., *Self-sustaining reactions induced by ball milling.* Progress in Materials Science 2002. **47**: p. 355-414.
268. Tullberg, E., Peters, D., Frejd, T., *The Heck reaction under ball-milling conditions.* Journal of Organometallic Chemistry, 2004. **689**(23): p. 3778–3781.
269. Dunyushkina, L.A., Adler, S.B. , *Influence of Electrolyte Surface Planarisation on the performance of Porous SOFC cathodes.* Journal of Electrochemical Society, 2005. **152**(10): p. A2040-A2045.
270. Ovenstone, J., Jung, Jae-Il, White, J.S., Edwards, D.D., Misture, S.T. , *Phase stability of BSCF in low oxygen partial pressures.* Journal of Solid State Chemistry 2008. **181**: p. 576-586.
271. *Electrochemical Dictionary*, ed. A.J. Bard, Inzelt, G., Scholz, F. 2008: Springer.
272. Jorcin, J.B., Orazem, M.E., Pébère, N., Tribollet, B., *CPE analysis by local electrochemical impedance spectroscopy.* Electrochimica Acta, 2006. **5**(8-9): p. 1473-1479.
273. Adler, S.B., Lane J.A., Steele, B.C.H. , *Electrode kinetics of Porous Mixed-Conducting Oxygen Electrodes.* Journal of the Electrochemical Society, 1996. **143**(11): p. 3554-3564.
274. Lai, E., Haile, S.M. , *Impedance Spectroscopy as a Tool for Chemical and Electrochemical Analysis of Mixed Conductors: A case Study of Ceria.* Journal of American Ceramic Society 2005. **88**(11): p. 2979-2997.
275. Kim, J.W., Virkar, A.V., Fung, K.Z., Mehta, K., Singhal, S.C., *Polarization Effects in Intermediate Temperature Anode-Supported Solid Oxide Fuel Cells.* Journal of The Electrochemical Society, 1999. **146**(1): p. 69-78.
276. Etsell, T.H., Flengas, S. N., *Overpotential Behavior of Stabilized Zirconia Solid Electrolyte Fuel Cells.* Journal of Electrochemical Society, 1971. **118**(12): p. 1890-1900.
277. Schouler, E.J.L., Mesbahi, N., Vitter, G. , *In situ study of the sintering process of yttria stabilised zirconia by impedance spectroscopy* Solid State Ionics 1983. **9&10**: p. 989-996.
278. Sayers, R., *Electrochemical Performance and Transport Properties of $La_2NiO_{4+\delta}$,* in *Department of Materials*. 2010, Imperial College London.
279. Li, N., Lu, Z., Wei, B., Huang, X., Chen, K., Zhang, Y., Su, W., *Characterization of $GdBaCo_2O_{5+\delta}$ cathode for IT-SOFCs.* Journal of Alloys and Compounds 2008. **454**: p. 274-279.
280. Adler, S.B., *Mechanism and kinetics of oxygen reduction on porous $La_{1-x}Sr_xCoO_{3-\delta}$ electrodes.* Solid State Ionics 1998. **111**: p. 125-134.
281. Perry Murray, E., Tsai, T., Barnett, S.A., *Oxygen transfer in (La,Sr)MnO_3/Y2O_3-stabilised ZrO_2 cathodes: an impedance spectroscopy study.* Solid State Ionics, 1998. **110**: p. 235-243.
282. Perry Murray, S., M.J., T., Barnett, S.A., *Electrochemical performance of (La,Sr)(Co,Fe)O_3-(Ce-Gd)O_3.* Solid State Ionics, 2002. **148**: p. 27-34.

283. Nallamuthu, N., Prakash, I., Satyanarayana, N., Venkateswarlu, M. , *Preparation, characterization and electrical conductivity studies of nanocrystalline La doped $BaMoO_4$.* Materials Research Bulletin 2011. **46**: p. 32-41.
284. Wang, L., *$Ba_{1-x}Sr_xCo_yFe_{1-y}O_{3-\delta}$ SOFC cathode materials: Bulk properties, kinetics and mechanism of oxygen reduction*. 2009, Max-Planck-Institut: Stuttgart.

Appendix A: Information for BSCF

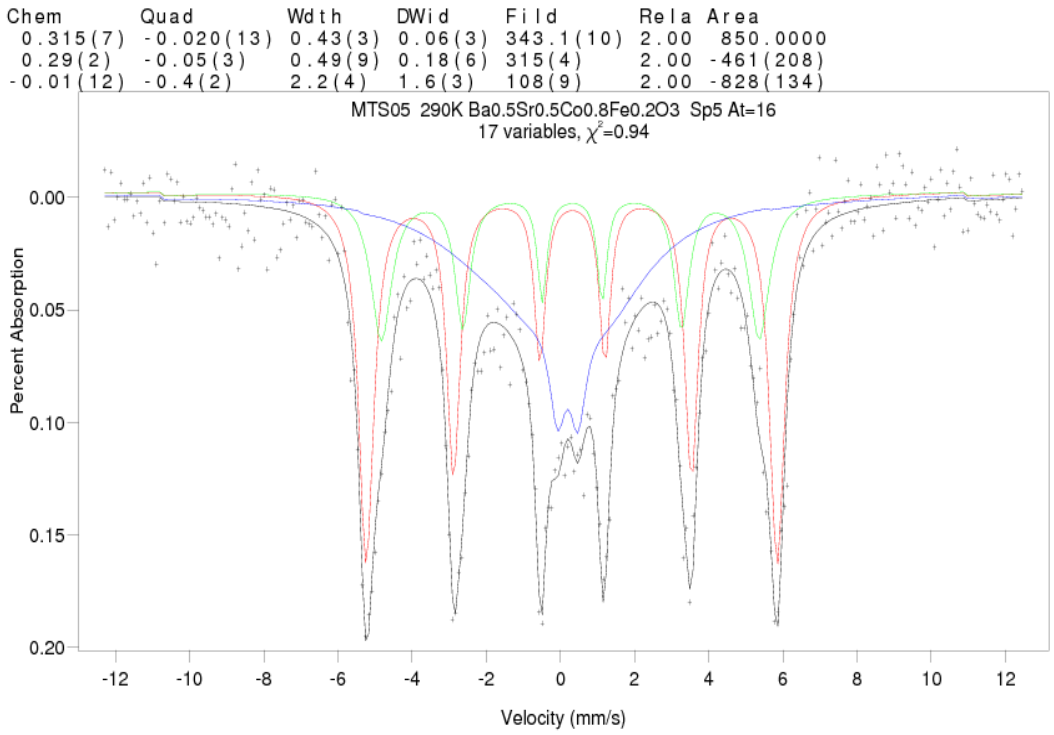

Figure A1: Mössbauer spectrum for BSCF ($Ba_{0.5}Sr_{0.5}Co_{0.8}Fe_{0.2}O_{3-\delta}$) fitted with 3 sextets. Two of these sextets are from Fe^{3+} and the third one is from Fe^{4+}. The ratio of Fe^{3+} to Fe^{4+} is about 1 to 0.63, i.e. 61% Fe^{3+} and 39% Fe^{4+}.

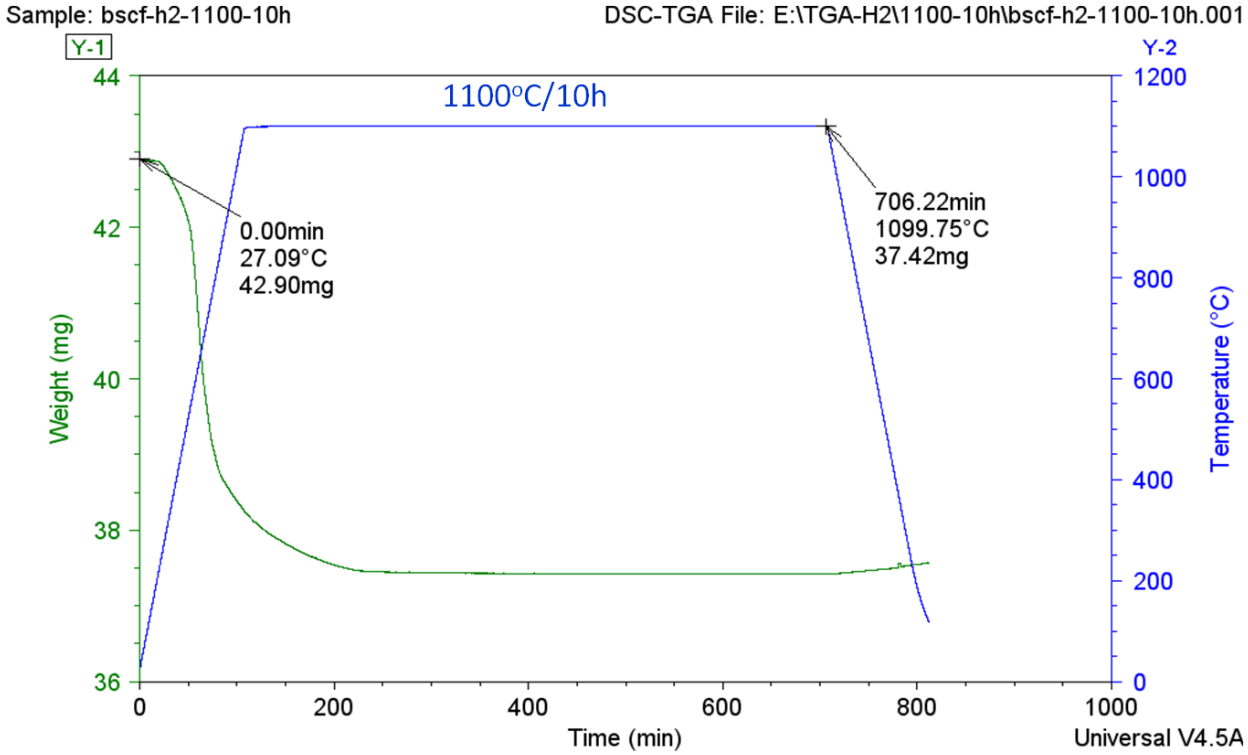

Figure A2: Thermogravimetric analysis (TGA) showing the weight loss of BSCF ($Ba_{0.5}Sr_{0.5}Co_{0.8}Fe_{0.2}O_{3-\delta}$) after heating at 1100oC for 10h in reducing conditions (in a mixture of 50ml/min 5% H_2/N_2 and 80ml/min N_2 as the carrier gas). The oxygen content was determined to 0.29, according to Equation 4.1(page 150) considering total reduction of the transition metals.

Combing the information obtained for BSCF for Fe oxidation state, form Mössbauer determination and oxygen content, it is can be written $Ba_{0.5}Sr_{0.5}Co_{0.8}(Fe^{3+}_{0.12}Fe^{4+}_{0.078})O_{2.71}$and thus the cobalt oxidation state is calculated to +3.435.

Appendix B: HRPD 90^{o} bank

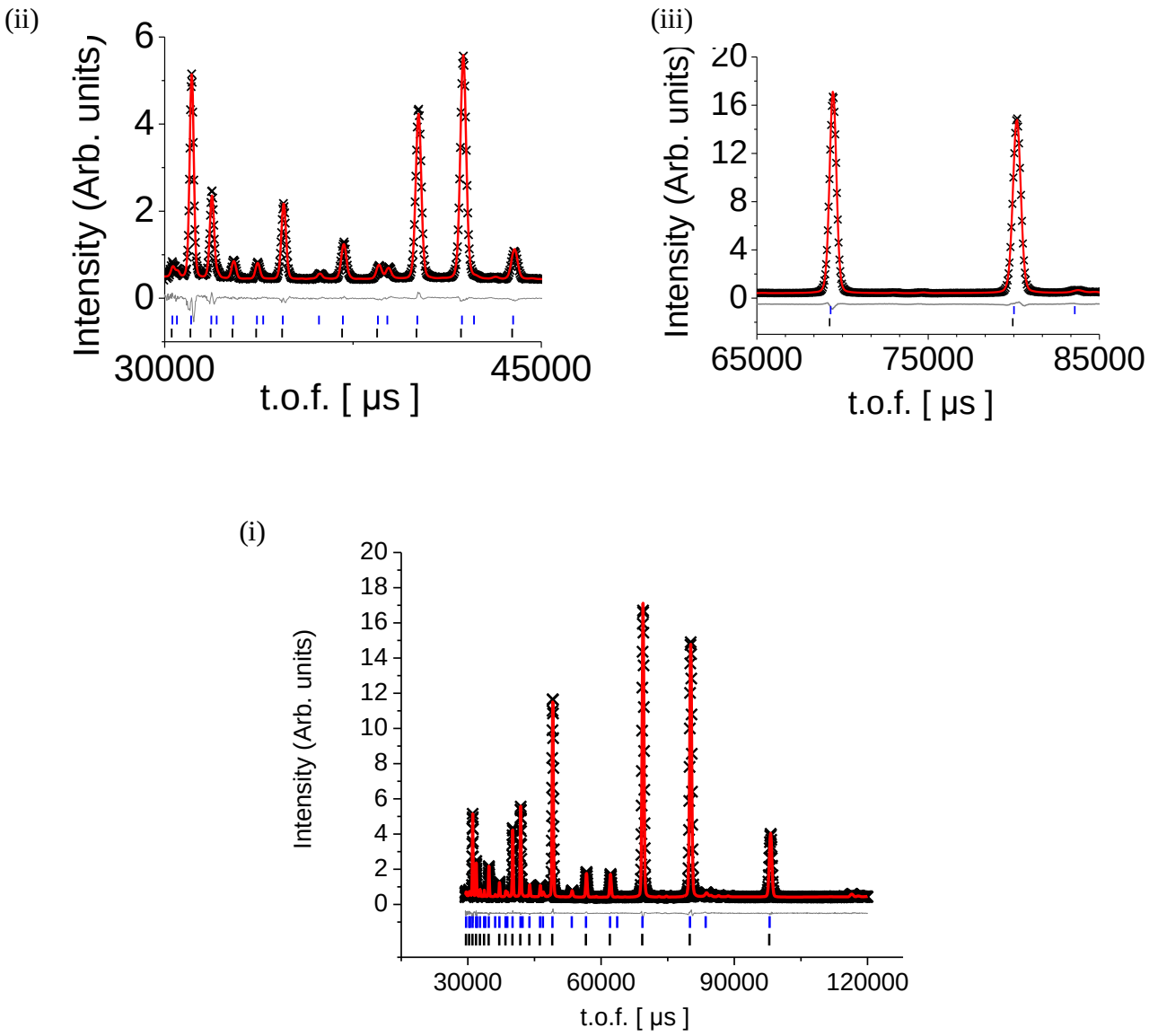

χ^2= 4.32, R_{exp}= 1.067%, R_{wp}= 3.460% , R_{Bragg}(SP)=1.19%, R_{Bragg}(DP)= 1.12%

<u>Figure B:</u> (i) Observed (black), calculated (red) and difference (grey) plots of Rietveld fit against room temperature ND data at the 90^{o} bank for $Ba_{0.5}Sr_{0.5}Co_{0.5}Fe_{0.125}Mo_{0.375}O_{3-d}$ (BSCFMo0.375-(Co/Fe=4) using the structural model the structural model of a SP and a DP phase crystallizing in space groups $Pm\bar{3}m$ and $Fm\bar{3}m$, with the black and blue tick marks showing the allowed reflections respectively, (ii) magnification of the t.o.f. range 30,000-45,000 μs, showing the fit of lower intensity reflections and (iii) magnification of the t.o.f. range 65,000-85,000 μs, focusing on the fit of the most intense perovskite reflections.

Appendix C: In-situ variable temperature XRD

Table C: Structural outcomes for the single (SP) and double perovskite (DP) components in BSCFMo0.375-(Co/Fe=4) from refinements of Synchrotron in-situ X-ray data for at room temperature, 300°C and from 500 to 900°C in steps of 50°.

T (^{o}C)	Lattice parameters (Å)	Phase ratio(%)	Crystallites sizes (nm)
	a (SP) a (DP)	SP(%), DP(%)	SP DP, DP-odd
RT	3.98557(8), 7.98299(3)	22.0 (4), 78.0(4)	78 (1) 211(4), 58(3)
300	3.99823(10), 8.01014(3)	22.5(4), 77.5(4)	69 (1) 199(4), 63(3)
500	4.00932(7), 8.03219(3)	22.4(3), 77.6(3)	80 (1) 182(2), 58(2)
550	4.01218(7), 8.03787(3)	23.0(3), 77.0(3)	86(1) 185(2), 57(2)
600	4.01503(7), 8.04359(3)	23.4(3), 76.6(4)	90(1) 174(2), 57(2)
650	4.01813(6), 8.04941(3)	24.9(3), 75.1(3)	96(1) 177(2), 62(2)
700	4.02097(6), 8.05516(3)	24.8(3), 75.2(3)	101(1) 173(2), 57(2)
750	4.02386(5), 8.06094(3)	26.5(3), 73.5(3)	102(1) 174(2), 60(2)
800	4.02663(5), 8.06664(3)	27.0(3), 73.0(3)	106(1) 174(2), 61(2)
850	4.02931(5), 8.07230(3)	27.2(3), 72.8(3)	107(1) 170(2), 69(2)
900	4.02314(4), 8.07803(3)	98.96% perovskite (27.4(2)%SP 71.6(2)%DP) +1.04(8) $BaMoO_4$	107(2) 173(2), 62(2)

Appendix D: ECM fitting Outcomes

Table D: Summary of resistance (R) and pseudo-capacitance (C) values derived from the fitting of the impedance arcs, at the temperature range 600-850^{o}C, to the equivalent circuit model consisting of 3 R-CPE elements, each one describing the response of each of the arcs present at high (HF, f_r= 10^3-10^2Hz), medium (MF, f_r=10^2-10^0 Hz) and low (LF, f_r=10^0-10^{-1} Hz) frequency, for the whole range of oxygen partial pressure for the experiment in *Section 5.1.2*. The total area specific resistance (ASR) is also included, where ASR= R(HF)+ R(MF)+ R(LF)).

pO_2 (atm)	**Total** ASR ($\Omega.cm^2$)	**HF** R ($\Omega.cm^2$)	C ($F.cm^{-2}$)	**MF** R ($\Omega.cm^2$)	C ($F.cm^{-2}$)	**LF** R ($\Omega.cm^2$)	C ($F.cm^{-2}$)
Temperature: 600^{o}C							
0.21	0.460	0.014	5.24E-02	0.406	1.41E-01	0.040	1.07E-01
0.10	0.953	0.036	3.43E-02	0.815	1.48E-01	0.103	7.43E-02
0.01	3.249	0.030	7.31E-02	2.762	1.26E-01	0.457	1.22E-01
0.05	4.146	0.227	3.34E-02	3.167	1.29E-01	0.752	9.87E-02
0.0028	6.211	0.499	4.70E-02	4.163	1.45E-01	1.550	7.62E+00
Temperature: 650^{o}C							
0.21	0.230	0.006	7.74E-02	0.209	8.70E-02	0.015	1.50E-01
0.10	0.370	0.013	4.97E-02	0.305	9.46E-02	0.052	1.04E-01
0.01	1.218	0.026	6.23E-02	0.785	1.88E-01	0.407	9.59E-02
0.05	1.737	0.030	5.65E-02	0.969	7.80E-02	0.738	2.89E-01
0.0028	2.775	0.071	5.68E-02	1.488	9.66E-02	1.217	7.62E+00
Temperature: 700^{o}C							
0.21	0.072	0.011	1.33E-01	0.060	1.20E-01	0.001	3.98E+00
0.10	0.178	0.010	1.33E-01	0.158	7.10E-02	0.010	3.98E+00
0.01	0.641	0.018	1.14E-01	0.423	7.38E-02	0.200	2.33E+00
0.05	0.849	0.007	1.54E-01	0.677	6.10E-02	0.165	3.06E+00
0.0028	1.396	0.007	1.53E-01	0.970	6.19E-02	0.419	2.46E+00

Temperature: 800^{o}C						
0.21	0.227	-	0.008	1.50E-01	0.009	7.93E-01
0.10	0.143	-	0.024	6.25E-02	0.019	1.97E+00
0.01	0.231	-	0.087	5.39E-02	0.134	2.21E+00
0.05	0.356	-	0.128	4.96E-02	0.224	2.14E+00
0.0028	0.682	-	0.195	5.21E-02	0.484	2.04E+00
Temperature: 850^{o}C						
0.21	0.219	-	0.004	3.33E-01	0.005	2.90E+00
0.10	0.128	-	0.009	1.12E-01	0.019	1.96E-02
0.01	0.193	-	0.044	5.65E-02	0.139	2.23E+00
0.05	0.305	-	0.068	5.15E-02	0.232	2.12E+00
0.0028	0.616	-	0.116	5.20E-02	0.498	2.02E+00

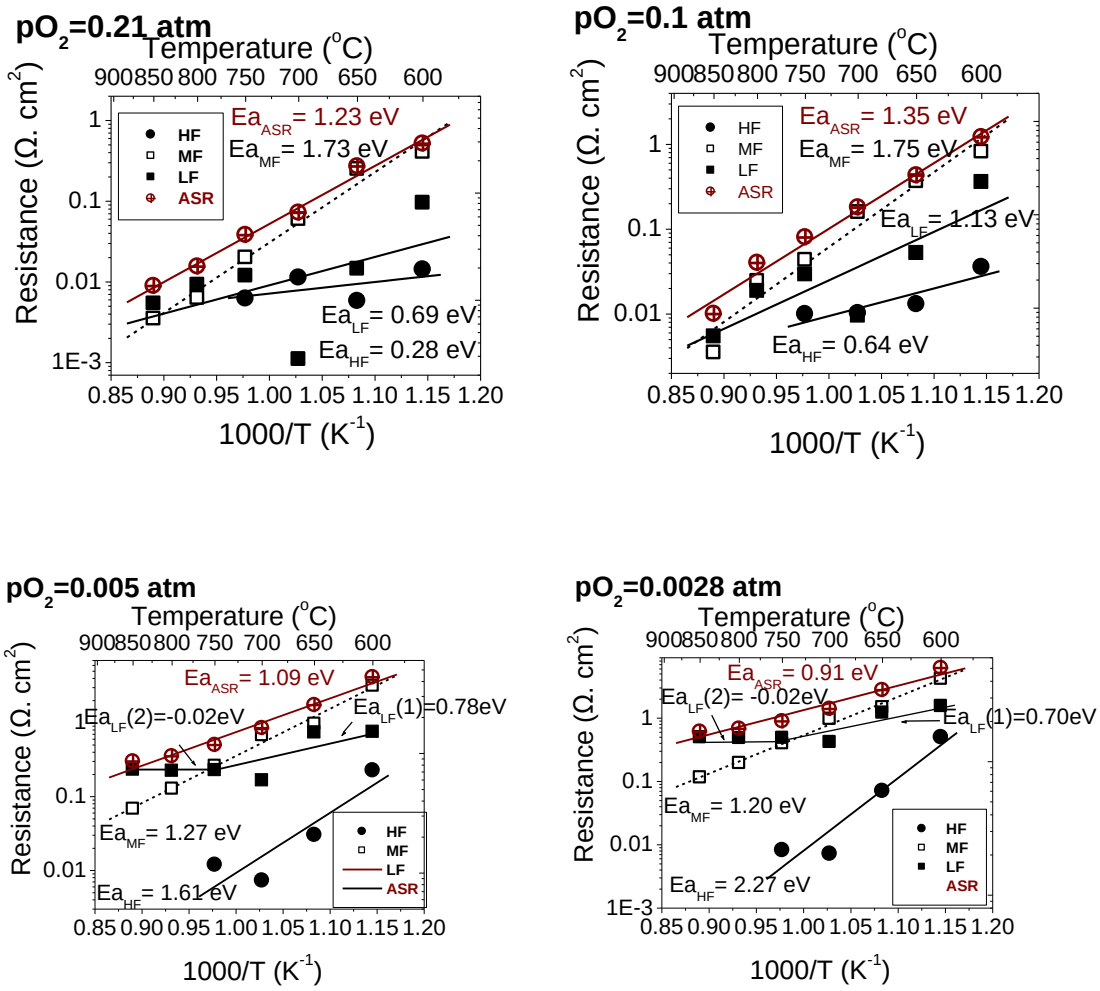

Figure D1: Arrhenius plots of the resistance against temperature for the high (HF, f_r= 10^3-10^2Hz), medium (MF, f_r=10^2-10^0 Hz) and low (LF, f_r=10^0-10^{-1} Hz) frequency arcs at different oxygen partial pressure (pO_2), shown in closed circles, open squares and closed squares respectively and calculated activation energies. The total area specific resistance (ASR) is represented in red crossed circles, where ASR= R(HF)+ R(MF)+ R(LF)).

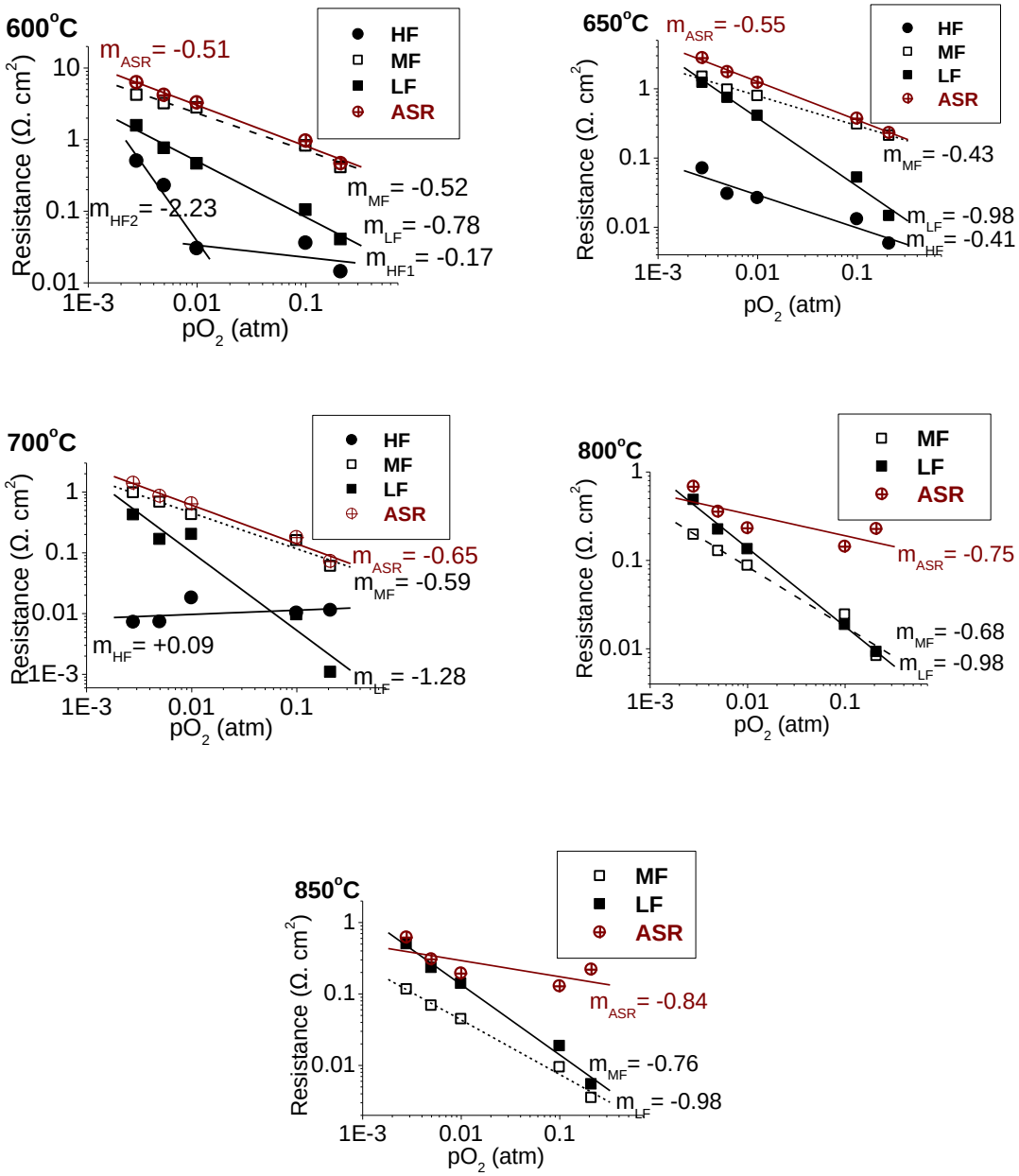

Figure D2: Effect of oxygen partial pressure (pO_2) on the resistance (R) of the high (HF, f_r= 10^3-10^2Hz), medium (MF, f_r=10^2-10^0 Hz) and low (LF, f_r=10^0-10^{-1} Hz) frequency arcs, shown in closed circles, open squares and closed squares respectively and the exponent m. The total area specific resistance (ASR) is represented in red crossed circles, where ASR= R(HF)+R(MF)+R(LF)).

Appendix E: Rietveld refinements of X-ray data

E1. Silicon standard

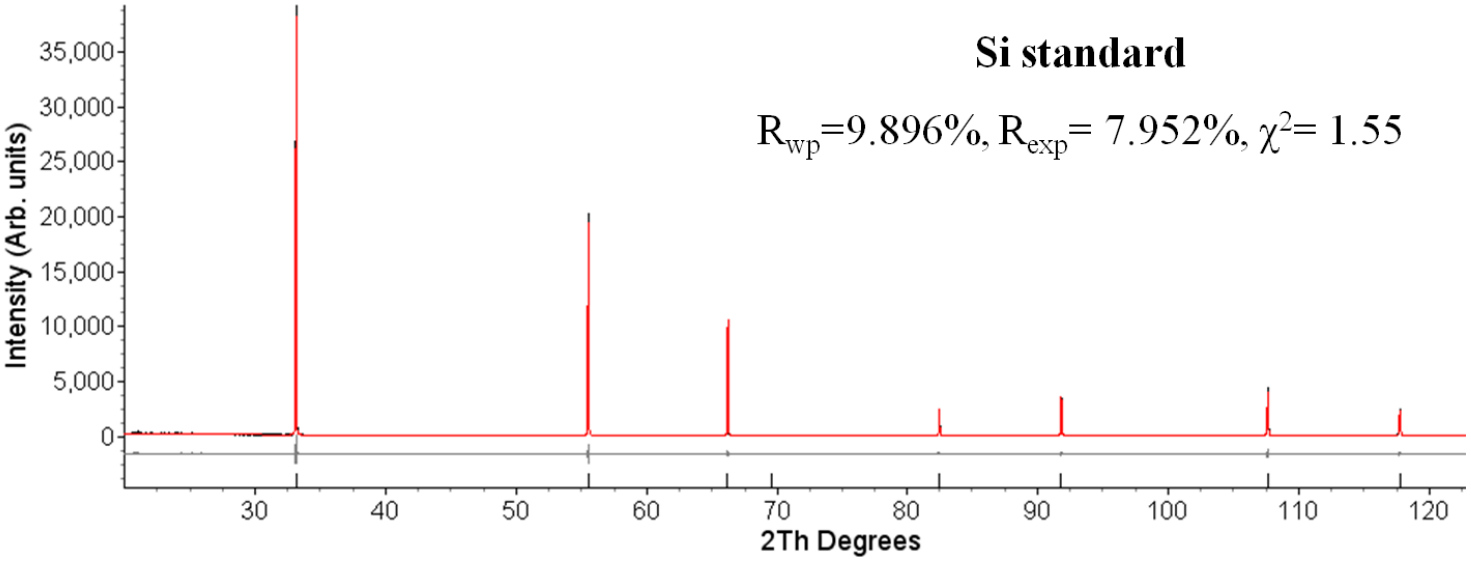

E2. BSCFM compositions

For all the refinements of BSCFM compositions shown below:

Observed (black), calculated (red) and difference (grey) plots of Rietveld fits against XRD data with the black and blue tickmarks showing the allowed reflections a single (SP) and a double (DP) perovskite phase, crystallising in space groups P$m\bar{3}m$ and F$m\bar{3}m$ respectively. Red tickmarks indicate the presence of $BaMoO_4$ impurity phase.

E2.1. Reproducibility of BSCFMo0.375-(Co/Fe=4) (from Section 4.1.7)

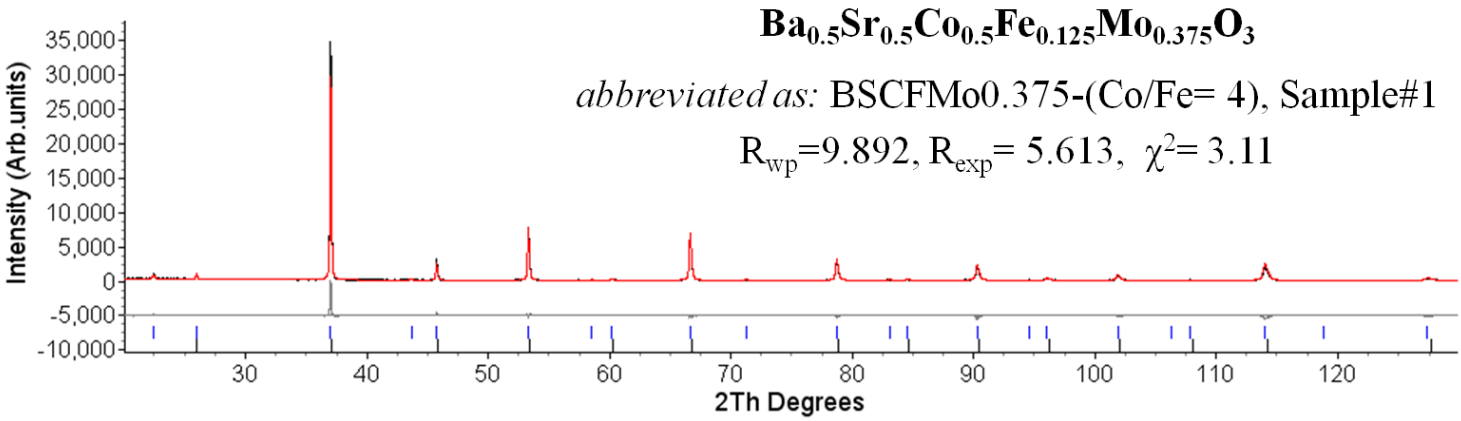

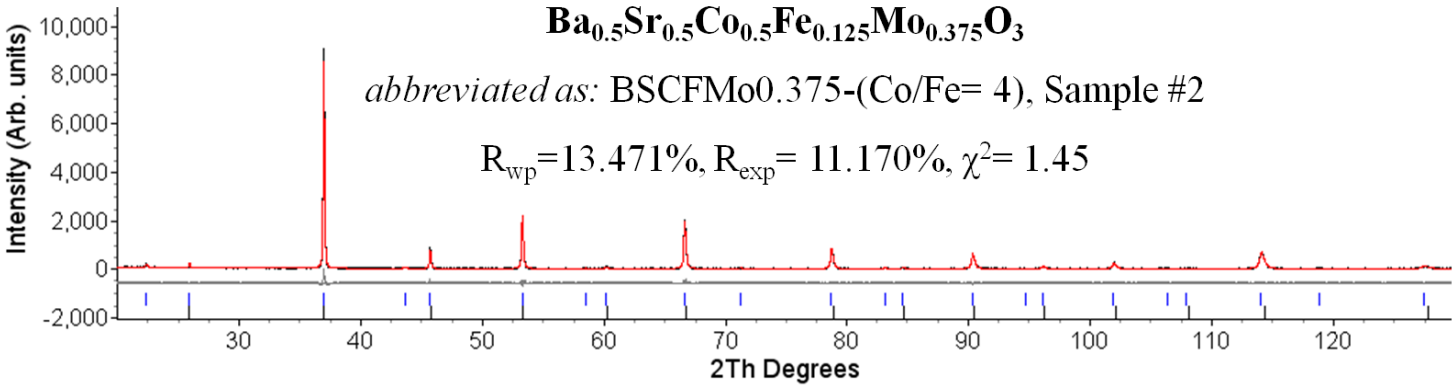

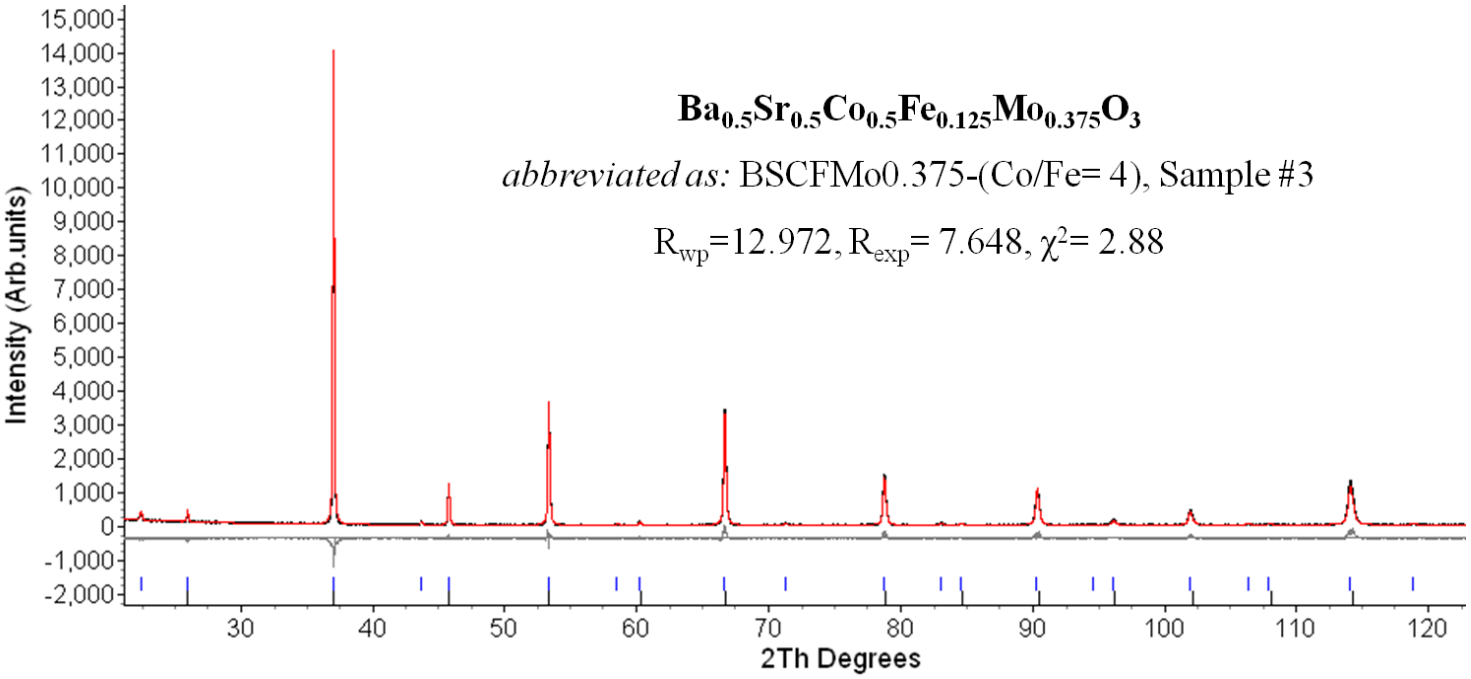
Ba0.5Sr0.5Co0.5Fe0.125Mo0.375O3
abbreviated as: BSCFMo0.375-(Co/Fe= 4), Sample #3
Rwp=12.972, Rexp= 7.648, χ2= 2.88
Intensity (Arb.units)
15,000
14,000
13,000
12,000
11,000
10,000
9,000
8,000
7,000
6,000
5,000
4,000
3,000
2,000
1,000
0
-1,000
-2,000
30
40
50
60
70
80
90
100
110
120
2Th Degrees

E2.2. Targeting isolated SP and DP phases (from Section 4.1.9)

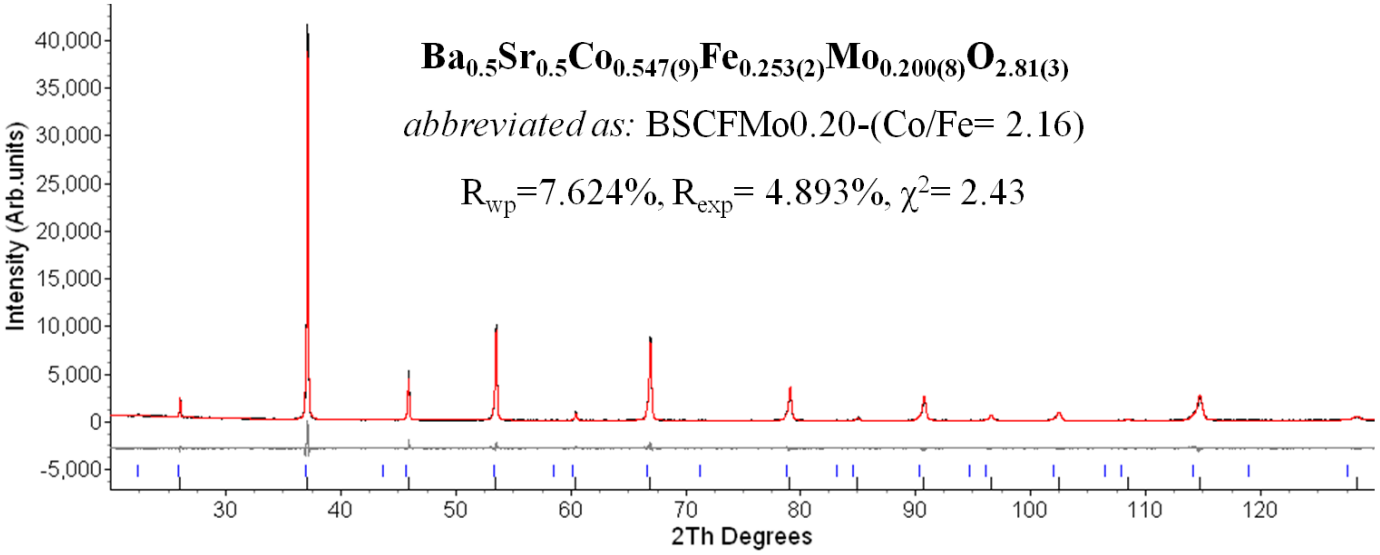

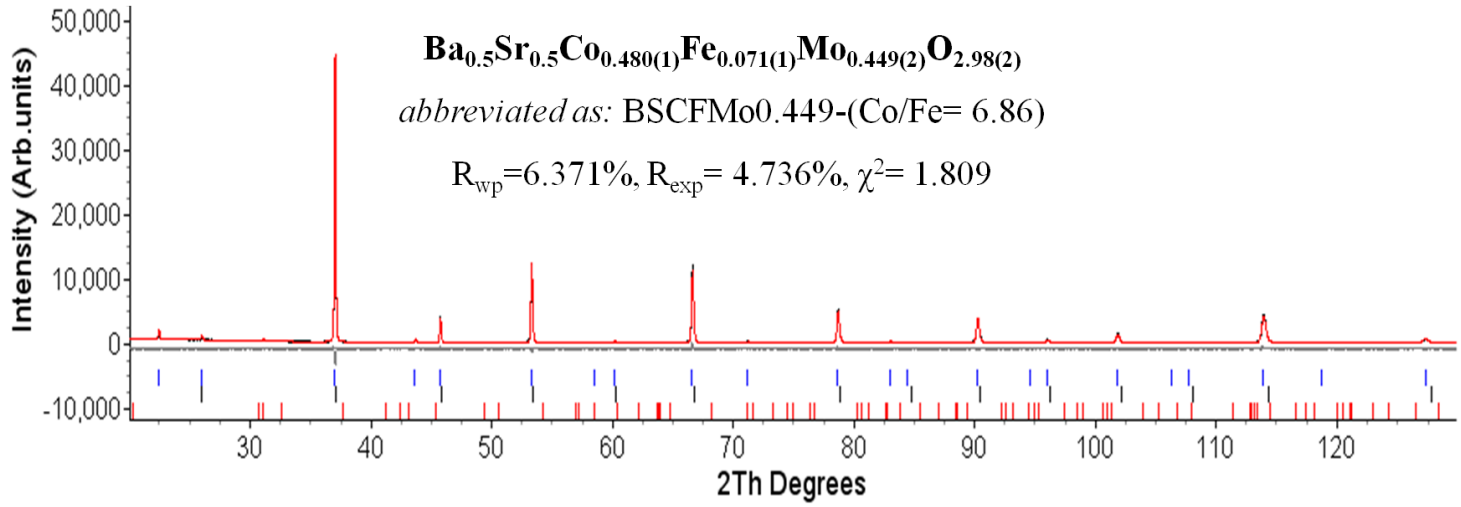

E2.3. Evolution of the biphasic assemblage in BSCFMo0.375-(Co/Fe=4) with temperature (from Section 4.2)

E2.3.1. Variable temperature in situ Synchrotron data (from Section 4.2.1)

$Ba_{0.5}Sr_{0.5}Co_{0.5}Fe_{0.125}Mo_{0.375}O_3$ -*abbreviated as:* BSCFMo0.375(Co/Fe=4)

I11 data, Room temperature

R_{wp}=8.439%, R_{exp}= 2.855%, χ^2= 8.74

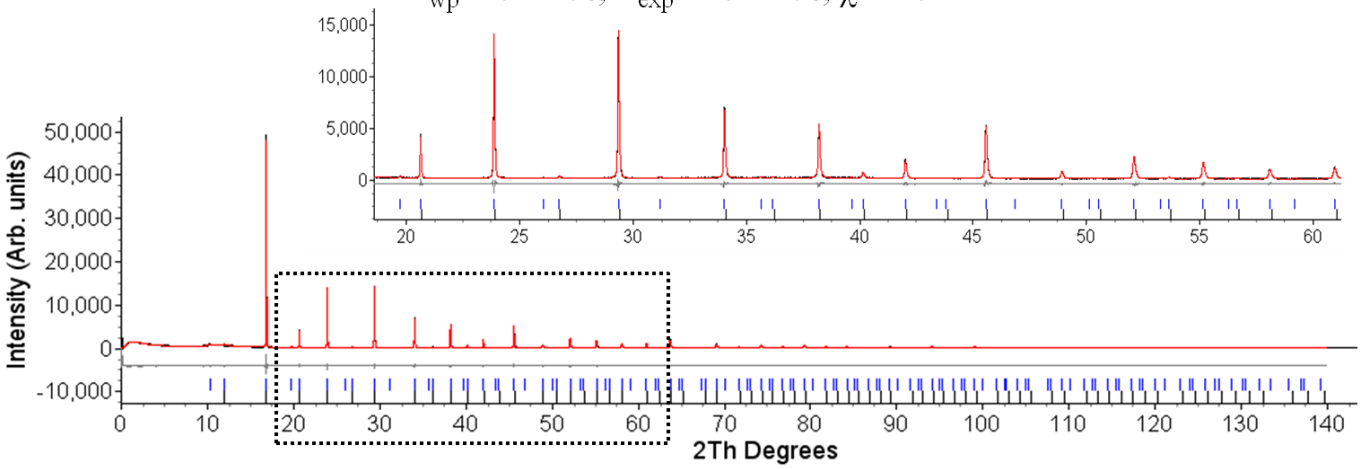

$Ba_{0.5}Sr_{0.5}Co_{0.5}Fe_{0.125}Mo_{0.375}O_3$ -*abbreviated as:* BSCFMo0.375(Co/Fe=4)

I11 data, 300°C

R_{wp}=8.301%, R_{exp}= 2.883%, χ^2= 8.29

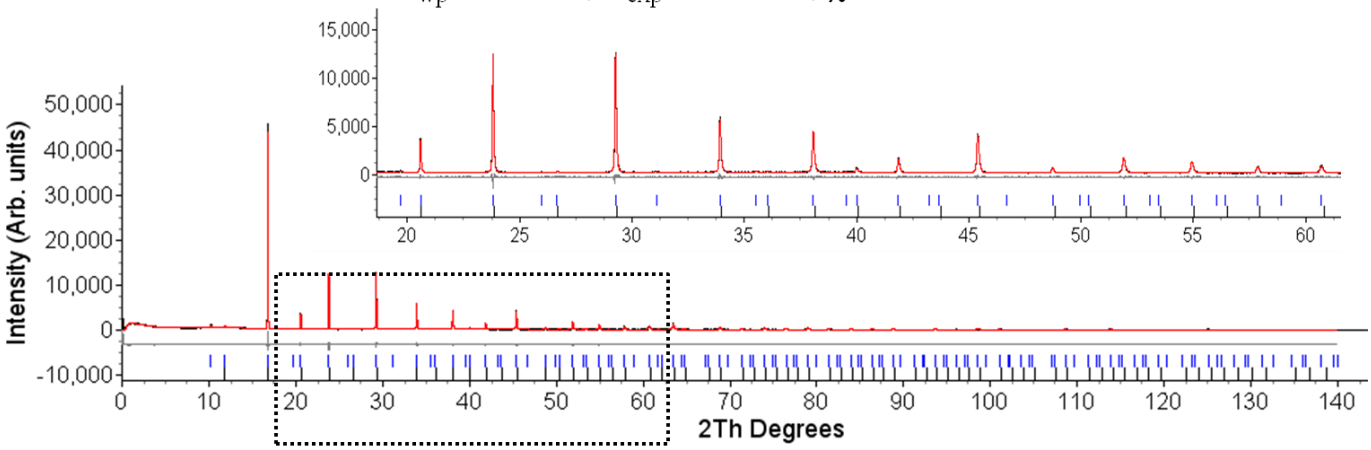

$Ba_{0.5}Sr_{0.5}Co_{0.5}Fe_{0.125}Mo_{0.375}O_3$ -*abbreviated as:* BSCFMo0.375(Co/Fe=4)

I11 data, 550°C

R_{wp}= 8.138%, R_{exp}= 2.815%, χ^2= 8.36

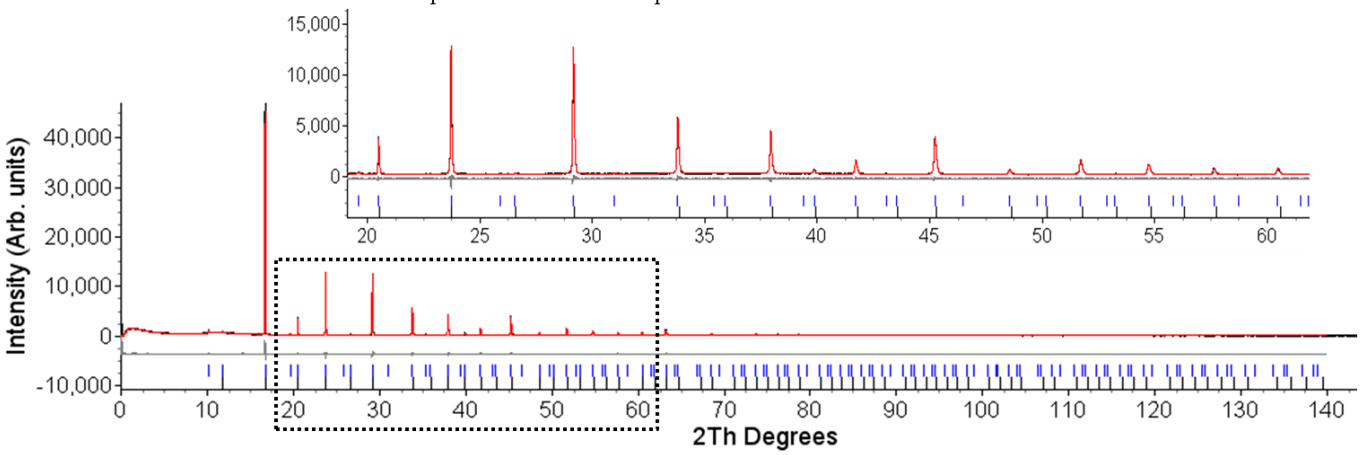

$Ba_{0.5}Sr_{0.5}Co_{0.5}Fe_{0.125}Mo_{0.375}O_3$ -*abbreviated as:* BSCFMo0.375(Co/Fe=4)

I11 data, 600°C

R_{wp}= 8.273%, R_{exp}= 2.816%, χ^2= 8.63

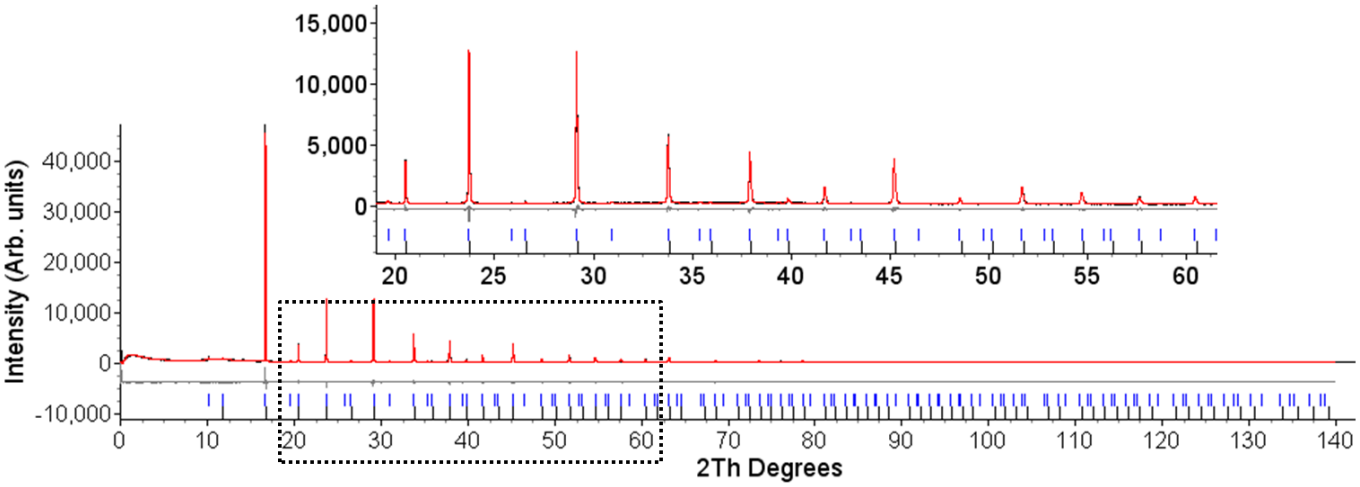

$Ba_{0.5}Sr_{0.5}Co_{0.5}Fe_{0.125}Mo_{0.375}O_3$ -*abbreviated as:* BSCFMo0.375(Co/Fe=4)

I11 data, 650°C

R_{wp}= 8.078%, R_{exp}= 2.819 %, χ^2= 8.21

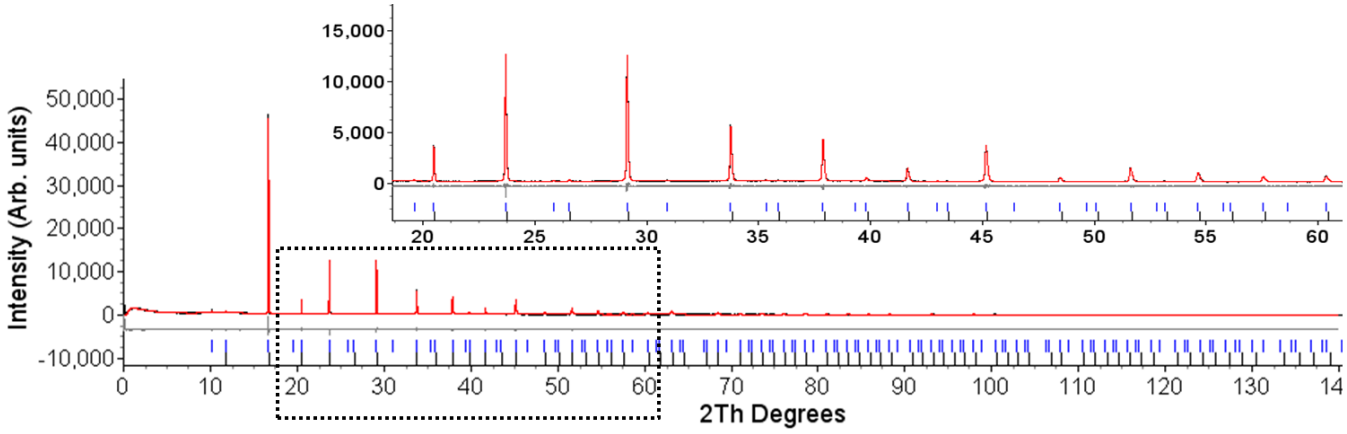

$Ba_{0.5}Sr_{0.5}Co_{0.5}Fe_{0.125}Mo_{0.375}O_3$ -*abbreviated as:* BSCFMo0.375(Co/Fe=4)

I11 data, 700°C

R_{wp}= 8.123%, R_{exp}= 2.821%, χ^2= 8.29

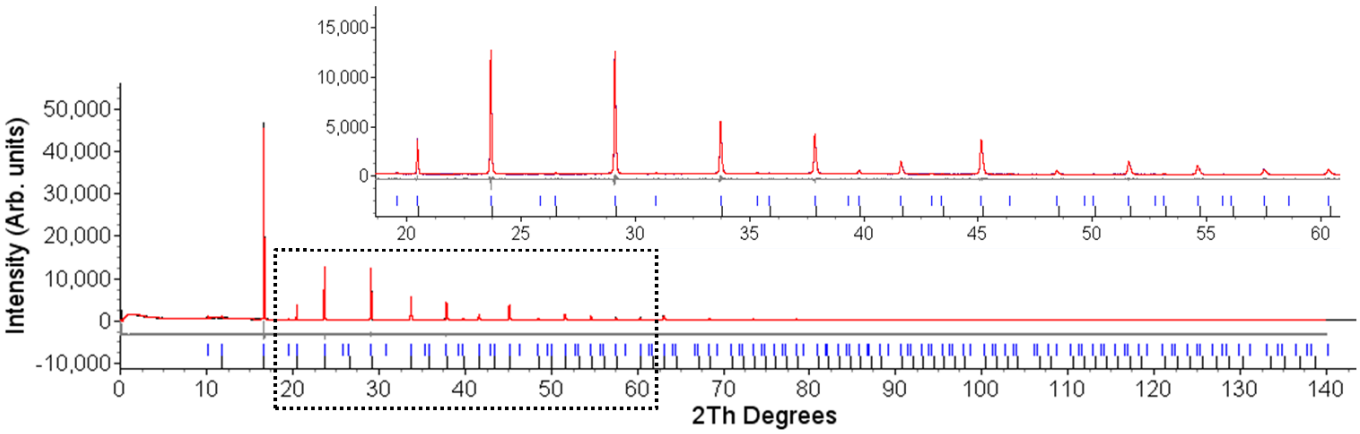

$Ba_{0.5}Sr_{0.5}Co_{0.5}Fe_{0.125}Mo_{0.375}O_3$ -*abbreviated as:* BSCFMo0.375(Co/Fe=4)

I11 data, 750°C

R_{wp}= 8.036%, R_{exp}= 2.823%, χ^2= 8.11

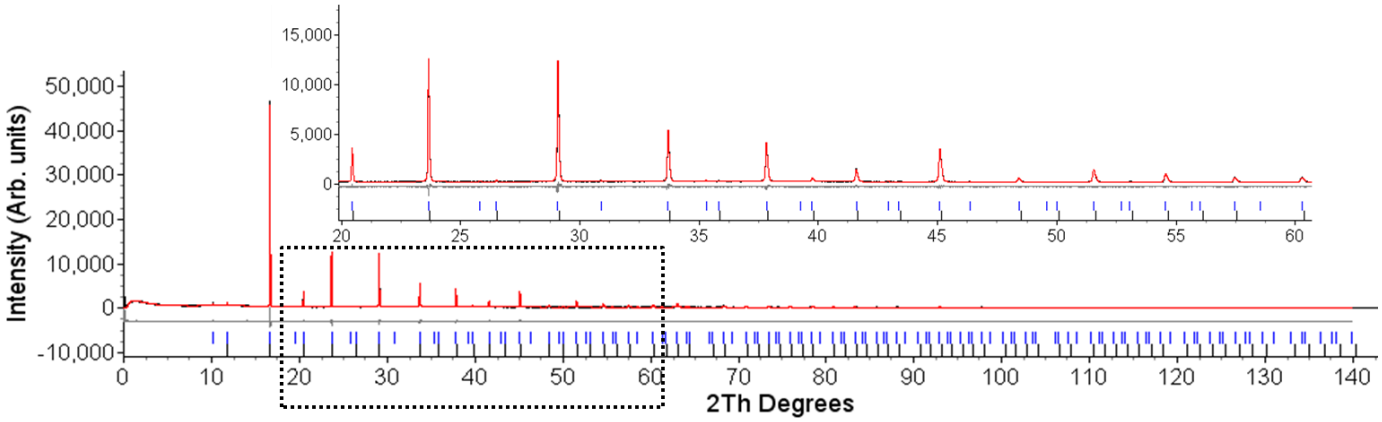

$Ba_{0.5}Sr_{0.5}Co_{0.5}Fe_{0.125}Mo_{0.375}O_3$ -*abbreviated as:* BSCFMo0.375(Co/Fe=4)

I11 data, 800°C

R_{wp}= 8.228%, R_{exp}= 2.822%, χ^2= 8.50

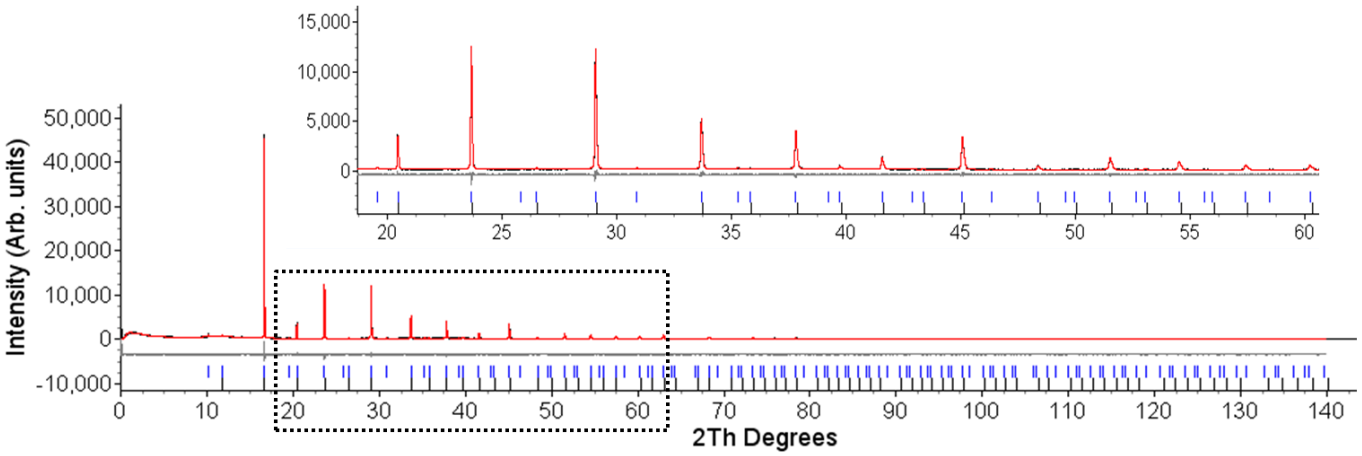

$Ba_{0.5}Sr_{0.5}Co_{0.5}Fe_{0.125}Mo_{0.375}O_3$ -*abbreviated as:* BSCFMo0.375(Co/Fe=4)

I11 data, 850°C

R_{wp}= 8.250%, R_{exp}= 2.826%, χ^2= 8.53

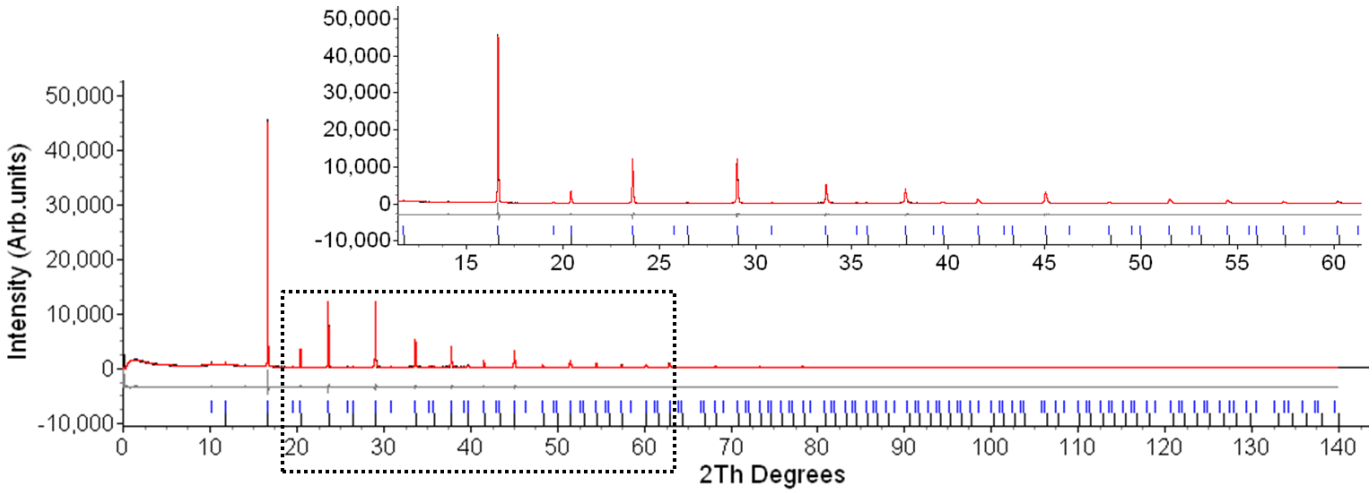

$Ba_{0.5}Sr_{0.5}Co_{0.5}Fe_{0.125}Mo_{0.375}O_3$ -*abbreviated as:* BSCFMo0.375(Co/Fe=4)

I11 data, 900°C

R_{wp}= 8.058%, R_{exp}= 2.689%, χ^2= 8.98

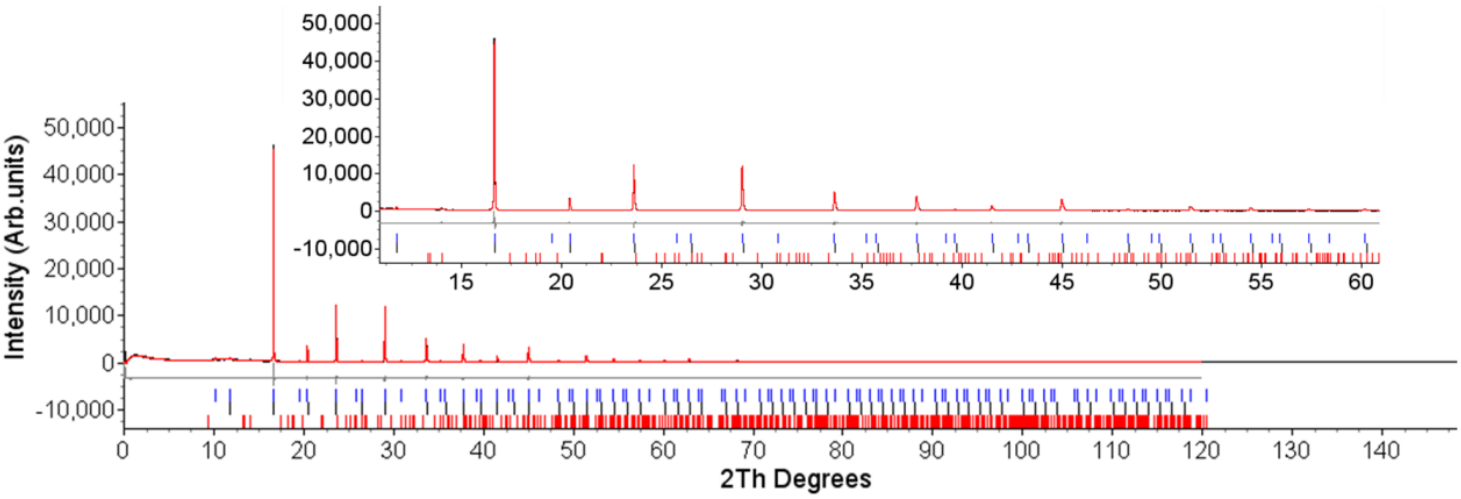

E2.3.2. Quenching (rapid cooling experiments) (from Section 4.2.2)

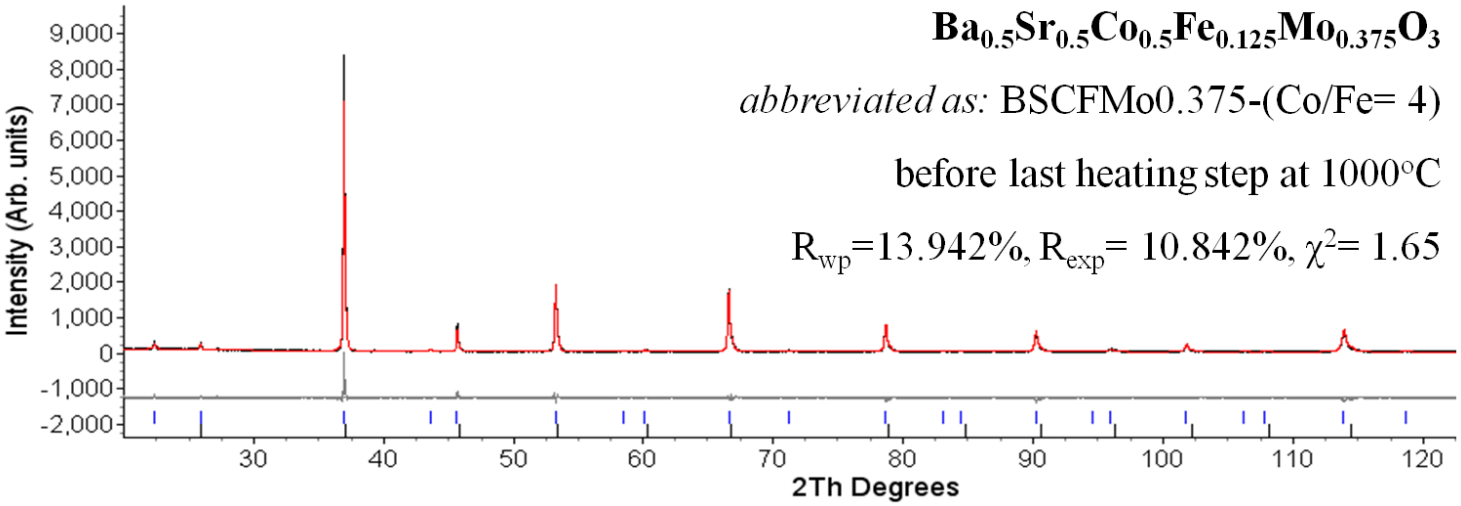

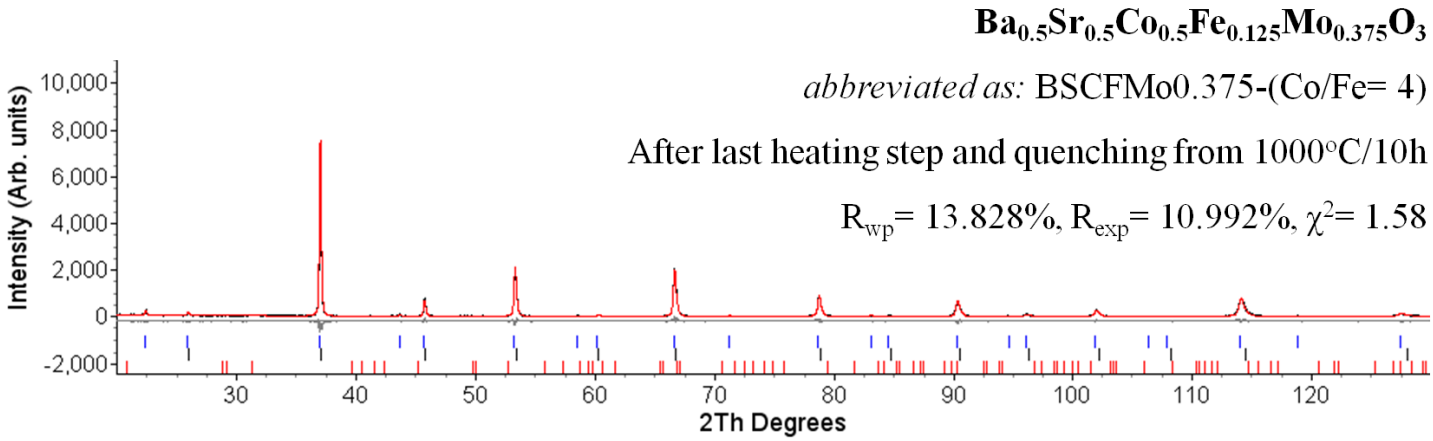

$Ba_{0.5}Sr_{0.5}Co_{0.5}Fe_{0.125}Mo_{0.375}O_3$

abbreviated as: BSCFMo0.375-(Co/Fe= 4)

After last heating step and quenching from 1200°C/10h

R_{wp}= 15.537%, R_{exp}=11.298%, χ^2= 1.89

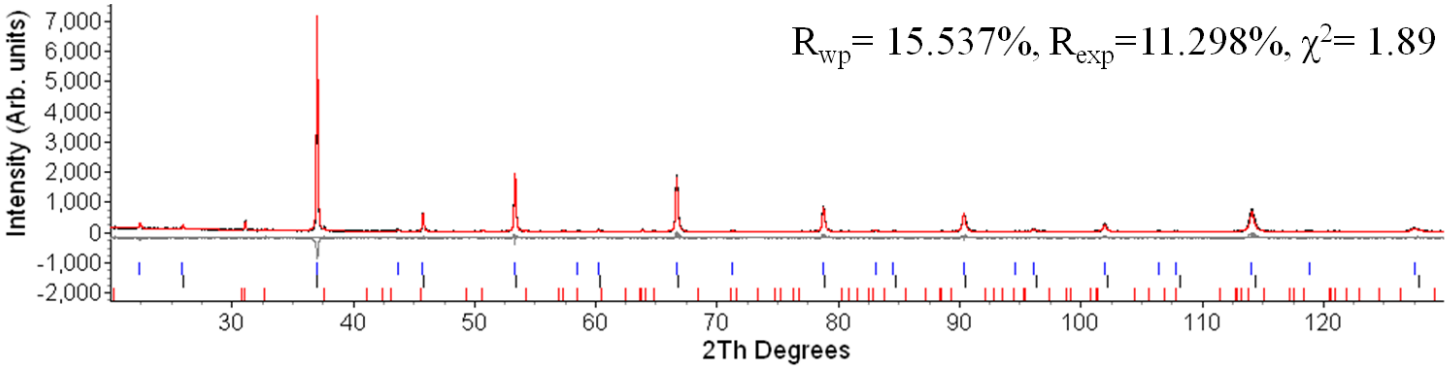

$Ba_{0.5}Sr_{0.5}Co_{0.5}Fe_{0.125}Mo_{0.375}O_3$

abbreviated as: BSCFMo0.375-(Co/Fe= 4)

After last heating step at 1200°C/10h

R_{wp}= 14.600%, R_{exp} = 10.472%, χ^2= 1.94

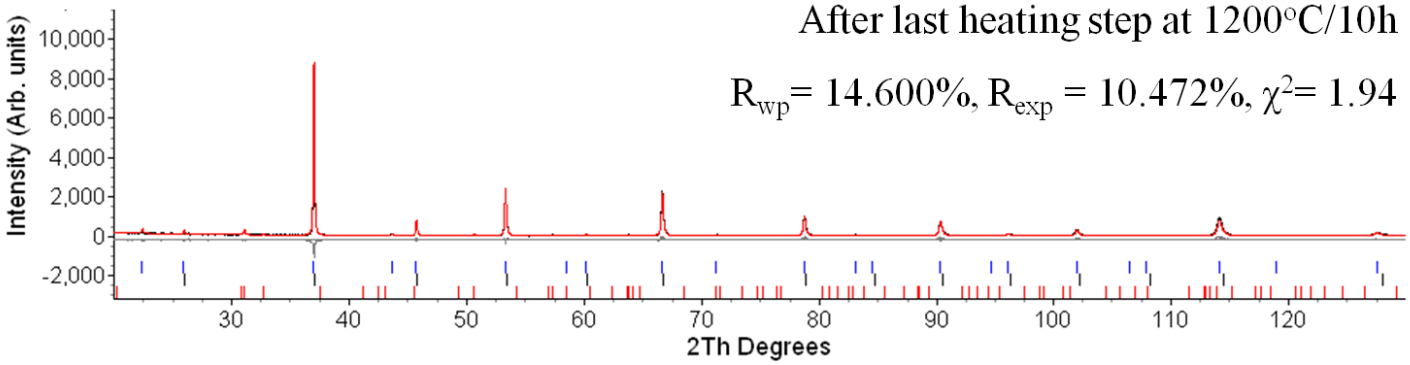

E2.4. Other BSCFM compositions (from Section 4.3)

E2.4.1. Effect of Mo content (from Section 4.3.3)

$Ba_{0.5}Sr_{0.5}Co_{0.8}Fe_{0.2}O_3$

abbreviated as: BSCF

R_{wp}= 21.794%, R_{exp}= 16.604%, χ^2= 1.72

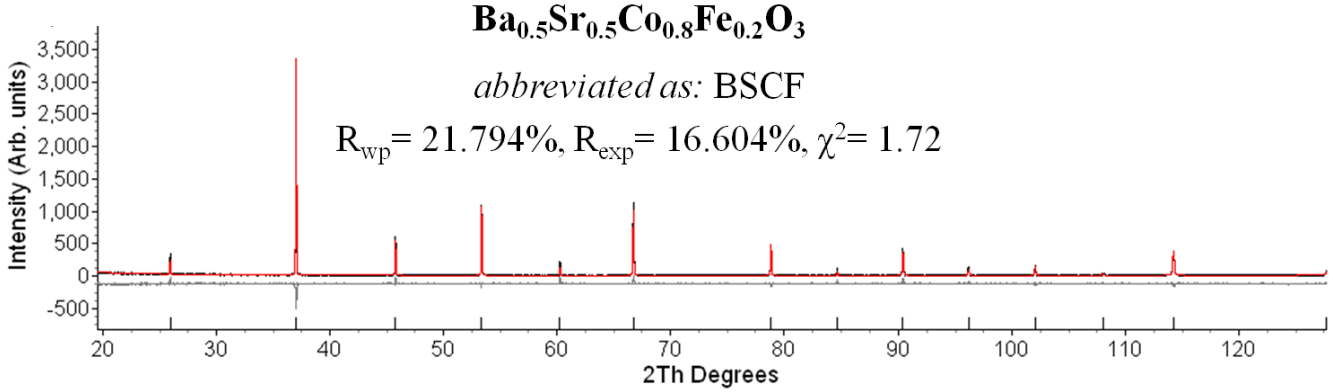

$Ba_{0.5}Sr_{0.5}Co_{0.7}Fe_{0.175}Mo_{0.125}O_3$

abbreviated as: BSCFMo0.125-(Co/Fe=4)

R_{wp}= 06.546%, R_{exp}= 4.715%, χ^2= 1.93

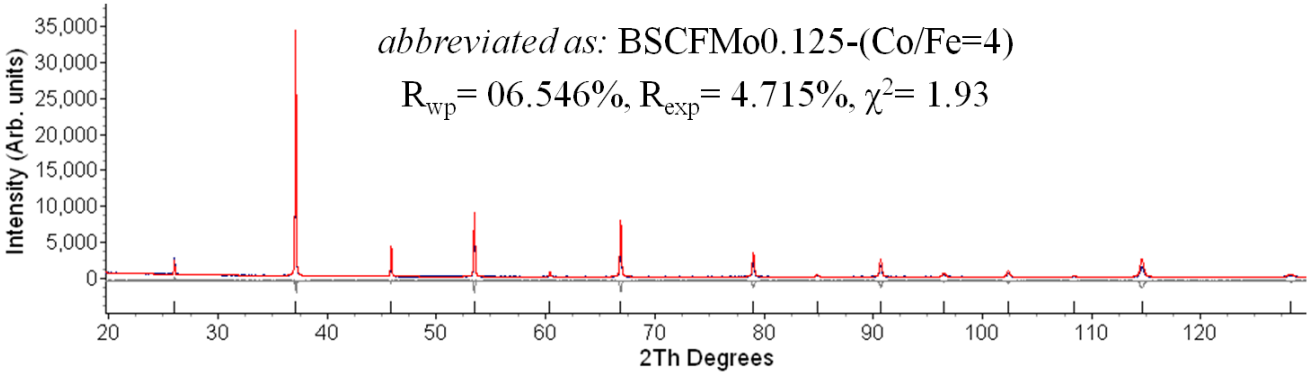

$Ba_{0.5}Sr_{0.5}Co_{0.64}Fe_{0.16}Mo_{0.200}O_3$

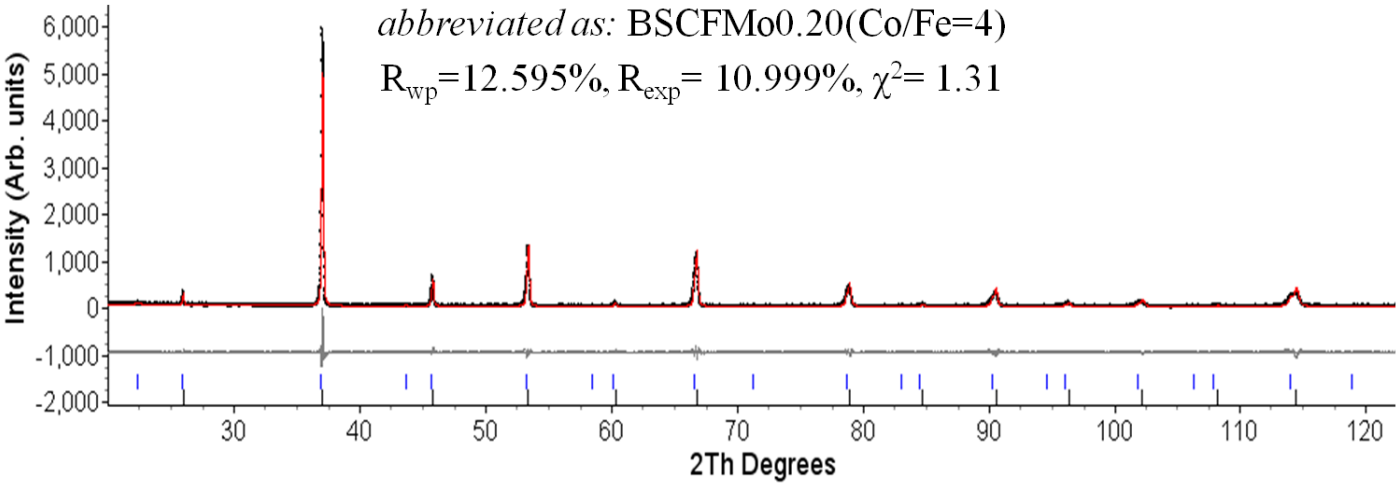

$Ba_{0.5}Sr_{0.5}Co_{0.60}Fe_{0.15}Mo_{0.250}O_3$

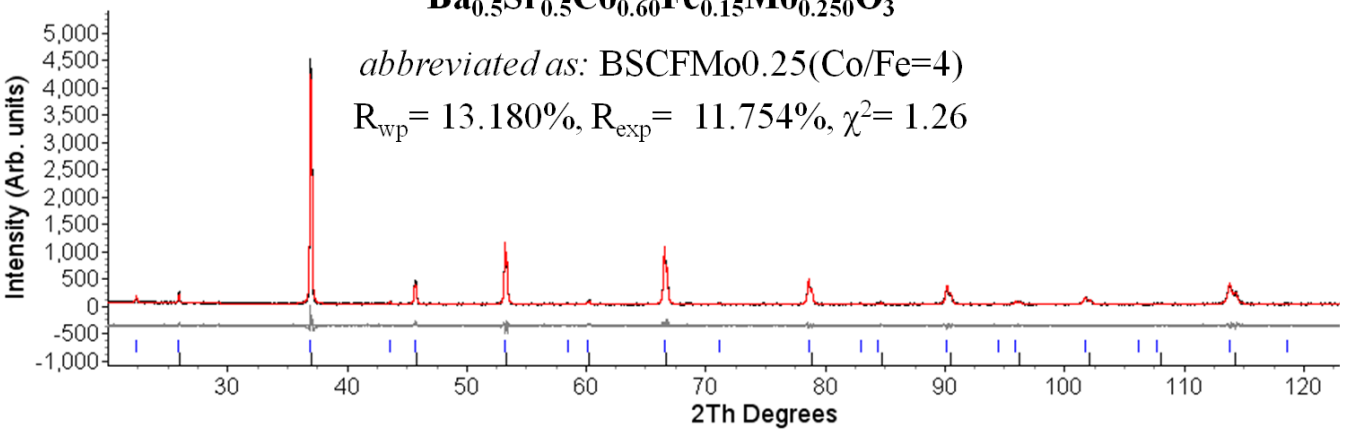

$Ba_{0.5}Sr_{0.5}Co_{0.566}Fe_{0.142}Mo_{0.292}O_3$

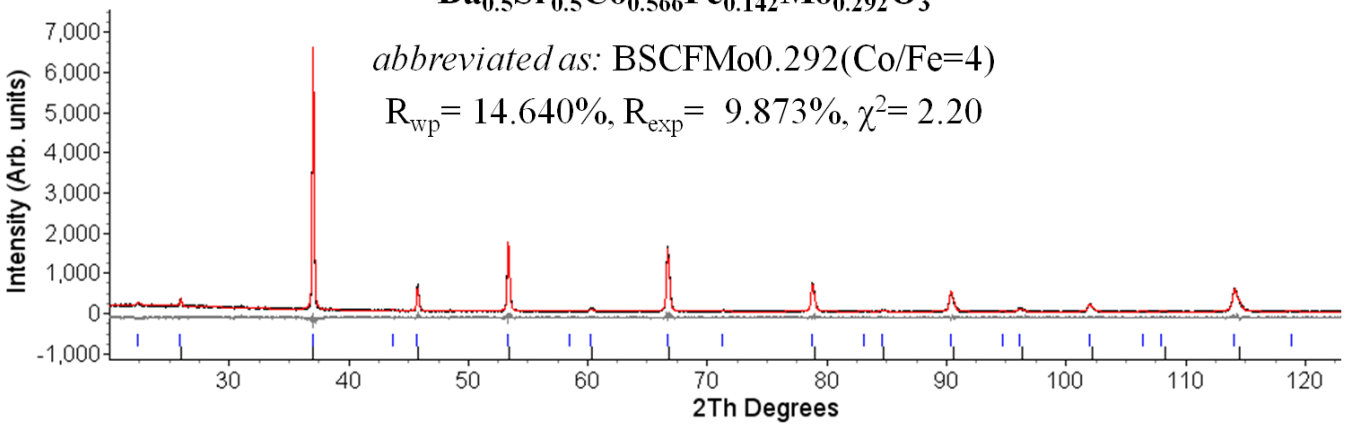

$Ba_{0.5}Sr_{0.5}Co_{0.536}Fe_{0.134}Mo_{0.330}O_3$

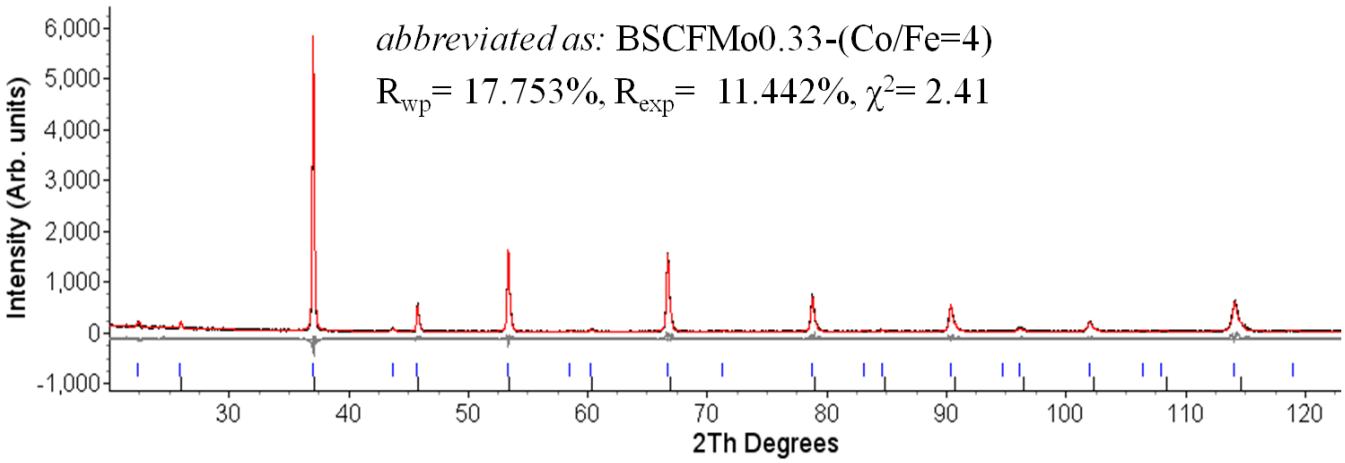

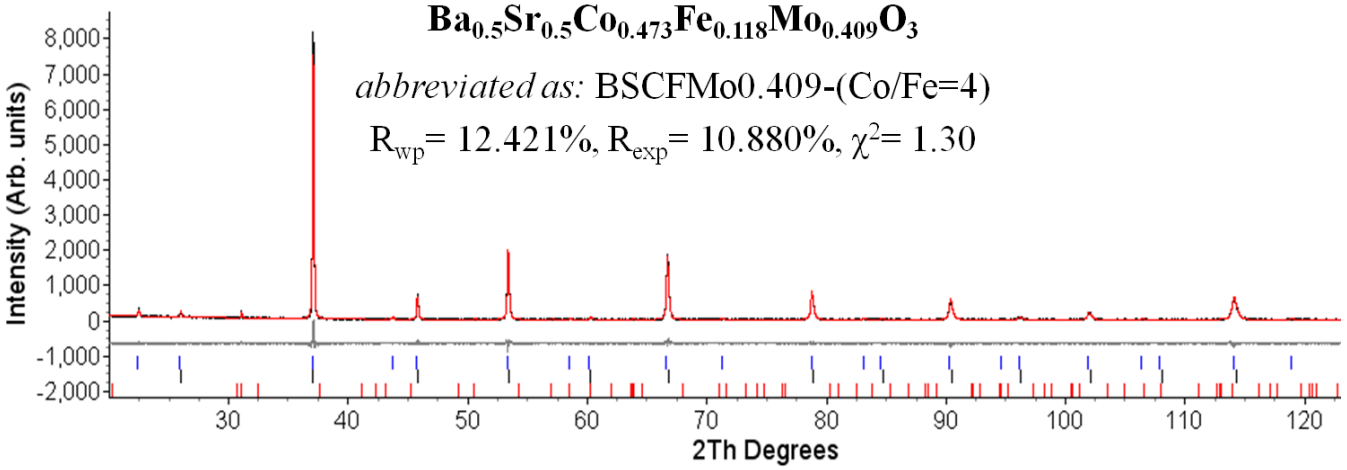
$Ba_{0.5}Sr_{0.5}Co_{0.473}Fe_{0.118}Mo_{0.409}O_3$
abbreviated as: BSCFMo0.409-(Co/Fe=4)
R_{wp}= 12.421%, R_{exp}= 10.880%, χ^2= 1.30
Intensity (Arb. units)
2Th Degrees

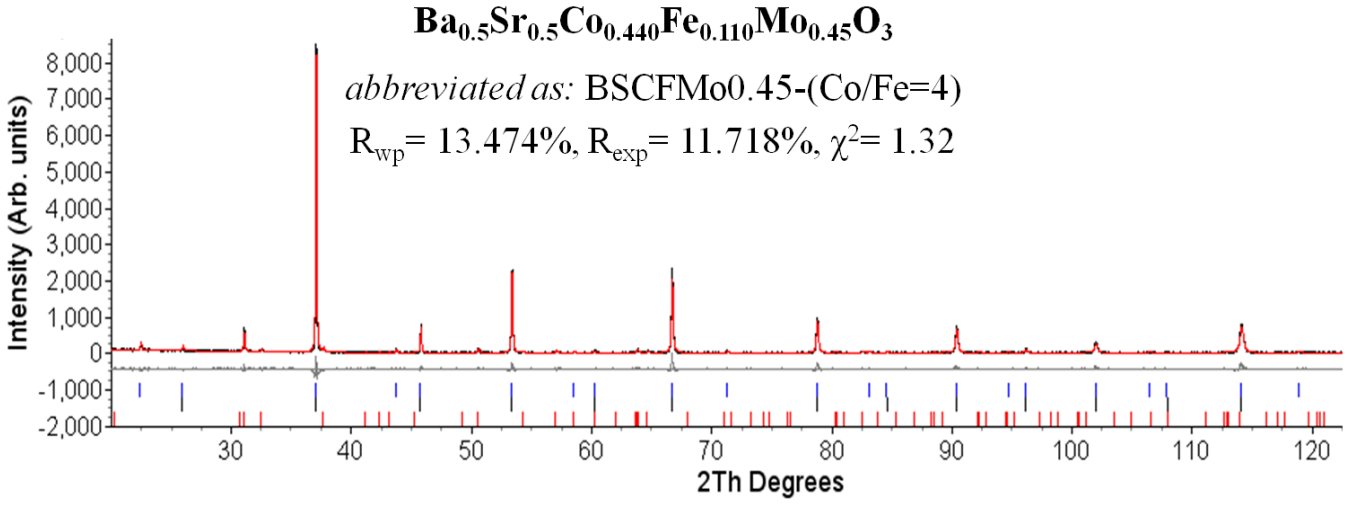
$Ba_{0.5}Sr_{0.5}Co_{0.440}Fe_{0.110}Mo_{0.45}O_3$
abbreviated as: BSCFMo0.45-(Co/Fe=4)
R_{wp}= 13.474%, R_{exp}= 11.718%, χ^2= 1.32
Intensity (Arb. units)
2Th Degrees

E2.4.2. Effect of Co/Fe ratio (from Section 4.3.4)

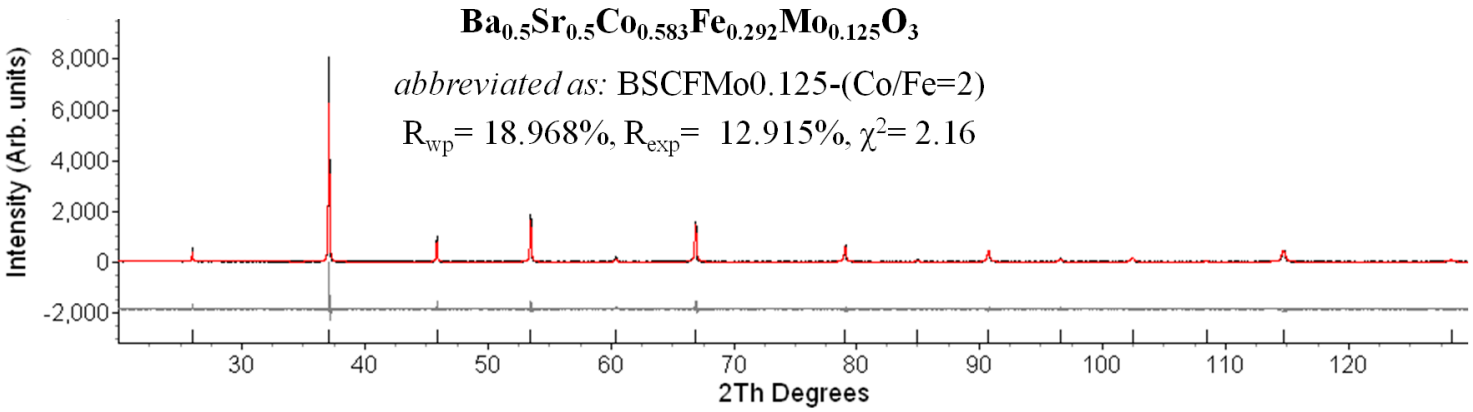

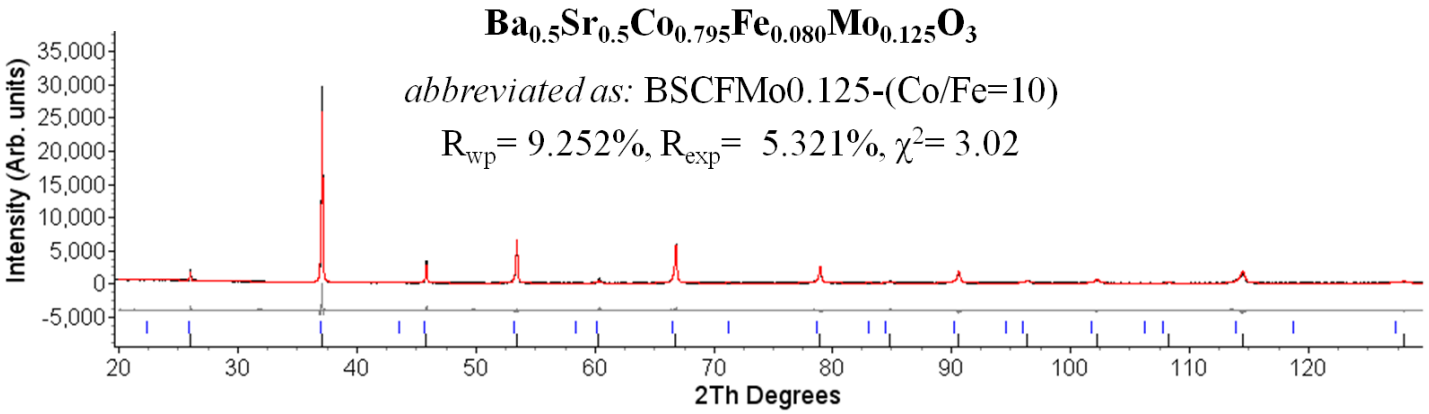

$Ba_{0.5}Sr_{0.5}Co_{0.6}Fe_{0.20}Mo_{0.20}O_3$

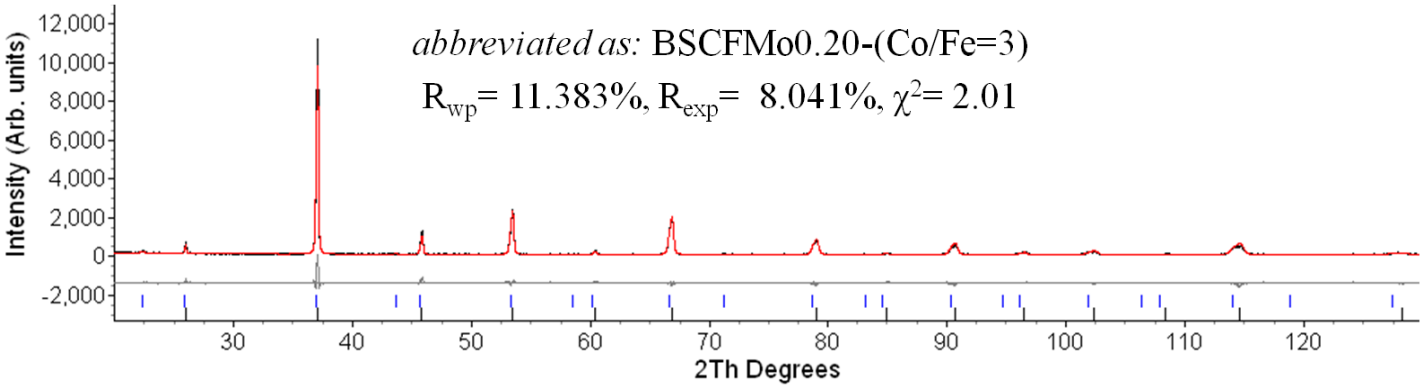

$Ba_{0.5}Sr_{0.5}Co_{0.5}Fe_{0.25}Mo_{0.25}O_3$

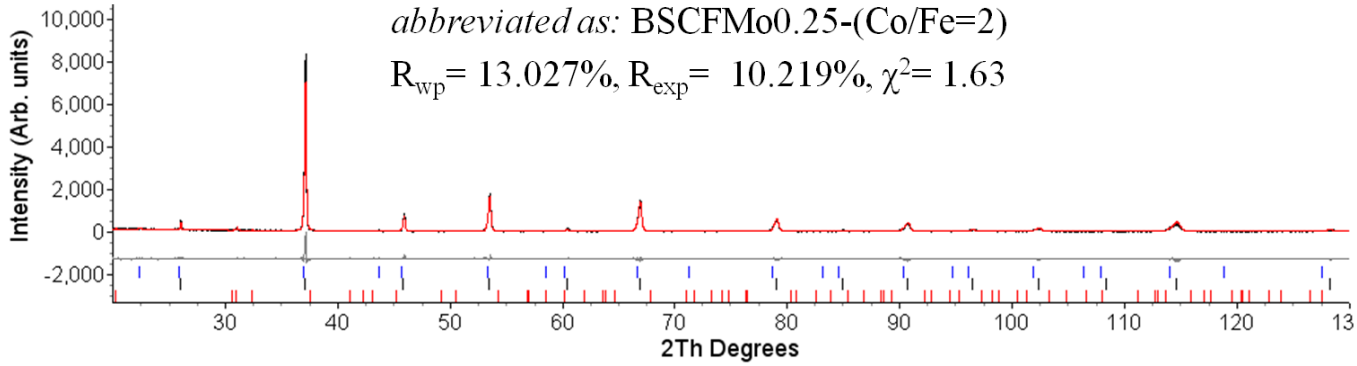

$Ba_{0.5}Sr_{0.5}Co_{0.582}Fe_{0.043}Mo_{0.375}O_3$

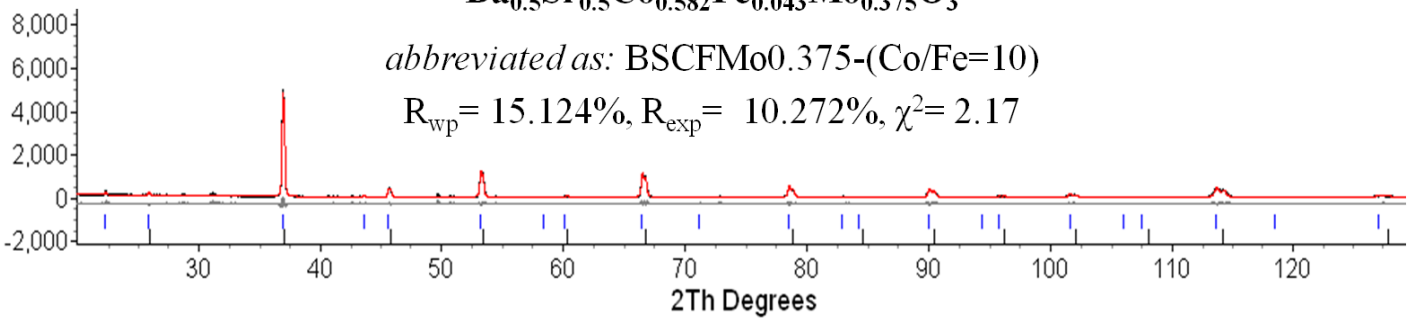

$Ba_{0.5}Sr_{0.5}Co_{0.500}Fe_{0.091}Mo_{0.409}O_3$

abbreviated as: BSCFMo0.409-(Co/Fe=6)

R_{wp}= 16.359%, R_{exp}= 10.325%, χ^2= 2.51

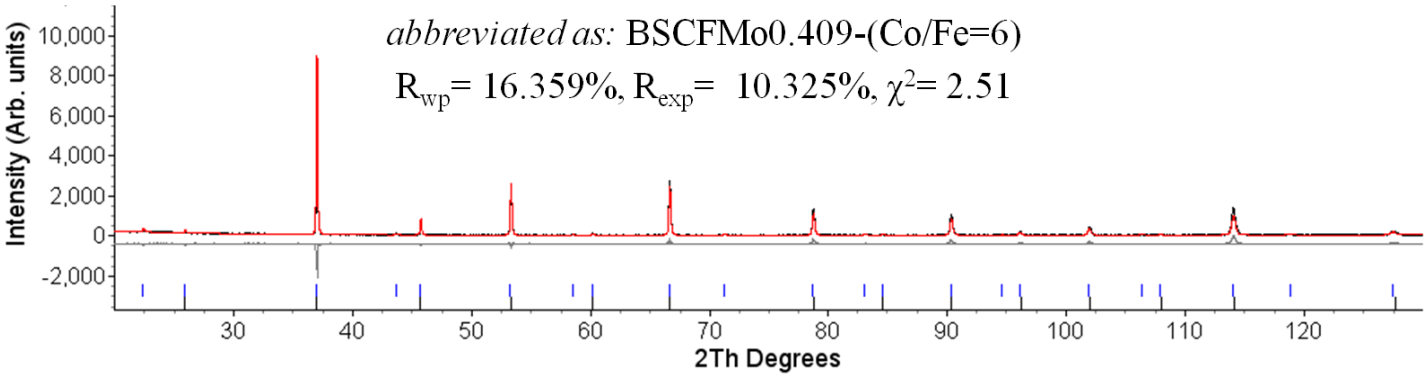

$Ba_{0.5}Sr_{0.5}Co_{0.500}Fe_{0.05}Mo_{0.45}O_3$

abbreviated as: BSCFMo0.45-(Co/Fe=10)

R_{wp}= 9.053%, R_{exp}= 7.256%, χ^2= 1.56

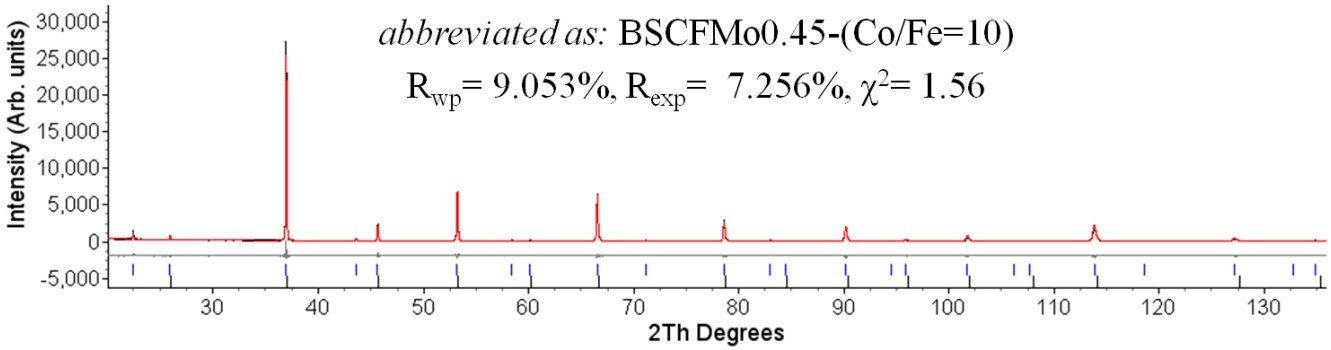

$Ba_{0.5}Sr_{0.5}Co_{0.500}Fe_{0.025}Mo_{0.475}O_3$

abbreviated as: BSCFMo0.475-(Co/Fe=20)

R_{wp}= 9.183%, R_{exp}= 5.648%, χ^2= 2.64

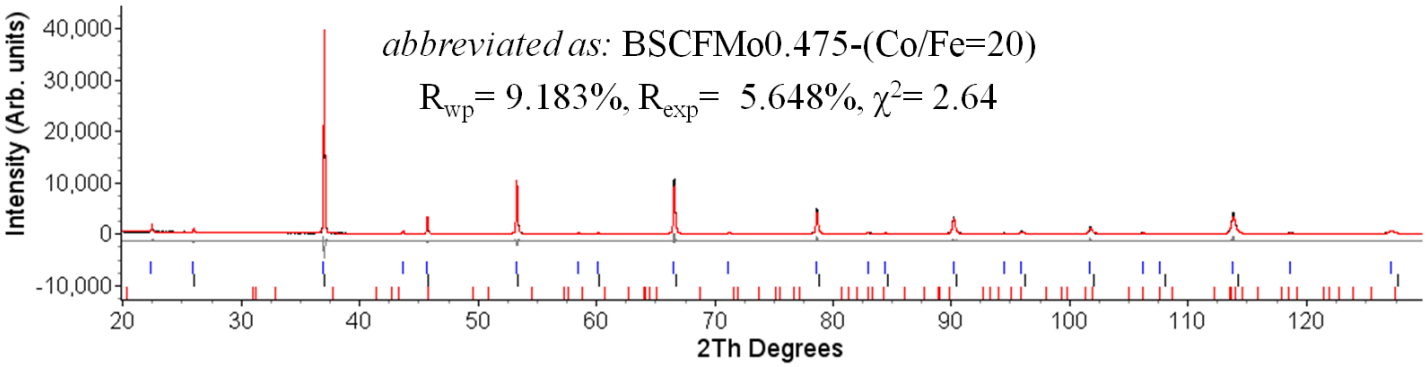

$Ba_{0.5}Sr_{0.5}Co_{0.500}Fe_{0.00}Mo_{0.50}O_3$

abbreviated as: BSCFMo0.5-(Co/Fe=∞)

R_{wp}= 15.044%, R_{exp}= 9.575%, χ^2= 2.47